SISSA **ISAS**

SCUOLA INTERNAZIONALE SUPERIORE DI STUDI AVANZATI
INTERNATIONAL SCHOOL FOR ADVANCED STUDIES

Relic Signatures of Reionization Sources

Thesis submitted for the degree of
Doctor Philosophiæ

CANDIDATE:
Michela Mapelli

SUPERVISOR:
Prof. Andrea Ferrara

October 2006

Si fallor, sum. Nam qui non est utique nec falli potest.

(Augustine of Tagaste)

Table of Contents

Title Page i
Table of Contents v
Citations to Previously Published Works ix

1 The cosmic reionization **1**
1.1 Introduction 1
1.2 Observational constraints 1
1.3 Sources of reionization 6
1.4 Relic signatures of reionization sources 18

2 Population III stars and the near infrared background (NIRB) **25**
2.1 Introduction 25
2.2 Observations of the extragalactic background light (EBL) 26
2.3 First stars and NIRB excess 29
2.4 The photon-photon absorption 31
2.4.1 Summary of the adopted EBL models 34
2.5 TeV blazar spectra 36
2.6 Results 37
2.6.1 Galaxy counts only 37
2.6.2 Including a NIRB excess 39
2.6.3 Including the optical excess 41
2.6.4 An alternative analysis 41
2.7 Conclusions 48

3 Intermediate mass black holes **50**
3.1 Introduction 50
3.2 How do IMBHs form? 51
3.2.1 The final fate of metal free stars 52
3.2.2 Direct collapse of low angular momentum gas 54
3.2.3 Runaway collapse in young clusters 56
3.2.4 Repeated mergers of binary BHs 57
3.3 ULXs and IMBHs 58
3.4 Numerical simulations 60
3.4.1 Milky Way model 60

3.4.2 Intermediate mass black holes . . . 62
3.4.3 Description of runs . . . 66
3.5 IMBHs accreting molecular gas . . . 67
3.5.1 IMBH density constraints from ULXs . . . 67
3.5.2 Radial and luminosity distribution of ULXs . . . 70
3.5.3 Non ULX sources . . . 72
3.6 IMBHs accreting atomic hydrogen . . . 74
3.7 Comparison with observations . . . 78
3.8 Conclusions . . . 81

4 Intermediate mass black holes in globular clusters 83
4.1 Introduction . . . 83
4.2 Candidate IMBHs in globular clusters . . . 83
4.2.1 G1 and M15 . . . 83
4.2.2 NGC 6752: the pulsar PSR J1911-5958A . . . 84
4.3 Dynamical signatures of IMBHs in globular clusters: suprathermal stars and angular momentum alignment . . . 86
4.3.1 How do three-body interactions work? . . . 86
4.3.2 What are suprathermal stars and angular momentum alignment? . . . 88
4.3.3 Our reference globular clusters: NGC 6752 and M4 . . . 89
4.3.4 The simulations . . . 90
4.3.5 Suprathermal stars . . . 91
4.3.6 Angular momentum transfer and alignment . . . 94
4.3.7 Detecting suprathermal stars and angular momentum alignment . . . 98
4.3.8 Summary . . . 106

5 Dark matter decays and annihilations 107
5.1 Introduction . . . 107
5.2 Method . . . 109
5.3 Heavy cold dark matter . . . 111
5.3.1 Gravitinos . . . 111
5.3.2 Heavy dark matter: neutralinos . . . 113
5.4 Energy injection in the IGM for light particles (< 100 MeV) . . . 115
5.4.1 Photons . . . 116
5.4.2 Pair production . . . 118
5.4.3 The energy absorbed fraction . . . 123
5.5 Sterile neutrinos . . . 123
5.6 Light dark matter . . . 128
5.6.1 Decays . . . 129
5.6.2 Annihilations . . . 131
5.7 Effects on the CMB spectrum . . . 135
5.8 Conclusions . . . 138

6 Impact of dark matter on structure formation 140
6.1 Introduction . . . 140
6.2 Method . . . 142
6.2.1 The code . . . 142
6.2.2 DM profiles . . . 144
6.2.3 Treatment of the DM energy injection . . . 145
6.2.4 DM models . . . 147
6.2.5 The free-streaming/damping lengths . . . 152
6.2.6 The simulations . . . 153
6.3 IGM evolution . . . 154
6.3.1 Chemistry and temperature . . . 155
6.3.2 Jeans mass . . . 155
6.4 Evolution inside halos . . . 157
6.4.1 Chemistry and temperature . . . 157
6.4.2 Critical mass . . . 159
6.5 Discussion . . . 161
6.5.1 Gas fraction . . . 161
6.5.2 Concentration and local contribution . . . 163
6.6 Conclusions . . . 165

A Initial conditions for the N-body model of the Milky Way 167
A.1 Bulge . . . 167
A.2 Disk . . . 168
A.3 Halo . . . 171

B Initial conditions for three body encounters 173
B.1 Range of the initial parameters . . . 174
B.2 Probability distribution of the initial parameters . . . 176
B.3 The initial conditions . . . 177

C Upper limits on sterile neutrino mass 179
C.0.1 Photon flux from neutrino decays . . . 179
C.0.2 X-ray background radiation . . . 183

D Absorbed energy fraction for LDM and sterile neutrinos 189
D.0.3 Sterile neutrinos . . . 189
D.0.4 Light Dark Matter . . . 190

E Blue stragglers: radial distribution and progenitors 192
E.1 Introduction . . . 192
E.2 The simulations . . . 194
E.3 The sample of globular clusters . . . 198
E.4 Results and Discussion for M3, 47 Tuc and NGC 6752 . . . 199
E.4.1 M3 . . . 200
E.4.2 47 Tuc . . . 200

E.4.3 NGC 6752 201
E.4.4 The location of the minimum in the BSS radial distributions 202
E.5 The case of ω Centauri 204
E.6 Number of BSS versus M_V 206
E.7 Summary 209

Bibliography **211**

Citations to Previously Published Works

Part of the contents of this Thesis has already appeared in the following papers:

Refereed Journals:

- *Probing the Presence of a Single or Binary Black Hole in the Globular Cluster NGC 6752 with Pulsar Dynamics.*
  Colpi M., **Mapelli M.** & Possenti A., 2003, ApJ, **599**, 1260.
- *The Contribution of Primordial Binaries to the Blue Straggler Population in 47 Tucanae.*
  Mapelli M., Sigurdsson S., Colpi M., Ferraro F. R., Possenti A., Rood R. T., Sills A. & Beccari G., 2004, ApJL, **605**, 29.
- *Background radiation from sterile neutrino decay and reionization.*
  Mapelli M. & Ferrara A., 2005, MNRAS, **364**, 2.
- *The fingerprint of binary intermediate mass black holes in globular clusters: suprathermal stars and angular momentum alignment.*
  Mapelli M., Colpi M., Possenti A. & Sigurdsson S., 2005, MNRAS, **364**, 1315.
- *Gamma-ray constraints on the infrared background excess.*
  Mapelli M., Salvaterra R. & Ferrara A., 2006, NewAr, **11**, 420.
- *Constraints on Galactic Intermediate Mass Black Holes.*
  Mapelli M., Ferrara A. & Rea N., 2006, MNRAS, **368**, 1340.
- *Impact of dark matter decays and annihilations on reionization.*
  Mapelli M., Ferrara A. & Pierpaoli E., 2006, MNRAS, **369**, 1719.
- *The radial distribution of blue stragglers and the nature of their progenitors.*
  Mapelli M., Sigurdsson S., Ferraro F. R., Colpi M., Possenti A. & Lanzoni B., MNRAS, in press
- *Intergalactic medium heating from dark matter.*
  Ripamonti E., **Mapelli M.** & Ferrara A., MNRAS, accepted

Submitted papers:

- *The impact of dark matter decays and annihilations on the formation of the first structures.*

Ripamonti E., **Mapelli M.** & Ferrara A., MNRAS, submitted

In Preparation:

– *Intermediate mass black holes in dwarf galaxies: the case of Holmberg II.*
Mapelli M.

Proceedings:

– *Is NGC 6752 Hosting a Single or a Binary Black Hole?.*
Colpi M., **Mapelli M.** & Possenti A., 2004, Carnegie Observatories Astrophysics Series, Vol. 1: Coevolution of Black Holes and Galaxies, ed. L. C. Ho, astro-ph/0302545.

– *Extragalactic Background Light: new constraints from the study of the photon-photon absorption on blazar spectra.*
Mapelli M., Salvaterra R. & Ferrara A., 2004, Proceedings of "Baryons in Dark Matter Halos", 5-9 October 2004, Novigrad, Croatia, astro-ph/0411134.

– *The Dynamical Fingerprint of Intermediate Mass Black Holes in Globular Clusters.*
Colpi M., Devecchi B., **Mapelli M.**, Patruno A. & Possenti A., 2005, Invited review in: "Interacting binaries", July 4-10 Cefalu, eds. Antonelli et al., to be published with AIP, astro-ph/0504198.

Chapter 1

The cosmic reionization

1.1 Introduction

In a seminal paper, Gunn & Peterson (1965) showed that the hydrogen in a diffuse uniform inter galactic medium (IGM) must have been ionized at redshift $z \gtrsim 2$, in order to avoid complete absorption of the transmitted flux at wavelengths bluewards of the Lyα emission line of the quasars (QSOs). This is, historically, the first evidence that the Universe has been reionized at some point after the recombination epoch ($z \sim 1100$). This process, universally known as reionization, has been intensely studied in the last decade, but it is far from being understood. In particular, we do not know yet when reionization exactly began, how long it lasted and what sources have been able to reionize the Universe.

In this chapter I firstly summarize the main observational constraints and the possible sources of reionization. Then, I will discuss the relic features of reionization which could be detected today.

1.2 Observational constraints

QSO absorption lines

The Sloan Digital Sky Survey (SDSS; http://www.sdss.org/) has discovered a certain number of QSOs at $z \gtrsim 6$, whose spectra show very long absorption troughs (Becker et al. 2001;

Djorgovski et al. 2001; Fan et al. 2001, 2002, 2003; White et al. 2003). Considering that all the spectra of QSOs at $z < 6$ do not show significant absorption, this means that at $z \gtrsim 6$ the fraction of neutral hydrogen starts increasing. Then, from SDSS we conclude that the reionization must be nearly complete at $z \sim 6$. However, from the SDSS we cannot derive any further information about the behavior of the IGM neutral hydrogen fraction ($x_{HI} = n_{HI}/(n_{HI} + n_{H+})$, where n_{HI} and n_{H+} are the density of neutral and ionized hydrogen respectively) at $z \gtrsim 6$. In fact, even a neutral fraction $x_{HI} \sim 10^{-3}$ would produce an optical depth higher than what is required to achieve the observed troughs.

In addition, there is a marked dependence of the troughs on the line of sight. For example, the analysis of the spectrum of the most distant known QSO (SDSS J1148+5251; $z = 6.37$) shows some residual flux both in the Lyα and Lyβ troughs (Furlanetto & Oh 2005); whereas in the spectrum of the quasar SDSS J1030+0524 ($z = 6.28$) no transmitted flux is detected over a large region (300 $\mathring{A}$) blueward of the Lyα emission line (Becker et al. 2001). In general, reionization is described as divided into a 'pre-overlap' phase (where the hydrogen is ionized only in bubbles surrounding the sources), an 'overlap' phase (where these bubbles start overlapping) and a 'post-overlap' phase (where most of the volume of the Universe is ionized). In this scenario, the differences in the ionization state of the IGM along different lines of sight observed in the SDSS quasars have been interpreted as a possible signature of the 'pre-overlap' phase of the reionization.

Cosmic microwave background radiation

The reionization can affect both the temperature and polarization power spectrum of the cosmic microwave background (CMB). In the case of the CMB temperature power spectrum, the reionization can damp the fluctuations on small scales due to photon diffusion in the ionized plasma. In particular, the scattering of electrons on CMB photons suppresses the anisotropies on angular scales below the horizon at the reionization epoch, by a damping factor $e^{-\tau_e}$. τ_e is the Thomson optical depth, defined by:

$$\tau_e = \sigma_T \, c \int_0^z \mathrm{d}t \, x_e \, n_b \, (1+z)^3, \tag{1.1}$$

where σ_T is the Thomson optical depth, c the light speed, x_e the ionization fraction at redshift z and n_b the current density of baryons ($n_b = 2.5 \times 10^{-7}$ cm^{-3}, Spergel et al. 2006).

However, it is difficult to measure τ_e from the damping in the temperature-temperature (TT) power spectrum, because there is a strong degeneracy between the spectral index n_s (which parameterizes the dark matter fluctuation power spectrum) and τ_e itself.

Luckily, the reionization acts also on the CMB polarization. The polarization can be generated only at scales smaller than the photon mean free path (otherwise the plasma is too homogeneous due to multiple scattering) and larger than the Silk length (otherwise perturbations are suppressed by Silk damping). The photon mean free path at the last scattering surface is of the order of the horizon size, which corresponds to a multipole number $l \sim 100$. Then, polarization signatures at larger scales (i.e. multipoles $l < 100$) cannot be originated at the last scattering surface. Instead they are due to later processes such as reionization (Choudhury & Ferrara 2006a). In particular, the reionization increases the mean free path for photons and, consequently, the CMB polarization. For models with sudden reionization at redshift z_{re}, it can be shown that the polarization signal peaks at a position $l \propto z_{re}^{1/2}$ with an amplitude proportional to the total optical depth τ_e. Thus both the polarization-polarization (EE) and the temperature-polarization (TE) power spectrum are sensitive probe of the reionization at low multipoles.

After the first reliable detection of CMB temperature anisotropies by the COsmic Background Explorer (COBE) satellite (Smoot et al. 1992), many experiments have improved our knowledge of CMB power spectra. Among them, we can cite the Balloon Observations Of Millimetric Extragalactic Radiation and Geomagnetics (BOOMERanG), the Millimeter Anisotropy eXperiment IMaging Array (MAXIMA) and the Degree Angular Scale Interferometer (DASI). However, these experiments are able only to give upper limits for τ_e (see MacTavish et al. 2006 for BOOMERANG). The first possibly accurate evaluation of τ_e has been allowed by the more recent Wilkinson Microwave Anisotropy Probe (WMAP). The best fit of τ_e after the first year of WMAP observations was 0.17 ± 0.04 (Spergel et al. 2003; Kogut et al. 2003), which suggested a very early reionization ($z \sim 17$ assuming sudden reionization). However, 2 more years of observations and an improved model of foreground subtraction strongly changed this result. In fact, the value of τ_e indicated by the recent three year WMAP results (Spergel et al. 2006; Page et al. 2006) is 0.09 ± 0.03, significantly lower than the first year evaluation, and consistent with a sudden

reionization at $z \sim 11$. This result mainly comes from a more accurate measurement of the TE power spectrum (see Fig. 1.1; bottom panel) with respect to first year WMAP results (Spergel et al. 2003; Kogut et al. 2003). Instead, the measurement of the EE spectra is still subject to many uncertainties about the subtraction of the Galactic foreground[1] (Fig. 1.1; central panel).

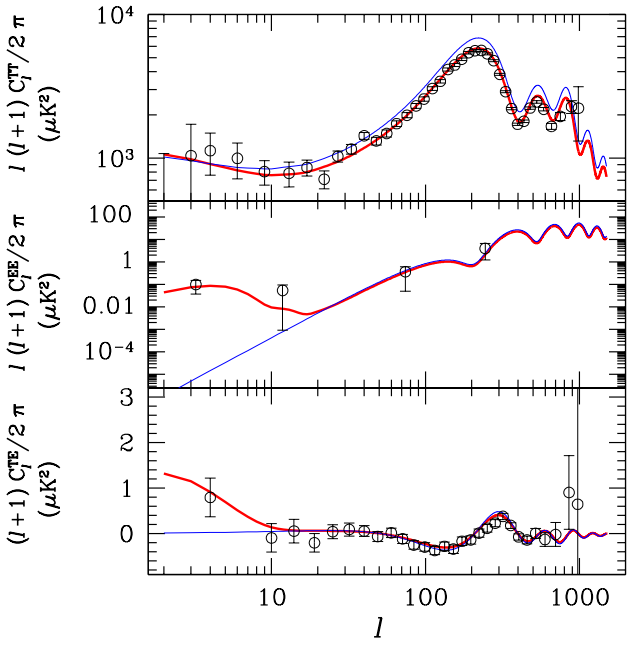

Figure 1.1: Temperature-temperature (top panel), polarization-polarization (central panel) and temperature-polarization (bottom panel) spectra. Open circles in all the panels indicate the three year WMAP data (Hinshaw et al. 2006; Page et al. 2006; Spergel et al. 2006). Thick red lines indicate the CMB spectrum derived assuming Thomson optical depth $\tau_e = 0.09$ and a sudden reionization model (consistent with the three year WMAP data); thin blue lines indicate the CMB spectrum derived assuming $\tau_e = 0$. The spectra have been calculated using CMBFAST (Seljak & Zaldarriaga 1996).

Lyα emitters at high redshift

Lyα emission by galaxies at redshift higher than the reionization redshift is expected to be suppressed by neutral hydrogen absorption. Then, the luminosity function of Lyα emitters

[1] A complex template of the Milky Way was required in order to subtract the foreground in the EE spectra (Page et al. 2006).

should be strongly modified by the reionization epoch (Furlanetto, Hernquist & Zaldarriaga 2004; Malhotra & Rhoads 2004; Haiman & Cen 2005). The Lyα emission line luminosity function of star forming galaxies at high redshift ($z \sim 6-7$) has been recently studied (Malhotra & Rhoads 2004; Stern et al. 2005). It was found that the neutral hydrogen fraction should be less than 50% at $z = 6.5$ (Malhotra & Rhoads 2006). This technique presents some disadvantages (such as the bias due to the clustering of bright galaxies and to the extension of the ionized region surrounding them) with respect to other methods.

High redshift Gamma Ray Bursts (GRBs)

Gamma Ray Bursts (GRBs) at high redshift can give important information about the neutral fraction of the surrounding gas. For example, the highest redshift ($z = 6.3$) detected GRB can be fit by assuming $x_{HI} < 0.17$ (at 68%; Totani et al. 2006). Unfortunately, also this measurement can be biased by the extension of the ionized region surrounding the GRB progenitor. The statistics of high redshift GRBs could also be employed to constrain the number of primordial massive stars, which is a critical point to understand reionization sources (Weinmann & Lilly 2005; Wise & Abel 2004; see next section). Furthermore, it is necessary, in order to improve this method, to widen the number of high redshift GRBs.

21 cm emission

A new generation of radio telescopes [LOw Frequency ARray (LOFAR); Primeval Structure Telescope (PAST); Square Kilometre Array (SKA)] is being built in order to map fluctuations in the neutral hydrogen density during the (pre-)ionization era, by observing the 21 cm line emission (Ciardi & Madau 2003). This is the neutral hydrogen hyperfine transition line, and its intensity, in emission or absorption, depends only on the coupling between the spin temperature of the gas and either the temperature of the CMB or the kinetic temperature of the gas. The study of the angular power spectrum of the brightness temperature fluctuations could be a direct way to know the neutral hydrogen distribution.

1.3 Sources of reionization

Not only the epoch of reionization but also the nature of the ionizing sources remains an open problem. Is the radiation from high redshift stars sufficient to produce the reionization or do we have to invoke more exotic sources (such as miniquasars or decaying particles)? If stars are sources of reionization, what sort of stars are they? In the following, we will briefly review the main candidates for the cosmic reionization.

Population III stars

The first generation of stars must have formed from metal-free primordial mixture, because most of the heavier elements cannot be synthesized without nuclear burning. So, they are referred as "metal-free" or population III stars (while solar metallicity stars are called population I stars and globular cluster-like metallicity stars are called population II stars; Baade 1944).

No direct observations of metal free stars are available. The more metal poor stars detected in the Milky Way, HE 0107-5240 (Christlieb et al. 2002) and HE 1327-2326 (Frebel et al. 2005), have metallicity sensibly higher than zero. In fact they are quite iron poor ([Fe/H]=-5.3±0.2 and [Fe/H]=-5.4±0.2, respectively), but considerably carbon rich ([C/Fe]=3.6±0.2 and [C/Fe]=4.1±0.2, respectively). So they could be either self-enriched first generation population III (hereafter pop III) stars or could be born from gas already polluted by a previous star formation episode. However, the first hypothesis seems unlikely (Christlieb et al. 2004; Aoki et al. 2006), and these two stars are thought to be 'second generation'. Many attempts have been done to infer the mass function and the evolution (*e.g.* chemical pollution, winds and supernova explosion) of first generation stars from the abundances of HE 0107-5240 and HE 1327-2326 (see Fig.1.2). For example, Iwamoto et al. (2005) suggest that 'faint' supernovae of $\sim 25\,M_{\odot}$ pop III stars, implying the fallback of gas into a compact object, can reproduce the metallicity pattern of HE 0107-5240 and HE 1327-2326; whereas pair-instability supernovae of more massive ($\sim 100-260\,M_{\odot}$ pop III stars) lead to a very different chemical composition. In general, the abundance patterns suggest pre-enrichment produced by pop III stars in the mass range 20-130 $M_{\odot}$ (Umeda &

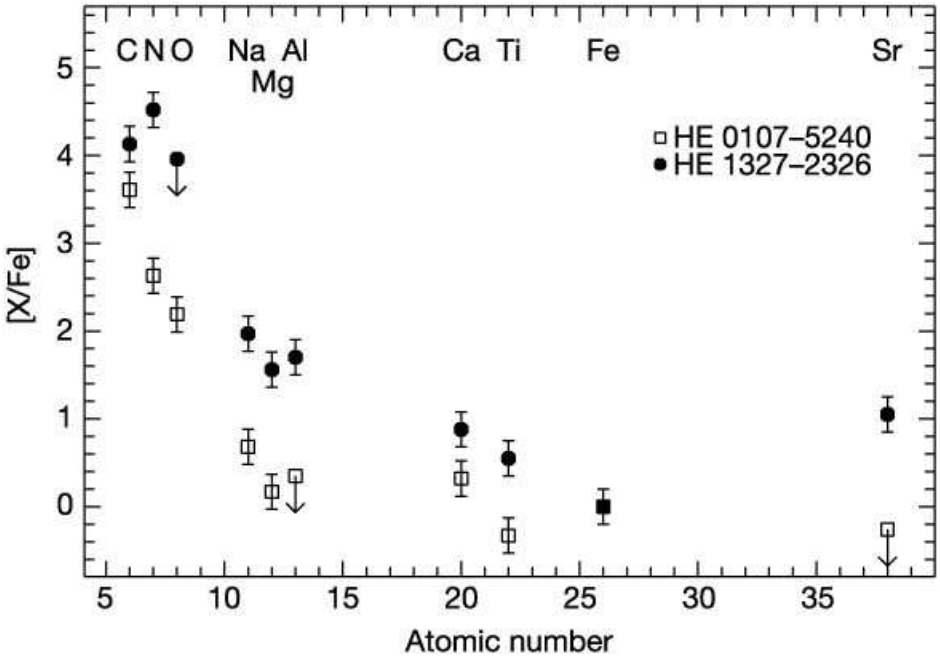

Figure 1.2: Abundance patterns of HE1327-2326 (filled circles) and HE0107-5240 (open squares). Typical 1-σ errors are shown in the plot. Upper limits are indicated by an arrow. The values are obtained by adopting $[Fe/H]_{non-LTE}$ = -5.2 (Christlieb et al. 2002; Frebel et al. 2005) as the iron abundance for HE0107-5240. These two most Fe-poor stars both have very large C enhancement relative to Fe by a factor of 5000 (HE0107-5240) and 10000 (HE1327-2326). N/Fe is 30000 times the solar value (considering the subgiant solution) in HE1327-2326, whereas it is 200 times the solar value in HE0107-5240. The upper limit for the O abundance of HE1327-2326 is [O/Fe] $<$ 4.0. Oxygen in HE0107-5240 has recently been determined to be [O/Fe] = 2.3, which is of the same order as its [N/Fe] value. These enormous overabundances in CNO elements suggest that both stars belong to a group of objects sharing a common formation scenario. HE1327-2326 and HE0107-5240 have Ca/Fe and Ti/Fe abundance ratios that are enhanced by factors of less than 10 compared to the Sun. The light-element ratios Na/Fe, Mg/Fe and Al/Fe, as well as, surprisingly, Sr/Fe, are all enhanced by factors of 10 to 100 in HE1327-2326. Of these four elements, only Na and Mg are detected in HE0107-5240, with element/Fe ratios close to the solar value. As for several other elements, an upper limit for Ba has been measured in both stars. The Sr/Ba ratio is crucial to identify the origin for the Sr and other heavy elements (from Frebel et al. 2005).

Nomoto 2005). However, these hypotheses can explain the origin of these two stars; but do not exclude the existence of pair-instability supernovae and of more massive pop III stars.

Thus, due to the lack of direct observations, the initial mass function, the formation redshift, the spatial distribution (clustered in small galaxies or isolated in mini-halos), the

final fate ('faint' supernova, pair-instability supernova or direct collapse?) and the other properties of pop III stars are highly uncertain, and have been studied mainly from a theoretical point of view.

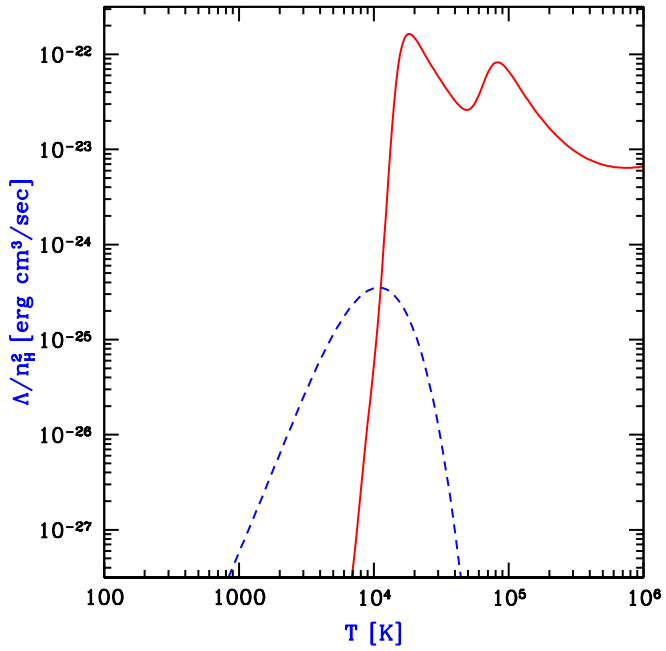

Figure 1.3: Cooling rate per atomic mass unit of metal-free gas as a function of temperature. The solid line assumes the gas to be completely atomic; the dashed line shows the contribution of a small (f_{H_2}=10^{-3}) fraction of molecular hydrogen (from Barkana & Loeb 2001).

The first question to address is what is the mechanism that allows pop III stars to form in a metal free Universe. In fact, in the present-day Universe gaseous clouds can collapse and coalesce into stars thanks to the cooling from dust and metals. But what happens if there are no metals to drive the cooling? In metal free small halos (i.e. with virial temperature $T_{vir} \lesssim 10^4$ K) the main coolant agent is represented by H_2 (see Fig. 1.3). Its cooling properties are poor if compared not only to metals, but also to other molecules, because H_2 has no dipole moment and emits only via quadrupole transitions. Its importance as a coolant arises from its high abundance ($\gtrsim 10^{-4}$) if compared to other molecules (*e.g.* HD).

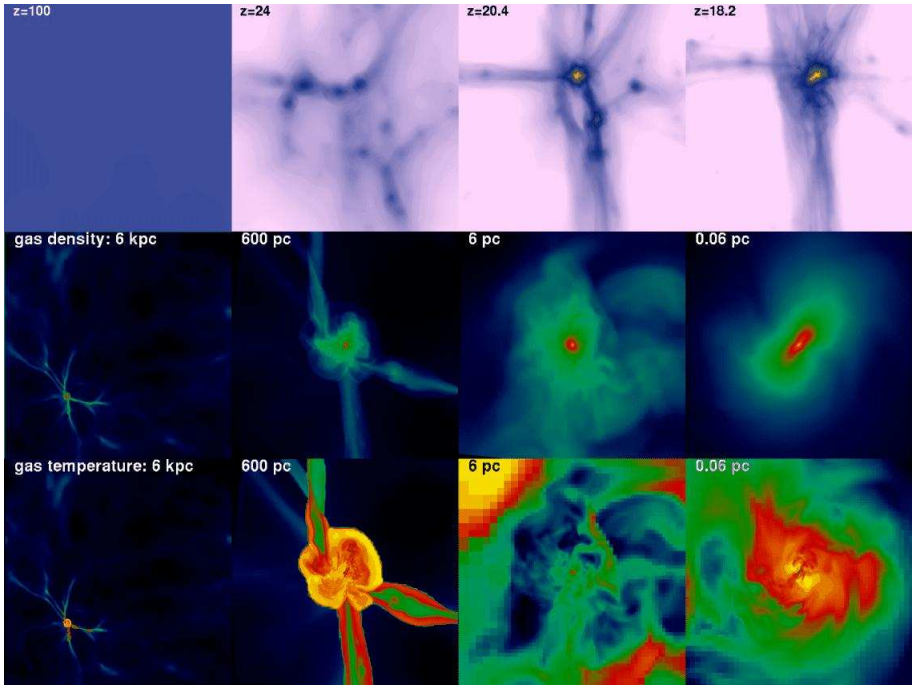

Figure 1.4: Overview of the evolution leading to the formation of a primordial star. The top row shows the gas density, centered at the pre-galactic object within which the star is formed. The four projections are labelled with their redshifts. Pre-galactic objects form from very small density fluctuations and continuously merge to form larger objects. The middle and bottom rows show thin slices through the gas density and temperature at the final simulation stage. The four pairs of slices are labelled with the scale on which they were taken, starting from 6 (proper) kpc (the size of the simulated volume) and zooming in down to 0.06 pc (12,000 AU). In the left panels, the larger scale structures of filaments and sheets are seen. At their intersections, a pre-galactic object of $\sim 10^6\,M_\odot$ is formed. The temperature slice (second panel, bottom row) shows how the gas shock heats as it falls into the pre-galactic object. After passing the accretion shock, the material forms H_2 molecules and starts to cool. The cooling material accumulates at the centre of the object and forms the high-redshift analog to a molecular cloud (third panel from the right), which is dense and cold ($T \sim 200K$). Deep within the molecular cloud, a core of $\sim 100\,M_\odot$, a few hundred K warmer, is formed (right panel) within which a $\sim 1\,M_\odot$ fully molecular object is formed (yellow region in the right panel of the middle row) (from Abel, Bryan & Norman 2002; see also Ripamonti & Abel 2004).

Hydro-dynamical simulations of the collapse of metal-free halos due to H_2 cooling (Bromm, Coppi & Larson 1999; Abel, Bryan & Norman 2000, 2002; Bromm, Kudritzki & Loeb 2001; Omukai & Palla 2001, 2002, 2003; Ripamonti et al. 2002) indicate that pop III stars should be very massive ($\gtrsim 100\,M_\odot$). In fact, three-dimensional simulations (Abel,

Bryan & Norman 2000, 2002) show that the initial halo fragments into a $\sim 100 - 1000\,M_{\odot}$ core, inhabited by a $1\,M_{\odot}$ molecular proto-star (see Fig.1.4 for details). The proto-star is likely to accrete all the gas in the $1000\,M_{\odot}$ core, since no efficient fragmentation mechanisms have been found (Omukai & Palla 2001, 2002, 2003; Ripamonti et al. 2002; Ripamonti & Abel 2004). So, the final mass of the star is expected to be $\gtrsim 100\,M_{\odot}$.

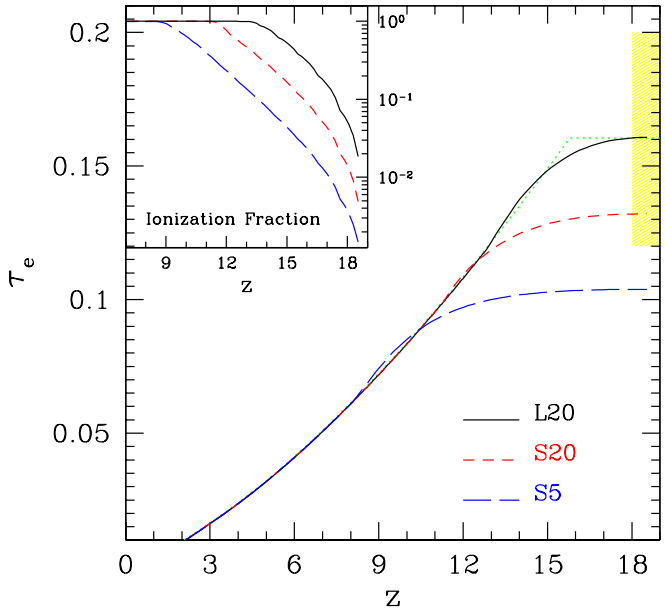

Figure 1.5: Redshift evolution of the electron optical depth, τ_e, assuming a Salpeter IMF and an escape fraction 0.05 (S5, long-dashed line) and 0.20 (S20, short-dashed), respectively, or assuming a Larson IMF and an escape fraction 0.20 (L20, solid). The dotted line refers to sudden reionization at $z = 16$. The shaded region indicates optical depth τ_e=0.16−0.04 (68% confidence level) implied by Kogut et al. (2003). In the inset the redshift evolution of the volume-averaged ionization fraction, x_V, is shown for the three models. Figure from Ciardi, Ferrara & White 2003.

This first star should form in isolation, at the center of the host minihalo (Abel, Bryan & Norman 2002), since its radiative feedback quenches further star formation in the father cloud. When this first object dies, unless the supernova explosion evacuates the surrounding gas, a second generation of stars is expected to form in the relic HII region produced by the first stars, thanks to the enhancement of molecular hydrogen abundance (O'Shea et al. 2005; Abel, Wise & Bryan 2006).

Very recently, Silk & Lager (2006) showed that magneto-rotational instabilities can induce fragmentation of metal free clouds. If confirmed, this would be the first proposed mechanism to form low mass ($\lesssim 10-100\,M_{\odot}$) metal free stars (but see also Tan & Blackman 2004 and Machida et al. 2006).

And what about first stars as sources of reionization? Do first stars need to be massive in order to reionize the Universe?

Ciardi, Ferrara & White (2003) show that pop III stars following a Salpeter Initial Mass Function (IMF), with masses up to 40 $M_{\odot}$, having a moderate escape fraction (5%, consistent with the value measured in the Milky Way, Dove & Shull 1994; Dove, Shull & Ferrara 2000) and hosted in $\sim 10^9\,M_{\odot}$ galaxies can produce a Thomson optical depth $\tau_e = 0.1$ (Fig. 1.5), fully consistent with the three year WMAP result ($\tau_e = 0.09$). Then, according to three year WMAP data, there is no need for exotic sources or heavy IMF or very massive pop III stars in order to reionize the Universe. The existence of massive metal free stars, even if not required to explain $\tau_e = 0.09$, is, nevertheless, not in contradiction with three year WMAP results (Choudhury & Ferrara 2006b).

In the next Chapter we will discuss one of the possible observational features of pop III stars, i.e. the hypothesis that the light emitted by first stars contributes to the near infrared background (NIRB).

Miniquasars

If first stars are very massive ($m > 260\,M_{\odot}$) their fate is to directly collapse into black holes (BHs) nearly without loosing mass (Heger & Woosley 2002; see Section 3.2). This can produce a population of Intermediate Mass Black Holes (IMBHs, i.e. BHs with mass $10^{1.3-5} M_{\odot}$), which, in the high density primordial Universe, are expected to efficiently accrete gas. Furthermore, the accretion of these IMBHs can be enhanced also during galaxy mergers, which tend to drive gas into the inner regions of the host galaxy (Madau et al. 2004; see Fig.1.6).

Recently, a completely different hypothesis for the formation of IMBHs at high redshift has been proposed: seed BHs can be produced by the direct collapse of dense, low angular momentum gas (Haehnelt & Rees 1993; Umemura, Loeb & Turner 1993; Loeb & Ra-

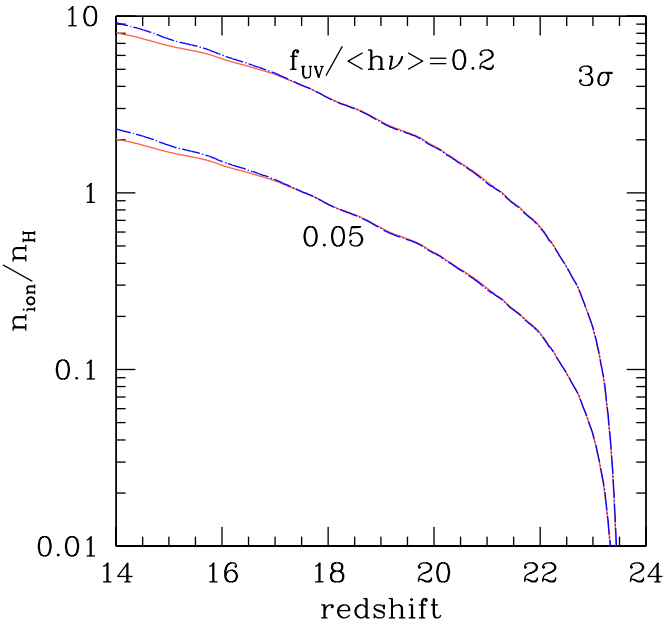

Figure 1.6: Cumulative number of ionizing photons per hydrogen atom produced by accreting IMBHs for different values of $f_{UV}/\langle h\nu\rangle$ (in units of ryd^{-1}), where f_{UV} is the fraction of the bolometric power radiated by a IMBH emitted as hydrogen-ionizing photons with mean energy $\langle h\nu\rangle$. *Solid curves:* in each major merger the BH in the main halo accretes a mass $\Delta m_{\rm acc} = 2m_{\rm BH}$. *Dashed curves:* same with $\Delta m_{\rm acc} = 10^{-3}\,M_h$. *Dotted curve:* same with $\Delta m_{\rm acc} = 10^{-3}\,M_h$, $f_{\rm UV}/\langle h\nu\rangle = 0.2\,{\rm ryd}^{-1}$, but with gas accretion suppressed in minihalos with virial temperature $T_{\rm vir} \leq 10^4\,{\rm K}$. From Madau et al. 2004.

sio 1994; Eisenstein & Loeb 1995; Bromm & Loeb 2003), driven by turbulence (Eisenstein & Loeb 1995) or gravitational instabilities (Koushiappas, Bullock & Dekel 2004; Begelman, Volonteri & Rees 2006; Lodato & Natarajan 2006). In particular, the so-called 'bars within bars' mechanism (Shlosman, Frank & Begelman 1989; Shlosman, Frank & Begelman 1990) implies that bars, which form in self-gravitating clouds under some assumptions, can transport angular momentum outwards on a dynamical time-scale via gravitational and hydrodynamical torques, allowing the radius to shrink. This shrinking produces greater instability and the process cascades. Begelman, Volonteri & Rees (2006) show that this process leads to the formation of a 'quasi-star', which rapidly collapses into a $\sim 20\,M_\odot$

BH at the center of the halo. The BH should encounter very rapid growth due to efficient gas accretion. Lodato & Natarajan (2006) generalize this model, investigating what is the range of spin parameter (Mo, Mao & White 1998), mass of the pre-galactic disk and stability parameter (Toomre 1964), for which gravitational instabilities take place, leading to the collapse of gas into a massive BH ($\lesssim 10^6\, M_\odot$). They conclude that $\sim$ 5% of disks resulting from the collapse of $\sim 10^7\, M_\odot$ halos should host a $\sim 10^5\, M_\odot$ BH.

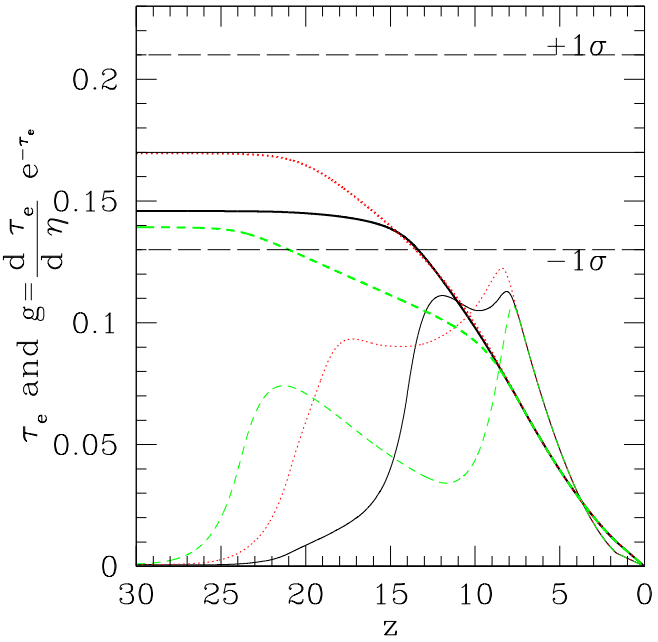

Figure 1.7: Thomson scattering optical depth, τ_e, and visibility function, $g(z)$, as a function of redshift, in the case of a pre-ionization due to IMBHs followed by a complete reionization by pop III and II stars (from Ricotti & Ostriker 2004). The fraction of stellar mass that collapses into BHs is 0.2 (solid line), 2 (dotted) and 20 % (dashed), respectively; while the duration of the X-ray burst for the IMBHs is 100 (solid line), 10 (dotted) and 1 Myr (dashed), respectively. The horizontal solid line represents the best value for τ_e from Kogut et al. (2003).

Whatever is their formation mechanism, the spectrum of IMBHs is harder than stellar spectra, leading to a significant production of soft X-ray photons (Madau et al. 2004; Ricotti & Ostriker 2004). These photons have high escape fraction and are particularly efficient in ionizing the dense IGM. In particular, Madau et al. (2004) show that, under reasonable assumptions, IMBHs emit 1-10 ionizing photons per baryon at redshift ~ 15, a

number sufficient to ionize the Universe (Fig. 1.6).

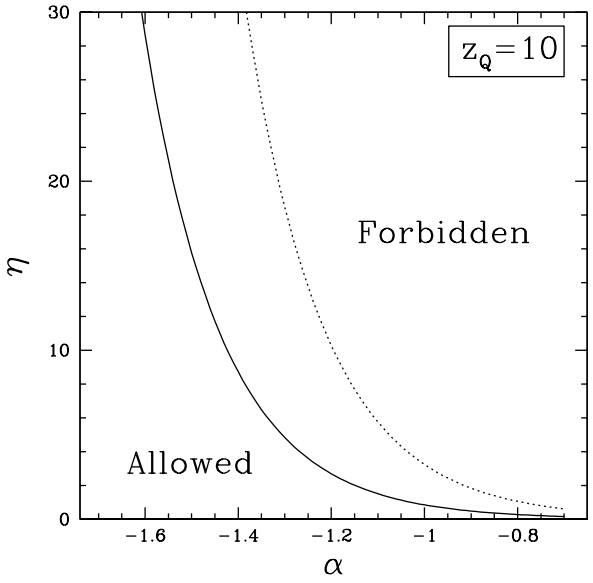

Figure 1.8: Constraints on the number of ionizing photons per H atom, η, and the power-law index for the slope of the ionizing background, α, based on the intensity of the present-day soft X-ray background. The mini-quasars are assumed to form at $z = 10$. The curves bracket the allowed parameter space for the mean (solid line) or maximum (dotted) unaccounted flux in the soft X-ray background. From Dijkstra, Haiman & Loeb (2004).

However, due to the high recombination rate at high redshift, high redshift IMBHs can achieve only partial early reionization. In order to have complete reionization, additional sources (*e.g.* stars) at lower redshift ($z \sim 7$) are required (Ricotti & Ostriker 2004; see Fig. 1.7).

At present, the only constraint on the role of IMBHs in reionizing the Universe comes from the comparison with the unaccounted fraction of the X-ray background (Moretti et al. 2003; Bauer et al. 2004). Dijkstra, Haiman & Loeb (2004) show that high redshift IMBHs are expected to produce a significant flux of hard X-ray photons, which should contribute to the observed soft ($\sim 0.5 - 2$ keV) X-ray background. By imposing that the flux due to IMBHs does not overproduce the unaccounted soft X-ray background, Dijkstra,

Haiman & Loeb (2004) found that models in which $z > 6$ accreting IMBHs significantly contribute to reionization are not allowed (Fig.1.8). Models in which IMBHs are assumed to partially ionize the IGM up to a ionization fraction ~ 0.5 at $6 \lesssim z \lesssim 20$ are still allowed; but could be severely constrained by improved determinations of the unaccounted X-ray background.

However, the number, the masses and the very existence of these IMBHs are still uncertain (for a discussion of these problems see Chapter 3 and 4).

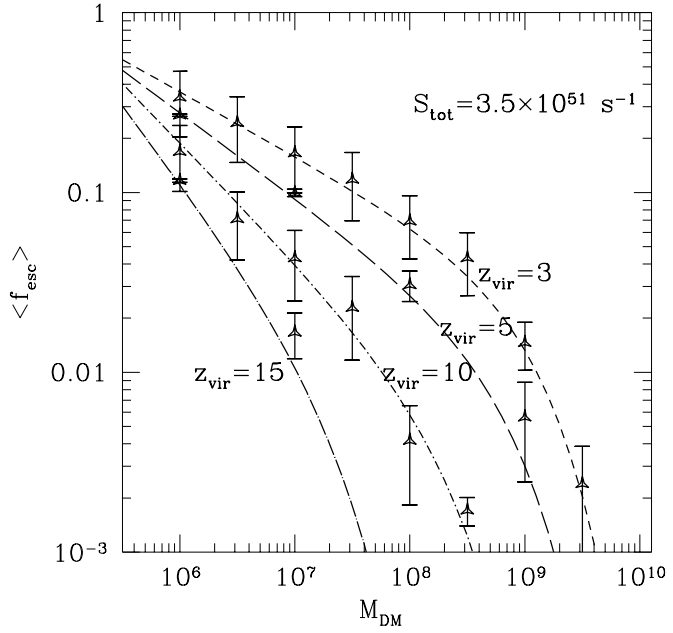

Figure 1.9: Escape fraction $\langle f_{esc} \rangle$ of ionizing photons as a function of the mass of the dark matter halo for a constant starburst that produces 3.5×10^{51} ionizing photons per second. Each point is the mean of five Monte-Carlo simulations with identical parameters; the error bars show the variance of the mean. The four curves refer to virialization redshifts from $z_{vir} = 3$ to 15. From Ricotti & Shull 2000.

Globular clusters/Low mass galaxies

Globular clusters and low mass primordial galaxies inhabited by population II stars are a viable reionization source, thanks to their high escape fraction of ionizing photons, $\langle f_{esc} \rangle$ (Ricotti & Shull 2000; Ricotti 2002, 2004; see Fig. 1.9). In fact, most of photons that escape

the halo of spiral galaxies like the Milky Way come from the most luminous OB associations located in the outermost parts of the galaxy. Thus, a star formation history which favors the formation of OB associations enhances $\langle f_{esc} \rangle$, contributing to the reionization. In such model, globular clusters can be the relics of those reionization sources: they have an age consistent with the reionization epoch, and represent the high luminosity tail of the initial distribution of OB associations. In fact, less massive OB associations are disrupted by the tidal field of galaxies, while globular clusters can survive, thanks to their high central densities.

However, the radiative feedback induced by the reionization can strongly suppress star formation in these small mass systems (Bullock, Kravtsov & Weinberg 2000; Moore et al. 2006). Then, the possible role of globular clusters on reionizing the Universe critically depends on various parameters, such as the epoch and the duration of reionization.

Particle decays/annihilations

Sufficiently light dark matter particles (i.e. with mass $\lesssim 100$ MeV) can decay remaining viable dark matter candidates. This is the case of sterile neutrinos (with mass of a few keV; Mapelli, Ferrara & Pierpaoli 2006) and the so called Light Dark Matter (LDM, with mass 1-100 MeV; Hooper & Wang 2004; Mapelli et al. 2006).

Sufficiently massive dark matter particles ($> 0.5\,\mathrm{MeV}$) can annihilate, producing e^+e^- pairs, photons or other particles (depending on their mass).

A schematic representation of the dark matter decays and annihilations considered in this Thesis is given in Fig. 1.10.

Both decays and annihilations can, directly or indirectly, produce ionizing photons. The effect of dark matter decays is quite different from that of annihilations. Dark matter decays start to influence ionization and heating at redshift $z \lesssim 100$ and their effect rapidly increases as the redshift decreases (as an example, see Fig. 1.11 for sterile neutrino decays). Instead, annihilations start producing some effect at redshift as high as 900, and do not give any substantial contribution at low redshift. As a consequence, the fraction of free electrons due to annihilations remains nearly constant in time (see Fig. 1.12 for LDM annihilations). This difference is mainly due to the fact that the annihilation rate scales as the square of

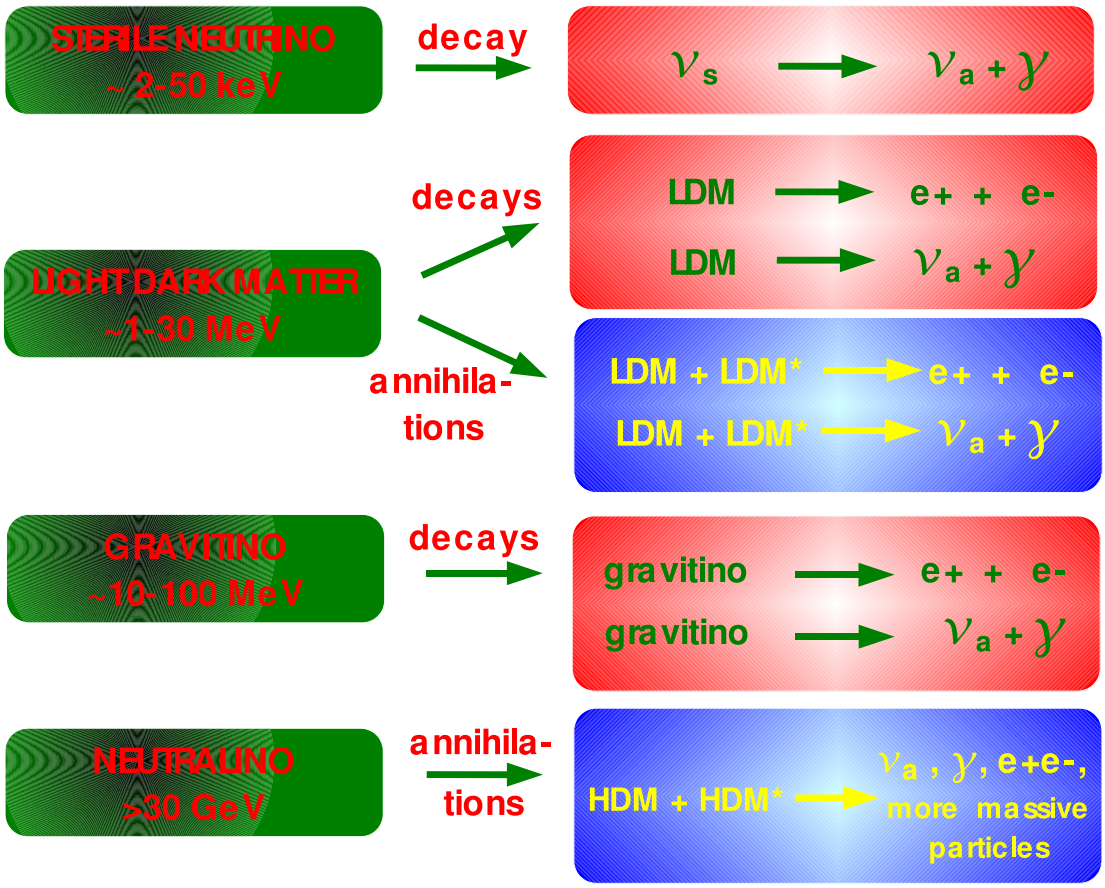

Figure 1.10: Scheme of the dark matter decays and annihilations considered in this Thesis. Green boxes indicate different dark matter particles; red (blue) boxes represent various decay (annihilation) channels. See Chapter 5 for more details on each model. The symbols ν_s, ν_a, γ, LDM and HDM indicate sterile neutrinos, active neutrinos, photons, light dark matter and neutralinos (i.e. heavy dark matter), respectively. The symbol $*$ (after LDM or HDM) indicates anti-particles.

the particle density; whereas the decay rate is proportional to the particle density.

However, the contribution of both decays and annihilations is not sufficient to achieve complete ionization (Chen & Kamionkowski 2004; Mapelli & Ferrara 2005; Biermann & Kusenko 2006; Mapelli et al. 2006). Nevertheless, particle decays and annihilations remain possible sources of early partial reionization and can also affect the behavior of matter temperature and the formation history of first luminous objects (see Chapter 5).

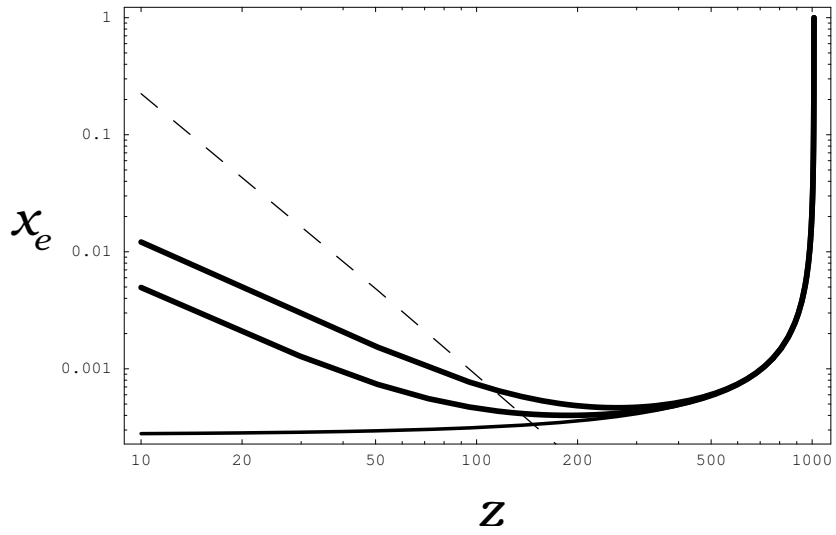

Figure 1.11: The fraction of ions, x_e, in the absence of sterile neutrinos (thin line), and for the dark-matter sterile neutrinos with masses 4 and 7 keV (lower and upper thick lines, respectively). Also shown is the limit of baryon decoupling from CMB (dashed line). From Biermann & Kusenko 2006.

1.4 Relic signatures of reionization sources

In the previous Section, I briefly reviewed the most popular reionization sources and their effect on reionization. However, the direct detection of these sources is still a challenging task. For example, the next generation of infrared telescopes (such as the James Webb Space Telescope, JWST, `http://www.jwst.nasa.gov/`) might be able to observe the first metal free stars (Gardner et al. 2006) or at least their supernova explosions (Weinmann & Lilly 2005; Wise & Abel 2005). As an alternative to direct measurements, one can think whether reionization sources leave other detectable signatures, independent of reionization, on the present-day Universe. These signatures can be dubbed as '*relics*', in the sense that they are the remnants of sources which produced some effect on the thermal history of the Universe at high redshift. Searching for relic signatures is an important issue to understand reionization, since it allows to find independent information about primordial sources.

In this thesis I will focus on the search of relic signatures of reionization, studying the following topics (see Fig. 1.13 for a schematic representation).

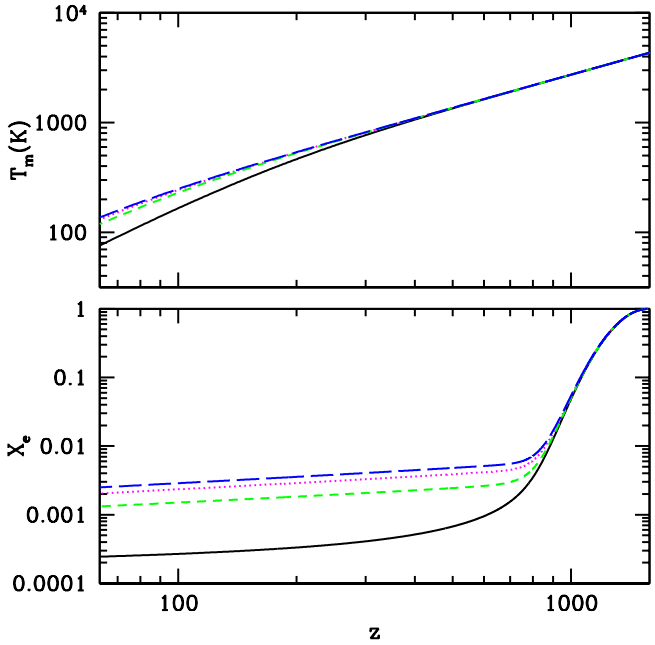

Figure 1.12: Ionized fraction (bottom panel) and gas temperature (upper) as a function of redshift. The black solid line represents the unperturbed case (without dark matter annihilations). The green short-dashed, pink dotted and blue long-dashed line represent the cases with dark matter annihilations and intensity parameter F_{26} =1.0, 2.6 and 4.0, respectively. I remind that the intensity parameter is defined as the annihilation cross section times the fraction of energy which is absorbed by gas times the mass-energy of the annihilating particle (Zhang et al. 2006). From Zhang et al. 2006.

Near infrared background and pop III stars (Chapter 2)

Part of the radiation emitted in the optical/UV range by pop III stars is expected to be redshifted to infrared wavelengths in the local Universe (Santos, Bromm & Kamionkowski 2002). Is this radiation detectable as a component of the infrared background light? Previous measurements (Matsumoto et al. 2000, 2005; Wright 2001; see also Hauser et al. 1998 and reference there) indicated the existence of an excess in the near-infrared background with respect to the level expected by galaxy counts (Madau & Pozzetti 2000). Salvaterra & Ferrara (2003) found that this excess can be produced by massive pop III stars formed at redshift $z \gtrsim 8$. However, the amount of the near-infrared excess (if any) is subject to many uncertainties (such as the model of zodiacal light, Kelsall et al. 1998; Wright 2001). For this reason, I studied the photon-photon absorption on blazar spectra, in order to put

stronger constraints on the near-infrared background (Mapelli, Salvaterra & Ferrara 2006). The results exclude the most extreme estimates of the near-infrared background (a flux $\nu\, I_\nu \simeq 7 \times 10^{-5}$ erg cm^{-2} s^{-1} sr^{-1} at a wavelength $\lambda \simeq 1.4\,\mu$m), but are still consistent with the existence of a moderate excess ($\nu\, I_\nu \simeq 3 \times 10^{-5}$ erg cm^{-2} s^{-1} sr^{-1} at $\lambda \simeq 1.4\,\mu$m), which is in agreement with the model of Salvaterra & Ferrara (2003).

Unidentified X-ray sources, ultra-luminous X-ray sources and IMBHs (Chapter 3)

Very massive pop III stars ($\gtrsim 260\, M_\odot$) are expected to end their life directly collapsing into IMBHs. If we were able to know the number and the mass range of IMBHs, we could derive strong constraints on the IMF and on the number of metal free stars. Furthermore, these IMBHs could also be sources of partial reionization, as we said in the previous Section. Thus, the natural question which arises is: are these IMBHs somehow detectable in the local Universe?

If these IMBHs exist, it is likely that, passing through dense gas regions, they accrete gas and emit X-ray radiation (Krolik 2004; Mii & Totani 2005; Mapelli, Ferrara & Rea 2006). In this case, the number of IMBHs can be constrained by imposing that the expected number of detectable X-ray sources powered by these IMBHs is lower than the total number of observed X-ray sources lacking certain identification.

In particular, it has been suggested that an entire class of X-ray sources, the so-called ultra-luminous X-ray sources (ULXs), could be accreting IMBHs (see Colbert & Miller 2005 for a review). In fact, the ULXs are sources with X-ray luminosity higher than 10^{39} erg s^{-1}, roughly correspondent to the Eddington luminosity of a 10 $M_\odot$ BH.

According to these ideas, I simulated the population of IMBHs which are expected to inhabit the Milky Way and I studied how these IMBHs accrete dense gas, switching on as X-ray sources. From a comparison of these simulations with unidentified X-ray sources in the IBIS/ISGRI catalogue (Bird et al. 2006) and from the null detections of ULXs in the Milky Way, I found strong upper limits on the density of IMBHs (Mapelli, Ferrara & Rea 2006; Mapelli, in preparation).

Suprathermal stars and IMBHs in globular clusters (Chapter 4)

A part from ULXs, the only IMBHs candidates which have been proposed until now are hosted in globular clusters (G1, Gebhardt, Rich & Ho 2002, 2005; M15, Gerssen et al. 2002, 2003; van den Bosch et al. 2006; NGC6752, Colpi, Mapelli & Possenti 2003). This hypothesis arises from photometric and spectroscopic measurements (G1 and M15) or from the spatial distribution and the period derivative of millisecond pulsars (NGC 6752).

Globular clusters are gas poor environments. So, in this case the model of IMBHs accreting gas cannot be used to derive any constraint. However, thanks to the high density reached in the core of globular clusters, IMBHs can form binaries with stars or stellar mass BHs, and can undergo three-body encounters with cluster stars (Sigurdsson & Hernquist 1993). Are there any features that IMBH binaries can imprint on stars, as a consequence of gravitational encounters? I studied two of these possible features, i.e. the formation of 'suprathermal' stars and the angular momentum alignment (Mapelli et al. 2005). The suprathermal stars are a bunch of some hundreds of stars, which, after the interaction with a IMBH binary, acquire recoil velocity much higher than the velocity dispersion of stars in their host cluster (but lower than the escape velocity). A fraction of these stars ($\lesssim 100$) are expected to be detectable before thermalization. In addition, the stars which interact with the IMBH binary tend to align their angular momentum to the orbital angular momentum of the IMBH binary. The amount of this alignment depends on the properties of the IMBH binary. Unfortunately, the cases in which the alignment is detectable are expected to be quite rare.

X-ray background, 511 keV and heating of the Universe by dark matter decays/annihilations (Chapter 5)

Particle decays/annihilations are expected to inject a significant amount of energy in the intergalactic medium, from the recombination to present-day epoch. This energy can partially contribute to reionization (Mapelli, Ferrara & Pierpaoli 2006; Ripamonti, Mapelli & Ferrara 2006a), especially at high redshift ($z \simeq 30 - 50$).

On the other hand, this energy injection can produce (and be detected via) many other effects, both in the high redshift and in the local Universe. For example, from the

comparison between the unresolved hard X-ray background (Bauer et al. 2004) and the X-ray flux which is expected to be produced by sterile neutrino radiative decays, we can put strong upper limits on the mass ($\lesssim 11$ keV, if the mixing angle is $\sin^2 2\theta \simeq 1.2 \times 10^{-9}$, Abazajian & Koushiappas 2006) of these warm dark matter particles (Mapelli & Ferrara 2005). Similar constraints ($\lesssim 6.3$ keV) can be derived from the lack of unidentified keV emission lines from galaxy clusters (Abazajian 2006; Abazajian & Koushiappas 2006 and references there).

Furthermore, the measurement by the INTEGRAL satellite of an excess in the 511 keV emission from the Galactic center (Knödlseder et al. 2005) can be explained by invoking decays and/or annihilations of light dark matter particles ($\lesssim 100$ MeV; Hooper & Wang 2004, Ascasibar et al. 2006).

In general, decays and/or annihilations of dark matter particles can affect the thermal and chemical history of the Universe, depending on their mass and lifetime (Ripamonti, Mapelli & Ferrara 2006a, 2006b). Moderately massive dark matter particles ($\lesssim 100$ MeV) can heat the Universe before than stars start forming. The implications of this effect are numerous. For example, an early increase on the gas temperature due to dark matter particles could imprint some feature on the 21 cm maps (Shchekinov & Vasiliev 2006; Valdes et al., in preparation).

Instead, annihilations of massive dark matter particles (> 30 GeV) have negligible effect both on reionization and on heating, even adopting the most favorable assumptions (Mapelli, Ferrara & Pierpaoli 2006). Thus, the detection of whatsoever effect associated with dark matter decays/annihilations should definitely indicate the existence of light dark matter particles.

Impact of dark matter decays/annihilations on structure formation (Chapter 6)

Dark matter decays and annihilations can influence structure formation in two different ways. First, increasing the fraction of free electrons, dark matter decays and annihilations act as catalysts of molecular hydrogen (H_2) and HD. These molecules are the most important coolants of the early Universe. Thus, one can think that decays and annihilations favor

the formation of first structures. On the other hand, energy injection from dark matter decays/annihilations can also heat the Universe, delaying structure formation. Ripamonti, Mapelli & Ferrara (2006b) find that the effect due to heating is dominant, and that structure formation is slightly delayed by dark matter decays and annihilations.

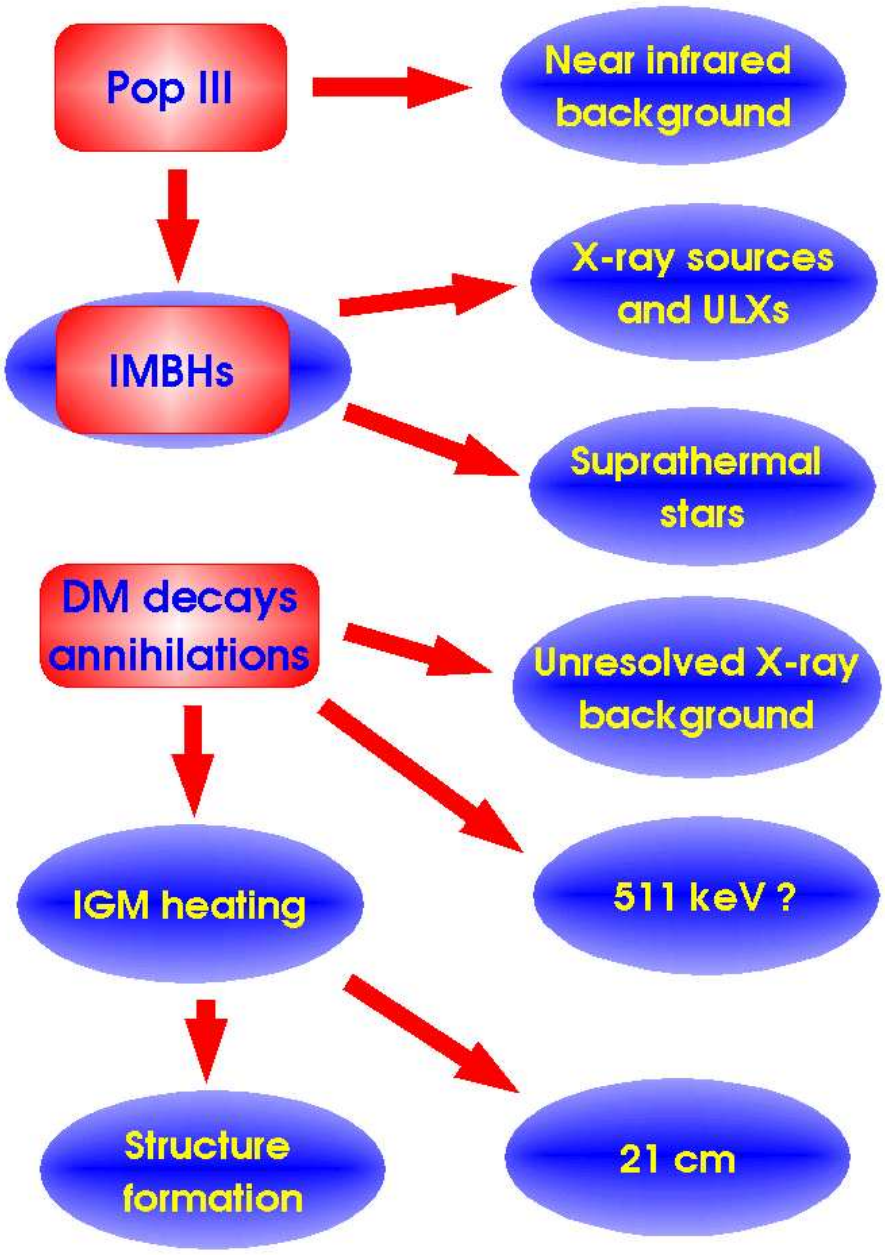

Figure 1.13: Schematic representation of the relic signatures of reionization sources considered in this Thesis. Red squared boxes indicate the reionization sources, elliptical boxes the possible relic signatures.

Chapter 2

Population III stars and the near infrared background (NIRB)

2.1 Introduction

Different methods have been proposed to (indirectly) probe the existence and the mass distribution of population III (pop III) stars. One of these methods is the study of the infrared background radiation. The basic idea is that the redshifted UV and optical light emitted by pop III stars can contribute to the near infrared background (NIRB) radiation, depending on the redshift formation, the mass distribution, the emission spectrum and other characteristics of these stars (Bond et al. 1986; Santos et al. 2002; Salvaterra & Ferrara 2003). Then, from a comparison between the observed NIRB and the theoretical models, one could constrain the main properties of first stars. A severe problem of this method is our limited observational knowledge of the infrared background radiation itself. In this Chapter, I will firstly describe what we know from the direct measurement of the optical-infrared background. Then, I will summarize the model of Salvaterra & Ferrara (2003), explaining the link between NIRB and first stars. Finally, I will present an alternative way to constrain the NIRB: the photon-photon absorption on blazar spectra (Mapelli, Salvaterra & Ferrara 2006).

2.2 Observations of the extragalactic background light (EBL)

The major difficulty in measuring the Extragalactic Background Light (EBL) arises from the subtraction of the interplanetary dust scattered sunlight (i.e. zodiacal light, ZL) contribution. This problem presents different aspects and complexity according to the range of observed wavelengths. A vast amount of literature is present on the subject (see Hauser & Dwek 2001 for a complete review). All the measurements mentioned in the following are reported in Fig. 2.1.

Galaxy counts

Deep optical and near infrared galaxy counts give an estimate of the EBL fraction coming from normal galaxies. Madau & Pozzetti (2000) derived the contribution of known galaxies in the $UBVIJHK$ bands from the *Southern Hubble Deep Field* imaging survey. In particular for the U, V, B and I bands (corresponding to the wavelengths λ = 3600, 4500, 6700 and 8100 Å) they found a mean flux respectively $2.87^{+0.58}_{-0.42}$, $4.57^{+0.73}_{-0.47}$, $6.74^{+1.25}_{-0.94}$ and $8.04^{+1.62}_{-0.92}$ in units of 10^{-6} erg s^{-1} cm^{-2} sr^{-1}.

Optical excess

Estimates of the optical EBL based on photometric scans across dark nebulae (Mattila 1976; Spinrad & Stone 1979) and on photoelectric measurements (Dube et al. 1977, 1979) provide upper limits that are higher than the flux given by galaxy counts alone at the same wavelengths. In particular the most recent work by Dube et al. (1979) provides an upper limit of 2.6×10^{-5} erg s^{-1} cm^{-2} sr^{-1} at λ= 5115 Å. Bernstein et al. (2002) measured the mean flux of the optical EBL at 3000, 5500, and 8000 Å, using the Wide Field Planetary Camera 2 (WFPC2) and the Faint Object Spectrograph, both on board the *Hubble Space Telescope*, combined with the du Pont 2.5 m Telescope at the Las Campanas Observatory. They found for these three bands a mean flux of the EBL respectively $12.0^{+17.7}_{-6.3}$, $14.9^{+19.3}_{-10.5}$, and $17.6^{+22.4}_{-12.8}$ in units of 10^{-6} erg s^{-1} cm^{-2} sr^{-1}, considerably higher than the contribution of the galaxy counts alone. In this band not only ZL is likely to provide a substantial contribution, but also terrestrial airglow, and dust-scattered Galactic

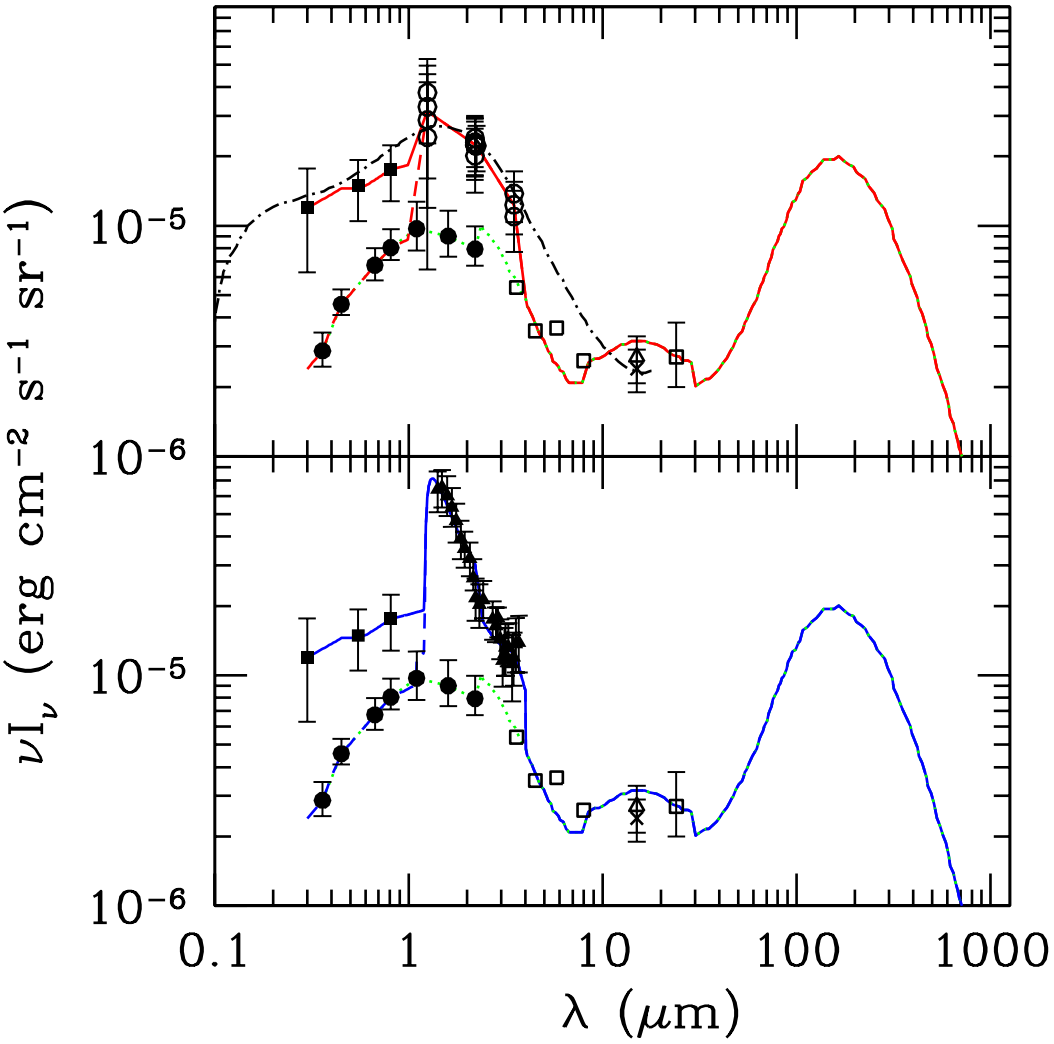

Figure 2.1: EBL data and corresponding models. In both the two panels are shown: data from Bernstein et al. (*filled squares*), Madau & Pozzetti (*filled circles*), Elbaz et al. (*cross*), Metcalfe et al. (*open triangle*), Fazio et al. (*open squares* from 3 to 10 μm) and Papovich et al. (*open square* at 24 μm). The *dotted line* indicates C1 model. **Upper panel:** DW1 (*dashed line*) and DW2 (*solid line*) models. The DW data (Gorjian et al. 2000; Wright & Reese 2000; Wright 2001; Wright & Johnson 2001) are represented with *open circles*. For comparison, the *dot-dashed line* shows the P1.0 model of Aharonian et al. 2005b. **Lower panel:** MK1 (*dashed line*) and MK2 (*solid line*) models. The MK data (Matsumoto et al. 2000) are represented with *filled triangles*.

starlight (diffuse Galactic light) might represent a potential problem for the measurement. The impact of such systematic errors has led Mattila (2003) to question the claim by Bernstein et al. of the discovery of an optical EBL excess.

Near Infrared Background: DIRBE and NIRS data

The available NIRB data come from the Diffuse Infrared Background Experiment (DIRBE) on board of the Cosmic Background Explorer (COBE) and from the Near InfraRed Spectrometer (NIRS) on board of the InfraRed Telescope in Space (IRTS). The DIRBE instrument provided a survey of the sky in 10 photometric bands at 1.25, 2.2, 3.5, 4.9, 12, 25, 60, 100, 140, and 240 μm using a $0.7^\circ \times 0.7^\circ$ field of view. A summary of the DIRBE results can be found in Hauser et al. (1998). The NIRS instrument covers the wavelength range from 1.4 to 4.0 μm with a spectral resolution of 0.13 μm. Matsumoto et al. (2000) made a preliminary analysis of the NIRS data, estimating the NIRB on the basis of the 5 NIRS observation days unperturbed by atmospheric, lunar and nuclear radiation effects.

Both the DIRBE and the NIRS data show an excess in the NIRB with respect to galaxy counts. An estimate of this excess depends on a critical point: the subtraction of the contribution of the ZL from the measurements. There are at least two models of ZL. The model described in Kelsall et al. (1998) exploits the temporal variability of the signal caused by looking at the sky through different amounts of the interplanetary dust as the Earth orbits the Sun. Wright & Reese (2000) noted that the high value of the EBL flux derived by Kelsall from the DIRBE data at 25 μm might indicate that a residual ZL flux could remain after subtraction. Thus they suggest a different approach, which requires that the EBL signal at 25 μm after ZL subtraction is zero (Wright 1997, 1998). In practice, subtracting the ZL both with the Kelsall and with the Wright method the presence of a NIRB excess is unquestionable, even if the amount of this excess depends on the ZL model assumed.

Mid Infrared Background: *SPITZER* data

Before the *SPITZER* satellite, the only MIRB available data came from the ISOCAM deep extragalactic surveys. From the analysis of the ISOCAM number counts Elbaz

et al. (2002) computed an EBL flux (integrated down to 50 μJy) of 2.4 ± 0.5 nW m^{-2} sr^{-1} at 15μm (68% confidence level). In deriving this value, Elbaz et al. took into account, among other surveys, of 15 μm counts from a portion of the ISO gravitational lensing survey. Metcalfe et al. (2003) use a full lensing survey (covering Abell 2218, Abell 2390 and Abell 370), and, by integrating from 30 μJy up-wards, obtain an EBL flux of 2.7 ± 0.62 nW m^{-2} sr^{-1} at 15μm (68% confidence level).

Recently, integrating to 60 μJy the counts from the Multiband Imaging Photometer on board of the *SPITZER* satellite (MIPS, Rieke et al. 2004), Papovich et al. (2004) found a lower limit to the EBL flux at 24μm of 1.9 ± 0.6 nW m^{-2} sr^{-1}. Extrapolating to fainter flux densities, they derive an estimate of the total 24 μm background of $2.7^{+1.1}_{-0.7}$ nW m^{-2} sr^{-1}, in good agreement with the result of Metcalfe et al. (2003). Other lower limits to the EBL flux at wavelengths ranging from 3 to 10 μm, derived by *SPITZER* measurements (Fazio et al. 2004), are reported in Fig. 2.1.

2.3 First stars and NIRB excess

In Section 2.2 we said that both DIRBE and NIRS data indicate the existence of an excess in the NIRB, with respect to the level derived by galaxy counts alone. This excess remains if we reduce the data both with the Kelsall and the Wright model of ZL light subtraction, even if its amount strongly depends on the adopted ZL model. It has been proposed that this NIRB excess is due to the redshifted UV and optical light emitted by pop III stars (Bond et al. 1986; Santos et al. 2002; Salvaterra & Ferrara 2003). In particular Salvaterra & Ferrara (2003) developed a model of the NIRB which, accounting for the most recent predictions of pop III stellar spectra (Schaerer 2002) and IMF, nebular emission (i.e. the radiation coming from the nebula surrounding the star), and $L_{y\alpha}$ photons scattered by the intergalactic medium, is able to fit the NIRS data (Matsumoto et al. 2000) and the DIRBE data with both the methods of ZL subtraction. Their best fit predicts, for a star formation efficiency $f_* = 0.1 - 0.5$, depending on the adopted IMF, a transition from (very massive) pop III to pop II stars occurring at $z \approx 9$. This model is supported also by the analysis of the Infrared Background fluctuations performed by Magliocchetti et al.

(2003). Such interpretation of the NIRB in terms of pop III stars, although very intriguing, might be somewhat extreme in terms of the high star formation efficiencies and production of intermediate mass black holes, as pointed out also by Madau & Silk (2005). Fig. 2.2 shows the best fit of the Salvaterra & Ferrara (2003) model (solid line) superimposed to the Matsumoto et al. (2000) data and to the DIRBE data (assuming a Kelsall ZL model).

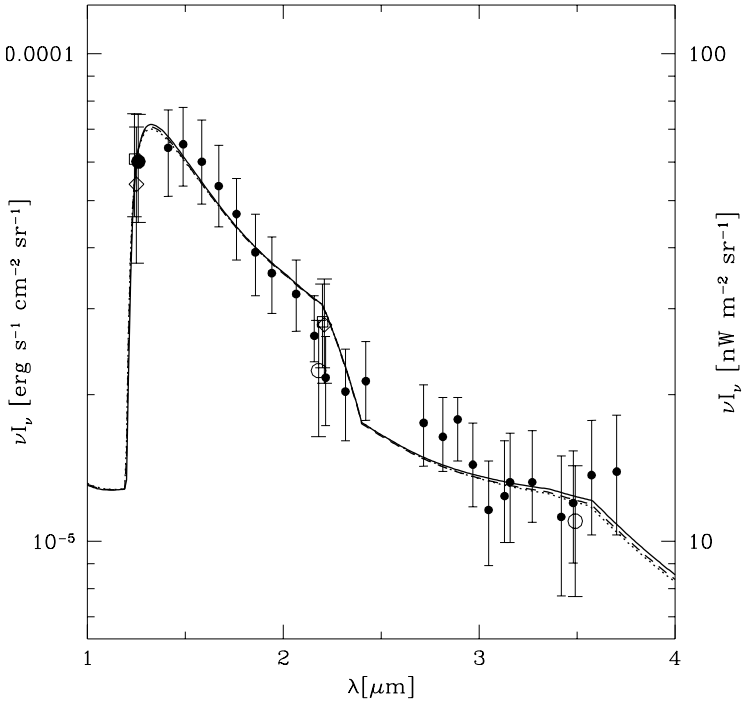

Figure 2.2: Best fit of the Salvaterra & Ferrara (2003) model for different IMFs. *Dashed line*: Salpeter IMF $z_{end} = 8.79$, $f_\star = 0.53$. *Dotted line*: heavy IMF $z_{end} = 8.8$, $f_\star = 0.21$. *Solid line*: very heavy IMF $z_{end} = 8.82$, $f_\star = 0.14$. The small filled circles are the NIRS data (Matsumoto et al. 2000). The open symbols are the DIRBE results: squares for Wright (2001), diamonds for Cambresy et al. (2001), and circles for Gorijan, Wright & Chary (2000). The big filled circle is the Kiso star count measurement. The data are slightly offset for clarity. The errors are at 1σ and for all the data the Kelsall et al. (1998) model for the zodiacal light is applied.

2.4 The photon-photon absorption

The main problem of the model of Salvaterra & Ferrara (2003) is represented by the observational uncertainties on the EBL. In particular, the existence of a NIRB excess, even if suggested by all the data, is still far from being accepted. In addition, there are no reasons (from a theoretical point of view) to prefer the Kelsall or the Wright description of ZL. A quite efficient method to constrain the infrared background is represented by the analysis of the photon-photon absorption on blazar spectra (Mapelli, Salvaterra & Ferrara 2006).

It is known that gamma rays in the GeV-TeV energy bands can be absorbed by softer (mainly optical and infrared) photons, via electron-positron pair production (Nikishov 1962). Stecker, de Jager & Salamon (1992) pioneered the method on the spectrum of 3C 279 to first study the EBL. Their attempt stimulated a plethora of works on the subject (Stecker, de Jager & Salamon 1993; Madau & Phinney 1996; Stecker & de Jager 1997; Aharonian et al. 2003; Konopelko et al. 2003; Stecker 2003; Costamante et al. 2004; Dwek & Krennrich 2005) that were encouraged by the availability of new measurements of blazar spectra in the TeV regime based on the Cherenkov imaging technique (Aharonian et al. 1999b; Krennrich et al. 1999 and Aharonian et al. 2002b for Mkn 421; Aharonian et al. 1999a, 2001a, 2002b for Mkn 501; Aharonian et al. 2003 for H 1426+428).

The optical depth due to photon-photon absorption can be written (Stecker et al. 1992; Madau & Phinney 1996) as

$$\tau(E) = \int_0^{z_{em}} dz \frac{dl}{dz} \int_{-1}^{1} dx \, \frac{(1-x)}{2} \int_{\epsilon_{th}}^{\infty} d\epsilon \, n(\epsilon) \, \sigma(\epsilon, E, x), \tag{2.1}$$

where dl/dz is the proper line element[1]

$$\frac{dl}{dz} = \frac{c}{H_0} \left[(1+z) \, \mathcal{E}(z) \right]^{-1},$$

c is the speed of light and

$$\mathcal{E}(z) = \left[\Omega_M (1+z)^3 + \Omega_\Lambda + (1 - \Omega_\Lambda - \Omega_M)(1+z)^2 \right]^{1/2}.$$

[1]We adopt the following cosmological parameters: Hubble constant H_0=71 km s^{-1} Mpc^{-1}, Ω_M=0.27, Ω_Λ=0.73, which are in agreement with the first year WMAP data (Spergel et al. 2003).

In eq. 2.1, $x \equiv \cos\theta$, θ being the angle between the directions of the two interacting photons. $E = E_0\,(1+z)$ is the observed energy of the blazar photon and $\epsilon = \epsilon_0(1+z)$ is the observed energy of the background photon; z_{em} is the redshift of the considered blazar; finally, $n(\epsilon)$ is the specific number density of background photons. The energy threshold for the interaction, ϵ_{th}, is defined by:

$$\epsilon_{th} = \frac{2\,m_e^2\,c^4}{E\,(1-x)} \tag{2.2}$$

where m_e is the electron mass.

The photon-photon absorption cross section (Heitler 1960; Gould & Schréder 1967) is given by

$$\sigma(\epsilon, E, x) = \frac{3\,\sigma_T}{16}(1-\beta^2)\left[2\,\beta(\beta^2-2) + (3-\beta^4)\ln\left(\frac{1+\beta}{1-\beta}\right)\right] \tag{2.3}$$

where σ_T is the Thomson cross section and

$$\beta \equiv \left[1 - \frac{2\,m_e^2\,c^4}{E\,\epsilon\,(1-x)}\right]^{1/2}$$

The cross section σ peaks sharply at $\lambda \sim hc\,E/(2m_e^2c^4) \sim 2.4(E/\mathrm{TeV})\mu\mathrm{m}$ (where λ is the wavelength of the interacting background photon). Fig. 2.3 shows the behavior of $\sigma(\lambda)$ integrated over the angle θ. Fig. 2.4 shows how the cross section depends on the interaction angle θ.

Substituting into eq. 2.1 the relation $n(\epsilon) = n(\epsilon_0)(1+z)^3$ (Madau & Phinney 1996), we finally obtain:

$$\tau(E) = \frac{c}{2\,H_0}\int_0^{z_{em}} dz \frac{(1+z)^2}{\mathcal{E}(z)}\int_{-1}^{1} dx\,(1-x)\int_{\epsilon_{th0}}^{\infty} d\epsilon_0\,n(\epsilon_0)\,\sigma(\epsilon_0, E_0, x, z); \tag{2.4}$$

$n(\epsilon_0)$ is related to the observable quantity $F(\epsilon_0)$, the background photon flux at redshift $z = 0$, by the simple relation:

$$n(\epsilon_0) = 4\pi\,\frac{F(\epsilon_0)}{c\,\epsilon_0^2} \quad \mathrm{cm}^{-3}\ \mathrm{erg}^{-1} \tag{2.5}$$

We have calculated numerically $\tau(E)$ using a three-dimensional integral based on the method of Gaussian quadratures (Press et al. 1992). The integration accuracy varies between $3\times10^{-5}\%$ and $8\times10^{-3}\%$ in the range 0.1-10 TeV. $\tau(E)$ has been estimated for

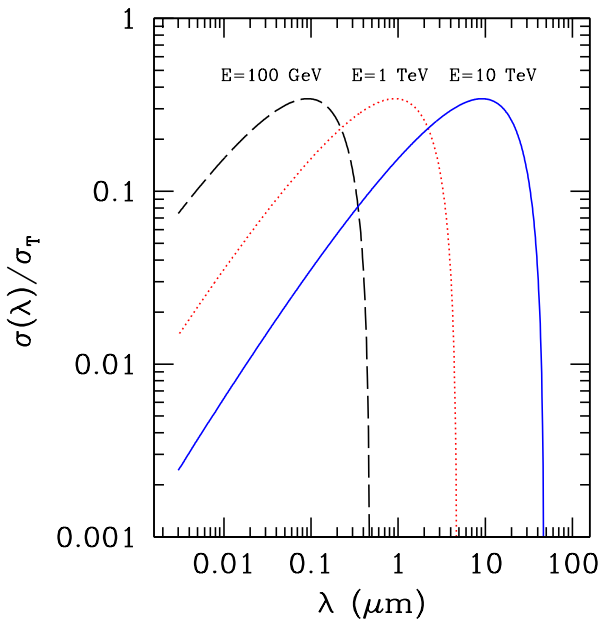

Figure 2.3: Photon-photon absorption cross section, $\sigma(\lambda)$, as a function of the background photon wavelength, λ, integrated over the interaction angle, for three values of the observed energy of the blazar photon: 100 GeV (*dashed line*), 1 TeV (*dotted*) and 10 TeV (*solid*). σ_T= 6.652×10^{-25} cm^2 is the Thomson cross section.

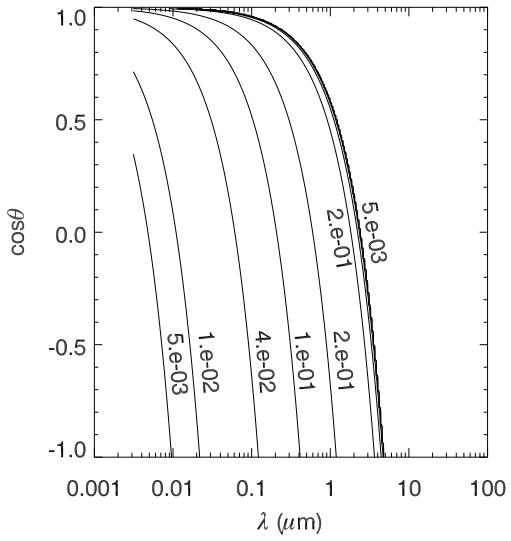

Figure 2.4: Isocontours of the cross section (in units of σ_T) as a function of θ and λ for E=1 TeV.

different values of $F(\epsilon_0)$, whose choice has been guided by both observational data and theoretical models (see next Section). To discriminate among these different estimates of $\tau(E)$ we need a comparison with observational data of blazar spectra, which we have performed in two independent ways:

1. The first method assumes a theoretical model of the unabsorbed blazar spectrum. In particular, we adopt a simple power-law spectrum $(dN/dE)_{unabsorbed} \propto E^{-\alpha}$ for the blazar H 1426+428, the main target of our analysis. For some of the other blazars considered (Mkn 421 and Mkn 501) the unabsorbed spectrum is better fitted by a power-law with an exponential cut-off (Konopelko et al. 2003). Some theoretical models suggest that the blazar spectrum must present a cut-off in the TeV range (Inoue and Takahara 1996; Tavecchio, Maraschi & Ghisellini 1998; Fossati et al. 2000).

   The absorbed spectrum is then obtained by convolving the unabsorbed spectrum with $\tau(E)$,
   $$\left(\frac{dN}{dE}\right)_{absorbed} = e^{-\tau(E)} \left(\frac{dN}{dE}\right)_{unabsorbed}, \tag{2.6}$$
   and by changing the spectral index α to obtain the best fit to the observed blazar spectrum.

2. The alternate method consists in inverting equation 2.6. In this case we apply $\tau(E)$ directly to the observational data, to derive the unabsorbed spectrum and check if the intrinsic spectral index α is consistent with the current theoretical predictions. This procedure does not require any *a priori* assumption about the unabsorbed spectrum shape. An important sanity check is to verify whether the values of α derived from the two methods are consistent.

2.4.1 Summary of the adopted EBL models

We calculated the photon-photon absorption adopting the following assumptions on the EBL.

- For the optical background (i.e. between 0.3 and 1.2 μm) we have considered both the values obtained from galaxy counts only, following Madau & Pozzetti (2000), and

Table 2.1: Summary of the considered EBL models.

Model	Optical Background	NIRB
C1	Madau & Pozzetti (2000)	
MK1	Madau & Pozzetti (2000)	Matsumoto et al. (2000) (K)[a]
MK2	Bernstein et al. (2002)	Matsumoto et al. (2000) (K)
DW1	Madau & Pozzetti (2000)	Wright (2001) (W)[a]
DW2	Bernstein et al. (2002)	Wright (2001) (W)

[a](K) and (W) indicate the ZL subtraction obtained using Kelsall's model and Wright's model, respectively. For the MIRB and FIRB we adopted always the Totani & Takeuchi (2002) model rescaled to the Spitzer data (Papovich et al. 2004).

the case of a background excess (Bernstein et al. 2002 data, including their upper and lower limits).

- For the NIRB ($1.2 < \lambda < 4.\,\mu$m) we have used both the NIRS data (Matsumoto et al. 2000; Salvaterra & Ferrara 2003) with the Kelsall's model of ZL subtraction, and the DIRBE data with the Wright model of ZL subtraction (Gorjian et al. 2000; Wright & Reese 2000; Wright 2001; Wright & Johnson 2001).

- For the MIRB and FIRB ($\lambda > 4.\,\mu$m) we adopt the Totani & Takeuchi (2002) model (because the number of observational points is too small to be used without theoretical assumptions), rescaled by a factor 1.2 in the 8-30 μm range to match the *SPITZER* 24 μm data point; in this wavelength range the uncertain contribution of spiral galaxies allows such rescaling.

Finally we have considered a case in which the optical/NIRB in $0.3 < \lambda < 4\,\mu$m is contributed purely by galaxies as given by their counts (i.e. no excess) leaving the MIRB/FIRB as above. A summary of the considered models is given in Table 2.1. Fig. 2.1 shows these models and the considered data.

In our work we neglect a possible redshift evolution of the EBL. This assumption is reasonable given the low redshift of the considered blazars, including the most distant one ($z = 0.186$). We also neglect the possible self-absorption of the blazar, i.e. the contribution to the photon-photon absorption given by infrared photons produced by the blazar, as it

can be shown to be irrelevant (Protheroe & Biermann 1997).

2.5 TeV blazar spectra

Sufficiently high resolution blazar spectra in the TeV regime, obtained with imaging Cherenkov techniques, are available for at least three blazars: H 1426+428, Mkn 421 and Mkn 501. Data have become recently available for other three blazars: PKS 2155-304 (Aharonian et al. 2005a), 1ES1101-232 and H 2356-309 (Aharonian et al. 2005b). H 1426+428 is at relatively high redshift ($z = 0.129$); its TeV spectrum determination is therefore significantly less accurate than that for Mkn 421 and Mkn 501. For this blazar available data from CAT (Djannati-Ataï et al. 2002), Whipple (Horan et al. 2002) and HEGRA (Aharonian et al. 2003) exist. These data must be distinguished in two sets. The first set includes the HEGRA data taken in 1999-2000, CAT data taken in 1998-2000 and Whipple data taken in 2001. The second set is represented by HEGRA data taken in 2002 and it is characterized by a much lower flux level than for the previous campaigns. Mkn 421 and Mkn 501 are maybe the best observed blazars in the high energy gamma-ray band and are characterized by nearly equal redshifts ($z = 0.031$ and $z = 0.034$, respectively), considerably lower than that of H 1426+428. Because of this, differences in their spectra (for example in the cut-off energies) cannot be explained by different amounts of intervening absorption, but as due to intrinsic spectral characteristics (Aharonian et al. 2002b; Konopelko et al. 2003). The spectrum of Mkn 501 was measured up to 22 TeV both by HEGRA (Aharonian et al. 1999a, 2001a) and by Whipple (Samuelson et al. 1998; Krennrich et al. 1999): the observations of these two Cherenkov telescopes are in good agreement. Mkn 421 was also measured up to 20 TeV both by HEGRA (Aharonian et al. 1999b, 2002b) and Whipple (Krennrich et al. 1999, 2002), yielding similar fluxes. HESS spectra have been collected for PKS 2155-304 ($z = 0.117$), 1ES1101-232 ($z = 0.186$) and H 2356-309 ($z = 0.165$) (Aharonian et al. 2005a, 2005b). In Section 2.6 we will present spectral fits obtained for these blazars through the photon-photon absorption calculation, dwelling mainly on H 1426+428.

Table 2.2: χ^2 values and best fit spectral indexes (α) of the considered models.

	C1	MK1	MK2	DW1	DW2
χ^2	8.66	17.88	19.86	6.43	7.57
α	2.65	1.60	1.70	1.80	1.90

Statistical analysis based on 12 observational data of the spectrum of H 1426+428 (reported in Fig. 2.8) with 2 parameters (the spectral index α and a normalization factor).

2.6 Results

As discussed in Section 2.4, we have considered several models of optical and near infrared background (see Tab. 2.1). For all these models we have calculated the optical depth due to photon-photon absorption using eq. 2.4, and applied it to the theoretical unabsorbed blazar spectrum (eq. 2.6), changing the spectral index and the normalization until the best fit was found through the χ^2 method. Let us consider now the results obtained for each different model.

2.6.1 Galaxy counts only

We start from the analysis of the most conservative case (C1) in which the optical and the NIRB come only from normal galaxies as derived by Madau & Pozzetti (2000); while the MIRB/FIRB are from the rescaled Totani & Takeuchi model. Fig. 2.5 shows the best fit, obtained through χ^2 minimization, to the H 1426+428 data for model C1. The best fit is obtained for spectral index $\alpha = 2.65$ with $\chi^2 \sim 9$ (Table 2.2), derived considering 12 observational data (CAT 1998-2000, Whipple 2001, HEGRA 1999-2000) and 2 free parameters (spectral index α and normalization factor). This spectral index seems to be uncommonly high for this blazar. In particular, for H 1426+428 previous literature indicates a spectral index $\alpha = 1.9$ (Aharonian et al. 2002a) or $\alpha = 1.5$ (Aharonian et al. 2003). If we consider a spectral index $\alpha \leq 2$, we obtain $\chi^2 > 21$, a considerably higher value.

Another problem of the C1 model is that the HEGRA point at E$\sim$ 5 TeV is more than 2σ away from the curve. Moreover, the best fit drops at E$>$ 3 TeV, hence providing a very poor

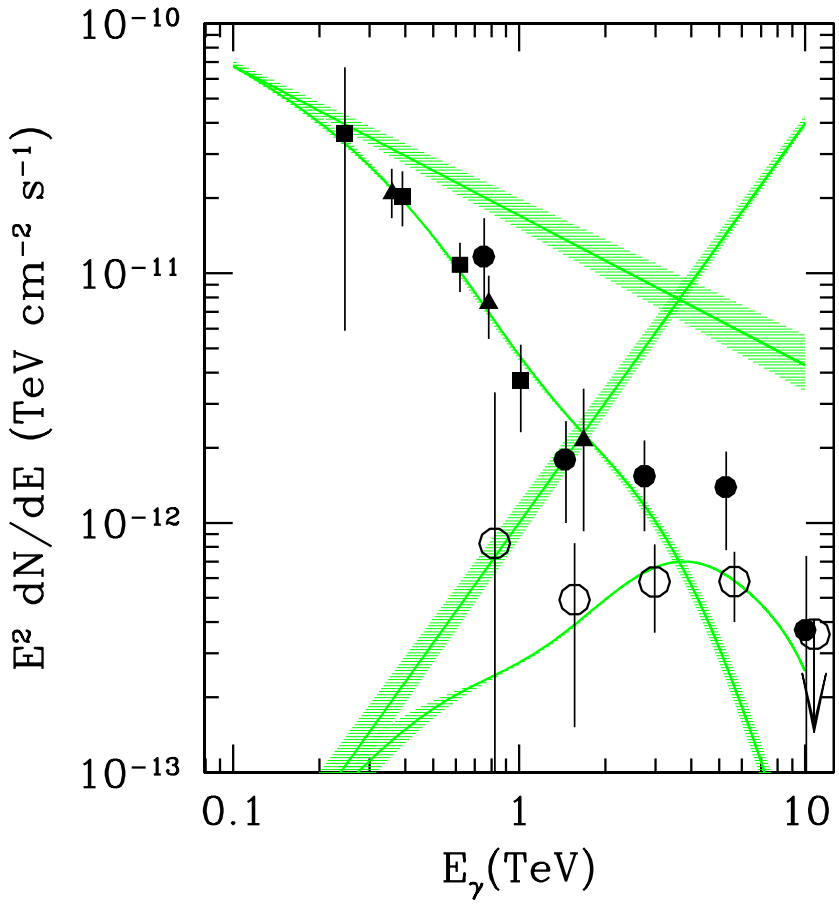

Figure 2.5: The *solid line* represents the best fit to the spectrum of H 1426+428 obtained for the model C1 (see Table 2.1). The shaded area indicates the $\pm 1\sigma$ uncertainty introduced by the error in galaxy counts on the absorbed spectrum. The observational data reported here are from CAT 1998-2000 (*filled squares*), Whipple 2001 (*filled triangles*), HEGRA 1999-2000 (*filled circles*), HEGRA 2002 (*open circles*). All error bars are at 1 σ (Aharonian et al. 2003).

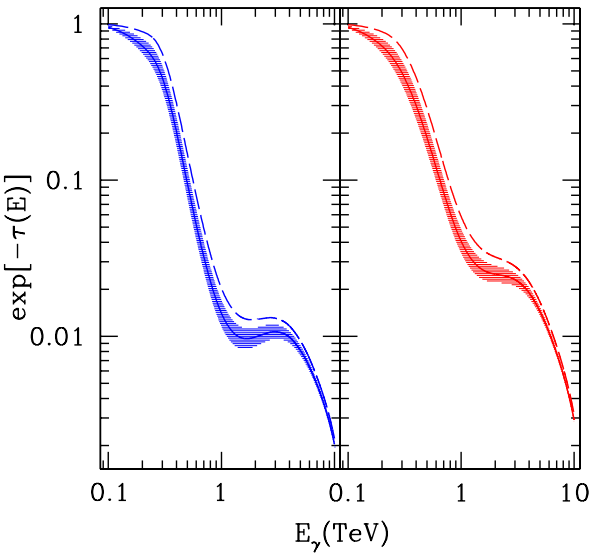

Figure 2.6: Optical depth for photon-photon absorption with $z_{em} = 0.129$, the redshift of H 1426+428. The EBL models assumed are the following. **Left panel:** MK1 (*dashed line*) and MK2 (*solid*); **Right panel:** DW1 (*dashed line*) and DW2 (*solid line*). Shaded areas refer to $\pm 1\sigma$ errors.

match to the observed shape of the absorbed spectrum derived from experiments, which flattens in the energy range 1-6 TeV. In conclusion, although model C1 cannot be rejected on the basis of χ^2 analysis alone, we consider it unlikely given its poor performance in terms of spectral slope and shape.

2.6.2 Including a NIRB excess

We next consider models including a NIRB excess in the range $1.2 - 4\,\mu$m as the Matsumoto et al. (2000) data with the Kelsall's subtraction of the ZL (hereafter MK), and the DIRBE data with the Wright subtraction of the ZL (DW); again, we fix the MIRB/FIRB according to the rescaled Totani & Takeuchi model in both cases. For the optical background we experimented with all available measurements (Madau & Pozzetti 2000; Bernstein et al. 2002; Mattila 2003).

Fig. 2.6 shows the photon-photon absorption optical depth for a blazar at redshift

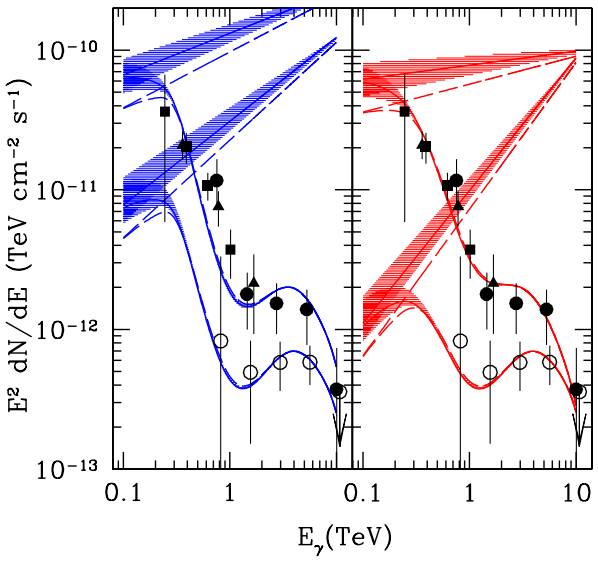

Figure 2.7: Fit to the H 1426+428 spectrum. The EBL models are the same as in Fig. 2.6; the observational data are the same as in Fig. 2.5.

0.129 (i.e. the redshift of H 1426+428), assuming the EBL models MK1+MK2 (left panel) and DW1+DW2 (right panel). The optical depth in the MK1 and MK2 cases (those which are characterized by the MK data in the NIRB) is considerably higher, especially at 1 TeV (where the absorption comes primarily from NIRB photons, see Fig. 2.3). Fig. 2.7 shows the best fits for the H 1426+428 spectrum, again with the NIRB from MK1 and MK2 models (left panel) and from DW1 and DW2 models (right panel). DW1 and DW2 provide an excellent fit, with χ^2 respectively 6.4 and 7.6 (Table 2.2). None of the observational data is more than 1σ away from the fit, that correctly reproduces the shape of the absorbed spectrum suggested by the data, with the plateau at E$>$ 1 TeV.

On the contrary, the MK1 and the MK2 cases are only marginally consistent with at least 4 Cherenkov data (CAT at $\sim$ 1 TeV and $\sim$ 0.6 TeV, HEGRA at $\sim$ 0.75 TeV and Whipple at $\sim$ 0.78 TeV). Also the χ^2 is considerably higher than in the case of DW1 and DW2, even if not so high that we can reject MK1 and MK2 models. The good result obtained adopting DW1 and DW2 models supports the evidence for a NIRB excess, although not as pronounced as suggested by the MK1 and MK2 models.

2.6.3 Including the optical excess

We finally consider the differences among various measurements of the optical background. The left and the right panel of Fig. 2.7 show the differences in the spectrum of H 1426+428 due to the assumption of an optical background produced by galaxies only or including an "optical excess" as measured by Bernstein et al. In both cases the fit seems to favor an optical background consistent with galaxy counts only (*dashed line*), although the differences between various types of optical background are smaller than the error bars in the blazar data. Thus more solid conclusions on the optical excess have to await for more precise data.

2.6.4 An alternative analysis

As discussed in Section 2.4, there is a different way to tackle the data analysis. So far we have assumed a theoretical shape (i.e. a power-law) for the unabsorbed blazar spectrum and convolved it with the optical depth for photon-photon absorption. Alternatively, one can apply $\tau(E)$ directly to the Cherenkov data by inverting eq. 2.6 and derive the unabsorbed blazar spectrum without making any *a priori* assumption about its shape. This second approach is particularly indicated when the blazar cannot be fitted by a simple power-law (for example Mkn 421 and Mkn 501). As a sanity check, we now use this alternative approach to show that the two methods yield a coherent picture.

Fig. 2.8 shows the results of such attempt for H 1426+428. We find that the C1 model yields an intrinsic spectrum which is inconsistent not only with a power-law, but also with an exponential cut-off, as a significant rise in the spectrum above 3 TeV is seen. Models MK1, and especially DW1, do not show this peculiar spectral rise at high energies. Unfortunately, though, because of the large experimental errors in H 1426+428 data, we cannot assess clearly whether the intrinsic spectrum of this blazar is better fit by a simple/broken power-law or a power-law with an exponential cut-off. If we assume a power-law intrinsic spectrum, we can derive the best fit spectral index with the weighted least square method. With this method we derive $\alpha = 1.8$ for the case DW1, $\alpha = 1.4$ for MK1 and $\alpha = 2.5$ for C1, consistent with what we found minimizing the χ^2 (Table 2.3).

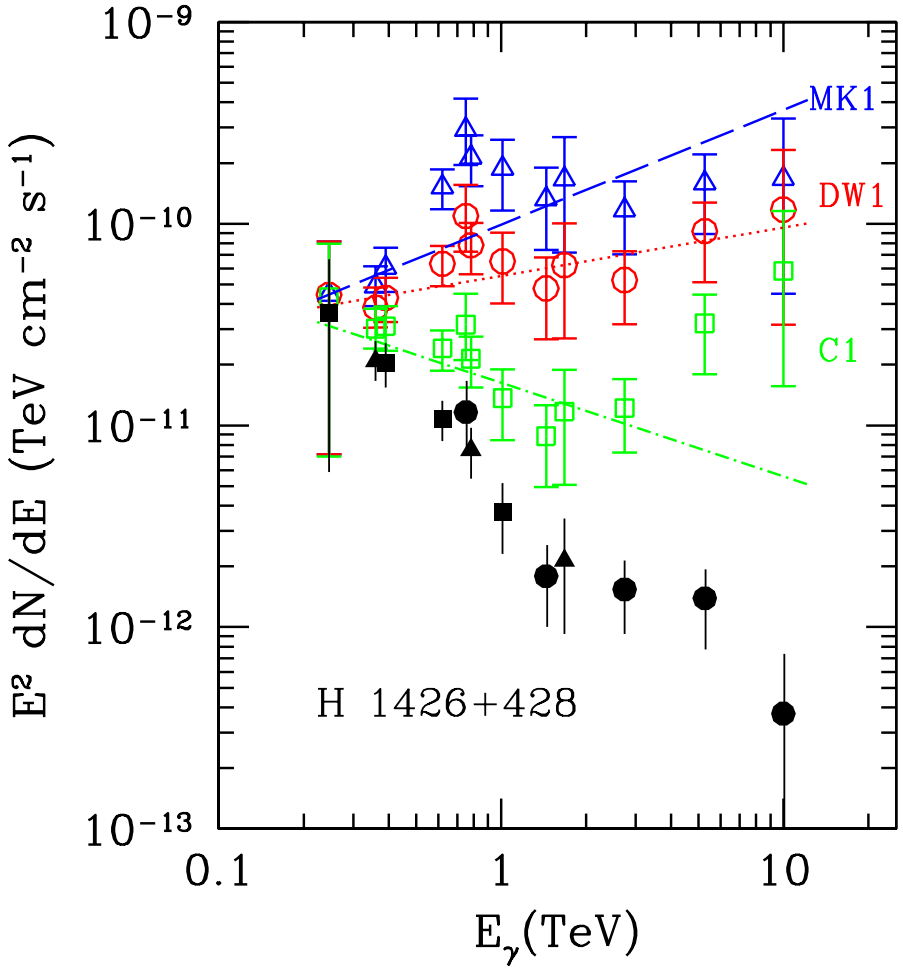

Figure 2.8: Unabsorbed spectrum of H 1426+428 obtained by convolving the photon-photon optical depth with the data assuming EBL models C1 (*open squares*), DW1 (*open circles*) and MK1 (*open triangles*). The lines are the least square fits for the unabsorbed spectrum power-law index: C1 (*dot-dashed line*, $\alpha = 2.5$), DW1 (*dotted*, $\alpha = 1.8$) and MK1 (*dashed*, $\alpha = 1.4$). The observational data reported here are from CAT 1998-2000 (*filled squares*), Whipple 2001 (*filled triangles*), HEGRA 1999-2000 (*filled circles*). The error bars are obtained from the 1σ error bars of the blazar data.

Table 2.3: Spectral indexes (α) derived using the least square fits for our models C1, DW1, MK1 and for model P1.0 of Aharonian et al. 2005b.

	H 1426+428	PKS 2155-304	1ES1101-232	H 2356-309
C1	2.5	2.7	1.4	2.0
DW1	1.8	2.0	0.4	1.0
MK1	1.4	1.6	-0.1	0.1
P1.0	-	-	-0.1	0.7

Hence, the results of this analysis, and in particular the anomalous rise in the spectrum above 3 TeV, tend to disfavor the C1 model; the DW1 model is found again to give the best fit to the data.

Fig. 2.9 and Fig. 2.10 show the same procedure applied to Mkn 421 and Mkn 501. The calculated optical depths for these two blazars in the range 0.7–2 TeV are in agreement with the results by Konopelko et al. (see Fig. 2 of their paper); above 2 TeV our results are slightly different, due to the higher MIRB flux of the EBL model (Malkan & Stecker 2001; Stecker 2003) they assume. The data for these two blazars have significantly higher quality than those available for H 1426+428; unfortunately, because of their low redshift, the effect of photon-photon absorption on the spectrum of these two blazars is too weak to provide additional constraints on the EBL.

Figs. 2.11-2.13 show the results of this procedure applied to the new data available for PKS 2155-304, 1ES1101-232 and H 2356-309, respectively. In the case of PKS 2155-304 both the spectrum derived from the DW1 model and that derived from the MK1 model show a peculiar peak at energy $\sim$ 1 TeV. This peak is mainly due to the fact that these EBL models are characterized by a high flux at 1-4 μm and a rapid decrease at wavelengths $> 4\,\mu$m. This finding is at odd with the conclusions from the analysis of H 1426+428. This is even more puzzling if we note that the two blazars are nearly at the same redshift. Instead, the unabsorbed spectrum derived from the model C1 is quite smooth.

Dwek, Krennrich & Arendt (2005) use the theoretical emission models of Chiappetti et al. (1999), based on the EGRET data (Vestrand, Stacy & Sreekumar 1995), to put a constraint on the hardness of the spectrum of PKS 2155-304. We have compared

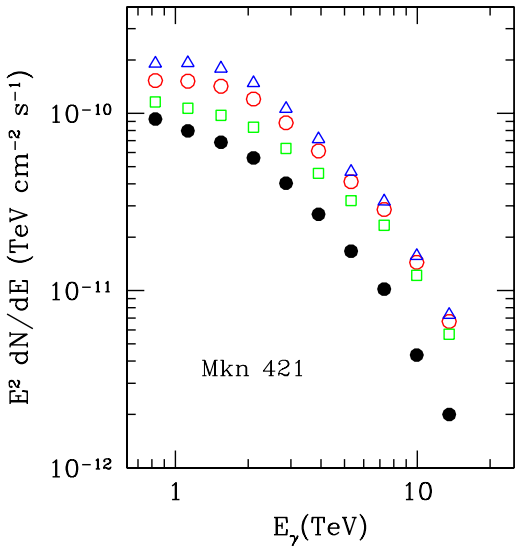

Figure 2.9: Unabsorbed spectrum of Mkn 421 obtained by applying the photon-photon absorption to the 2000/2001 HEGRA data (Aharonian et al. 2002b). The adopted EBL models are as in Fig. 2.8.

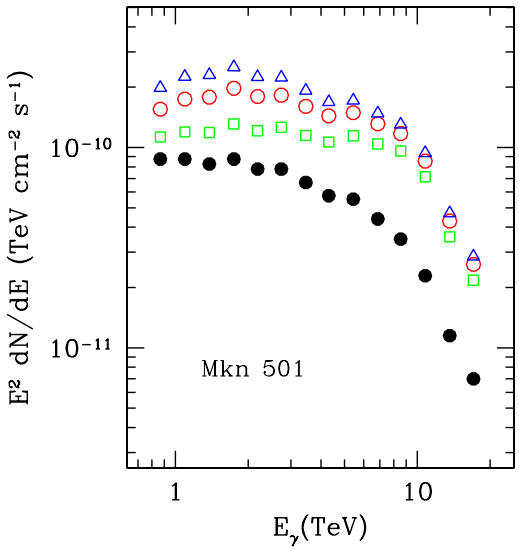

Figure 2.10: Unabsorbed spectrum of Mkn 501 obtained by applying the photon-photon absorption to the 1997 HEGRA data (Aharonian et al. 2002b; *filled squares*). The adopted EBL models are as in Fig. 2.8.

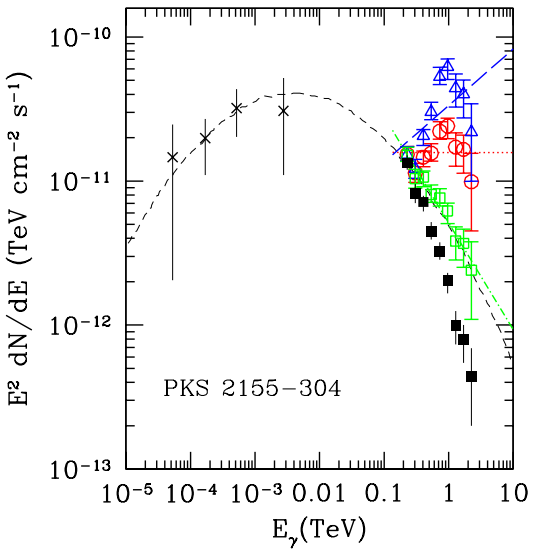

Figure 2.11: Unabsorbed spectrum of PKS 2155-304 obtained by applying the photon-photon absorption to the HESS data (Aharonian et al. 2005a). The adopted EBL models are as in Fig. 2.8. The lines are the least square fits for the unabsorbed spectrum power-law index: C1 (*dot-dashed line*, $\alpha = 2.7$), DW1 (*dotted*, $\alpha = 2.0$) and MK1 (*dashed*, $\alpha = 1.6$). The error bars are obtained from the 1σ error bars of the blazar data. The *crosses* are the EGRET data (Vestrand, Stacy & Sreekumar 1995) and the *thin short dashed line* represents the best fit synchrotron self-Compton model of Chiappetti et al. (1999).

the results of our models with EGRET data and Chiappetti et al. models (Fig. 2.11). In agreement with Dwek et al. (2005), we find that the model C1 is perfectly consistent with Chiappetti et al. (1999) model. It is outside the scope of this Thesis to discuss the details of synchrotron self-Compton models. Nevertheless, taking into account the errors on the least square fits ($\gtrsim 0.8$ for both DW1 and MK1 models), on the EGRET measurements and the uncertainties of the Chiappetti et al. model, we find that the DW1 model is close to be acceptable, whereas the MK1 model has, probably, to be rejected. On the other hand, we also have to take into account that EGRET data and observations in the TeV range are separated by a considerable time interval (about 10 years); this can be crucial, given the variability of blazar spectra (Ghisellini, personal communication). Thus, the comparison between EGRET and TeV data, although interesting in principle, must be taken with some care.

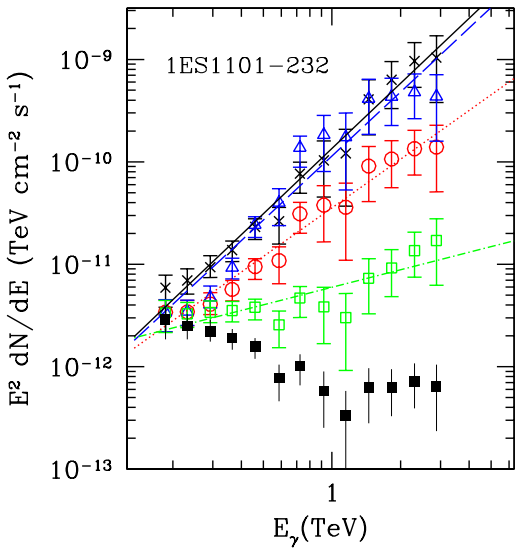

Figure 2.12: Unabsorbed spectrum of 1ES1101-232 obtained by applying the photon-photon absorption to the HESS data (Aharonian et al. 2005b). The adopted EBL models are: C1 (*open squares*), DW1 (*open circles*) and MK1 (*open triangles*). In addition we show also the results obtained for the P1.0 model of Aharonian et al. 2005b (*crosses*). The lines are the least square fits for the unabsorbed spectrum power-law index: C1 (*dot-dashed line*, $\alpha = 1.4$), DW1 (*dotted*, $\alpha = 0.4$), MK1 (*dashed*, $\alpha = -0.1$) and P1.0 (*solid*, $\alpha = -0.1$). The error bars are obtained from the 1σ error bars of the blazar data.

In Fig. 2.12 the results for the blazar 1ES1101-232 are presented. Aharonian et al. (2005b) have shown that the EBL models with a high excess in the NIRB must be rejected, since they imply an unabsorbed spectrum so hard that it would be difficult to explain it within the standard hadronic or leptonic scenario (Aharonian 2001b). This conclusion is supported by our study: our model MK1 gives a spectral index $\alpha = -0.1$ (Table 2.3), which is too hard to be allowed by current theoretical models. However, for the model DW1 we obtain a spectral index $\alpha = 0.4$ (Table 2.3), and for model DW2, in which the optical EBL matches the data by Bernstein et al. (2002), we get $\alpha = 0.5$. Taking into account that the error on the spectral index from the least square fits is large ($\gtrsim 0.3$ for all the considered models), we conclude that the unabsorbed spectra derived both from DW1 and DW2 models are hard, but consistent with the lower limit $\alpha = 0.6$ predicted for 1ES1101-232 by synchrotron self-Compton models (Ghisellini, personal communication). Then, EBL

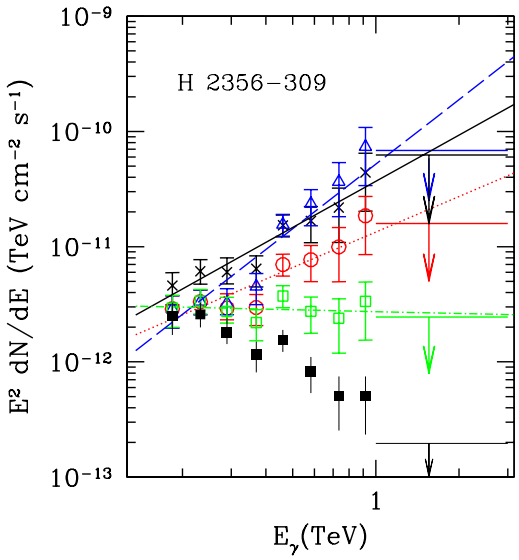

Figure 2.13: Unabsorbed spectrum of H 2356-309 obtained by applying the photon-photon absorption to the HESS data (Aharonian et al. 2005b). The adopted EBL models are the same as Fig. 2.12. The lines are the least square fits for the unabsorbed spectrum power-law index: C1 (*dot-dashed line*, $\alpha = 2.0$), DW1 (*dotted*, $\alpha = 1.0$), MK1 (*dashed*, $\alpha = 0.1$) and P1.0 (*solid*, $\alpha = 0.7$). The error bars are obtained from the 1σ error bars of the blazar data.

models with Wright-subtracted-ZL NIRB excess cannot be rejected on the basis of the HESS data of 1ES1101-232. In Fig. 2.12 we show, for comparison, the model P1.0 of Aharonian et al. (2005b). This model matches the COBE/DIRBE measurements with the Wright model of ZL subtraction, as the DW1 model does, but it has a higher flux from 4 to 10 μm (Fig. 2.1) with respect to the latter. It is important to note that the model P1.0 gives a spectral index $\alpha = -0.1$, which is as hard as predicted by MK1. This points out the importance of the spectral region 4-10 μm to understand the EBL.

Finally, Fig. 2.13 shows the blazar H 2356-309. Also in this case, the spectral index for the MK1 model is very hard ($\alpha = 0.1$, Table 2.3), whereas both C1 and DW1 models give unabsorbed spectra of acceptable hardness.

2.7 Conclusions

In this Chapter, we have explored the effects produced by photon-photon absorption on blazar spectra to put constraints on extragalactic background light from the optical to the far infrared bands. We mostly focused on the high redshift blazar H 1426+428, for which we adopted a power-law unabsorbed spectrum. This might be a simplifying assumption, as some theoretical models indicate a more complex spectral shape (Inoue and Takahara 1996; Tavecchio, Maraschi & Ghisellini 1998; Fossati et al. 2000). On the other hand, the data for H 1426+428 are not sufficiently accurate to suggest the existence of a cut-off or to exclude a power-law spectrum.

We have considered three different models of the NIRB, based respectively on galaxy counts (C1) and on the presence of an excess (DW and MK). In the case of H 1426+428 the DW model provides the best fit both using the method presented in Section 2.6.1-2.6.3, and the alternative one of Section 2.6.4. The MK model has a higher χ^2 but cannot be rejected. For the same reasons, C1 model cannot be excluded either; however, in this case a very peculiar blazar intrinsic spectrum must be assumed (Fig. 2.8). We conclude that the presence of a NIRB excess with respect to galaxy counts, at the level given by the DW model, seems to be required to fit the blazar spectrum.

The very recent HESS data of the blazars PKS 2155-304 (Aharonian et al. 2005a), 1ES1101-232 and H 2356-309 (Aharonian et al. 2005b) allow us to put stronger constraints to the NIRB. In particular, from the analysis of all these blazar, we conclude that the MK models, based on the Kelsall method of ZL subtraction, must be rejected, since they imply too hard blazar spectra. The spectra of PKS 2155-304 and 1ES1101-232 are marginally consistent with DW models, based on Wright ZL subtraction, which can be considered as an upper limit to the NIRB. The model C1, without NIRB excess, is favored by all these new data. These findings are quite different from those we derived for H 1426+428. Since the available data for H 1426+428 are old, new measurement of this blazar are eagerly required, to shed some light on this puzzling inconsistency.

The derived constraints on the optical EBL are weaker, due to the fact that deviations between different optical EBL models are comparable to the experimental errors.

The fit tends to favor models without an optical excess over galactic light, contrary to the result obtained by Bernstein et al. (2002). A more solid conclusion on the amplitude of the optical EBL has to await for the next generation of Cherenkov Telescopes as *MAGIC, VERITAS, HESS, GLAST*, or infrared satellites (*CIBER*).

Finally, in the mid-infrared the *SPITZER* measurement of νI_ν=2.7 nW m^{-2} sr^{-1} at 24 μm, combined with the EBL model by Totani & Takeuchi (2002), allows us to obtain a good fit for all the blazars available. Again, a tremendous advance on the determination of the MIRB/FIRB is expected from *SPITZER* and the next generation of infrared satellites as *ASTRO-F*, and *SPICA*.

In summary, recent measurements of blazars in the TeV range seem to exclude the existence of a strong NIRB excess consistent with Kelsall's model of ZL subtraction. The COBE/DIRBE measurements, after Wright's model ZL subtraction, represent a firm NIRB upper limit.

Chapter 3

Intermediate mass black holes

3.1 Introduction

There are strong observational evidences for the existence of two classes of black holes (BHs): stellar mass BHs, with mass from 3 to 20 $M_{\odot}$ (Orosz 2003), thought to be the relics of massive stars, and super massive black holes (SMBHs) in the mass range $10^{6-9}M_{\odot}$, hosted in the nuclei of many galaxies. Recently, the existence of a third class of Intermediate Mass BHs (IMBHs) has been inferred. They are characterized by masses in the range from $20M_{\odot}$ to a few $\times 10^4 M_{\odot}$ (see van der Marel 2004 for a review). Several IMBH formation mechanisms have been proposed: *(i)* IMBHs could be the relics of very massive metal free stars (Heger & Woosley 2003), *(ii)* they could form from the direct collapse of low angular momentum gas (Haehnelt & Rees 1993; Begelman, Volonteri & Rees 2006; Lodato & Natarajan 2006), *(iii)* could have been assembled in young clusters via runaway collapse of stars (Portegies Zwart & McMillan 2002), or *(iv)* could have been built up in globular clusters (GCs) through repeated mergers of stellar mass BHs in binaries (Miller & Hamilton 2002).

Their number is nearly unknown. In principle, IMBHs could contribute to all the baryonic dark matter (van der Marel 2004): their density $\Omega_{\bullet}$ could be essentially equal to that of luminous baryonic matter, $\Omega_{b,\,lum} = 0.021$ (Persic & Salucci 1992; Fukugita, Hogan & Peebles 1998), and equal to 50% of all baryons ($\Omega_b = 0.044$, Spergel et al. 2003) . Only

weak constraints on the IMBH mass have been inferred from dynamical studies of the Milky Way. For example, the observed velocity dispersion of stars in the Galactic disk requires that halo BH masses are $\leq 3 \times 10^6 M_\odot$, if the Milky Way dark halo is entirely made of compact objects (Carr & Sakellariadou 1999; see also Lacey & Ostriker 1985; Wasserman & Salpeter 1994; Murali, Arras & Wasserman 2000 and reference herein). Other dynamical constraints on the IMBH mass can be derived by imposing that they do not disrupt too many Galactic globular clusters (Moore 1993; Arras & Wasserman 1999). By this request, Klessen & Burkert (1996) found that, if the dark halo of the Milky Way is exclusively composed by IMBHs, their mass must be $\leq 5 \times 10^4\, M_\odot$. For the same reason, the halo BHs cannot represent more than 2.5-5 per cent of the dark halo mass, if they are as massive as $10^6 M_\odot$ (Murali et al. 2000). However, constraints on IMBHs obtained from globular cluster disruption are very uncertain, as we do not know what are the characteristics of globular clusters when they form, and how many of them have been destroyed. It could even be that IMBHs have played a role in determining the current number and distribution of globular clusters (Ostriker, Binney & Saha 1989).

In this Chapter we will firstly review the various mechanisms proposed for the origin of IMBHs. Then, we will briefly describe the possible link between IMBHs and Ultra-Luminous X-ray sources (ULXs). Finally, we will show how the number and the distribution of IMBHs in the Galaxy can be constrained by assuming that IMBHs accrete gas and become observable as X-ray sources.

3.2 How do IMBHs form?

The very existence of IMBHs is still uncertain, because there are not clear detections of these objects. However, from the theoretical point of view many scenarios have been proposed to explain the formation of IMBHs. Here the four most viable processes are considered, i.e.:

- gravitational collapse of first massive stars;

- direct collapse of dense, low angular momentum gas;

- runaway collapse of star clusters;

- repeated mergers of BHs in globular clusters.

Let us present in more detail each one of these models.

3.2.1 The final fate of metal free stars

The main difference between the late stages of the life of a metal free and a solar metallicity star is probably represented by the mass losses. In fact, the lack of initial metals in population III (pop III) stars results in a strongly reduced mass loss, down to the point of negligibility (Kudritzki 2002). This influences the nature of the supernova (SN) explosion for massive metal free stars in the following ways (Heger & Woosley 2003; Heger et al. 2003).

- Pop III stars with mass $8\,M_\odot < M < 25\,M_\odot$ suffer SN explosions and their core collapses into a neutron star. This process is nearly the same as for solar metallicity stars.

- Pop III stars with mass $25\,M_\odot < M < 35\,M_\odot$ form BHs by fall back after SN explosion. Also this process is the same as for solar metallicity stars.

- For pop III stars with mass $35\,M_\odot < M < 140\,M_\odot$ the SN shock cannot be launched due to the strong infall of the increasingly larger oxygen and silicon core masses. Then a BH is formed directly without SN explosion and its mass is close (within a factor 2) to the initial mass of the progenitor star. This behavior is completely different from that of solar metallicity stars of the same initial mass (which encounter stronger mass losses before the SN and then suffer a disruptive SN explosion). Stars with $110\,M_\odot < M < 140\,M_\odot$ encounter the electron-positron creation instability after central carbon burning (Bond, Arnett & Carr 1984; Woosley 1986), ejecting the external layers and the hydrogen envelope.

- In metal free stars with $140\,M_\odot < M < 260\,M_\odot$ the pair instability is strong enough to end with the complete disruption of the star: no remnant is left.

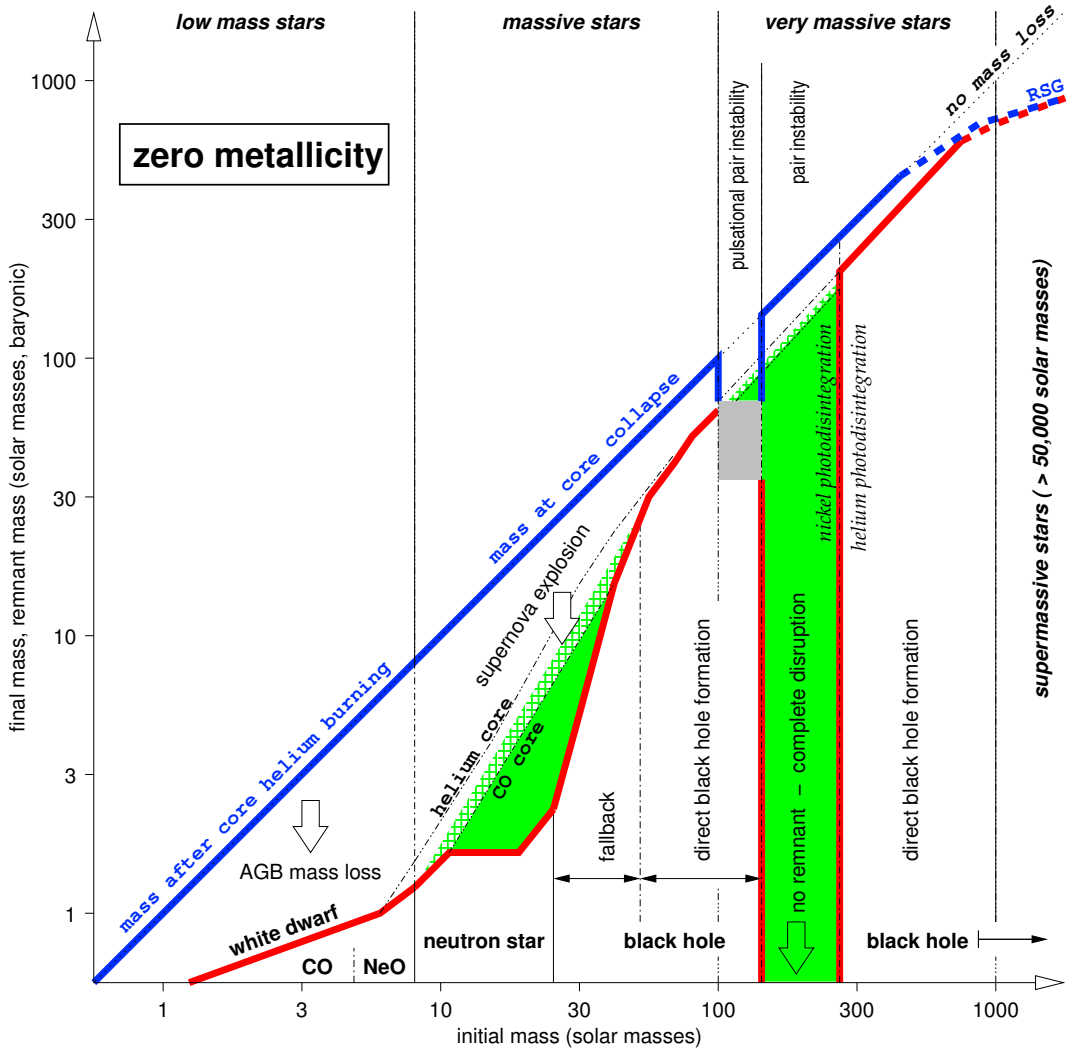

Figure 3.1: Stellar mass at time of final explosion/remnant formation (*blue line*), remnant mass (*red line*) and metals released (*green fill and hatching*) as a function of initial mass of the star for primordial (metal-free, pop III) stars. From Heger et al. 2003.

- In pop III stars with mass $M > 260\,M_{\odot}$ the photo-disintegration of α-particles reduces the pressure enough that the collapse of the star directly continues into a BH (Fryer, Woosley & Heger 2001). The mass of the BH is close to the mass of the progenitor star. Then, metal free stars with mass $M > 260\,M_{\odot}$ directly collapse into IMBHs. However, there is a caveat: if the mass of the progenitor is above several hundreds of solar masses, then even the metal free star can evolve into a red supergiant becoming pulsationally unstable and, then, loosing mass.

These different processes are shown in Fig. 3.1 (Heger et al. 2003). To summarize, metal free stars with mass $M > 260\,M_\odot$ should end their life forming IMBHs with mass $m_\bullet > 150\,M_\odot$. Because the density of the gas at the formation redshift of metal free stars is higher than in the current Universe these IMBHs can probably accrete with moderately larger efficiency (Ricotti & Ostriker 2004; Ricotti, Ostriker & Gnedin 2005; Shapiro 2005; Volonteri & Rees 2005), increasing their mass of a factor $\sim 10 - 100$. So they can easily end up as IMBHs of $10^{3-4}\,M_\odot$.

3.2.2 Direct collapse of low angular momentum gas

The previous scenario requires that IMBHs form from the death of pop III stars. Instead, in various models the stellar phase can be bypassed: the IMBH forms directly from the collapse of low angular momentum gas, possibly experiencing a 'quasi-star' transient state. The mechanism of IMBH formation from low angular momentum gas was originally studied by Haehnelt & Rees (1993) and Umemura, Loeb & Turner (1993), and then considered by many authors (Loeb & Rasio 1994; Eisenstein & Loeb 1995; Bromm & Loeb 2003; Koushiappas, Bullock & Dekel 2004; Begelman, Volonteri & Rees 2006; Lodato & Natarajan 2006). The crucial problem of this scenario is the disposal of angular momentum, needed to start the collapse. The mechanisms which have been proposed to remove angular momentum are either turbulence (Eisenstein & Loeb 1995) or gravitational instabilities (Koushiappas, Bullock & Dekel 2004; Begelman, Volonteri & Rees 2006; Lodato & Natarajan 2006).

In particular, Begelman, Volonteri & Rees (2006) proposed that the collapse is driven by the 'bars within bars' mechanism (Shlosman, Frank & Begelman 1989; Shlosman, Frank & Begelman 1990): bars (which form in halos under certain assumptions) can efficiently transport angular momentum outwards, allowing a first shrinking of the radius. Then, if the gas is able to cool, the collapse proceeds faster and faster. During this process an unstable 'quasi-star' is formed, i.e. an object which cannot establish stable nuclear burning, because of compression due to the high accretion rate, and which rapidly collapses into a seed BH. Begelman et al. (2006) found that halos with virial temperature $T_{vir} \sim 10^4$ K are likely to suffer this instability and form central seed BHs of $\lesssim 20\,M_\odot$.

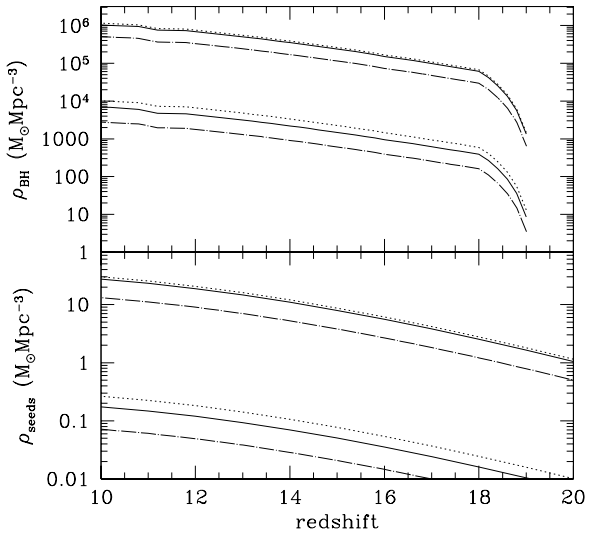

Figure 3.2: Lower panel: comoving density of $20\,M_\odot$ BH seeds as a function of redshift. Upper panel: comoving density of BHs, assuming continuous formation and growth of seeds to $10^6\,M_\odot$, starting from $z = 20$. Solid line: Mestel disc, dotted line: rigid disc, dot-dashed line: exponential disc. The upper set of lines assumes $f_d = 0.5$, the lower set assumes $f_d = 0.1$, where f_d is the fraction of baryonic mass which ends up in the pre-galactic disk hosting the BH. From Begelman, Volonteri & Rees 2006.

In these conditions, the initial seed grows very rapidly (super-Eddington, Volonteri & Rees 2005), reaching $10^{4-6}\,M_\odot$. Thus, this mechanism is likely to form more massive IMBHs than the previous one (based on massive pop III stars). The IMBHs which possibly form via this process can be the progenitors of present-day SMBHs (see Fig. 3.2).

Lodato & Natarajan (2006) showed that the angular momentum transfer required to start the collapse can be established also without the formation of a bar, for a certain range of initial halo parameters. In particular, they found that low spin and more massive halos are most efficient in concentrating gas into their centers. These halos can form IMBHs in their center only if they are able to accrete gas and if fragmentation does not take place. These conditions are satisfied mainly in halos where the $T_{vir} \lesssim 1.8\,T_{gas}$ (where T_{vir} and T_{gas} are the virial and the gas temperature, respectively). In this case, IMBHs with mass up to $10^5\,M_\odot$ can be formed. Lodato & Natarajan (2006) concluded that $\sim$ 5% of disks resulting from the collapse of $\sim 10^7\,M_\odot$ halos should host a $\sim 10^5\,M_\odot$ BH.

3.2.3 Runaway collapse in young clusters

Vishniac (1978) demonstrated that a Salpeter (1955) IMF is Spitzer unstable (1969). Then, Vishniac suggested that young clusters can suffer core collapse on the timescale required for the most massive stars to segregate into the core, possibly leading to the formation of a central massive compact object. Portegies Zwart et al. (1999) showed by N-body simulations that Vishniac's idea was correct, i.e. that core collapse can induce runaway collisions in young clusters, and that runaway collisions may lead to the growth of a single massive stars. Portegies Zwart et al. (1999) also included the presence of primordial binaries, showing that stellar mergers are enhanced by binaries.

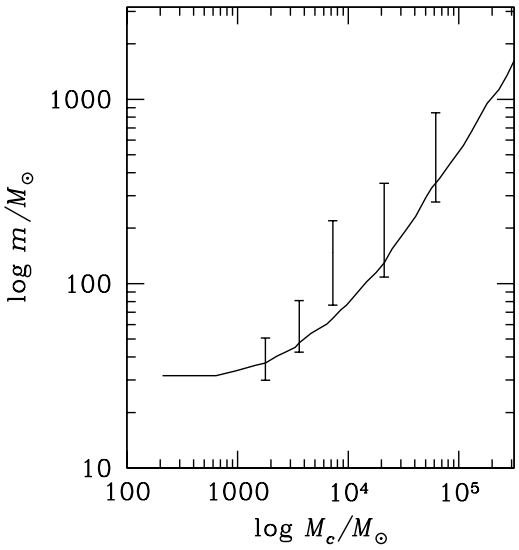

Figure 3.3: Mass of the product of the runaway growth as a function of the mass of the cluster (Portegies Zwart & McMillan 2002). The solid line indicates the semi-analytical model by Portegies Zwart & McMillan 2002. The five error bars give a summary of the results of different N-body simulations.

In particular, the core collapse, drastically increasing the density, initiates physical collisions between stars, which occur mainly during three-body encounters involving binaries. The product of the first collision is likely to be among the most massive stars in the system. Therefore, this star (which can be dubbed as 'target' star) is likely to experience subsequent collisions, resulting in a collision runaway. This leads to the formation of an

object containing up to $\sim 0.1\%$ of the total mass of the cluster itself (Portegies Zwart & Mcmillan 2002). The central object could be a star or a IMBH. Its expected mass as a function of the cluster mass is showed in Fig. 3.3 (from Portegies Zwart & McMillan 2002).

The only two factors that can prevent the runaway growth are the following (Portegies Zwart & Mcmillan 2000).

- The target star explodes in SN before experiencing runaway growth. This can be avoided if the core collapse timescale, t_{cc}, is much shorter than the star lifetime, τ_*. Since $t_{cc} \sim 0.2\, t_{rh}$ (where t_{rh} is the half mass relaxation time) and $\tau_* \sim 5$ Myr, the runaway growth can occur if $t_{rh} \lesssim 25$ Myr (which is a reasonable limit for young clusters, but too short for globular clusters).

- The cluster is disrupted by the galaxy before the core collapse. To avoid that the runaway growth is stopped by tidal disruption, the initial distance of the cluster from the galactic center must be $r_i > 1.7$ pc $(r_c/0.1\ \mathrm{pc})^{0.71}\, (M_c/10^5\, M_\odot)^{0.71}$, where r_c is the core radius and M_c the cluster mass.

3.2.4 Repeated mergers of binary BHs

The core of some globular clusters is a very dense environment, with density $n_c \sim 10^6$ stars pc^{-3}. Then, close gravitational encounters play a significant role in the evolution of these systems. In particular, if the binary fraction is non-negligible ($> 10^{-4}$), three and four body encounters dominate the dynamics.

Sigurdsson & Hernquist (1993) hypothesize that in the early stages of globular cluster life stellar BHs, being the most massive objects hosted in them, have rapidly segregated towards the cluster core. In the core they formed binaries and participated to repeated three and four body encounters. The recoil velocity acquired from these interactions caused the ejection of nearly all the BHs with mass $m_\bullet \leq 50\, M_\odot$ (Miller & Hamilton 2002). This is thought to be the reason why stellar BHs have not been observed in globular clusters. However, if a BH seed with mass $m_\bullet \gtrsim 50\, M_\odot$ happened to be in the core, it has not been ejected due to gravitational encounters. Instead, given its large mass, it probably formed a binary with another BH and this binary hardened, i.e. reduced its orbital separation

due to gravitational encounters with other BHs/stars (see next chapter for details), until it merged via gravitational wave emission (Miller & Hamilton 2002). The product of the first merger probably formed a new binary and the process repeated, leading to a series of mergers. Miller & Hamilton estimated that the mass growth of the BH due to these repeated mergers is of the order of $m_\bullet \sim 50\,M_\odot \left\{t/\left[3\times10^8\,(n/10^6\ \mathrm{pc}^{-3})^{-1}\,(m/10\,M_\odot)^{-5/2}\ \mathrm{yr}\right]\right\}^2$, where m is the mass of the secondary component of the binary (a stellar BH or a star). Then, within a Hubble time, IMBHs with mass $m_\bullet \sim 10^3 - 10^4 M_\odot$ can form via repeated three-body interactions and binary mergers in globular clusters. This is the third possible mechanism of IMBH formation; but it is not independent from the other two. In fact, a seed BH with mass $m_\bullet \gtrsim 50\,M_\odot$ can be formed only by collapse of a massive metal poor star or by runaway collision.

In the next Chapter we will investigate further the possible existence of IMBHs in globular clusters and their role in gravitational encounters.

3.3 ULXs and IMBHs

ULXs are, by definition, point sources with X-ray luminosity higher than 10^{39} erg s^{-1}, exceeding the isotropic Eddington limit for a 10 $M_\odot$ BH (see Colbert & Miller 2005 for a review). ULXs have not been found, up to now, in the Milky Way; but they are present in many spiral and starburst galaxies (Swartz et al. 2004). ULXs tend to be associated with star forming regions; but they often lie near, not in them (Mushotzky 2004).

ULXs were initially identified with SMBHs with a low accretion rate; but this interpretation was found to be in conflict with their position in the host galaxies, far off from the galaxy center (Colbert & Miller 2005). Later on ULXs have been suggested to be high-mass X-ray binaries (HMXBs) with beamed X-ray emission (King et al. 2001; Grimm, Gilfanov & Sunyaev 2003; King 2003). Even though low luminosity ULXs ($L_X \lesssim 5\times10^{39}$ erg s^{-1}) are consistent with this HMXB scenario, the highest luminosity ULXs show various characteristics which can be hardly reconciled with the beaming model (Miller, Fabian & Miller 2004), such as the existence of a ionized nebula surrounding some bright ULXs (Pakull & Mirioni 2002; Kaaret, Ward & Zezas 2004).

An intriguing hypothesis, at least for these highest luminosity ULXs (Miller et al. 2004), is their identification with accreting IMBHs. This idea is also supported by some observational evidences. First, the spectra of many high luminosity ULXs have a soft component well fitted by a multicolor black-body disk, whose inner temperature is typical of BH masses in the IMBH range (Miller et al. 2004; Colbert & Miller 2005). In addition, high luminosity ULXs often show long term variability on timescales of months to years (Kaaret et al. 2001; Matsumoto et al. 2001; Miyaji, Lehmann & Hasinger 2001) and quasi periodic oscillations (Strohmayer & Mushotzky 2003), inconsistent with the beaming scenario. King & Dehnen (2005) propose that very high luminosity ULXs in interacting galaxies can be IMBHs hosted in the merging satellite and whose accretion is activated by tidal forces.

Many studies have been dedicated to check the possibility that ULXs are IMBHs accreting in binary systems (Baumgardt et al. 2004; Hopman, Portegies Zwart & Alexander 2004; Kalogera et al. 2004; Portegies Zwart, Dewi & Maccarone 2004; Hopman & Portegies Zwart 2005; Patruno et al. 2005). However, the observed population of ULXs is not well reproduced by this binary system scenario (Blecha et al. 2006; Madhusudhan et al. 2006), mainly because the ULX phase of simulated IMBHs is too short. A better agreement between simulations and observations can be obtained only by considering very massive IMBHs ($\gtrsim 1000\, M_{\odot}$; Baumgardt et al. 2005). In addition, very few optical counterparts have been detected for ULXs so far and can unambiguously be identified as companion stars (Liu et al. 2005; Colbert & Miller 2005). Then, it is still open the possibility that ULXs are IMBHs accreting gas during the transit through a dense molecular cloud, as recently suggested by Krolik (2004) and by Mii & Totani (2005).

I explored in detail this last hypothesis by dedicated N-body simulations (Mapelli, Ferrara & Rea 2006). In particular, I simulated a Milky Way model and derived an upper limit of the density of IMBHs, by requiring that no ULX is produced in the Milky Way by IMBHs passing through molecular clouds (see Section 3.4-3.5 of this Thesis). Then, I studied the distribution of both ULX and non-ULX sources produced by IMBHs passing through molecular clouds (Section 3.5) and atomic hydrogen regions (Section 3.6). I finally compared the derived distributions with observations (Section 3.7-3.8).

3.4 Numerical simulations

The simulations have been carried out using the parallel N-body code Gadget-2 (Springel 2005). The simulations were performed using 8 nodes of the 128 processor cluster *Avogadro* at the *Cilea* (http://www.cilea.it). Our aim is to generate a suitable N-body model of the Milky Way (see Appendix A of this Thesis for more details), in which we embed a halo population of IMBHs.

3.4.1 Milky Way model

To reproduce the Milky Way we simulated an exponential disk and a Hernquist spherical bulge, whose density profiles are given, respectively, by the following relations (Hernquist 1993):

$$\rho_d(R,z) = \frac{M_d}{4\pi R_d^2\, z_0}\, \exp -(R/R_d)\, \mathrm{sech}^2(z/z_0) \tag{3.1}$$

$$\rho_b(r) = \frac{M_b\, a}{2\pi}\, \frac{1}{r\,(a+r)^3}, \tag{3.2}$$

where M_d (M_b) is the disk (bulge) mass, R_d is the disk scale radius, z_0 is the disk scale height, a is the bulge scale length and $r = \sqrt{R^2+z^2}$. We choose $a = 0.2\, R_d$, consistent with Kent, Dame & Fazio (1991; $a = 0.7 \pm 0.2$ kpc). The value of z_0 is quite difficult to constrain. Recent observations (Larsen & Humphreys 2003; Yoachim & Dalcanton 2005) suggest the presence of two components in the thin disk of the Milky Way: a "young star forming" thin disk (with scale height ~ 200 pc) and an "old" thin disk (with scale height ~ 600 pc). Then, we assume $z_0 = 0.1\, R_d = 350$ pc, which is approximately an average of the scale height of these two components and correlates in a simple way with R_d.

Disk and bulge are embedded in a rigid dark matter halo, whose density profile is (Navarro, Frenk & White 1996, hereafter NFW; Moore et al. 1999):

$$\rho_h(r) = \frac{\rho_s}{(r/r_s)^\gamma\, [1+(r/r_s)^\alpha]^{(\beta-\gamma)/\alpha}}, \tag{3.3}$$

where we choose $(\alpha,\beta,\gamma) = (1,3,1)$, and $\rho_s = \rho_{crit}\, \delta_c$, ρ_{crit} being the critical density of the Universe and

$$\delta_c = \frac{200}{3}\, \frac{c^3}{\ln(1+c) - (c/(1+c))}, \tag{3.4}$$

where c is the concentration parameter and r_s is the halo scale radius, defined by $r_s = R_{200}/c$. R_{200} is the radius encompassing a mean overdensity of 200 with respect to the background density of the Universe, i.e. the radius containing the virial mass M_{200}. Given the concentration c and the Hubble parameter[1] $H(z)$, R_{200}, M_{200} and the circular velocity at the virial radius, V_{200}, are related by the following expressions.

$$R_{200} = \frac{V_{200}}{10\,H(z)}$$
$$M_{200} = \frac{V_{200}^3}{10\,G\,H(z)}; \tag{3.5}$$

G is the gravitational constant. In our simulations we assume $c = 12$, $V_{200} = 160$ km s^{-1} (see Klypin, Zhao & Somerville 2002), yielding $M_{200} = 1.34 \times 10^{12} M_\odot$, $R_{200} = 225$ kpc and $r_s = 19$ kpc (Table 3.1 reports the initial parameters); finally, we use for $H(z)$ its actual value H_0.

Rigid halos can induce $m = 1$ instabilities in the disk. To check this effect, we performed test simulations with a non-rigid halo (with halo particles ten times more massive than disk particles); we did not observe significant differences in the evolution with respect to rigid-halo models. Since simulations with non-rigid halos are prohibitively time consuming for the very high resolution required by the problem, we have chosen to adopt a rigid halo.

To derive M_d, M_b and R_d we followed the prescriptions of Mo, Mao & White (1998), imposing that the disk is a thin, dynamically stable and centrifugally supported structure, whose mass is a fraction of the halo mass and whose angular momentum is a fraction of the halo angular momentum. In particular, our best, stable model is obtained for a choice of the spin parameter $\lambda = 0.035$, where $\lambda \equiv J\,|E|^{1/2} G^{-1} M^{-5/2}$ (J, E and M being the angular momentum, the total energy and the mass of the halo, respectively). Requiring that $M_d + M_b \approx 0.04\,M$ and that $M_d : M_b = 4 : 1$ (in agreement with Kent et al. 1991; Freudenreich 1998; Binney & Merrifield 1998), we obtain $M_d = 4 \times 10^{10}\,M_\odot$ and $M_b = 1 \times 10^{10}\,M_\odot$. Our choices are in agreement both with the best model of Milky Way described in Klypin et al. (2002) and with the COBE measurements of the bulge mass ($M_b = 1.3 \pm 0.5 \times 10^{10} M_\odot$, Dwek et al. 1995). For these values, the scale radius of the disk

[1] We adopt $H(z \lesssim 1) = H_0 = 71$ km s^{-1} Mpc^{-1} in agreement with first year WMAP results (Spergel et al. 2003)

is $R_d = 3.5$ kpc, consistent with recent estimates (Binney & Merrifield 1998). Given the uncertainty on the M_d/M_b ratio, we also made some test simulations for $M_d : M_b = 5 : 1$ observing no significant differences in our results. In order to account for the SMBH in the nucleus of the Milky Way, we located a point mass $M_{SMBH} = 3.5 \times 10^6 M_\odot$ (Ghez et al. 2003; Shödel et al. 2003) at the center of the rigid halo.

Initial velocities of disk and bulge particles are simulated using the Gaussian approximation (Hernquist 1993) for dispersion velocities (see Appendix A of this Thesis). This choice introduces a transient behavior, represented by outwards propagating rings of overdensity from the warmer disk center, as it was already noted by Kuijken & Dubinsky 1995 (see also Kazantzidis, Magorrian & Moore 2004; Widrow & Dubinski 2005). In agreement with the findings of Kuijken & Dubinsky 1995, in the highest resolution runs (when the mass of each particle is $m \lesssim 10^5 M_\odot$ and the total number of particles approaches one million) this transient is stronger; nevertheless, it always disappears within about 1 timescale[2], when the system relaxes into a new equilibrium configuration. We consider this new relaxed configuration as initial condition for our analysis. This procedure is legitimate in our case, since we are not investigating processes such as disk instabilities, but we are only interested in the dynamical evolution of halo IMBHs.

After relaxation, we continue the simulation for about 5 Gyr, i.e. from redshift $z \approx 0.5$ until today, about half of the time elapsed from the last major merger (Governato et al. 2004). This allows us to follow the evolution of an already relaxed and nearly unperturbed (by mergers) Milky Way. During the entire simulation disk and bulge remain perfectly stable.

3.4.2 Intermediate mass black holes

How many IMBHs are hosted in the Milky Way? What is their spatial distribution? These are yet unanswered questions. Nevertheless, we need an *Ansatz* on the IMBH number, mass and distribution to generate the initial conditions of our simulations. A reasonable estimate for the initial IMBH number follows from Volonteri, Haardt & Madau 2003. Assuming that the IMBHs are born in $\nu\,\sigma$ fluctuations (with $\nu = 3 - 3.5$) collapsing

[2]The timescale of our simulation is defined as the rotation period of the simulated galaxy, i.e. about 0.27 Gyr.

Table 3.1: Initial parameters for the Milky Way model.

c	12
V_{200}	160 km s^{-1}
M_{200}	$1.34\times10^{12} M_\odot$
R_{200}	225 kpc
λ	0.035
M_d/M_b	4
M_d	$4\times10^{10} M_\odot$
M_b	$10^{10} M_\odot$
R_d	3.5 kpc
z_0	0.1 R_d
a	0.2 R_d

at a given redshift, Volonteri et al. (2003) derive the density of IMBHs at the formation redshift $\Omega_{\bullet,\,f}$ as

$$\Omega_{\bullet,f} = \left[1 - \mathrm{erf}\left(\nu/\sqrt{2}\right)\right]\, \Omega_M\, \frac{m_{\bullet,f}}{M(\nu)}, \tag{3.6}$$

where $[1 - \mathrm{erf}(\nu/\sqrt{2})]\Omega_M$ is the fraction of the Universe matter in halos with $M > M(\nu)$ ($\Omega_M = 0.27$ being the matter density), as derived from the Press & Schechter (1974) formalism, and $m_{\bullet,f}/M(\nu)$ is the fraction of mass of the halo collapsed in IMBHs ($m_{\bullet,f}$ being the average initial IMBH mass, and $M(\nu)$ the mass of the $\nu\,\sigma$ peak halo). For example, assuming that IMBHs form in $3\,\sigma$ fluctuations collapsing at redshift $z = 24$, the corresponding halo mass is $M(3) = 1.7 \times 10^5 M_\odot$ (Barkana & Loeb 2001). Under these assumptions equation (3.6) gives $\Omega_{\bullet,f} = 10^{-4}\,\Omega_b\,(m_{\bullet,f}/10^3 M_\odot)$.

Given $\Omega_{\bullet,\,f}$, one can roughly estimate the number of IMBHs in the Milky way, $N_\bullet$ as

$$N_\bullet = \frac{\Omega_{\bullet,\,f}}{\Omega_b}\frac{M_{b,MW}}{m_{\bullet,f}}, \tag{3.7}$$

where $M_{b,MW} = (0.5 - 1) \times 10^{11} M_\odot$ is the mass in baryons of the Milky Way. Adopting a value of $\Omega_{\bullet,\,f} = 10^{-4}\,\Omega_b$, we find $N_\bullet \approx 10^4$. Instead, if we assume that IMBHs form in $3.5\,\sigma$ fluctuations collapsing at $z = 24$, this number becomes $N_\bullet = 5 \times 10^2$. We will adopt equations (3.6) and (3.7) to calculate how many IMBHs to include in our simulations.

How massive are the IMBHs today? We have assumed that their average mass at formation was $m_{\bullet,f} = 10^3\,M_\odot$. However, it is likely that they accreted gas for some

period of their life (Ricotti & Ostriker 2004; Madau et al. 2004; Shapiro 2005; Volonteri & Rees 2005). The duration and the efficiency of accretion are highly uncertain, making hard to determine the amount of accreted mass. Shapiro (2005) suggests that the IMBH mass evolution $m_\bullet(t)$, assuming Eddington rate accretion, can be written as:

$$m_\bullet(t) = m_{\bullet,f}\, \exp\left(\frac{1-\epsilon}{\epsilon}\,\frac{t}{t_{Salp}}\right), \tag{3.8}$$

where ϵ is the radiative efficiency ($\epsilon \approx 0.1$) and t_{Salp} is the Salpeter time ($t_{Salp} \approx 0.45$ Gyr). In our case t is the fraction of IMBH life during which it accretes at the Eddington rate, i.e. $t = f_{duty}\, t_{birth}$, where t_{birth} is the time elapsed from the IMBH formation (≈ 13.5 Gyr) and f_{duty} is the fraction of t_{birth} during which the IMBH accretes. Assuming $f_{duty} \approx 0.01$ ($f_{duty} \lesssim 0.03$ for quasars at $z \approx 6$, Steidel et al. 2002), we obtain $m_\bullet(t) \approx 10\, m_{\bullet,f}$. For our choice of $m_{\bullet,f} = 10^3 M_\odot$, this means that the average mass of IMBHs today is $m_\bullet(t) \approx 10^4 M_\odot$, consistent with the value $1.8 \times 10^4 M_\odot$ of the recently detected IMBH candidate in the globular cluster G1 (Gebhardt et al. 2005) and with previous theoretical estimates (Volonteri et al. 2003). This estimate is affected by a number of uncertainties, and we consider it only as an educated guess.

Due to accretion, the current density of IMBHs $\Omega_\bullet$ will be

$$\Omega_\bullet = \frac{m_\bullet(t)}{m_{\bullet,f}}\,\Omega_{\bullet,f} \approx 10\,\Omega_{\bullet,f} = 10^{-3}\Omega_b(m_{\bullet,f}/10^3 M_\odot), \tag{3.9}$$

our reference value.

We note that other models predict very different values for $\Omega_\bullet$. For example, Salvaterra & Ferrara (2003) derived $\Omega_\bullet \approx 0.1\,\Omega_b$, under the assumption that pop III stars are the sources of the observed near-infrared excess with respect to galaxy counts. One of the aims of this study is to check which part of the $\Omega_\bullet$ range is allowed by the link between IMBHs and ULXs (see next section). For this reason, we also carried out two runs adopting the estimate by Salvaterra & Ferrara (2003).

The last problem we have to address is the selection of initial conditions for the position and velocity distribution of IMBHs. White & Springel (2000) suggested that remnants of pop III stars should be much rather concentrated inside present-day halos. N-body cosmological simulations by Diemand, Madau & Moore (2005, hereafter DMM) seem to

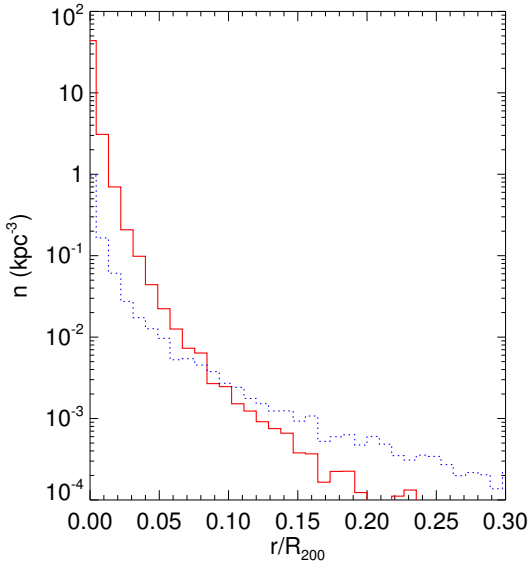

Figure 3.4: Density profile of IMBHs for a DMM (case A1; solid line) and for a NFW distribution (case A2; dotted line).

support this idea; they also show that the present spatial distribution of objects formed in high-σ fluctuations depends only on the rarity of the peak in which they are born. In particular, DMM find that the spatial distribution, in present halos, of objects formed in a $\nu\,\sigma$ fluctuation is well fitted by a modified NFW profile:

$$\rho_\bullet(r) = \frac{\rho_s}{(r/r_\nu)^\gamma\,(1+(r/r_\nu)^\alpha)^{(\beta_\nu-\gamma)/\alpha}}, \tag{3.10}$$

where ρ_s, α and γ are the same as defined in the previous section; $r_\nu \equiv r_s/f_\nu$ is the scale radius for objects formed in a $\nu\,\sigma$ fluctuation (with $f_\nu = \exp(\nu/2)$), and $\beta_\nu = 3 + 0.26\,\nu^{1.6}$. As DMM simulations are collisionless, they cannot take into account the possible formation of binaries containing IMBHs (eventually with the central SMBH) and the occurrence of three-body encounters, which likely lead to the ejection of one of the involved IMBHs (Volonteri et al. 2003). Thus, the actual IMBH distribution could be slightly more "diluted" than that obtained by DMM.

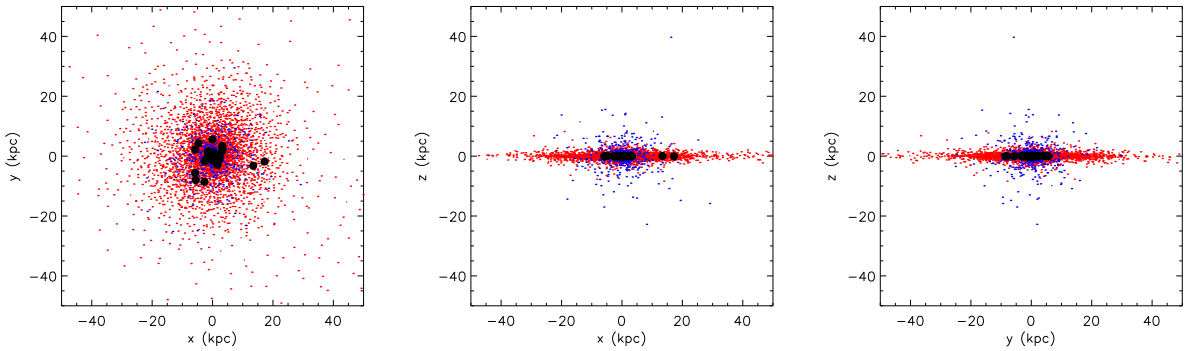

Figure 3.5: Snapshots at $t = 1.4$ Gyr (about 5 Galactic timescales) of the simulated Milky Way; only 1/200 of the total bulge and disk particles are plotted. Big dots indicate the IMBHs passing through the molecular disk in the case A1. Left panel: particle positions in the $x - y$ plane; central: in the $x - z$ plane; right: in the $y - z$ plane.

3.4.3 Description of runs

We made three different sets of simulations, A, B and C, whose characteristics are described in Table 3.2. Simulations labeled as A are characterized by $\Omega_\bullet = 10^{-3}\Omega_b$ (corresponding to IMBHs formed in 3 σ fluctuations), simulations B have $\Omega_\bullet = 10^{-1}\Omega_b$ (corresponding to the Salvaterra & Ferrara 2003 model), and the simulation C has $\Omega_\bullet = 3 \times 10^{-5}\Omega_b$ (corresponding to IMBHs formed in 3.5 σ fluctuations). Simulations A1, B1 and C adopt the DMM spatial distribution, assuming that IMBHs form in 3 σ (A1, B1) or 3.5 σ (C) peaks. Instead, runs A2 and B2 were performed assuming that IMBHs follow a normal NFW profile. In Fig. 3.4 we compare the two considered distributions of IMBHs, i.e. DMM and NFW. In each simulation we evolved about 10^6 particles, each having a mass of $5 \times 10^4\, M_\odot$ (included the IMBH particles). These particles are divided in $\approx 8 \times 10^5$ disk particles and $\approx 2 \times 10^5$ bulge particles, plus a variable number of IMBH particles: 2000 in each run of the group A (corresponding to 10^4 IMBHs of $10^4\, M_\odot$; see equations (3.7) and (3.8)), $2{\times}10^5$ in each run of the group B (corresponding to 10^6 IMBHs of $10^4\, M_\odot$) and 100 in the run C (corresponding to 500 IMBHs of $10^4\, M_\odot$). CPU time limits require that we consider only equal mass particles, with mass no lower than $5 \times 10^4\, M_\odot$ (included the IMBH particles), making impossible to investigate the impact of dynamical friction on the

Table 3.2: Initial parameters for the IMBHs.

Run	Number of IMBH particles	$\Omega_\bullet/\Omega_b$	IMBH profile
A1	2000	10^{-3}	DMM[a]
A2	2000	10^{-3}	NFW[b]
B1	2×10^5	10^{-1}	DMM
B2	2×10^5	10^{-1}	NFW
C	100	3×10^{-5}	DMM

[a]Diemand, Madau & Moore 2005.

[b]Navarro, Frenk & White 1996.

IMBH spatial distribution.

3.5 IMBHs accreting molecular gas

As discussed in the Introduction, one of the possible explanations for the existence of ULXs is that they are IMBHs, accreting both in binary systems (Patruno et al. 2005) or in molecular clouds (Mii & Totani 2005). Here we investigate the possibility that ULXs are IMBHs accreting gas during their transit within a molecular cloud. We also checked how many non-ultra-luminous X-ray sources ($L_X < 10^{39}$ erg s^{-1}) could be produced by IMBHs passing through molecular clouds.

3.5.1 IMBH density constraints from ULXs

The X-ray luminosity[3] of a BH with mass $M_\bullet$, expected from the Bondi-Hoyle accretion in a gas cloud, can be expressed as (Edgar 2004; Mii & Totani 2005):

$$L_X(\rho, v) = 4\,\pi\,\eta\,c^2 G^2 M_\bullet^2 \rho\,\tilde{v}^{-3}, \tag{3.11}$$

where η takes into account the radiative efficiency and the uncertainties in the accretion rate, c is the light speed, ρ the density of the molecular cloud and $\tilde{v} = (v^2 + \sigma_{MC}^2 + c_s^2)^{1/2}$, v

[3]More precisely, equation (3.11) refers to the bolometric luminosity due to the Bondi-Hoyle accretion. However, detailed models of spectra of BHs accreting in the Bondi-Hoyle regime (Beskin & Karpov 2005) or forming ADAF disks (Narayan, Mahadevan & Quataert 1998) show that more than 60% of the bolometric luminosity is emitted in the X-ray range and more than 40% between 0.2 and 10 keV (approximately the bandpass of Chandra and XMM). Because of the other uncertainties in our calculations, we think that the approximation that nearly all the Bondi-Hoyle luminosity is emitted in the X-ray band is acceptable.

being the IMBH velocity relative to the gas; σ_{MC} and c_s are the molecular cloud turbulent velocity and gas sound speed, respectively. Recently, Krumholz, McKee & Klein (2006) have shown that accretion rate in a turbulent medium might slightly differ from the above one. Because of the many uncertainties in our model, we do not attempt to deal with these subtleties. From equation (3.11) and following Agol & Kamionkowski (2002), Mii & Totani (2005) derive the number of ULXs with luminosity higher than L_X as[4]:

$$N_{ULX}(>L_X) \approx 2.2\times10^{-2} N_\bullet \, f_{disk} \, \mu^{-1} \, \eta \left(\frac{M_\bullet}{10^4 M_\odot}\right)^2 \left(\frac{10^{39}\mathrm{erg\ s^{-1}}}{L_X}\right), \qquad (3.12)$$

where μ is the mean molecular weight ($\mu \approx$ 1.2-2.3 depending on the fraction of H_2 molecules), $N_\bullet$ is the number of IMBHs in the Milky Way (see equation 3.7) and η is the radiative efficiency. The correct value of η is completely uncertain. In fact, we do not even know whether an accretion disk forms at all. Agol & Kamionkowski (2002) show that most of BHs accreting gas should form accretion disks; but these disks are not necessarily thin. If the accreting gas is able to form a thin accretion disk (Shakura & Sunyaev 1974), then $\eta = 0.1$, as assumed by Mii & Totani (2005). However, it seems to be more realistic that the gas forms an ADAF (i.e. Advection-Dominated Accretion Flow) disk, whose radiative efficiency[5] is of the order of $\eta = 0.001$ for IMBHs of mass $M_\bullet \sim 10^4\, M_\odot$ (Quataert & Narayan 1999). Finally, models which take into account gas magnetization (Beskin & Karpov 2005) show that a high efficiency ($\eta \approx 0.1$) is allowed, even if the thin disk does not form. To decide among these different models is beyond the scope of this study; we will consider the two different values $\eta = 0.1$ and $\eta = 0.001$ bracketing the above possibilities in all our cases.

In equation (3.12) f_{disk} is the fraction of IMBHs passing through the molecular disk of the Galaxy, for which we assume a scale height $z_{MC} = 75$ pc and a radial extension $R_{MC} \approx 20$ kpc (Sanders, Solomon & Scoville 1984). Mii & Totani estimated $f_{disk} \approx 4.5\times10^{-4}$, based on the hypothesis that IMBHs are a halo population following a standard

[4]We consider only the particular case of the equation by Mii & Totani (2005) in which $M_\bullet \gtrsim 10^3 M_\odot$

[5]The luminosity for an ADAF disk scales as $\dot{M}^2$, where $\dot{M}$ is the accretion rate. However, if $\log(\dot{M}/\dot{M}_{Edd}) \sim -4, -2$, where $\dot{M}_{Edd}$ is the Eddington accretion rate, the efficiency of an ADAF disk is about two orders of magnitude lower than the efficiency of a thin disk (see Figure 7 of Narayan et al. 1998). We can assume that the efficiency of an ADAF disk is $\eta = 10^{-3}$, because the accretion rates of the IMBHs we are considering fall in the range above.

NFW profile. Our simulations allow a more precise and direct estimate of f_{disk} from our simulations. As an example, in Fig. 3.5 we show a snapshot of our simulations, where the positions of IMBHs passing through the molecular disk are shown. Table 3.3 reports the simulated values for f_{disk} and N_{ULX} with luminosity $L_X \geq 10^{39}$ erg s^{-1}.

For $\eta = 0.1$, we find that, if IMBHs are born in 3 σ fluctuations (corresponding to $\Omega_\bullet \approx 10^{-3}\Omega_b$) and their present distribution in the Milky Way follows the DMM model (case A1), the number of ULXs associated with these IMBHs is still consistent with zero ($N_{ULX} \approx 0.2$; Table 3.3, third column). Instead, if $\Omega_\bullet \approx 10^{-1}\Omega_b$ (case B1), the Milky Way should host about 30 active ULXs. Then, we conclude that, if the IMBHs follow a DMM distribution, $\Omega_\bullet \approx 10^{-3}\Omega_b$ can be considered as an upper limit for the present density of IMBHs. If, on the contrary, the IMBHs follow a standard NFW profile, as assumed by Mii & Totani (2005), the number of ULXs obtained for $\Omega_\bullet \approx 10^{-1}\Omega_b$ (case B2) is still marginally consistent with zero. Finally, if IMBHs follow the DMM distribution but form only in fluctuations with $\sigma \gtrsim 3.5$, they are so rare that no ULX is expected to be seen in the Milky Way (case C1).

However, if IMBHs are surrounded by low efficiency ADAF disks ($\eta = 10^{-3}$), the upper limit for a DMM profile becomes $\Omega_\bullet = 0.1\,\Omega_b$; whereas there are nearly no constraints for the NFW profile. It is worth noting that Mii & Totani (2005) mainly considered the case of maximal efficiency ($\eta = 0.1$), which is probably unlikely according to Agol & Kamionkowski (2002).

Equation 3.12 tells us even another information: the dark matter halo of the Milky Way cannot be entirely composed by BHs with mass $\gtrsim 10^5\,M_\odot$. In fact, if $M_\bullet = 10^5\,M_\odot$ and $N_\bullet = 10^7$ (corresponding to the assumption that the Milky Way dark matter halo is composed by BHs as massive as $10^5\,M_\odot$), $N_{ULX}(> 10^{39}\text{erg s}^{-1}) \sim 2 \times 10^5\,\eta$ for a DMM profile and $N_{ULX}(> 10^{39}\text{erg s}^{-1}) \sim 9 \times 10^3\,\eta$ for a NFW model. This means $N_{ULX} \gg 1$ both for a thin and an ADAF disk model (unless $\eta \ll 10^{-3}$). Then, the dark matter halo can be entirely composed by BHs only if their mass is less than $10^5\,M_\odot$, ruling out the scenario proposed by Lacey & Ostriker (1985), in which halo BHs can account for the galactic disk heating.

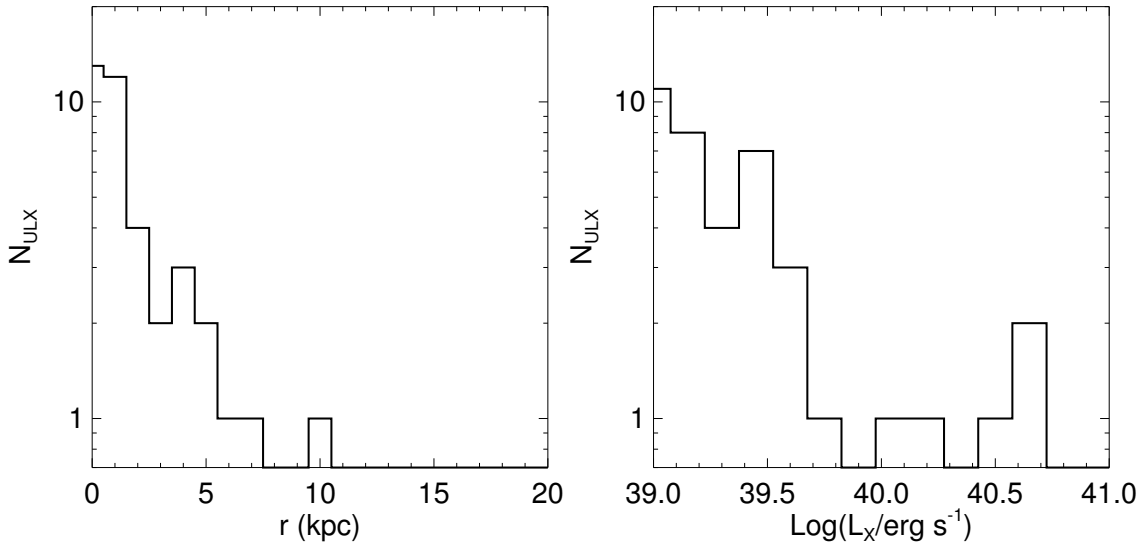

Figure 3.6: Distribution of ULXs as a function of their Galactocentric distance (left panel) and X-ray luminosity (right panel) for the case B1 and $\eta = 0.1$, after ≈ 0.5 Gyr.

3.5.2 Radial and luminosity distribution of ULXs

The previous results can be refined by using our simulations instead of equation (3.12). In fact, from the simulations we know the number $N(z < z_{MC})$ of IMBH particles which at a given time are in the molecular disk (defined by the scale height $z_{MC} = 75$ pc and the radial extension $R_{MC} \approx 20$ kpc). It is well known that H_2 in the Galaxy is not distributed uniformly within such disk, but it has a clumpy structure made of molecular clouds. Following Agol & Kamionkowski (2002) we derive the actual volume fraction of the molecular disk occupied by the clouds, i.e.

$$f_{MC} = \frac{(\beta-2)\langle\Sigma_{MC}\rangle}{(\beta-1)2\,\mu\,m_p\,z_{MC}\,n_{min}}\left[1-\left(\frac{n_{max}}{n_{min}}\right)^{(1-\beta)}\right] \approx 0.017, \qquad (3.13)$$

where $\beta = 2.8$ for an H_2 cloud, $\langle\Sigma_{MC}\rangle = 29\,M_\odot$ pc^{-2} (Sanders et al. 1984; Mii & Totani 2005) is the average surface density of molecular clouds, m_p is the proton mass, $n_{min} = 10^2$ cm^{-3} and $n_{max} = 10^5$ cm^{-3} are the minimum and maximum density, respectively, observed in molecular clouds. Thus, the number of IMBHs which at a given time t are embedded into a molecular cloud is $N(z < z_{MC})f_{MC}$. In practice, we randomly select from our simulations

a fraction f_{MC} of the IMBHs which at a given time t have $z < z_{MC}$ and $R < R_{MC}$. For this sample of IMBHs, we derive the Bondi-Hoyle luminosity L_X as in equation (3.11), assuming that $c_s = 0.3$ km s^{-1} and $\sigma_{MC} = 3.7$ km s^{-1} (Larson 1981; Solomon et al. 1987; Mii & Totani 2005). We then identify as ULXs those IMBHs which have $L_X > 10^{39}$ erg s^{-1}. Averaging this number over the entire simulation, we obtain an estimate $\tilde{N}_{ULX}(> L_X)$ of the number of ULXs in the Milky Way. For all the considered cases, the number $\tilde{N}_{ULX}(> L_X)$ (Table 3.3, fourth column), derived in this way, is consistent with the value $N_{ULX}(> L_X)$ (Table 3.3, third column), derived from equation (3.12), confirming the validity of the Mii & Totani calculation.

This alternative method to derive the number of ULXs contains additional important pieces of information concerning the spatial distribution of ULXs and their luminosities (see Fig. 3.6 for the case B1). These distributions are meaningless for the Milky Way, where no ULXs have been detected. Nevertheless, it could be interesting to compare them with the distributions of ULXs observed in other spiral galaxies. Fig. 3.6 shows that, if a DMM profile is adopted for IMBHs, ULXs appear to be mostly concentrated towards the Galactic center. This seems to be at odds with observations, which have shown that ULXs of external galaxies tend to be preferentially located in spiral arms (Liu & Bregman 2005). We have to keep in mind, though, that the present calculation is based on the molecular hydrogen distribution of the Milky Way, which could be quite different from that of other galaxies hosting ULXs; the latter are often starbursting, very gas rich systems.

The predicted ULX luminosities (Fig. 3.6) are mostly in the range 1 - 5 $\times 10^{39}$ erg s^{-1} with only few sources showing luminosities higher than 10^{40} erg s^{-1}. This rapid falloff of the number of ULXs for increasing X-ray luminosities is consistent with observations (Grimm et al. 2003). On the contrary, simulations following the accretion of IMBHs in binary systems indicate a number of low luminosity ULXs which is only a factor ≈ 2 higher than the number of sources with $L_X > 10^{40}$ erg s^{-1} (Madhusudhan et al. 2005). As a caveat, we recall that our calculations assume a Bondi-Hoyle luminosity, which might be a relatively oversimplified approximation.

3.5.3 Non ULX sources

By using the technique described in Section 3.5.2, we can also derive the number of low luminosity X-ray (in brief, non-ULX) sources with $L_X < 10^{39}$ erg s^{-1} (Table 3.3; fifth column). An interesting result is that, if $\eta = 0.1$, IMBH luminosities are always as high as 10^{37} erg s^{-1} (see Fig. 3.7, where the dotted line represents IMBHs accreting molecular gas, including ULXs). Instead, if only ADAF disks can form, the luminosities reached by accreting IMBHs in molecular clouds are lower, in the range from 10^{35} to 10^{38} erg s^{-1}. Luminosities from 10^{37} to 10^{39} erg s^{-1} are reached, in our Galaxy, only by a few supernova remnants (Vink 2006) and by high mass and low mass X-ray binaries (HMXBs, LMXBs; Psaltis 2006). Then, IMBHs accreting gas in molecular clouds should be among the most powerful Galactic X-ray sources and therefore should have been already detected, provided they are not transient. A strong constraint on the density of IMBHs thus descends from the requirement that the number of IMBHs with $L_X < 10^{39}$ erg s^{-1} is lower than the number of detected Galactic sources emitting at the same luminosities which lack of certain identifications with other kind of objects (such as HMXBs and LMXBs). This analysis will be carried out in Section 3.7, considering X-ray sources produced by IMBHs accreting both within molecular clouds and atomic hydrogen regions.

Table 3.3: Results.

Run	f_{disk}[a]	N_{ULX}[b]	$\tilde{N}_{ULX}$[c]	N_{H_2}[d]	N_H[e]	$N(10^{36-39}$ erg s$^{-1})$[f]
A1	0.022±0.003	0.2 (0.002)	0.2±0.2 (0.002±0.002)	1.0±0.6 (1.2±0.5)	45±12 (45±12)	18±7 (1.2±1.0)
A2	0.0008±0.0006	0.008 (8×10^{-5})	0±0 (0±0)	0±0 (0±0)	5±4 (5±4)	0.4±0.4 (0±0)
B1	0.025±0.002	28 (0.28)	40±6 (0.5±0.5)	310±24 (350±24)	4056±125 (4058±125)	1650±70 (236±15)
B2	0.00090±0.00007	1 (0.01)	0.5±0.5 (0.007±0.007)	5.6±1.5 (6.1±1.5)	495±39 (495±39)	148±21 (5±3)
C	0.039±0.018	0.02 (0.0002)	0±0 (0±0)	0±0 (0±0)	3±3 (3±3)	0.09±0.09 (0±0)

The values refer to a thin disk with $\eta = 0.1$ (the values in parenthesis refer to an ADAF disk with $\eta = 0.001$).

[a] Average fraction of IMBHs passing through the molecular disk (see Section 3.5.1).

[b] Number of ULXs with $L_X \geq 10^{39}$ erg s^{-1} derived from equation (3.12) adopting $\mu = 2$ (see Section 3.5.1).

[c] Number of ULXs with $L_X \geq 10^{39}$erg s^{-1} derived from our simulations (see Section 3.5.2 and Fig. 3.5).

[d] Number of sources which accrete molecular hydrogen (see Section 3.5.3) with X-ray luminosities $L_X < 10^{39}$ erg s^{-1}, derived from our simulations (see Fig. 3.6 and 3.7).

[e] Number of sources which accrete atomic hydrogen (see Section 3.6), derived from our simulations. All of them have $L_X \leq 10^{39}$ erg s^{-1} (see Fig. 3.6 and 3.7).

[f] Number of sources which accrete atomic or molecular hydrogen and have X-ray luminosity $10^{36} \leq L_X < 10^{39}$ erg s^{-1} (see Section 3.7).

3.6 IMBHs accreting atomic hydrogen

Mii & Totani (2005) neglected in their analysis IMBHs passing through atomic hydrogen regions, because their lower density ($\lesssim 1$ cm^{-3}) powers much lower X-ray luminosities than in molecular gas (King et al. 2001). However, atomic hydrogen is much more diffuse in the Milky Way than H_2, and IMBHs are so massive that they can have non-negligible luminosity even accreting in such rarefied environment. Current models of the hydrogen distribution in the Milky Way (McKee & Ostriker 1977; Rosen & Bregman 1995) suggest the existence of three different phases: a neutral cold component ($T \approx 10^2$ K), a warm ($T \approx 10^4$ K) and a hot ($T \approx 10^6$ K) component. In our work we neglect the hot component, since, even if its filling factor is high (up to 0.7, Rosen & Bregman 1995), it has an average density of $\approx 10^{-3}$ cm^{-3} and a sound speed of ≈ 100 km s^{-1}, so that the X-ray luminosity of IMBHs accreting hot gas is expected to be very low. We define an atomic hydrogen disk as a disk having cut-off length $R_H = 20$ kpc (the data show an exponential fall of neutral hydrogen density outside 20 kpc; Lockman 2002) and scale height $z_H = 100$ pc (Baker & Burton 1975; Sanders et al. 1984; Dickey & Lockman 1990). Adopting the procedure described in Agol and Kamionkowski (2002), we derive the volume fraction occupied by cold neutral hydrogen, f_{CH}, as:

$$f_{CH} = \frac{(\beta_{CH}-2)\langle\Sigma_{CH}\rangle}{(\beta_{CH}-1)2\,\mu\,m_p\,z_H\,n_{min,CH}}\left[1-\left(\frac{n_{max,CH}}{n_{min,CH}}\right)^{(1-\beta_{CH})}\right], \qquad (3.14)$$

where $\beta_{CH} = 3.8$ (Agol & Kamionkowski 2002), $\langle\Sigma_{CH}\rangle$ is the average surface density of neutral hydrogen ($\langle\Sigma_{CH}\rangle = 4.5\,M_\odot$ pc^{-2} if $R > 4$ kpc and $\langle\Sigma_{CH}\rangle \approx 0$ if $R \leq 4$ kpc; Agol & Kamionkowsky 2002; Sanders et al. 1984), $n_{min,CH}$ and $n_{max,CH}$ are the minimum and maximum density of neutral hydrogen, respectively ($n_{min,CH} \approx 1$ cm^{-3}, $n_{max,CH} \approx 5$ cm^{-3}; Bregman, Kelson & Ashe 1993). Substituting these values into equation (3.14), we obtain $f_{CH} = 0.48$ if $R > 4$ kpc and $f_{CH} \approx 0$ if $R \leq 4$ kpc. This value is in good agreement with run E of Rosen & Bregman (1995), which is a suitable fit of cold and warm hydrogen observations (Dickey & Lockman 1990). For consistency, we assume that the filling factor of the warm component is f_{WH}=0.2, as in run E of Rosen & Bregman (1995). Then, the number of IMBHs which, at a given time t, are passing through cold (warm) hydrogen

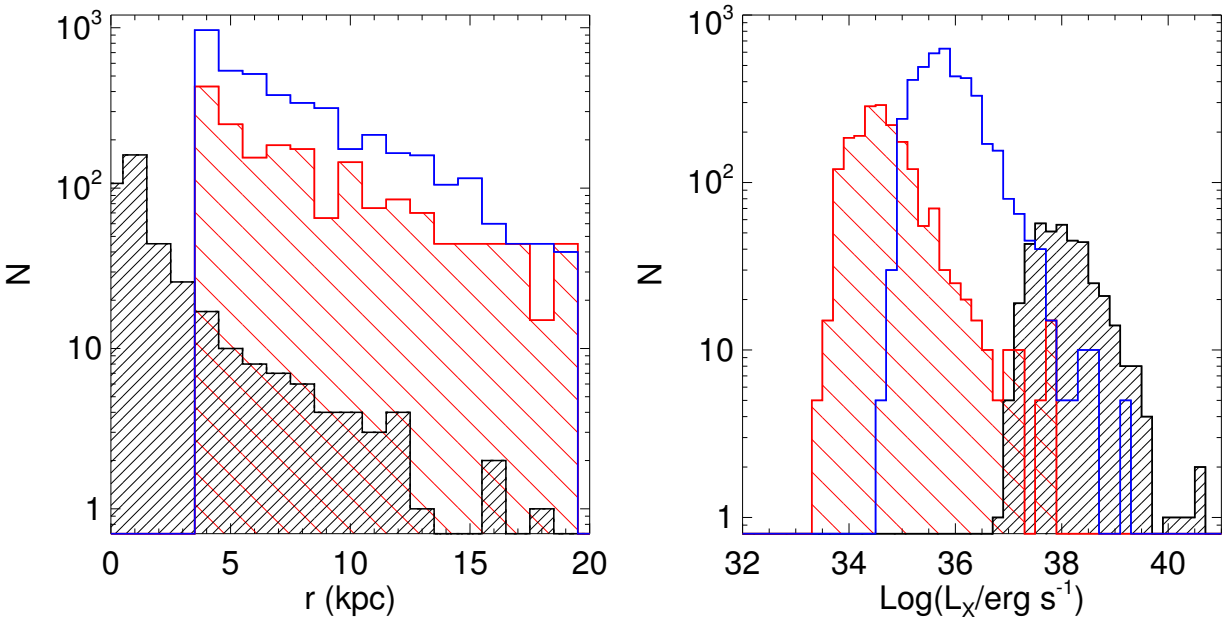

Figure 3.7: Distribution of all the X-ray sources as a function of their Galactocentric distance (left panel) and luminosity (right panel) for the case B1 and $\eta = 0.1$, after ≈ 0.5 Gyr. Open histogram: IMBHs passing through cold neutral hydrogen; light shaded histogram: IMBHs passing through warm hydrogen; heavy shaded histogram: IMBHs passing through molecular hydrogen. Although the distributions slightly change with time due to the small statistics, their main features remain unaltered.

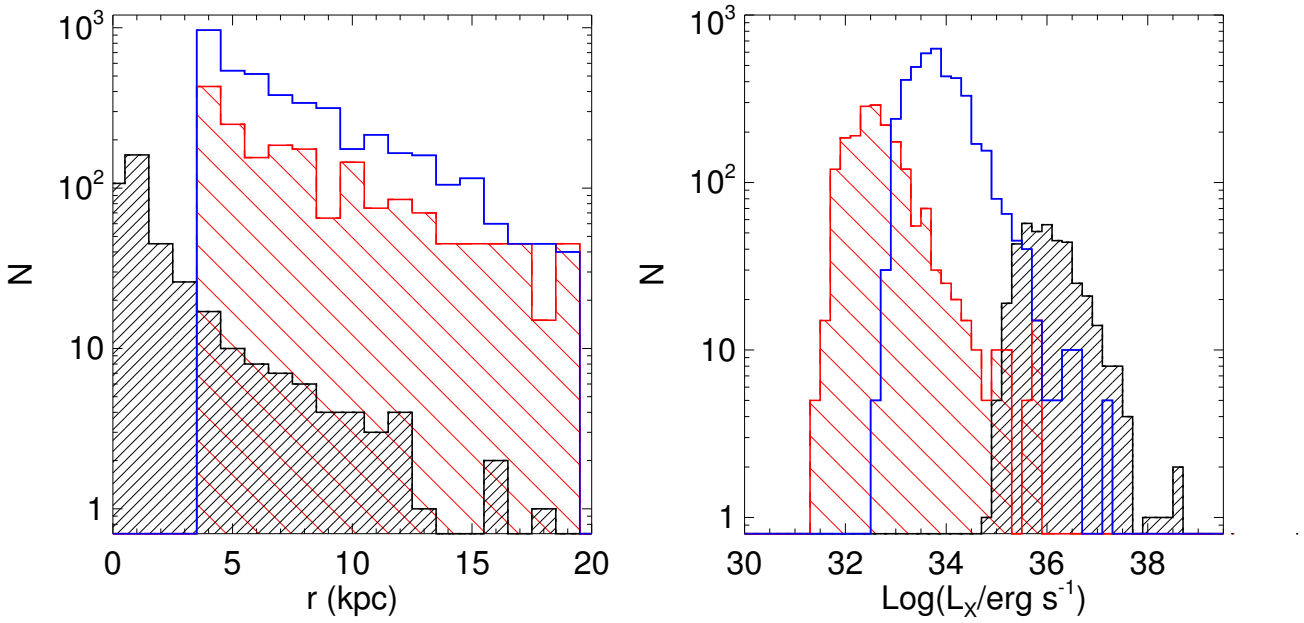

Figure 3.8: Distribution of all the X-ray sources as a function of their Galactocentric distance (left panel) and luminosity (right panel) for the case B1 and $\eta = 0.001$, after ≈ 0.5 Gyr. Open histogram: IMBHs passing through cold neutral hydrogen; light shaded histogram: IMBHs passing through warm hydrogen; heavy shaded histogram: IMBHs passing through molecular hydrogen. Although the distributions slightly change with time due to the small statistics, their main features remain unaltered.

regions is $N(z < z_H)\, f_{CH}$ ($N(z < z_H)\, f_{WH}$). Adopting the same procedure as in Section 3.5.2, we randomly select a fraction f_{CH} (for cold hydrogen) or f_{WH} (for warm hydrogen) of the IMBHs which, at a given time, pass through the neutral hydrogen disk, and we derive the Bondi-Hoyle luminosity[6] for each of them using equation (3.11). The results are shown in Table 3.3, sixth column, and in Fig. 3.7−3.8.

If $\eta = 0.1$, IMBHs passing through cold neutral hydrogen regions show luminosities of the order of 10^{35-37} erg s^{-1}, with a high luminosity tail at $> 10^{38}$ erg s^{-1}; IMBHs passing through warm hydrogen regions produce lower luminosities, ranking from 10^{33} to 10^{35} erg s^{-1} with an extended high luminosity tail extending to 10^{38} erg s^{-1} (Fig. 3.7). Due to the large filling factor of the atomic hydrogen with respect to the molecular one, the number of IMBHs accreting HI is a factor $\approx 10 - 30$ higher than the number of IMBHs which accrete H_2, even if the luminosities are lower and nearly no ULX can be produced in atomic regions.

Most interestingly, we note from the column 6 of Table 3.3 that for $\Omega_\bullet = 0.1\,\Omega_b$ (both for $\eta = 0.1$ and for $\eta = 0.001$), the expected number of X-ray sources is huge, both for in the case of a DMM profile (case B1, ≈ 4000 sources) and for a NFW profile (case B2, ≈ 500 sources). The reason the case B2 (which yielded the acceptable number of ULXs ≈ 1) predicts so many X-ray sources depends on the HI distribution properties: atomic gas is less concentrated than molecular clouds. Because a number of X-ray sources (not identified with HMXBs or LMXBs) > 500 is definitely too high for the Milky Way, we can robustly exclude $\Omega_\bullet \gtrsim 0.1\,\Omega_b$.

For $\eta = 0.001$, such as for an ADAF disk, IMBH luminosities are much lower, spanning 10^{31-35} to 10^{37} erg s^{-1} (Fig. 3.8). Even if the total number of sources remains nearly unmodified (Table 3.3; sixth column), the fact that most of them present luminosities $\ll 10^{37}$ erg s^{-1} makes comparison with observations more difficult. In the next section we attempt to constrain the Galactic IMBH density by comparison with X-ray observations, considering X-ray sources produced collectively by IMBHs accreting both within molecular clouds and atomic regions.

[6] We assume a turbulent velocity $\sigma_H = 10$ km s^{-1} both for cold and warm hydrogen (Lockman & Gehman 1991). The adopted sound speed is 1 km s^{-1} for cold hydrogen and 10 km s^{-1} for warm hydrogen regions.

3.7 Comparison with observations

In the previous Sections (3.5.1-3.5.2) we tried to constrain the density of IMBHs in our Galaxy by the fact that no ULXs have been detected in the Milky Way. From our simulations we found that some accreting IMBHs might also emit as non-ultraluminous X-ray sources, being in some cases bright enough to had been reliably detected by current X-ray satellites.

Hereafter, we match the results of our simulations with the X-ray observations. In particular, we compare the predicted IMBH X-ray emission with our knowledge of the X-ray sky in order to define an upper limit on the presence of these objects in our Galaxy.

So far we have predicted IMBH X-ray luminosities (for a summary see Table 3.3) of $\approx 10^{31-39}\,\mathrm{erg\,s^{-1}}$, mostly depending on the assumed accretion efficiency η, disk model and molecular or atomic accreting material. Searching in the observations for an upper limit of possible IMBHs in such a wide luminosity range is a non-sense, mainly because at the low luminosities many sources were certainly missed.

Then, what we study here are only the IMBHs with a predicted hard X-ray luminosity between $10^{36} - 10^{39}\,\mathrm{erg\,s^{-1}}$ (see Table 3.3, last column). In all these cases, the high luminosity of these sources makes us confident that we should have seen them in the monitoring campaign of the Galaxy with the new generation satellites (within a certain distance depending of the flux resolution of the given satellite).

The most uncertain point is whether IMBHs accreting gas are transient or persistent sources. If the IMBH would be able to form a (thin or ADAF) accretion disk, it should also be a transient source. Instead, IMBHs accreting in the Bondi-Hoyle regime without forming a disk, as suggested by Beskin & Karpov (2005), should show flares; it remains unclear if they can be transient sources or not. On the other hand, the IMBH could be transient also as a consequence of properties of the interstellar medium. In fact the accretion rate is roughly proportional to the density of the gas, and the scintillation measures show that the density fluctuations of the interstellar medium can be as high as a factor 100 on scales from $\approx 10^{18}$ down to $\approx 10^{12}$ cm (Rickett 1990; Lambert & Rickett 2000; Cordes & Lazio 2001; Ferrara & Perna 2001). A halo IMBH can easily travel $\approx 10^{12}$

cm in about one day, and thus could suffer, in principle, changes of a factor ≈ 100 in its flux in this range of time. As a consequence, we have considered all the sources meeting our requirements, both persistent or transient during the observations.

The most wide and sensitive survey available for our aims is the soft gamma-ray survey recently obtained by the IBIS/ISGRI (Imager on Board INTEGRAL Satellite/INTEGRAL Soft Gamma-Ray Imager) instrument on board of the INTEGRAL satellite (Bird et al. 2004, 2006). This survey observed 50% of the sky with a flux limit of 1 mCrab in the 20–100 keV energy range.

Among more than 200 sources detected by the IBIS/ISGRI soft gamma-ray survey scan, we excluded all the sources that certainly could not belong to the sample of possible IMBHs. In particular, we excluded all the well established X-ray binaries, which are a well known highly luminous Galactic class (both as transient and persistent sources). Furthermore we withdraw from our sample all the X-ray binaries known to host a neutron star (e.g. either because showing pulsations or thermonuclear bursts). We then filtered for a couple of highly energetic supernova remnants. After this first filtering we end up with a few tens of unknown objects.

Given the fact that what IBIS/ISGRI measures is a certain flux at Earth and not a luminosity, which is usually hard to derive because of the poorly known distances, we put the sample of sources we derived after the latter filtering, at distances between 1–15 kpc , and we took all the sources with an inferred luminosity $10^{36} - 10^{39}\,\mathrm{erg\,s^{-1}}$, which implies in terms of flux all the uncatalogued IBIS/ISGRI objects with a detected flux (within their errors) >4.8 mCrab in the 20–40 keV energy range. Note that this flux limit is derived placing a source emitting $10^{36}\,\mathrm{erg\,s^{-1}}$ at 15 kpc (e.g. the edge of our Galaxy). It would be detected by IBIS/ISGRI at a flux of 4.8 mCrab in the 20–40 keV energy range, well above the flux limit of the survey. Hence we are confident that, if present, our putative Galactic IMBHs would had been detected in the 50% of the Galaxy covered by the IBIS/ISGRI survey. Note that the flux limit of 4.8 mCrab we assumed includes, for the completeness of our analysis, the worst case of the faintest source at the largest distance: the fact that we are looking for an upper limit on the number of these possible IMBHs allow us to make this assumption.

Under these assumptions, we found only 3 IBIS/ISGRI unidentified sources which match our requirements. These sources were all persistent during the IBIS observations. Their luminosity falls in the 10^{36}-10^{39} erg s^{-1} range, all of them close to the 10^{36} erg s^{-1} bound. As the IBIS/ISGRI catalogue covers 50% of the Galaxy, we then tentatively predict an upper limit of 6 sources with these characteristics in the entire Galaxy, if the volume observed is a fair sample. In a few years all the Galaxy will be covered by the IBIS/ISGRI survey and our tentative extrapolation may be refined.

Let us now compare this number with that of IMBHs predicted by our simulations in the same luminosity range and reported in the last column of Table 3.3.

a) Thin disks

For a thin disk, even case A1 ($\Omega_\bullet = 0.001\,\Omega_b$, DMM profile) yields ≈ 18 sources, a value three times higher than observed. Furthermore, 4 of these simulated sources have $L_X > 10^{37}$ erg s^{-1}. From an additional run with $\Omega_\bullet = 10^{-4}\Omega_b$ and the DMM profile (not reported in Table 3.3 for simplicity) we saw that the number of sources with $10^{36} < L_X < 10^{39}$ erg s^{-1} is 0.6±0.6. We conclude that the upper limit in the case of a Shakura-Sunyaev disk and a DMM profile is $\Omega_\bullet = 10^{-4} - 10^{-3}\Omega_b$, similar to the upper limit found by the number of ULXs alone (see Section 3.5.1-3.5.2). Instead, for a NFW profile the allowed density of IMBHs is $> \Omega_\bullet = 10^{-3}\Omega_b$ (case A2; corresponding to 0.4±0.4 sources), but definitely $< \Omega_\bullet = 10^{-1}\Omega_b$ (case B2; 148±21 expected sources), strengthening the constraint we found from the number of ULX.

b) ADAF disks

For the more realistic case of an ADAF disk, the constraints we obtain from the comparison with the IBIS/ISGRI sources are stronger than for the number of ULXs alone. In fact, if we assume a DDM profile, the upper limit for the density of IMBHs is about $\Omega_\bullet = 10^{-3}\Omega_b$ (case A1; 1.2±1.0 expected sources), much lower than $\Omega_\bullet = 10^{-1}\Omega_b$ (case B1; 236±15 expected sources), derived from the number of ULXs. If we consider a NFW model, the upper limit is $\Omega_\bullet = 10^{-1}\Omega_b$ (case B2; 5±3 expected sources); whereas there were no significant constraints from the ULXs. In summary, we must take with care the results of this comparison between simulated and observed X-ray sources, because of the huge uncertainties of our model. However, from the comparison with the IBIS/ISGRI

unidentified sources we derive, in general, much stronger constraints than from the number of ULXs.

3.8 Conclusions

In this Chapter we have simulated the dynamical and emission properties of putative IMBHs which could inhabit our Galaxy. IMBHs are modeled as a halo population, distributed following a NFW or a more concentrated DMM profile. We assumed that IMBHs, passing through molecular or atomic hydrogen regions, could accrete gas, forming X-ray sources (either ultra-luminous or not). From the comparison of our simulations with the number of ULXs in the Galaxy (Section 3.5.1-3.5.2) and with the non-ultraluminous unidentified X-ray sources in the IBIS/ISGRI catalogue, we have derived the most stringent (to our knowledge) upper limits on the density $\Omega_\bullet$ of IMBHs. The main results can be summarized as follows:

- If IMBHs accrete with efficiency $\eta = 0.001$ (i.e. via an ADAF disk), we obtain a strong upper limit $\Omega_\bullet \leq 10^{-2}\Omega_b$ for a DMM profile and $\Omega_\bullet \leq 10^{-1}\Omega_b$ for a NFW profile.

- If the IMBHs accrete with efficiency $\eta = 0.1$ (i.e. if a thin accretion disk around the IMBH is formed), the upper limit of the density of IMBHs is $\Omega_\bullet \leq 10^{-3}\Omega_b$ for a DMM profile and $\Omega_\bullet \leq 10^{-2}\Omega_b$ for a NFW profile.

These results are still affected by some model uncertainties, as the emission mechanism and the IMBH distribution. In addition, computational requirements have forced us to use high and equal mass ($m_\bullet = 5 \times 10^4\, M_\odot$) IMBH particles. Constraints for lower IMBHs masses are expected to be weaker. We can guess how the above upper limits change for different values of the IMBH mass by using the equation (3.12). For example, if we assume $m_\bullet = 10^3 M_\odot$, $\eta = 0.1$ and a DMM profile, the upper limit of the IMBH density becomes $\Omega_\bullet = 10^{-2}\Omega_b$, about one order of magnitude lower than for $m_\bullet = 10^4 M_\odot$. As a further caveat, this extension to lower masses is possible only for the comparison with ULXs (and not with IBIS/ISGRI sources), because it is based on eq. (3.12). Therefore, higher resolution

simulations would be required to extend our studies to lower mass IMBHs or to consider a more realistic IMBH mass spectrum. Higher resolution simulations (where the mass of star particles can be orders of magnitude lower than the mass of IMBH particles) are also needed to take into account the dynamical friction, which could play a crucial role.

Another caveat concerns the validity of the DMM profile. The simulations by DMM neglect the contribution of IMBHs in building up SMBHs, either by mergers (Islam, Taylor, & Silk 2003, 2004a,b,c) or by accretion and close dynamical encounters (Volonteri et al. 2003). Monte Carlo simulations combined with semi-analytical models (Volonteri & Perna 2005) show that, if all these factors are taken into account, the number of IMBHs could be up to 2 orders of magnitude lower, leading to an $\Omega_\bullet \sim 10 - 100$ lower than our estimates, and therefore compatible with the non-detection of ULXs in the Milky Way. However DMM take into account the bias in the formation sites of IMBHs, the accretion into larger halos, the role of both dynamical friction and tidal stripping, which were neglected or described by rough models in the previous studies. Unfortunately current simulations cannot account for all these effects at the same time. In conclusions, even if our results could be improved under many aspects, we consider it as a success that our models strengthen by a factor 10-1000 the currently adopted upper limits for the density of IMBHs (i.e. $\Omega_\bullet \approx 0.02$; van der Marel 2004).

Chapter 4

Intermediate mass black holes in globular clusters

4.1 Introduction

Globular clusters represent a unique environment where we can search for IMBHs. As I said in the previous Chapter, two of the four most popular mechanisms for IMBH formation imply the presence of a star cluster. Furthermore, the only three existing IMBH candidates (if we neglect ULXs) happen to be in globular clusters (see next section).

In globular clusters IMBHs cannot be detected as X-ray sources, due to the lack of gas and to the rarity of tidal captures of stars (the estimated timescale for capture is of the order of 1 Gyr per cluster). However, given their high mass, IMBHs should play a role from the dynamical point of view, especially if they form binaries. In this Chapter, we will study the possible dynamical signatures of IMBHs in globular clusters.

4.2 Candidate IMBHs in globular clusters

4.2.1 G1 and M15

Gebhardt, Rich & Ho (2002) suggested the presence of a $2^{+1.4}_{-0.8} \times 10^4\,M_\odot$ IMBH, to explain the kinematics and the surface brightness profile of the globular cluster G1 in

M31. Gerssen et al. followed the same method to indicate the possible presence of a $1.7^{+2.7}_{-1.7} \times 10^3\,\mathrm{M}_\odot$ IMBH in the galactic globular cluster M15 (Gerssen et al. 2002, 2003).

These indications were strongly opposed by Baumgardt et al (2003a, 2003b), who showed that both the measurements of M15 and those of G1 can be explained with a central concentration of compact objects (neutron stars and white dwarfs) instead of the presence of a massive BH.

In a more recent paper, Gebhardt, Rich & Ho (2005) further support the hypothesis of an IMBH in G1. They note that Baumgardt et al (2003a, 2003b) used the second moment of the velocity profile alone to constrain the BH mass; while it is known that using the second moment alone to measure the mass profile can lead to substantially biased results. On the other hand, Baumgardt et al (2003a, 2003b) could not do better, because the accuracy of current N-body simulations allows to derive only the second moment. Instead, the analysis of Gebhardt et al. (2002, 2005) is based on the full velocity profile, which contains complete information. Gebhardt et al. (2005) adopt higher resolution data than Gebhardt et al. (2002): a series of spectra from Keck and of *Hubble Space Telescope* (HST) images with the *High Resolution Camera* (HRC) on the *Advanced Camera for Surveys* (ACS). These data are used as input for two different kind of models: the nonparametric model discussed in Gebhardt & Fisher (1995) and the general axisymmetric orbit-based model described in Gebhardt et al. (2000, 2003). In the former the spherical Jeans equation uniquely determines the mass density profile given a surface brightness profile and a velocity dispersion profile. The latter consists in running a set of stellar orbits covering the available phase space and choosing the set that best matches both the photometry and kinematics. Both the two analyses give a best fit for the mass of the IMBH candidate $1.8 \pm 0.5 \times 10^4\,M_\odot$.

Instead, the same techniques applied to kinematic and photometric data for M15 (van den Bosch et al. 2006) loosen the evidence of a IMBH in this cluster, the new best fit being $m_\bullet = 500^{+2500}_{-500}\,M_\odot$.

4.2.2 NGC 6752: the pulsar PSR J1911-5958A

A completely different approach has been followed for NGC 6752. This cluster hosts 5 millisecond pulsars (D'Amico et al. 2002). Three of them are in the core, and their

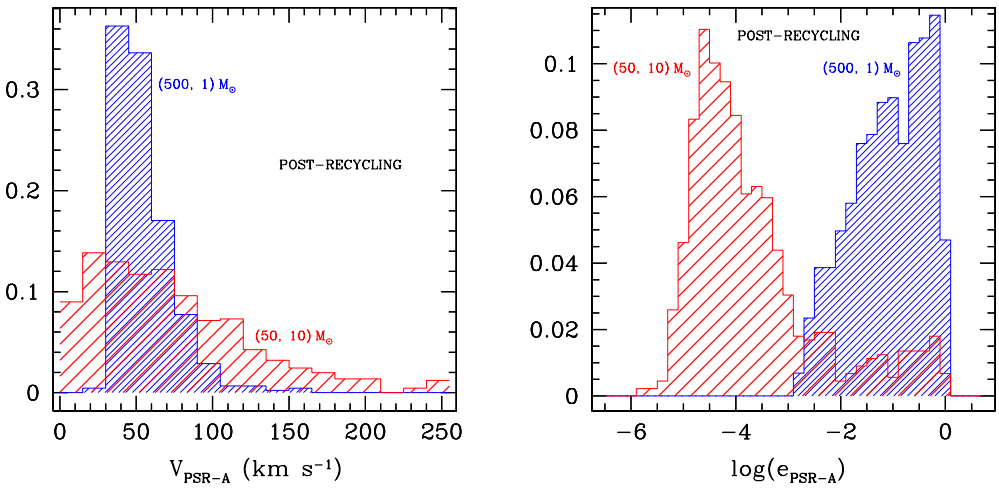

Figure 4.1: Post-encounter recoil velocity (left panel) and eccentricity (right panel) distribution of the binary PSRA. Red histogram: interaction with a binary composed by a $50\,M_\odot$ IMBH and a $10\,M_\odot$ stellar BH. Blue histogram: interaction with a binary composed by a $500\,M_\odot$ IMBH and a $1\,M_\odot$ star.

measured acceleration can be explained only by invoking the presence of $\sim 1000\,M_\odot$ of dark material at the center of the cluster (Ferraro et al. 2003). This implies a mass-to-light ratio $\sim 6-7$, which is quite high, even if it can be explained with a certain amount of dark remnants (neutron stars and white dwarfs). In addition, the other two millisecond pulsars are located very far from the center of the cluster. In particular, the distance of one of them, the binary pulsar PSRJ1911-5958A (PSRA), cannot be explained by dynamical friction or even by a three/four-body interaction with stellar mass binaries (Colpi, Possenti & Gualandris 2002).

Colpi, Mapelli & Possenti (2003) ran simulations of four-body encounters, showing that the position of PSRA can be due to a gravitational encounter with a binary IMBH. If the companion of the IMBH is a stellar BH (with mass $m = 10\,M_\odot$), the mass of the IMBH must be relatively low ($\lesssim 100\,M_\odot$), otherwise the average recoil velocity is too high to retain the pulsar in the cluster. If the companion of the IMBH is a star (with mass $m \sim 1\,M_\odot$), the mass of the IMBH must be larger ($\sim 500\,M_\odot$), because the recoil velocity of the pulsar depends on the binding energy of the binary (see next section for details on three/four body interactions). However, the interaction with a massive IMBH ($\sim 500\,M_\odot$)

significantly alters the eccentricity of the binary pulsar. Since the observed eccentricity of PSRA is close to 0, we conclude that the interaction with a $\sim 500\,M_{\odot}$ IMBH can have occurred only before the recycling of the pulsar (i.e. the spinning up of the pulsar due to mass accretion). In fact, after the accretion phase which produces the recycling, there are no other processes able to circularize the orbit of the binary pulsar. In Fig. 4.1 the distribution of post-encounter velocities (left panel) and eccentricities (right panel) of the simulated PSRA are shown. The post-encounter velocity of PSRA must be of the order of 40 km s^{-1} in order to eject the pulsar into the periphery of the cluster without expelling it from the cluster itself. The post-encounter eccentricity of PSRA must be ~ 0, to be consistent with the observations (D'Amico et al. 2002), unless we assume that PSRA was scattered before recycling.

4.3 Dynamical signatures of IMBHs in globular clusters: suprathermal stars and angular momentum alignment

4.3.1 How do three-body interactions work?

In this Section, I will show the possibility of detecting binary IMBHs in globular clusters by studying their role in three-body interactions. Before discussing this topic in details, it can be useful to introduce some basic concepts of three-body interactions.

Given the wider encounter cross-section of a binary with respect to a single star, three body encounters dominate the dynamics of a star cluster, even if the binary fraction is low.

During a three body encounter part of the internal energy of the binary is converted into kinetic energy of the interacting stars, or *vice versa*.

The behavior of a binary during a three-body interaction depends entirely on its hardness. A binary is hard (soft) when its binding energy is higher (lower) than the average kinetic energy of a cluster star, i.e.

$$\frac{G\,M_1\,M_2}{2\,a} \; > \; (<) \; \frac{1}{2}\langle m\rangle\sigma^2, \tag{4.1}$$

where G is the gravitational constant, M_1 and M_2 are the masses of the two components

of the binary, a is the orbital separation, $\langle m \rangle$ the average mass of a cluster star and σ the dispersion velocity.

The behavior of binaries during three-body encounters can be summarized by the Heggie's law (Heggie 1975; Hills 1990; Hut 1993):

hard (soft) binaries tend to harden (soften) during three-body encounters and the hardening rate of the binaries is approximately independent of their binding energy.

This means that a hard binary tends to transfer internal energy to the interacting star, or, in other words, that a hard binary acquires binding energy (reducing its orbital separation or exchanging one of its components), while the interacting star acquires kinetic energy. Instead, soft binaries gain internal energy from the interacting star, which looses kinetic energy.

The hardening rate is the rate at which the orbital separation of the binary changes during three-body encounters, and can be expressed as:

$$\frac{\mathrm{d}}{\mathrm{d}t}\left(\frac{1}{a}\right) = 2\,\pi\,\xi\left(\frac{G\,\rho}{\sigma}\right), \tag{4.2}$$

where ρ is the mass density of stars. ξ is the so called hardening factor, and is defined by:

$$\frac{\langle \Delta E_b \rangle}{E_b} = \xi \frac{m}{M_1 + M_2}, \tag{4.3}$$

where E_b is the initial binding energy of the binary, $\langle \Delta E_b \rangle$ the average variation of the binding energy during the three-body encounter and m the mass of the interacting single star. The Heggie's law states that $\frac{\mathrm{d}}{\mathrm{d}t}\left(\frac{1}{a}\right)$ (and then ξ) is nearly constant for a hard binary. This is confirmed by our simulations (see next Sections).

Three-body encounters can end in different ways.

- In the FLYBIES the final configuration is identical to the initial one (i.e. the single star remains single and the binary remains binary); but an energetic exchange occurs between the binary and the single star (hardening the binary, if it was initially hard, or widening it, if initially soft).

- In the EXCHANGES the single star substitutes itself to one of the components of the binary. Generally, the single star has a mass greater than the previous component of the binary. Then, in the final configuration the binary acquires binding energy.

- In the IONIZATIONS the binary is disrupted by the interaction. In order to produce an ionization, the binary must be quite soft or the target star very rapid (with kinetic energy higher than the binding energy of the binary).

IMBHs are much more massive than the other objects in globular clusters. So, if an IMBH resides in a globular cluster, it is likely that it exchanged itself in a binary (with a stellar BH or with a massive star) and the resulting binary is very hard. This binary hardens itself during the life of the cluster. It is unlikely that such a binary suffers ionizations or even exchanges (especially if the secondary component of the binary is a BH). Then, most of the interactions which occur to a binary IMBH are flybies which contribute to harden the binary. This is the reason why, in the following, we will discuss only flyby interactions.

4.3.2 What are suprathermal stars and angular momentum alignment?

Mapelli et al. (2005) proposed a new method to indirectly check the presence of binary IMBHs in globular clusters. They studied the effects of three-body interactions between a binary IMBH and stars on the velocity and the angular momentum distribution of cluster stars.

They found that the dynamical interactions with a binary IMBH produce a family of stars, the so called suprathermal stars, which maintain velocities higher than the thermal ones for a time interval of the order of the half mass relaxation time. In practice, suprathermal stars are defined as stars which have post-encounter velocity $\sim 3\,\sigma_{3D} \lesssim u^{fin} \lesssim v_{esc}$ (where σ_{3D} is the three-dimensional velocity dispersion in the core, u^{fin} is the post-encounter asymptotic velocity and v_{esc} the escape velocity from the core).

If the semi-major axis of the binary IMBH is sufficiently wide, the stars which have dynamically interacted with it tend to align their angular momentum with the orbital angular momentum of the binary IMBH. However, there are probably no traces of this angular momentum alignment left in present-day globular clusters. In fact, binary IMBHs are expected to have small orbital separations ($\gtrsim 1$ au), because they can form only in the first stages of the globular cluster life and then harden via gravitational encounters up to now.

Mapelli et al. (2005) conclude that the only measurable effect of three-body interactions with IMBHs is the existence of suprathermal stars; but their small number (a few hundreds) and the concurrence of many selection effects (projection effects, stellar types, Maxwellian contamination, etc) make very difficult such measurement.

4.3.3 Our reference globular clusters: NGC 6752 and M4

Mapelli et al. (2005) based their study on the globular cluster NGC 6752, because there are some indications of the existence of an IMBH in its core (see Section 4.2.2 of this Thesis). NGC 6752 is very concentrated ($c \sim 2$) and its core stellar density is quite high ($n \sim 10^{5-6}$ pc^{-3}). Its density profile shows a curious double-King shape (Ferraro et al. 2003).

In this Chapter, instead, we will focus on the loose globular cluster M4 ($n \sim 2.5 \times 10^4$ pc^{-3}). In fact, the probability of hosting binary IMBHs is maybe higher for loose than for high density clusters, for two reasons. Firstly, in low density clusters the interaction rate is lower, increasing the lifetime of the binary IMBH before it merges via gravitational wave emission. Secondly, the large, flat core of low density clusters could be due to the ejection of a consistent fraction of stars via dynamical interactions with the central binary IMBH (Colpi, Mapelli & Possenti 2003). Our aim is to investigate whether the effects of three-body interactions with binary IMBHs are different or more evident in loose clusters with respect to concentrated ones. In particular, we chose M4 as an example, because its proximity to the Sun (~ 2 kpc) makes easier photometric and spectral measurements of the velocity of its stars.

In Section 4.3.4 we will discuss our simulations. Then, the statistics of suprathermal stars (Section 4.3.5) and angular momentum alignment (Section 4.3.6) will be presented. In Section 4.3.7 the radial distribution of suprathermal stars and the consequences for detectability will be showed. We summarize and compare the results for M4 with those for NGC 6752 in Section 4.3.8.

4.3.4 The simulations

We simulated three-body encounters involving a binary IMBH (composed of two BHs of mass $M_1 = 100$ and $M_2 = 50\,\mathrm{M}_\odot$) and a cluster star of mass $m = 0.5\,M_\odot$.[1] The dynamics of the encounter is followed by solving the equations of motion through the numerical code FEBO (FEw-BOdy), based on a Runge-Kutta fifth order integration scheme with adaptive stepsize and quality control (explained in Colpi, Mapelli & Possenti 2003 and in Mapelli et al. 2005).

The binary has semi-major axis a of 1, 10, 100, and 1000 au and eccentricity $e = 0.7$, which is nearly the average binary eccentricity in statistical equilibrium (Hills 1975). The characteristics of runs are described in Table 4.1. The initial conditions, that are Monte Carlo generated as in Mapelli et al. 2005, are sampled using the prescriptions indicated in Hut & Bahcall (1983. See also Appendix B of this Thesis). In particular, the initial velocity u^{in} (i.e. the relative velocity between the single star and the center of mass of the binary) is distributed homogeneously between $5.5 - 6.6$ km s^{-1}, to reproduce the characteristic velocities in M4 (whose one-dimensional velocity dispersion is 3.5 ± 0.3 km s^{-1}; Peterson, Rees & Cudworth 1995). The three orientation angles and the phase of the binary are generated as indicated in Table 1 and 2 of Hut & Bahcall (1983).

The impact parameter b is drawn at random from a probability distribution uniform in b^2 and in a range going from 0 to a truncation value b_{max}. The truncation value b_{max} is chosen by requiring that the simulations include all the encounters with non-negligible energetic exchange, and, especially, all the encounters which can produce suprathermal stars. In particular, we take into account all the encounters with $\Delta E_{\rm BH}/E^{in}_{\rm BH} \gtrsim 10^{-3}$, where $E^{in}_{\rm BH}$ is the initial binding energy of the IMBH binary and $\Delta E_{\rm BH} = E^{fin}_{\rm BH} - E^{in}_{\rm BH}$ is the energetic exchange ($E^{fin}_{\rm BH}$ being the post-encounter binding energy of the binary). In fact, suprathermal stars are formed only in encounters with $\Delta E_{\rm BH}/E^{in}_{\rm BH} \gtrsim 10^{-3}$, depending on the binding energy of the binary. This can be easily understood by applying the following equation.

$$\frac{\Delta E_{\rm BH}}{E^{in}_{\rm BH}} \sim 4.5\times10^{-3}\left(\frac{m}{0.5\,\mathrm{M}_\odot}\right)\left(\frac{100\,\mathrm{M}_\odot}{M_1}\right)\left(\frac{50\,\mathrm{M}_\odot}{M_2}\right)\left(\frac{a}{1\,\mathrm{au}}\right)\left(\frac{u^{fin}}{20\,\mathrm{km\ s^{-1}}}\right)^2, \quad (4.4)$$

[1] In this Chapter we chose to fix the mass of the binary, for simplicity. The dependence of our results on the mass (total and reduced) of the binary was discussed in Mapelli et al. (2005).

Table 4.1: Initial Parameters.

CASE	M_1 ($M_\odot$)	M_2 ($M_\odot$)	a (au)	Range of b (au)	Number of simulations
A	100	50	1	0-150	5000
B	100	50	10	0-500	5000
C	100	50	100	0-1400	5000
D	100	50	1000	0-5000	5000

where u^{fin} is the post-encounter asymptotic velocity.

The study presented in this Chapter is more accurate in the choice of impact parameters with respect to Mapelli et al. 2005. So we assume its results as the fiducial ones for the asymptotic velocity u^{fin} and for the hardening factor $\xi \equiv [(M_1+M_2)/m]\langle \Delta E_{\rm BH}/E^{in}_{\rm BH}\rangle$, that are the only two parameters which strongly depend on b_{max}. We highlight that the results presented in this Chapter agree with the main findings of Mapelli et al. 2005, even if the choice of impact parameters is slightly different. In fact, the results presented here for the angular momentum alignment are close to those of Mapelli et al. 2005, being quite independent of the impact parameters. The statistic of observable suprathermal stars is also unchanged with respect to Mapelli et al. 2005, because the choice of the range of impact parameters for the binary with semi-major axis a=1 au (which is the only case considered for detectable suprathermal stars; see Section 4.3.7) is very similar to that of Mapelli et al. 2005.

We initiate (terminate) integration when the distance between the incoming (outcoming) star and the center of mass of the binary is comparable to the radius of gravitational influence of the IMBHs ($r_a \sim 2G(M_1+M_2)/\sigma^2$, where σ is the 1-D stellar dispersion velocity). At the start of each simulation, we place the binary BH and the single star on their respective hyperbolic trajectories.

4.3.5 Suprathermal stars

As in Mapelli et al. 2005, we extract from our simulations the statistics of suprathermal stars, i.e. stars with post-encounter asymptotic velocity in the range $3\,\sigma_{3D} \lesssim u^{fin} \lesssim v_{esc}$. For the characteristics of M4, this means that suprathermal stars are stars with post-encounter asymptotic velocity in the range $\sim$ 15-40 km s^{-1}. For NGC 6752,

Table 4.2: Statistics of the Outgoing States.

CASE	Bound stars (%)	Ejections (%)	UEs (%)[a]	Suprathermal stars (%)[b]
A	19.8	77.6	2.6	14.9
B	65.4	34.3	0.3	32.4
C	95.1	4.9	0.0	31.6
D	100.0	0.0	0.0	2.6

[a] We define UEs (unresolved encounters) those runs where the separation between the star and the binary IMBH never exceeds 30 a after 10^8 time steps.

[b] We define suprathermal stars those with velocities at infinity between 15 and 40 km s^{-1}.

where the dispersion velocity is slightly higher, the range for suprathermal stars was 20-40 km s^{-1}. In Table 4.2 we show the fraction of bound stars, defined as those having a final velocity lower than the escape velocity from the core ($\sim$ 40 km s^{-1}), and the fraction of suprathermal stars.

Fig. 4.2 shows the distribution of the velocity at infinity of stars scattering off a binary IMBH, for cases A, B, C and D (in Table 4.1). The shaded area indicates the strip of suprathermal stars. Most of the suprathermal stars are formed when the binary is very hard ($a \lesssim 10$ au).

The mean values of the speed at infinity u^{fin} and of the fractional binding energy exchange $\langle \Delta E_{\rm BH}/E^{in}_{\rm BH} \rangle = \langle (E^{fin}_{\rm BH} - E^{in}_{\rm BH})/E^{in}_{\rm BH} \rangle$ are given in Table 4.3 together with the dimensionless factor ξ, defined by (see also Section 4.3.1):

$$\langle \Delta E_{\rm BH}/E^{in}_{\rm BH} \rangle = \xi \, [m/(M_1 + M_2)] \; . \tag{4.5}$$

ξ is nearly independent of the semi-major axis of the binary and its average value is very close to 1 (Fig. 4.3). This finding is in complete agreement with the Heggie's law, which states that hard binaries tend to become more energetic (Heggie 1975; Hills 1990) and that the hardening rate of the binaries is approximately independent of their binding energy. On the contrary, Mapelli et al. 2005 found a partial violation of the second part of the Heggie law (i.e. they argued that ξ slightly depends on the binding energy of the binary). This discrepancy is due to the fact that Mapelli et al. 2005 made a less accurate

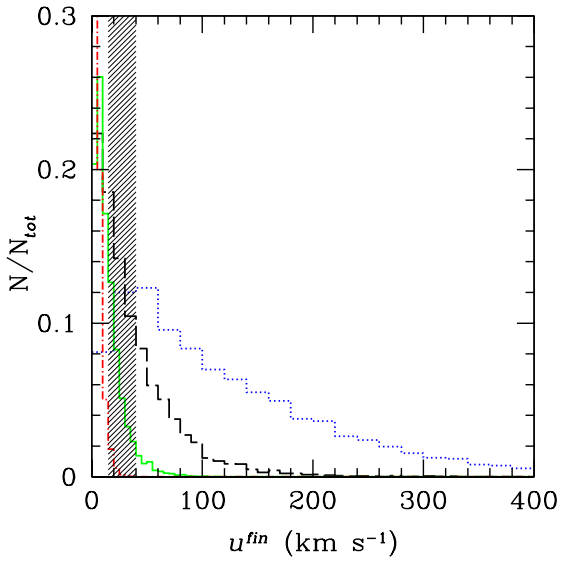

Figure 4.2: Post-encounter asymptotic velocity distributions of the cluster star in the case A (dotted line), B (dashed), C (solid), D (dot-dashed). The shaded area refers to the suprathermal stars. On the y-axis the number of cases for each bin is normalized to the total number of resolved runs (N_{tot}).

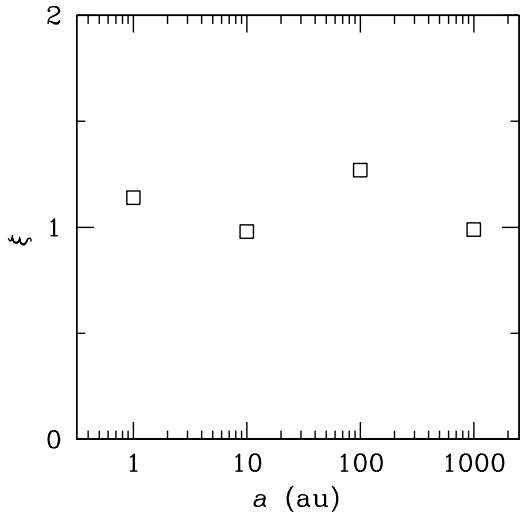

Figure 4.3: $\xi \equiv [(M_1 + M_2)/m]\langle \Delta E_{\rm BH}/E^{in}_{\rm BH}\rangle$ as a function of the semi-major axis a for all the considered cases.

Table 4.3: Final velocities and angular momentum exchanges.[a]

CASE	u^{fin} [b]	$\langle\frac{\Delta J}{J_*^{in}}\rangle$[c]	$\frac{\Delta J}{J_*^{in}}$[d]	$\langle\frac{\Delta E_{\rm BH}}{E_{\rm BH}^{in}}\rangle$[e]	ξ[f]
A	$37.5^{+200.0}_{-37.5}$	$0.060^{+19.989}_{-0.058}$	$0.005^{+0.100}_{-0.040}$	$0.0038^{+0.1714}_{-0.0031}$	1.14
B	$5.0^{+60.0}_{-5.0}$	$0.055^{+21.495}_{-0.053}$	$0.025^{+0.100}_{-0.100}$	$0.0033^{+0.1188}_{-0.0028}$	0.98
C	$5.0^{+20.0}_{-5.0}$	$0.085^{+24.443}_{-0.080}$	$0.010^{+0.180}_{-0.100}$	$0.0042^{+0.1356}_{-0.0034}$	1.27
D	$3.0^{+4.0}_{-3.0}$	$0.071^{+11.392}_{-0.069}$	$0.010^{+0.080}_{-0.060}$	$0.0033^{+0.1552}_{-0.0029}$	0.99

[a] We consider both bound and ejected stars. Only unresolved encounters are neglected in this Table.

[b] In units of km s^{-1}. Peak value of the velocity at infinity of the star cluster. The dispersion around the peak value is calculated considering those values which contain 50% of the total area descending from the peak.

[c] $\Delta J \equiv (J_*^{fin} - J_*^{in})$, where J_*^{in} and J_*^{fin} represent respectively the modulus of the initial and the final angular momentum of the cluster star. $\langle\frac{\Delta J}{J_*^{in}}\rangle$ is the mean value of the variation of the absolute value of the angular momentum of the cluster star, normalized to its initial value J_*^{in}. The dispersion around the mean value is calculated considering those values which contain 34% of the total area in the left and right wings, respectively.

[d] $\frac{\Delta J}{J_*^{in}}$ is the peak value of $\frac{\Delta J}{J_*^{in}}$. The dispersion around the peak value is calculated considering those values which contain 50% of the total area descending from the peak.

[e] $\langle\frac{\Delta E_{\rm BH}}{E_{\rm BH}^{in}}\rangle$ is the mean value of the variation of the binding energy of the binary IMBH, normalized to its initial binding energy $E_{\rm BH}^{in}$. The dispersion around the mean value is calculated considering those values which contain 34% of the total area in the left and right wings, respectively.

[f] ξ represents the hardening factor and is given by $\xi \equiv \frac{M_1+M_2}{m}\langle\frac{\Delta E_{\rm BH}}{E_{\rm BH}^{in}}\rangle$ (Colpi, Mapelli & Possenti 2003).

choice of the range of impact parameter (especially for the wide binaries) with respect to this Thesis (see Section 4.3.4). In fact, the hardening factor ξ is very sensible to the range of impact parameters.

4.3.6 Angular momentum transfer and alignment

In general, the BH binary is sufficiently massive and the orbit sufficiently wide that its orbital angular momentum exceeds that of the incoming star. Then, a direct transfer of orbital angular momentum occurs, from the binary to the star. The star coming close to the binary IMBH can be dragged into corotation, i.e. the star can emerge after the encounter with an angular momentum nearly aligned with the binary IMBH.

This sentence is explained by the following mathematical formalism. If we denote with $\mu = M_1 M_2/(M_1 + M_2)$ the reduced mass of the binary hosting the two BHs, the total angular momentum of the system is (Sigurdsson & Phinney 1993):

$$\mathbf{J} = \mathbf{J}_{\rm BH}{}^{in} + \mathbf{J}_*{}^{in} = \mu\sqrt{a\,G\,(M_1+M_2)}\mathbf{z} + b\,u^{in}\left[\frac{m(M_1+M_2)}{M_1+M_2+m}\right]\mathbf{z}' \tag{4.6}$$

where $\mathbf{z}$ and $\mathbf{z}'$ are the unit vectors indicating respectively the directions of $\mathbf{J}_{\rm BH}^{in}$ and $\mathbf{J}_*^{in}$ (the initial angular momentum of the binary BH and of the incoming star, respectively). Angular momentum transfer from the binary to the interacting star and partial alignment become important when $J_{BH}^{in} \gg J_*^{in}$, i.e., when

$$\frac{\mu}{b\,u^{in}\,m}\sqrt{(M_1+M_2)\,a\,G} \gg 1. \tag{4.7}$$

In our simulations, we confirm the tendency of angular momentum transfer from the binary to the cluster star. This tendency is quite independent of the hardness of the binary, as it can be noticed from Table 4.3. Here we reported the fractional angular momentum exchange (in modulus) $\langle \Delta J_*/J_*{}^{in}\rangle \equiv (J_*{}^{fin} - J_*{}^{in})/J_*{}^{in}$ (where $J_*{}^{in}$ and $J_*{}^{fin}$ are the modulus of the initial and the final angular momentum of the interacting star, respectively). $\langle \Delta J_*/J_*{}^{in}\rangle$ is always positive, indicating an average transfer toward the cluster star, and quite independent of the semi-major axis of the binary.

We also note the tendency of the cluster star to align its angular momentum to the angular momentum of the binary IMBH, if its semi-major axis is sufficiently wide ($a > 10$ au). This can be seen in Table 4.4, where we compare the percentage of bound stars which were corotating (i.e. for which the scalar product between their angular momentum and the angular momentum of the binary is positive, that is $\mathbf{J}_* \cdot \mathbf{J}_{\rm BH} > 0$) before the three-body interaction with the percentage of those stars which are corotating after the three-body interaction. We find that, for the cases C and D, the fraction of stars which after the interaction are corotating is significantly higher than the fraction of stars which were initially corotating (Table 4.4, second and third column). In addition, in all the considered cases (A, B, C, D) the post-encounter angular momentum of the interacting star is more aligned to that of the binary IMBH with respect to its initial angular momentum (Table 4.4,

Table 4.4: Statistics for bound stars[a].

CASE	Corot$_{in}$ (%)[b]	Corot$_{fin}$ (%)[c]	More aligned stars (%)[d]	$J_*^{fin} > J_*^{in}$ (%)[e]
A	35	35	50	67
B	46	47	53	69
C	50	56	59	68
D	50	57	58	63

[a] In this Table we consider only the stars which after the interaction with the binary remain bound to the cluster.

[b] Percentage (respect to the total of bound stars) of stars which, before the interaction, are corotating with the binary (i.e. for which the scalar product between their angular momentum and the angular momentum of the binary is positive).

[c] Percentage (respect to the total of bound stars) of stars which, after the interaction, are corotating with the binary, independently from the initial orientation of their angular momentum.

[d] Percentage of bound stars which, after the encounter, reduce the angle between their angular momentum and that of the binary.

[e] Percentage of bound stars which, after the encounter, increase the absolute value of their angular momentum.

forth column). Table 4.4 indirectly shows also another interesting effect. The second column indicates that generally less than 50% of the initially corotating stars remain bound to the cluster, while the post-encounter percentage of corotating stars is more than 50%. This means not only that a fraction of initially counter-rotating stars becomes corotating, but also that an initially corotating star is more easily ejected from the cluster than a counter-rotating star. This fact can be intuitively explained considering that, when a counter-rotating star interacts with the binary, its relative velocity with respect to the lighter BH is higher than in the case of a corotating star, and, then, the cross section is lower.

In Fig. 4.4 we show the cosine of the angle between the angular momentum of the interacting star and that of the binary IMBH. This plot clearly shows that the combination of two different tendencies, i.e. the tendency to remain corotating for initially corotating stars (left panel) and the tendency to become corotating for initially counterrotating stars (central panel), produces the net alignment between the angular momentum of the interacting star and that of the binary IMBH after the interaction (right panel).

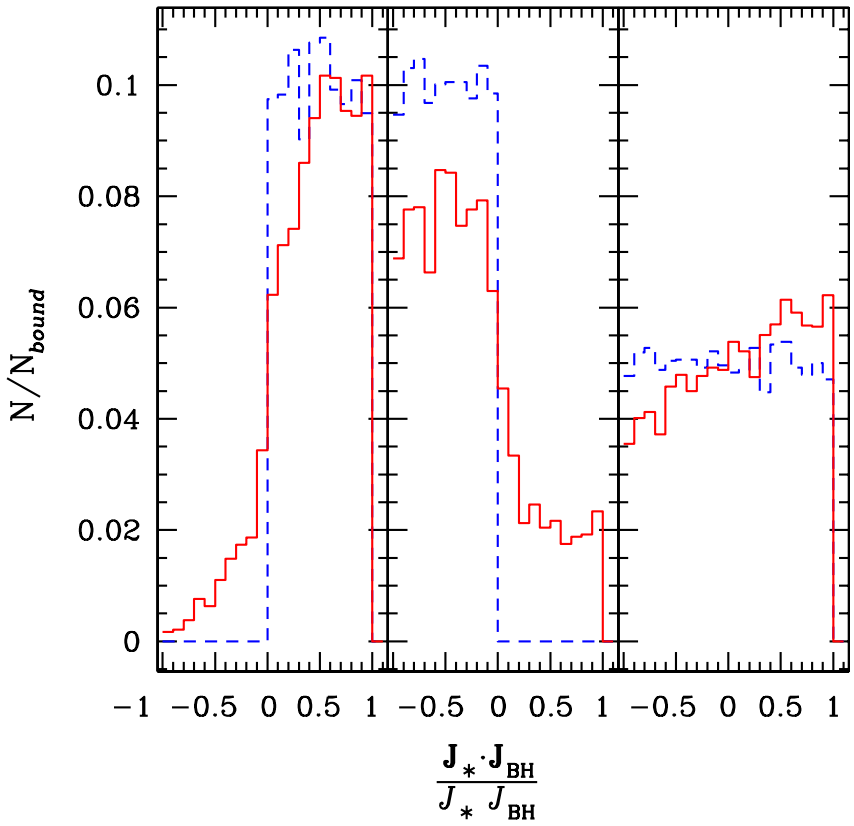

Figure 4.4: The histograms show the distribution of $\frac{\mathbf{J}_*\cdot\mathbf{J}_{\rm BH}}{J_*\,J_{\rm BH}}$ for the case C ($M_1 = 100\,M_\odot$, $M_2 = 50\,M_\odot$, $a = 100$ AU). The solid line indicates the distribution after the encounter; the dashed line indicates the distribution before the encounter. The left panel represents the distribution of $\frac{\mathbf{J}_*\cdot\mathbf{J}_{\rm BH}}{J_*\,J_{\rm BH}}$ for bound stars which before the encounter were corotating, the central panel the distribution for bound stars which before the encounter where counterrotating and the right panel the sum of the two distribution, i.e. the distribution for all the stars which after the encounter remain bound to the cluster. On the y-axis the number of cases for each bin is normalized to the total number of bound stars (N_{bound}).

4.3.7 Detecting suprathermal stars and angular momentum alignment

We want now to estimate how many suprathermal stars are produced by interactions with a binary IMBH and if they are observable with present instrumentation in a loose globular cluster, such as M4.

Estimating the number of suprathermal stars

The expected number of suprathermal stars is a fraction f of the total number N of stars strongly interacting with a binary IMBH. The latter is given by (cfr. Colpi, Mapelli & Possenti 2003; Mapelli et al. 2005):

$$N = \frac{(M_1 + M_2)}{m\,\xi} \ln\left(\frac{a_0}{a_{\rm st}}\right) \tag{4.8}$$

where a_0 is the initial semi-major axis of the binary and $a_{\rm st}$ is the minimum semi-major axis for the encounter to give a suprathermal star.

In equation (4.8) we impose $a_0 = 2000$ au, corresponding to the orbital separation below which the binary becomes reasonably hard to generate suprathermal stars, and $a_{\rm st} = 0.1$ au, the orbital separation below which the cross section for three-body encounters becomes negligible. We then calculate the number of stars that remain bound to the cluster and the number of suprathermal stars using the statistics derived from our simulations (see the percentages given in Table 4.2, second and fifth column for bound and suprathermal stars, respectively). The results are shown in Table 4.5. The total number of bound stars is greater than 1700 and the number of suprathermal stars is ~ 550.

As in Mapelli et al. 2005, to understand how many of these suprathermal stars are still observable today, we have to take into account three different timescales:

i) the half mass relaxation time is, by definition, the relaxation time at the half mass radius. It is important for our purposes, because it determines the time elapsed before a suprathermal star (which is expected to be ejected from the core) looses its excess of kinetic energy, reaching the thermodynamic equilibrium with the other stars. It can be defined as (Binney & Tremaine 1987):

$$t_{rh} = \frac{0.14N}{\ln\left(0.4N\right)} \left(\frac{r_h^3}{GM}\right)^{1/2} \tag{4.9}$$

where N and M are respectively the number of stars and the total mass of the cluster, G is the gravitational constant and r_h the half mass relaxation time.

ii) The hardening time is the timescale for a binary to harden via gravitational encounters:

$$t_{hard} = \frac{\sigma}{2\pi a\, \xi\, G\, m\, n}, \tag{4.10}$$

where σ is the dispersion velocity and n is the core density ($\sigma = 6$ km s^{-1} and $n = 2.5 \times 10^4$ pc^{-3} for M4; Peterson et al. 1995; Pryor & Meylan 1993).

iii) The gravitational wave timescale, t_{gw}, is the characteristic time for a binary IMBH to coalesce due to gravitational wave emission, defined as (Peters 1964; Quinlan 1996)

$$t_{gw} = \frac{5}{256} \frac{c^5 a^4 (1-e^2)^{7/2}}{G^3 M_1 M_2 (M_1+M_2)}, \tag{4.11}$$

where c is the speed of light.

In Fig. 4.5 we compare these three timescales for the case of M4. Since binary IMBHs, if exist, are thought to form only in the first stages of the globular cluster life (Miller & Hamilton 2002; Colpi, Mapelli & Possenti 2003), their current orbital separation is expected to be very small (Mapelli et al. 2005), due to hardening induced by gravitational encounters. The hardening time reported in Fig. 4.5 shows that, in the case of M4, we expect that a candidate binary IMBH has orbital separation $a \lesssim 2$ au. The gravitational timescale indicates that the binary IMBH must also be wider than $a \sim 0.5$ au, because harder binaries rapidly coalesce due to gravitational wave emission. If the current binary IMBH has semi-major axis $0.5 \lesssim a/\mathrm{au} \lesssim 2$, only the suprathermal stars produced in the last few Gyr have not lost yet their excess of kinetic energy, because the half mass relaxation time is much shorter than the current hardening time. Therefore, the number of suprathermal stars that is expected to inhabit M4 today is not 550, but much lower. In particular, we estimate that the only suprathermal stars still present in M4 are those produced in the last ~ 2 Gyr (about 3-4 t_{rh}, because a suprathermal star can have apo-center distance larger than the half mass radius and, therefore, relaxation time longer than t_{rh}). For this reason, in the forth line of Table 4.5 we report the number of suprathermal stars which are produced in the last 2 Gyr, which are about one hundred (~ 135). This scenario is very similar to what

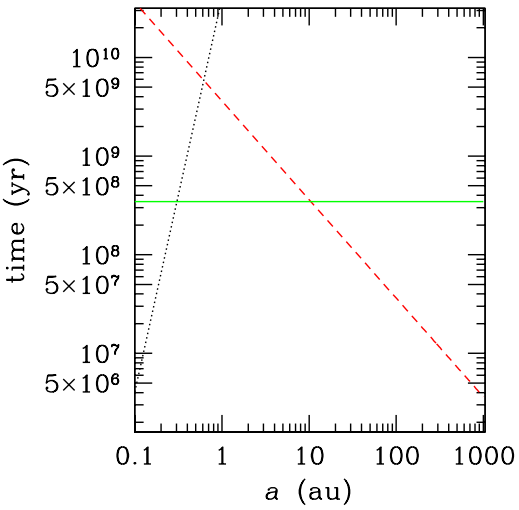

Figure 4.5: Half mass relaxation time, t_{rh} (solid line), and hardening time, t_{hard} (dashed line), as a function of the initial orbital separation a (in au) of the binary IMBH, for $n = 2.5 \times 10^4$ pc^{-3} (Pryor & Meylan 1993), $\xi = 1$, and $\sigma = 3.5$ km s^{-1}. The dotted line indicates the gravitational wave timescale t_{gw} for a binary IMBH with eccentricity $e = 0.7$.

we have found for NGC 6752: the only observable suprathermal stars are those formed in the last few Gyr and they do not show any angular momentum alignment, because they are formed by interactions with very hard binaries, unable to produce significant alignment.

As we noted in Mapelli et al. 2005, the number of observable suprathermal stars does not necessarily coincides with the total number of current suprathermal stars. Suprathermal stars may be recognized from their proper motion and/or Doppler line shift. Hence we have to take into account projection effects of velocity vectors. These effects depend in turn on the orientation of the angular momentum of the binary IMBH $\mathbf{J}_{\rm BH}$ with respect to the line of sight. We find that about 80% of the suprathermal stars can be recognized as such in the best case, i.e. when the line-of sight happens to be nearly parallel to the orbital angular momentum of the binary IMBH $\mathbf{J}_{\rm BH}$ (if we are measuring proper motions) or when the line-of-sight is nearly perpendicular to $\mathbf{J}_{\rm BH}$ (if we are measuring Doppler-shifts). On the contrary, the percentage reduces to about 60% when we are in the most unlucky cases, i.e. when the line of sight happens to be nearly perpendicular to the orbital angular

Table 4.5: Total number of interactions and suprathermal stars during the lifetime of a binary IMBH.

	M4	NGC 6752[a]
Interactions[b]	2717	1722
Bound stars[c]	1718	727
Suprathermal stars	550	262
Suprathermal stars (last 2 Gyr)[d]	135	158
Observable suprathermal stars[e]	50-65	30-60

[a] The values reported in this column are from Mapelli et al. 2005 and refer to a binary with $M_1 = 100\,M_\odot$, $M_2 = 50\,M_\odot$.

[b] Total number of stars which have an interaction with the binary IMBH.

[c] Number of stars which after the interaction remain bound to the cluster.

[d] Suprathermal stars formed in the last 2 Gyr.

[e] We define as "observable" suprathermal stars those suprathermal stars which are produced within the last 2 Gyr, which are expected to have mass from 0.6 to 0.9 $M_\odot$ and which should be identified as suprathermal even if we take into account the projection effects.

momentum of the binary IMBH $\mathbf{J}_{\rm BH}$ (if measuring proper motions), or when the line of sight is parallel to $\mathbf{J}_{\rm BH}$ (if measuring Doppler shifts). Assuming these percentages, we find that the number of recognizable suprathermal stars over the entire cluster is 80-110.

Our calculation refers to all stars, including also compact remnants (neutron stars, white dwarfs) and stellar types which are too faint for allowing a measurement of proper motion or radial velocity. Using the numerical code which will be described in the next Section, we find that the stars with mass from 0.6 to 0.9 $M_\odot$ (a mass range which includes red giant (RGB), horizontal branch (HB) and bright enough main sequence (MS) stars) represent about the 60% of the stars enclosed within[2] 0.1 r_c of a globular cluster like M4. This means that we are able to recognize only 50-65 suprathermal stars (Table 4.4; last row). This number is close to the estimate (30-60 suprathermal stars) that we derived for NGC 6752.

In this discussion we have not considered the effective instrumental errors so far. We now briefly report on them, without entering in details. Even if the Space Telescope Imaging Spectrograph (STIS) is no longer operative, its accuracy remains a good lower limit

[2]We consider the region within 0.1 r_c, because we are interested in those stars which have the highest probability of interacting with the central binary IMBH.

for future spectrographs. Observing with STIS stars in a globular cluster with distance from the Sun of the order of 2-10 kpc , one can expect an error of 1-2 km s^{-1} in the determination of radial velocity. For example, van der Marel et al (2002), reported spectra of about 130 stars in the core of M15 (distance from the Sun about 10 kpc) with an observational error of the order of 1.3 km s^{-1}. A somewhat higher error can be estimated for proper motion measurements with the Wide Field Photo Camera 2 on board of the Hubble Space Telescope (HST/WFPC2). Drukier et al. (2003) combined two sets of observations with the WFPC2 (one taken in 1994, the second in 1999) for a sample of 1281 stars in NGC 6752, estimating a median error of 0.31 mas yr^{-1} with a mode of 0.17 mas yr^{-1}. For the distance of NGC 6752 this means a median error of $\sim$ 6 km s^{-1} with a mode of $\sim$ 3 km s^{-1}, which is still an acceptable accuracy to distinguish suprathermal stars. Similar considerations hold for the Advanced Camera for Surveys on board of the HST (HST/ACS; see e.g. Anderson 2002; Anderson & King 2003). These estimates of the errors must be taken as upper limits in the case we are considering, because M4 is much closer to the Sun than M15 and even NGC6752.

Since we defined suprathermal stars in M4 those stars with projected velocity higher than $\sim$ 9 km s^{-1} (12 km s^{-1} for proper motion measurements), an error of 1-2 km s^{-1} (3-6 km s^{-1} for proper motion measurements) is sufficient to distinguish suprathermal from other cluster stars. In summary, the main problem in detecting suprathermal stars is not the error on the single measurement but the possibility of observing a sufficient large sample of stars, since suprathermal stars are expected to be a very small fraction of cluster stars.

Spatial distribution of the suprathermal stars

Since suprathermal stars are only few tens, the possibility of recognizing them may be significantly enhanced if their radial distribution shows some characteristic feature. Thus, it is of interest to study how suprathermal stars evolve in the cluster and what is their radial distribution.

Then, we want to explore the dynamics of suprathermal stars in M4, under the action of dynamical friction and the influence of two-body relaxation effects (as described

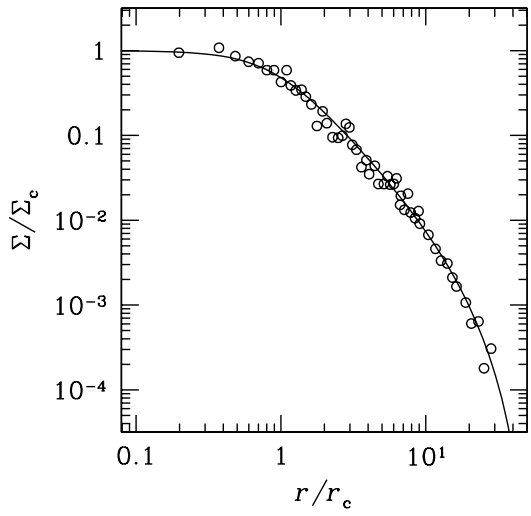

Figure 4.6: Surface density (Σ) normalized to the core surface density (Σ_c) of the globular cluster M4. Open circles are the data from Richer et al. (2004). The solid line is the best fit obtained by our simulations (assuming $n = 4 \times 10^4$ stars pc^{-3}, $\sigma = 3.5$ km s^{-1} and adimensional central potential $W_0 = 10$).

in Mapelli et al. 2005 for NGC 6752). We adopt an upgraded version of the code described in Sigurdsson & Phinney 1995. The code generates a cluster model (i.e. a multi-mass King density profile which reproduces that of M4; see Fig. 4.6), in which we embed suprathermal stars, whose initial positions and velocities are the outputs of our three-body simulations (Mapelli et al. 2005). We followed the dynamical evolution of these stars for a random time t uniformly distributed in the range $0 < t \leq 2$ Gyr (i.e. before than the suprathermal stars thermalize). We applied this procedure to the case A, the only scenario which can occur in the current stage of the cluster life.

The stars which were still suprathermal when the simulation stopped and that can be observed as suprathermal, taking into account two-dimensional (one-dimensional) projection effects and ejections, are about the 70% of the initial sample. The final radial distribution of these stars is shown in Fig. 4.7 (solid line) in comparison with the corresponding scenario (case D1, see Mapelli et al. 2005) for the cluster NGC 6752 (dashed line). The radial distribution of suprathermal stars in M4 is very similar to the distribution in

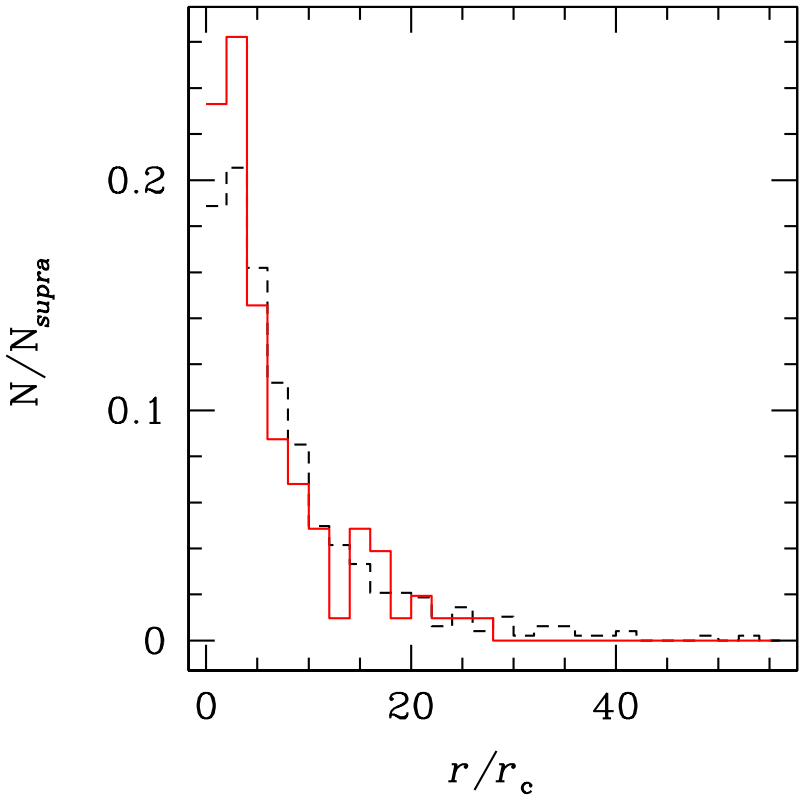

Figure 4.7: Final projected distribution of the high velocity suprathermal stars in the case A (solid line) and for the corresponding scenario in the case of NGC 6752 (dashed line; see Mapelli et al. 2005). On the x-axis the radial distance from the globular cluster center is normalized to the King core radius (r_c). On the y-axis the number of cases for each bin is normalized to the total number of suprathermal stars.

NGC 6752, both of them showing a peak at 3 r_c (where r_c is the core radius). The only difference is that the suprathermal distribution in M4 is slightly more concentrated than that in NGC 6752.

We have calculated that it is enough to measure radial velocities within a distance of 6 r_c from the cluster center, in order to avoid poissonian fluctuations to smear out the peak. The same result was obtained for NGC 6752.

Taking again into account both projection effects and luminosity criteria, only ~ 40 suprathermal stars are located within 6 r_c. We found that, if the velocity distribution is Maxwellian, ~ 10 stars with velocity in the suprathermal range are predicted to inhabit within a distance of 6 r_c from the center of M4. Then, the number of suprathermal stars produced by interactions with a binary IMBH prevails on the high velocity tail of the Maxwellian distribution. On the other hand the presence of this tail further dilutes the signature of suprathermal stars.

Detectability of angular momentum alignment

We now discuss the observability of the signature of the angular momentum alignment. Column 3 of Table 4.4 tells us that, in the most favorable case, about 60% of the stars which remain bound are corotating with the binary IMBH, whereas 40% are counterrotating. This means that, if there is a binary IMBH of M_1= 100 $M_\odot$ and M_2= 50 $M_\odot$, we should have about 330 corotating and only 220 counterrotating suprathermal stars. On the other hand, angular momentum alignment effects are visible only for sufficiently wide binaries ($a > 10$ AU). Thus, unless a binary IMBH is formed recently in a cluster, the alignment effect today is completely washed out by dynamical friction.

We note that a very low probability mechanism of binary IMBH formation in globular clusters in recent epochs exists. In fact, there is some possibility that a "last single BH" (Sigurdsson & Hernquist 1993), ejected from the core in the early stages of the globular cluster life, remains in the halo for several Gyrs. The relaxation timescale out in the halo is long, and if the orbits can circularize there (maybe due to time varying galactic tidal field), then the return time to the core is long. When this BH comes back to the core, there is a high probability that it forms a binary with the central IMBH. Such a binary IMBH

would be originated in late epochs. However, the probability for this process to occur is low, because it requires the BH to receive just the fine-tuned post-encounter velocity needed to remain in the outer halo: if the velocity is slightly too high, the BH will be ejected from the entire cluster; whereas, if the velocity is low, the return time to the core will be too short.

Thus, it is more likely that no binary IMBHs formed in the last few Gyrs and that the angular momentum alignment cannot be observed in globular clusters.

4.3.8 Summary

In this Chapter we explored the effects of three-body interactions between a binary IMBH and stars in loose globular clusters. We take the case of M4 as a prototype of loose globular cluster. As in the case of concentrated globular clusters (Mapelli et al. 2005), also in loose globular clusters the main fingerprint of the presence of a binary IMBH is the production of a family of suprathermal stars, i.e. stars which maintain an excess of kinetic energy for a few t_{rh}. Those stars could in principle show a partial alignment of their angular momentum to that of the binary IMBH; but this effect should not be visible in present globular clusters. The number of measurable suprathermal stars (once we take into account different selection effects) is very small ($\sim 50 - 60$ in the entire cluster), as we found also for concentrated globular clusters. Even the distribution of suprathermal stars is quite similar in loose and dense globular clusters.

Then, we can conclude that the number and the dynamical evolution of suprathermal stars are very similar in loose and dense globular clusters, i.e. they do not depend on the characteristics of the host globular cluster. Unfortunately, this means that suprathermal stars are very difficult to detect both in loose and in dense globular clusters.

Chapter 5

Dark matter decays and annihilations

5.1 Introduction

According to 3-yr WMAP results (Spergel et al. 2006), the dark matter (DM) constitutes about 20% of the cosmic energy density. However, the nature of such elusive component remains unclear.

In the so called cold dark matter (CDM) theory DM particles are defined "cold" particles, because of their low velocity dispersion, which is associated with a negligible free-streaming length (i.e. the length below which DM fluctuations are suppressed). The most famous alternative model to CDM is called warm dark matter (WDM), where DM particles are defined "warm" because of their higher velocity dispersion, and correspondingly longer free-streaming length. In WDM scenarios the velocity dispersion of the particles is sufficient to smear out the fluctuations up to galactic scales, depending on the mass of the particles (Padmanabhan 1995). This means that WDM models can alleviate the so called substructure crisis, which represents one of the most serious problems of CDM theories (Bode, Ostriker & Turok 2001; Ostriker & Steinhardt 2003). At present, there is no definitive evidence which allows us to exclude one of the two scenarios, and even the properties (mass, lifetime, etc) of cold and warm DM particles are substantially unknown.

One of the most direct ways to detect DM particles and, maybe, distinguish between CDM and WDM is represented by particle decays and annihilations (Chen & Kamionkowski 2004; Pierpaoli 2004). Sufficiently light DM particles (mass $\lesssim 100$ MeV; Hooper & Wang 2004) can decay into lighter particles remaining good DM candidates. On the other hand, DM particles could, in principle, annihilate with antiparticles (Ascasibar et al. 2006). The products of DM decays/annihilations can be photons, neutrinos, electron-positron pairs, and/or more massive particles, depending on the mass of the progenitor.

The decay/annihilation of DM particles into $e^+ - e^-$ pairs has been recently invoked to explain the observation, by the SPI spectrometer aboard ESA's INTEGRAL satellite, of an excess in the 511 keV line emission from the Galactic bulge (Knödlseder et al. 2005). Although exotic, this idea has triggered many theoretical studies (Ascasibar et al. 2006; Kawasaki & Yanagida 2005; Kasuya & Takahashi 2005; Cassé & Fayet 2005; Kasuya & Kawasaki 2006), aimed at constraining DM properties through SPI/INTEGRAL observations.

The products of decays and/or annihilations are expected to interact with the intergalactic medium (IGM), being partially absorbed by it. If so, DM decays/annihilations might change the IGM thermal/ionization history in a sensible and detectable way. Various flavors of this mechanism have been investigated in a considerable number of studies (Hansen & Haiman 2004; Chen & Kamionkowski 2004; Kasuya, Kawasaki & Sugiyama 2004; Kasuya & Kawasaki 2004; Pierpaoli 2004; Padmanabhan & Finkbeiner 2005; Mapelli & Ferrara 2005; Biermann & Kusenko 2006; Mapelli, Ferrara & Pierpaoli 2006; Zhang et al. 2006).

In this Chapter, we consider some of the most popular cold and warm DM particles, calculating their approximate annihilation/decay rate (Section 5.2), their influence on the ionization fraction, on the Thomson optical depth, on the behavior of matter temperature (Section 5.3-5.6) and on the cosmic microwave background (CMB) spectra (Section 5.7). Most of the results presented here were published in Mapelli & Ferrara 2005, in Mapelli, Ferrara & Pierpaoli 2006 and in Ripamonti, Mapelli & Ferrara 2006a, 2006b.
In all the cases, we make the assumption that the DM is composed by one single species of particles. We consider only "standard" DM candidates, neglecting more exotic scenarios (such as Q-balls, light scalar bosons, etc). In particular, we study three different candidates

for the case of CDM: (i) the light dark matter (LDM; 1-100 MeV; Hooper & Wang 2004), (ii) the gravitino and the (iii) neutralino, as heavy dark matter candidates ($\gtrsim$ 100 MeV). For the WDM we consider only the sterile neutrino. In fact, we do not pretend to present a complete overview of DM candidates. Instead, we would like to give a basic description of the effects of DM decays and annihilations, taking as an example some of the standard DM candidates. Our aim is to point out the differences among the considered DM particles, with particular care for cosmic reionization and heating.

5.2 Method

For each considered particle model we derived the rate of energy absorption per baryon in the IGM at redshift z, $\epsilon(z)$, through the following procedure.

In the case of decaying DM, $\dot{n}_{DM}$ (which we defined as the decrease rate of the number of DM particles per baryon) is given by

$$\dot{n}_{\rm DM}(z) = \frac{n_{\rm DM,0}}{\tau_{\rm DM}} e^{\frac{t(0)-t(z)}{\tau_{\rm DM}}} \simeq \frac{n_{\rm DM,0}}{\tau_{\rm DM}}, \tag{5.1}$$

where $n_{\rm DM,0}$ is the number of DM particles per baryon at present, $\tau_{\rm DM}$ is the lifetime of a DM particle, and $t(0)$ and $t(z)$ are the ages of the universe at present and at redshift z, respectively. The leftmost equality is valid when $\tau_{\rm DM} \gg t(0)$, which is generally the case.

Instead, in the case of annihilating DM, $\dot{n}_{\rm DM}$ is

$$\dot{n}_{\rm DM}(z) \simeq \frac{1}{2}\, n_{\rm DM,0}^2\, n_b\, < \sigma\, v > (1+z)^3, \tag{5.2}$$

where n_b the current density of baryons (we take $n_b = 2.5 \times 10^{-7}$ cm^{-3}, Spergel et al. 2006), and $< \sigma v >$ is the thermally averaged annihilation cross-section. The 1/2 factor is due to two reasons: first, the DM is split in half between particles and anti-particles, and this needs to be accounted by introducing a correction factor 1/4. However, this must be multiplied by 2, as each annihilation involves two DM particles.

Then, in both the cases $\epsilon(z)$ is simply:

$$\epsilon(z) = f_{abs}(z)\, \dot{n}_{\rm DM}(z)\, m_{\rm DM}\, c^2 \tag{5.3}$$

where $m_{\rm DM}\,c^2$ is the energy emitted by the DM decay/annihilation per DM particle (m_{DM} being the mass energy of the DM particle), and $f_{abs}(z)$ is the fraction of the total energy released by the DM which is absorbed by the IGM (see Section 5.4 for the details on the calculation of f_{abs}).

Now, we can use $\epsilon(z)$ to derive the effective influence of DM decays/annihilations on the cosmic reionization and heating. For this purpose, we ran the public version of the code RECFAST (Seager, Sasselov & Scott 1999, 2000), modified to account for the energy injection from DM decays and annihilations.

The IGM is heated, excited and ionized by the energy input due to DM decays/annihilations. It is important to note that the fraction of the absorbed energy going into each one of these components is quite unrelated to how the energy was deposited in the IGM in the first place. For example, if a keV a photon ionizes an atom, the resulting electron will generate a cascade of collisions, and the energy of the photon will go not only into ionizations, but also into excitations and heating.

In order to treat this process, we assume that a fraction $(1-x)/3$ (where x is the ionization fraction) of the energy absorbed by the IGM contributes to the ionizations (Chen & Kamionkowski 2004) and that a fraction $\mathcal{F}(x) = \tilde{C}\,\left[1-(1-x^{\tilde{a}})^{\tilde{b}}\right]$ (where $\tilde{C}$=0.9971, $\tilde{a}$=0.2663 and $\tilde{b}$=1.3163; Shull & van Steenberg 1985) goes into heating. This definition of $\mathcal{F}(x)$ comes directly from a fit to the results of the simulations given by Shull & van Steenberg (1985), replacing the significantly less accurate form that is used in Chen & Kamionkowski (2004), and in Mapelli, Ferrara & Pierpaoli (2006).

The evolution equations in RECFAST have been modified adding the DM energy injection terms:

$$-\delta\left(\frac{{\rm d}x_{\rm H}}{{\rm d}z}\right) = \frac{\epsilon(z)}{E_{\rm th,H}}\,\frac{1+4f_{\rm He}}{1+f_{\rm He}}\,\frac{1-x_{\rm H}}{3}\,\mathcal{E} \tag{5.4}$$

$$-\delta\left(\frac{{\rm d}x_{\rm He}}{{\rm d}z}\right) = \frac{\epsilon(z)}{E_{\rm th,He}}\,\frac{1+4f_{\rm He}}{1+f_{\rm He}}\,\frac{1-x_{\rm He}}{3\,(1+f_{\rm He})}\,\mathcal{E} \tag{5.5}$$

$$-\delta\left(\frac{{\rm d}T_{\rm IGM}}{{\rm d}z}\right) = \frac{2\,\epsilon(z)}{3\,k_{\rm B}}\,\frac{1+4f_{\rm He}}{1+f_{\rm He}}\,\frac{\mathcal{F}(x_{\rm H})+f_{\rm He}\,\mathcal{F}(x_{\rm He})}{(1+f_{\rm He})}\,\mathcal{E}, \tag{5.6}$$

where $x_{\rm H}$ ($x_{\rm He}$) is the ionized fraction of hydrogen (helium) atoms, $E_{\rm th,H} = 13.59$ eV ($E_{\rm th,He} = 24.6$ eV) is the ionization energy of hydrogen (helium) atoms, $f_{\rm He} \simeq 0.0789$ is the

helium-to-hydrogen number ratio, and $\mathcal{E} \equiv [H(z)\,(1+z)]^{-1}$. These equations are slightly different from the ones used e.g. in Padmanabhan & Finkbeiner (2005) because in our case $\epsilon(z)$ is the energy absorption rate *per baryon*, rather than *per hydrogen atom*.

We apply this formalism to various DM candidates, i.e. sterile neutrinos, LDM, gravitinos and neutralinos.

5.3 Heavy cold dark matter

First we consider the heaviest CDM particles ($\geq$ 100 MeV). Such particles are not considered a viable source for the 511 keV emission in the galactic center. In fact, in the case of neutralinos (with mass higher than 30 GeV), the request of a sizable R-parity violation, needed to allow considerable neutralino decays, would determine a too short lifetime and the neutralino would cease to be a good DM candidate (Hooper & Wang 2004). On the other hand, gravitino decays are possible; but the gravitino lifetime is far too long to match the 511 keV emission from the galactic center (Hooper & Wang 2004).

The decay/annihilation products of these very massive DM particles can generate cascades, which are nearly impossible to describe in detail. Then, in the case of gravitinos and neutralinos, we made the simplifying assumption that the absorbed fraction, $f_{abs}(z)$, is 1 (i.e. that all the energy injected by the decay/annihilation is immediately absorbed by the IGM). We will show that, even in this over-optimistic hypothesis, the contribution of heavy DM particles to heating and reionization is negligible.

5.3.1 Gravitinos

The most probable gravitino masses are $m_{3/2} < 1\,\mathrm{keV}$ and $m_{3/2} > 1\,\mathrm{TeV}$ (Nowakowski & Rindani 1995). In the first case, the gravitinos are the lightest supersymmetric particle (LSP) and then are stable: they are good WDM candidates; but their decay rate is negligible. In the second one, gravitinos are so unstable that they decay in the early universe, and, as a consequence, they are not viable DM candidates. Some models assume that gravitinos have mass $m_{3/2} \sim 10 - 100$ MeV, are the LSP and can violate the R-parity (Hooper & Wang 2004). In this case gravitinos are good DM candidates and have non-negligible decay

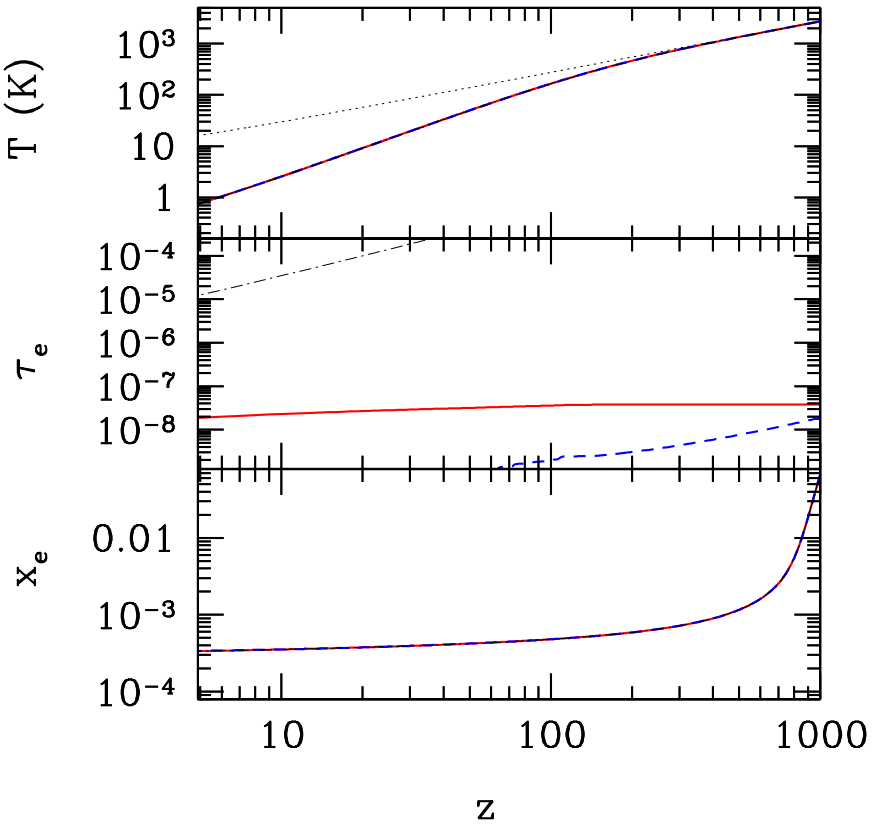

Figure 5.1: Ionized fraction (bottom panel), Thomson optical depth (central panel) and matter temperature (upper panel) as a function of redshift due to decaying gravitinos of masses 10 (dashed) and 100 MeV (solid). The thin dot-dashed line represents, from bottom to top, the relic fraction of free electrons, their contribution to Thomson optical depth and the IGM temperature without particle decays. In the top panel, the thin dotted line represents the CMB temperature.

rate. For this case, we calculated the gravitino contribution to reionization and heating, assuming lifetime:

$$\tau_{\rm DM} \sim 10^{31}\ {\rm s} \left(\frac{m_{\bar{l}}}{100\ {\rm GeV}}\right)^4 \left(\frac{0.1\ {\rm GeV}}{m_{3/2}}\right)^7 \left(\frac{0.1}{\lambda}\right)^2, \tag{5.7}$$

where $m_{\bar{l}}$ is the slepton mass and λ is the R-parity violating leptonic trilinear coupling. The current density of gravitinos can be derived as indicated for LDM. We find that, because of such a long lifetime, the contribution of gravitinos to heating and reionization is negligible (Fig. 5.1). For the same reason, Hooper & Wang (2004) show that gravitinos are unable to produce the 511 keV excess from the galactic center.

5.3.2 Heavy dark matter: neutralinos

Here we will consider as "heavy" DM the neutralinos. It is a merely indicative classification, given the uncertainties on the various models. The discussion of the details of different supersymmetric models is beyond the purpose of this Thesis. Neutralinos are thought to be very massive ($m_\chi > 30$ GeV). So, if they could decay (violating the R-parity), their lifetime should be very short, and they could not be a viable DM candidate. Then, the neutralino, if exists, must be perfectly stable, and we will not treat neutralino decay. However, neutralinos can annihilate. The annihilation cross-section is generally fit by (Bertone, Hooper & Silk 2005):

$$\sigma\, v = a + b\, v^2 + \mathcal{O}(v^4), \tag{5.8}$$

where a and b are constant, whose values are constrained by the DM relic density condition, and v is the neutralino velocity, which depends on the DM temperature and thus on the redshift. In the present epoch neutralinos are non-relativistic, then the current annihilation cross-section can be written as $\sigma\, v \sim a$. However, the cross-section at the freeze-out time should depend on v and be higher than the current value. As a rough approximation, Padmanabhan & Finkbeiner (2005) consider a thermally averaged, redshift independent cross-section, $\langle\sigma\, v\rangle = 2 \times 10^{-26}$ cm^3 s^{-1}. For comparison, we made the same assumption. Then, the annihilation rate per baryon becomes:

$$\dot{n}_{\rm DM}(z) = 1.15 \times 10^{-35}\,(1+z)^3\ {\rm s}^{-1} \left(\frac{n_0}{1.2 \times 10^{-8}{\rm cm}^{-3}}\right)^2 \left(\frac{\langle\sigma\, v\rangle}{2 \times 10^{-26}\ {\rm cm}^3\ {\rm s}^{-1}}\right), \tag{5.9}$$

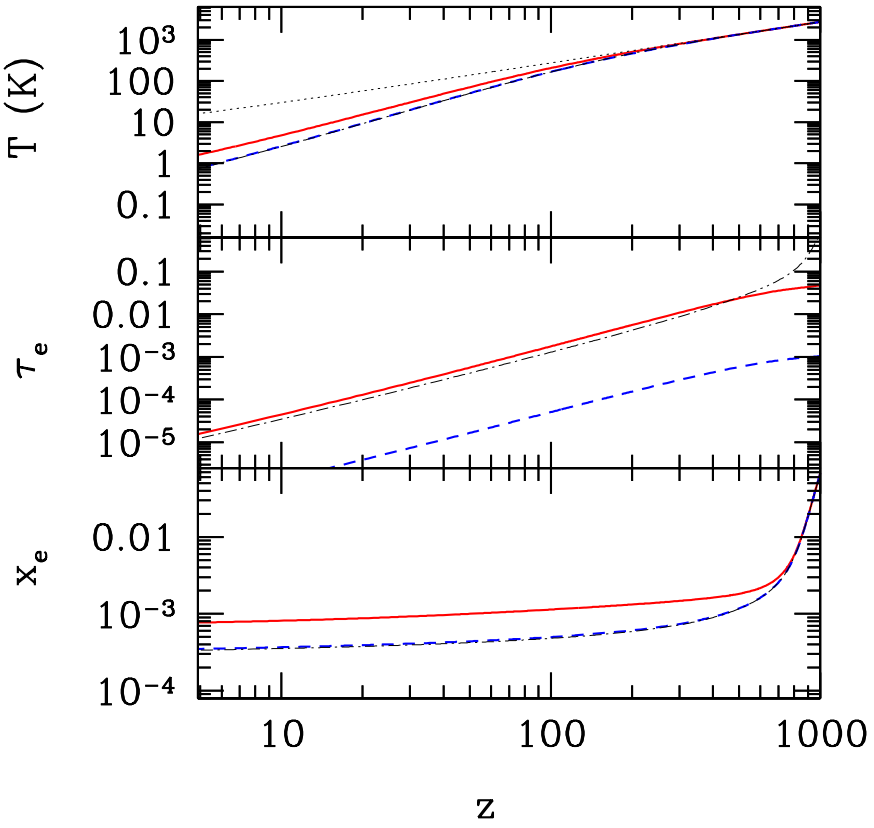

Figure 5.2: Ionized fraction (bottom panel), Thomson optical depth (central panel) and matter temperature (upper panel) as a function of redshift due to neutralinos for $\langle \sigma\, v \rangle = 2 \times 10^{-26}$ (thick dashed line) and 10^{-24} cm^3 s^{-1} (solid). In both the cases the neutralino mass is 100 GeV. The thin dotted line in the top panel and the thin dot-dashed line in all the panels are the same as in Fig. 5.1.

where $n_0 = \Omega_{DM}\,\rho_c/m_\chi$. In our calculations we assume m_χ=100 GeV. We have implemented this equation into RECFAST. The contribution of neutralino annihilations both to ionizations and heating is negligible (Fig.5.2; dashed line) for $\langle\sigma\,v\rangle = 2\times10^{-26}$ cm^3 s^{-1} (in agreement with Padmanabhan & Finkbeiner 2005). As an upper limit, we considered also the case where $\langle\sigma\,v\rangle = 10^{-24}$ cm^3 s^{-1}, which is the highest value to be consistent with the 1-yr WMAP data (see Colafrancesco, Profumo & Ullio 2006). Also in this case the contribution to heating is negligible and the ionization fraction remains of the order of 10^{-3} (Fig. 5.2). However, annihilations are particularly important at high redshift ($z \gtrsim 100$), where the particle density is very high. For this reason, even if the ionization fraction due to annihilations remains always low, the Thomson optical depth is significantly high ($\tau_e \sim 0.05$), even more than for LDM.

These results must be considered optimistic upper limits. In fact we are assuming that nearly all the energy of the DM particle is immediately deposited into ionization or heating; whereas we expect that the electrons produced by neutralino annihilations Compton-scatter the CMB photons up to a energy $\sim 1 - 10\,(1+z)$ MeV, which cannot be significantly absorbed by the intergalactic medium within a Hubble time (Chen & Kamionkowski 2004).

5.4 Energy injection in the IGM for light particles (< 100 MeV)

When the DM particle is relatively light (< 100 MeV), then it can only decay or annihilate into photons, neutrinos and pairs. In this case, we are able to model in detail the physical processes governing the interaction between the IGM and the decay/annihilation products, and we derive the effective absorbed energy fraction (f_{abs}). In particular, for photons we include the effects of Compton scattering and photo-ionization; for pairs, the relevant processes are inverse Compton scattering, collisional ionizations, and positron annihilations.

Some fraction of the energy of the newly created particles is immediately absorbed; the remainder will remain in the form of a *background*, eventually absorbed at later times.

In practice, at each redshift z, it is convenient to distinguish the particles which

were produced by DM decays and/or annihilations according to their "production redshift" z' and energy E. We define $n(z, z')$ as the number (per baryon) of product particles which at redshift z can still inject energy in the IGM, and were produced at redshift $z' \geq z$. Their energy spectrum is $\frac{dn}{dE}(z, z', E)$.

The rate of energy absorption per baryon in the IGM at redshift z is the sum of the contributions of all "product particles", obtained by the integration over production redshift and energy

$$\epsilon(z) = \int_z^{z_{\max}} dz' \int dE \, \frac{dn}{dE}(z, z', E) \, E \, \phi(z, E) \tag{5.10}$$

where $\phi(z, E)$ is the fraction of the energy E of a particle which is absorbed by the IGM per unit time, calculated at redshift z. We assume $z_{\max}$=1100, which is approximately the redshift of the last scattering surface (Spergel et al. 2006).

However, using equation (5.10) is both complicated and unnecessary: in fact, we know that the energy spectrum of "fresh" DM decay/annihilation products is essentially mono-energetic, and it is reasonable to expect that it will remain peaked at the average energy. Therefore, we assume that the energy integration inside equation (5.10) can be safely eliminated by using the average energy $\bar{E}(z, z')$ of the particles

$$\bar{E}(z, z') = \frac{1}{n(z, z')} \int dE \, \frac{dn}{dE}(z, z', E) \, E \tag{5.11}$$

so that equation (5.10) becomes

$$\epsilon(z) = \int_z^{z_{\max}} dz' \, n(z, z') \, \bar{E}(z, z') \, \phi(z, \bar{E}(z, z')). \tag{5.12}$$

The evolution of $n(z, z')$, $\bar{E}(z, z')$, and $\phi(z, E)$ obviously depends on the type of DM decay/annihilation product we are considering. If the product particles are neutrinos $\phi_\nu(z, E) = 0$; the cases of photons and electron-positron pairs are discussed in the following subsections.

5.4.1 Photons

If the DM decays or annihilations result in the production of photons, the only two important energy loss mechanisms in the considered energy and redshift ranges ($25\,\mathrm{eV} \lesssim E \lesssim 5\,\mathrm{MeV}$;

$z \lesssim 1000$) are ionizations and Compton scattering on cold matter (see Zdziarski & Svensson 1989; hereafter ZS89). All the energy lost by the photons is absorbed by the IGM, so we can write

$$\phi_\gamma(z, E) = \phi_{\gamma,\mathrm{ion}}(z, E) + \phi_{\gamma,\mathrm{com}}(z, E). \tag{5.13}$$

The photo-ionization term can be expressed as

$$\phi_{\gamma,\mathrm{ion}}(z, E) = \frac{\sigma_{\mathrm{He+H}}(E)}{16}\, n_b(z)\, c, \tag{5.14}$$

where $n_b(z) \simeq 2.5 \times 10^{-7}(1+z)^3(\Omega_b h^2/0.0224)\ \mathrm{cm}^{-3}$ is the number density of the baryons at redshift z, and

$$\sigma_{\mathrm{He+H}}(E) = \sigma_{\mathrm{He}} + 12\sigma_{\mathrm{H}} \simeq 5.1 \times 10^{-20} \left(\frac{E}{250\,\mathrm{eV}}\right)^{-p} \mathrm{cm}^2 \tag{5.15}$$

(with $p = 3.30$ for $E > 250\,\mathrm{eV}$, $p = 2.65$ for $25\,\mathrm{eV} \leq E \leq 250\,\mathrm{eV}$) is the photoionization absorption cross-section per helium atom of the cosmological mixture of H and He (see equation 3.2 of ZS89). Equation (5.14) implicitly assumes that the IGM is mostly neutral, which is true between the hydrogen recombination at $z \simeq 1100$, and its reionization at $z \sim 6 - 15$.

The Compton scattering term is

$$\phi_{\gamma,\mathrm{com}}(z, E) = [\sigma_\mathrm{T}\, \xi\, g(\xi)]\, n_\mathrm{e}(z)\, c \tag{5.16}$$

where $\xi \equiv E/(m_e c^2)$, $n_\mathrm{e}(z)$ is the electron number density, and the product $\sigma_\mathrm{T}\, \xi\, g(\xi)$ gives the average fraction of energy which is lost by a photon for each electron on its path ($\sigma_\mathrm{T} \simeq 6.65 \times 10^{-25}\,\mathrm{cm}^{-2}$ is the Thomson cross-section; see equation 4.9 of ZS89 for the definition of the function $g(\xi)$). In equation (5.16) the electron number density accounts for both free and bound electrons, as the energy losses due to Compton scattering only become important when E is so high that the interaction is insensitive to whether an electron is bound or free (Chen & Kamionkowski 2004). Then, $n_\mathrm{e}(z) = [(1 + 2f_\mathrm{He})/(1 + 4f_\mathrm{He})]\, n_b(z) \simeq 0.88\, n_b(z)$, where $f_\mathrm{He} = 0.0789$ is the helium-to-hydrogen number ratio.

We assume that the energy transfer through ionization results in a photon loss, whereas Compton scatterings reduce the average energy of the photons without changing

their number. So, for $z < z'$ the equations for the cosmological evolution of $n(z, z')$ and $E(z, z')$ are

$$\frac{n(z+dz, z')}{n(z, z')} = 1 - \phi_{\gamma,\mathrm{ion}}(z, \bar{E}(z, z'))\frac{dt}{dz}dz \tag{5.17}$$

$$\frac{\bar{E}(z+dz, z')}{\bar{E}(z, z')} = 1 - \phi_{\gamma,\mathrm{com}}(z, \bar{E}(z, z'))\frac{dt}{dz}dz + \frac{dz}{1+z} \tag{5.18}$$

where the energy equation also keeps into account the cosmological redshifting of photons (also note that dt/dz is negative).

These equations need to be supplemented with the injection of new photons at each redshift $z = z'$:

$$n(z'+dz, z') = \zeta_1\, \dot{n}_{\mathrm{DM}}(z')\, \frac{dt}{dz}dz \tag{5.19}$$

$$\bar{E}(z'+dz, z') = \zeta_2\, m_{\mathrm{DM}}\, c^2 \left(1 + \frac{dz}{1+z}\right) \tag{5.20}$$

where $\dot{n}_{\mathrm{DM}}(z')$ is the rate of decrease of the number of DM particles per baryon at redshift z', and m_{DM} is the mass of a DM particle (see §5.4.3). ζ_1 and ζ_2 are numerical coefficients which depend on the considered DM particle and on the details of its decay or annihilation.

5.4.2 Pair production

Even if the loss of kinetic energy from electrons and positrons can be treated in exactly the same way, the annihilation probability is negligible for the electrons, but must be kept into account for the positrons. For this reason, when DM decays/annihilations result in the production of an electron-positron pair[1], it is useful to distinguish between electrons and positrons. Note that in the following we will always include the rest energy $m_e c^2$ as part of the energy E of the particle.

Electrons

Electrons can transfer their kinetic energy to the IGM through collisional ionizations and ionizations by inverse Compton up-scattered cosmic microwave background

[1] In the case of pair production we neglect other processes, such as the internal Bremsstrahlung, which affect $\epsilon(z)$ only in a minor way.

(CMB) photons. Here we neglect the energy loss through synchrotron radiation, because the inverse Compton mechanism is more efficient by a factor $U_{\rm CMB}/U_{\rm B}$ (where $U_{\rm CMB}$ and $U_{\rm B}$ are the energy densities of the CMB and of the magnetic field, respectively), which is $\gg 1$ unless unrealistically strong magnetic fields ($B \gtrsim 10^{-5}$ gauss) are assumed to exist in the IGM at $z \geq 5$.

Photons produced by the inverse Compton mechanism are not necessarily absorbed by the IGM, and we must distinguish between the fractional energy loss rate by electrons

$$\Phi_{\rm e-}(z, E) = \Phi_{\rm e,ion}(z, E) + \Phi_{\rm e,com}(z, E), \tag{5.21}$$

and the fractional energy loss rate actually absorbed by the IGM,

$$\phi_{\rm e-}(z, E) = \phi_{\rm e,ion}(z, E) + \phi_{\rm e,com}(z, E) \tag{5.22}$$

The ionization losses are completely absorbed by the IGM, so that

$$\begin{aligned}\phi_{\rm e,ion}(z, E) = \Phi_{\rm e,ion}(z, E) \simeq \tfrac{v}{E}\tfrac{2\pi e^4}{m_e v^2} \times \{ Z_{\rm H}\, n_{\rm H}(z) \left[\ln\left(\tfrac{m_e v^2 \gamma^2 T_{\rm max,H}}{2E^2_{\rm th,H}}\right) + \mathcal{D}(\gamma)\right] + \\ + Z_{\rm He}\, n_{\rm He}(z) \left[\ln\left(\tfrac{m_e v^2 \gamma^2 T_{\rm max,He}}{2E^2_{\rm th,He}}\right) + \mathcal{D}(\gamma)\right]\}\end{aligned} \tag{5.23}$$

where v and e are the velocity and charge of the electron, $\gamma = E/(m_e c^2)$ is the electron Lorentz factor, $E_{\rm th,H} = 13.59$ eV ($E_{\rm th,He} = 24.6$ eV) is the hydrogen (helium) ionization threshold, $Z_{\rm H} = 1$ ($Z_{\rm He} = 2$) is the hydrogen (helium) atomic number, $n_{\rm H}(z) = n_{\rm b}(z)/(1 + 4f_{\rm He})$ is the H number density, $n_{\rm He}(z) = n_{\rm b}(z)\, f_{\rm He}/(1 + 4_{\rm He})$ is the He number density, $\mathcal{D}(\gamma) = \frac{1}{\gamma^2} - \left(\frac{2}{\gamma} - \frac{1}{\gamma^2}\right)\ln 2 + \frac{1}{8}\left(1 - \frac{1}{\gamma}\right)^2$, and

$$\begin{aligned}T_{\rm max,H} &= \tfrac{2\gamma^2 m_{\rm H}^2 m_e v^2}{m_e^2 + m_{\rm H}^2 + 2\gamma m_e m_{\rm H}} \\ T_{\rm max,He} &= \tfrac{2\gamma^2 (4m_{\rm H})^2 m_e v^2}{m_e^2 + (4m_{\rm H})^2 + 2\gamma m_e (4m_{\rm H})}\end{aligned} \tag{5.24}$$

(cfr. Longair 1992, Lang 1999, and also Chen & Kamionkowski 2004).

The total Compton fractional losses are given by

$$\Phi_{\rm e,com}(z, E) = \left(\frac{1}{E}\right)\frac{4}{3}\sigma_{\rm T}\, c\, a_{\rm rad}\, T_{\rm CMB}(z)^4\, (\gamma^2 - 1), \tag{5.25}$$

where $a_{\rm rad} \simeq 7.56 \times 10^{-15}$ erg cm^{-3} K^{-4} is the Stefan-Boltzmann constant for the radiation energy density, and $T_{\rm CMB}(z) \simeq 2.726\,(1 + z)$ K is the temperature of the CMB radiation

at redshift z (cfr. Rybicki & Lightman 1979; Longair 1992); the fractional loss rate that is actually absorbed by the IGM is

$$\phi_{\rm e,com}(z,E) = \Phi_{\rm e,com}(z,E)\frac{\gamma^2}{\gamma^2-1}\int_{\nu(\gamma)}^{\infty} d\nu \frac{4\pi B_\nu(T_{\rm CMB}(z))}{a_{\rm rad}\, c\, T_{\rm CMB}(z)^4} \tag{5.26}$$

where $B_\nu(T)$ is the Planck function for black-body radiation at temperature T, and

$$\nu(\gamma) = \frac{3\, E_{\rm th,H}}{4\, h_{\rm P}\, \gamma^2} \tag{5.27}$$

where $h_{\rm P}$ is the Planck constant. The correction to $\Phi_{\rm e,com}$ introduced in equation (5.26) amounts to neglecting photons with pre-interaction frequencies below $\nu(\gamma)$. This is necessary because on average the post-interaction energies of such photons are below $E_{\rm ion,H}$, so that they are hardly absorbed by the IGM[2].

As in the case of photons, we assume that ionization energy losses lead to the disappearance of electrons, whereas Compton losses reduce the average energy of the surviving electrons. Therefore, the equations describing the evolution of electrons are quite similar to those we used for photons. For redshifts $z < z'$ we have

$$\frac{n_{\rm e-}(z+dz,z')}{n_{\rm e-}(z,z')} = 1 - \Phi_{\rm e,ion}(z,\bar{E}_{\rm e-}(z,z'))\frac{dt}{dz}dz \tag{5.28}$$

$$\frac{\bar{E}_{\rm e-}(z+dz,z')}{\bar{E}_{\rm e-}(z,z')} = 1 - \Phi_{\rm e,com}(z,\bar{E}_{\rm e-}(z,z'))\frac{dt}{dz}dz, \tag{5.29}$$

whereas the injection of new electrons is described by

$$n_{\rm e-}(z'+dz,z') = \zeta_1\, \dot{n}_{\rm DM}(z')\, \frac{dt}{dz}dz \tag{5.30}$$

$$\bar{E}_{\rm e-}(z'+dz,z') = \zeta_2\, m_{\rm DM}\, c^2. \tag{5.31}$$

where, again, ζ_1 and ζ_2 depend on the details of the considered decaying or annihilating particle.

Positrons

In addition to the energy loss mechanisms of electrons, decay produced positrons can also annihilate with thermal electrons in the surrounding gas. The fractional energy

[2]Lyman α opacity generally results only in the scattering of the photon, rather than in its absorption, and only a small fraction of the energy is absorbed (Furlanetto & Pritchard 2006).

loss due to the annihilations of positrons of energy E is

$$\Phi_{\rm ann}(E) = v\, n_b(z)\, \sigma_{\rm ann}(E) \tag{5.32}$$

where the annihilation cross-section $\sigma_{\rm ann}$ is (cfr. Beacom & Yüksel 2005)

$$\sigma_{\rm ann}(E) = \frac{3\sigma_{\rm T}}{8}\,(\gamma+1)^{-1}\,\left[\frac{\gamma^2+4\gamma+1}{\gamma^2-1}\ln(\gamma+\sqrt{\gamma^2-1}) - \frac{\gamma+3}{\sqrt{\gamma^2-1}}\right]. \tag{5.33}$$

Every annihilation emits two photons, each of energy $E_\gamma \sim \frac{1}{2}(E + m_e c^2)$, as it involves a positron of energy E and an electron whose energy is likely to be close to $m_e c^2$. Such photons are absorbed only if the optical depth they encounter is sufficiently high. Here we do not follow their radiative transfer in detail, and simply assume that the fractional energy loss which actually goes in the IGM is

$$\phi_{\rm ann}(z, E) = \Phi_{\rm ann}(z, E)\; f_1\,[1 - e^{-\tau_\gamma(z, E_\gamma)}] \tag{5.34}$$

with

$$\tau_\gamma(z, E_\gamma) = \frac{f_2}{H(z)}\,\phi_{\gamma,\rm com}(z, E_\gamma) \tag{5.35}$$

where $H(z)$ is the expansion rate of the universe at redshift z, and $\phi_{\gamma,\rm com}(z, E_\gamma)$ is the Compton fractional energy loss of a photon of energy E_γ, as defined in equation (5.16). Equation (5.35) represents a fraction f_2 of the optical depth encountered by a photon of energy E_γ emitted at redshift z and traveling an Hubble radius, assuming that the baryonic density does not vary. The parameters $f_1 = 0.91$ and $f_2 = 0.6$ have been chosen in order to maximize the agreement between a full radiative transfer treatment and our simple approximation.

Equation (5.33) implies that annihilation energy loss is particularly efficient for positrons with very low kinetic energy, as $\sigma_{\rm ann}(E) \propto (\gamma - 1)^{-1/2}$ when $E \approx m_e\, c^2$ (and γ tends to 1).

For this reason, it is convenient to separate positron in two different groups: "fast" positrons (which effectively lose energy through ionizations, inverse Compton, and annihilations), and "thermal" positrons (whose kinetic energy is so low that annihilations are their only energy loss mechanism).

The treatment of fast positrons is very similar to that of electrons: their fractional energy loss rate is

$$\Phi_{\mathrm{e}+,\mathrm{f}}(z,E) = \Phi_{\mathrm{e,ion}}(z,E) + \Phi_{\mathrm{e,com}}(z,E) + \Phi_{\mathrm{ann}}(z,E), \tag{5.36}$$

and the fractional energy loss rate actually absorbed by the IGM is

$$\phi_{\mathrm{e}+,\mathrm{f}}(z,E) = \phi_{\mathrm{e,ion}}(z,E) + \phi_{\mathrm{e,com}}(z,E) + \phi_{\mathrm{ann}}(z,E), \tag{5.37}$$

where the ionization and Compton terms are exactly the same as in the case of electrons.

Their evolution is described by the equations which are simple modifications of those given for electrons, taking annihilations into account

$$\frac{n_{\mathrm{f}}(z+dz,z')}{n_{\mathrm{f}}(z,z')} = 1 - [\Phi_{\mathrm{e,ion}}(z,\bar{E}_{\mathrm{f}}(z,z')) + \Phi_{\mathrm{ann}}(z,\bar{E}_{\mathrm{f}}(z,z'))]\frac{dt}{dz}dz \tag{5.38}$$

$$\frac{\bar{E}_{\mathrm{f}}(z+dz,z')}{\bar{E}_{\mathrm{f}}(z,z')} = 1 - \Phi_{\mathrm{e,com}}(z,\bar{E}_{\mathrm{f}}(z,z'))\frac{dt}{dz}dz, \tag{5.39}$$

where the "f" subscripts refer to "fast" positrons (*e.g.* , $\bar{E}_{\mathrm{f}}$ is the average energy of the fast positrons). Their injection rate and average energy are identical to those given in equations (5.30) and (5.31) for electrons: $n_{\mathrm{f}}(z'+dz,z') = n_{\mathrm{e}-}(z'+dz,z')$, $E_{\mathrm{f}}(z'+dz,z' = E_{\mathrm{e}-}(z'+dz,z')$.

The fractional energy losses (total and absorbed by the IGM) of thermal positrons are simply

$$\Phi_{\mathrm{e}+,\mathrm{t}}(z,E) = \Phi_{\mathrm{ann}}(z,E) \tag{5.40}$$

$$\phi_{\mathrm{e}+,\mathrm{t}}(z,E) = \phi_{\mathrm{ann}}(z,E), \tag{5.41}$$

Their evolution equations are

$$n_{\mathrm{t}}(z+dz,z') = n_{\mathrm{t}}(z,z')[1-\Phi_{\mathrm{ann}}(z,\bar{E}_{\mathrm{t}}(z))] + n_{\mathrm{f}}(z,z')\Phi_{\mathrm{e,ion}}(z,\bar{E}_{\mathrm{f}}(z,z')) \tag{5.42}$$

$$\bar{E}_{\mathrm{t}}(z) = m_e c^2 + \frac{3}{2}k_{\mathrm{B}}T_{\mathrm{IGM}}(z) \tag{5.43}$$

where the "t" subscripts refer to "thermal" positrons, k_{B} is the Boltzmann constant, and $T_{\mathrm{IGM}}(z)$ is the temperature of the IGM at redshift z. We take the injection rate to be simply $n_{\mathrm{t}}(z',z') = 0$, as positrons are naturally "fast" when they are created.

In practice, these equations assume that the only mechanism which leads to the disappearance of a positron is its annihilation; instead, ionization energy losses simply turn a fast positron into a thermal one.

5.4.3 The energy absorbed fraction

The energy injection rate per baryon resulting from the integration of equation (5.12) can be expressed in the form of the fraction f_{abs} of the total energy released by the DM which is absorbed by the IGM

$$f_{abs}(z) = \frac{\epsilon(z)}{\dot{n}_{\rm DM}(z)\, m_{\rm DM}\, c^2}. \tag{5.44}$$

The definition of the absorbed fraction[3], f_{abs}, given in equation (5.44) is such that it can be easily plugged into the equations commonly used in studies concerned with decaying and annihilating DM (*e.g.* Padmanabhan & Finkbeiner 2005; Zhang et al. 2006).

In the next Sections, we will apply this formalism to two different DM candidates, i.e. sterile neutrinos and LDM, which are expected to have the maximum impact on reionization and heating (Mapelli, Ferrara & Pierpaoli 2006). In the case of sterile neutrinos only the decay process is allowed. For LDM particles we discuss both the decay and the annihilation process.

5.5 Sterile neutrinos

Sterile neutrinos are one of the most popular warm DM candidates (Colombi, Dodelson & Widrow 1996; Sommer-Larsen & Dolgov 2001). Their existence is predicted by the standard oscillation theory and required by various extensions of the Minimal Standard Model, such as the νMSM (Shaposhnikov 2006 and references therein). They are massive; so they can decay following different channels (Dolgov & Hansen 2002; see Dolgov 2002 for a complete review of sterile neutrino properties). In this Chapter we will consider only the so called radiative decay, i.e. the decay of a sterile neutrino into an active neutrino and a

[3]We remark that the term "absorbed fraction" might be slightly misleading, as it is theoretically possible to have $f_{abs} > 1$ in scenarios where $\epsilon(z)$ is dominated by the absorption from particles in the "background", rather than from the ones which were produced recently. This might happen, for example, when $\dot{n}_{\rm DM}$ decreases very rapidly.

photon (De Rújula & Glashow 1980; Stecker 1980; Drees & Wright 2000; Abazajian, Fuller & Patel 2001a; Abazajian, Fuller & Tucker 2001b; Dolgov 2002). For an alternative sterile neutrino model see Hansen & Haiman 2004 and Appendix C of this Thesis.

The mass of radiatively decaying sterile neutrinos can be constrained by the absence of any detection of X-ray lines consistent with photons due to sterile neutrino decays in nearby galaxy clusters (Abazajian, Fuller & Tucker 2001b; Abazajian 2006; Abazajian & Koushiappas 2006; Boyarsky et al. 2006b).

Recently, Watson et al. 2006 applied the same method to the X-ray emission from the Andromeda galaxy, finding an upper limit

$$m_{\nu\,s}\,c^2 \lesssim 2.1 \text{ keV } \left(\frac{\sin^2 2\theta}{10^{-7}}\right)^{-0.213}, \tag{5.45}$$

where θ is the mixing angle. This limit is valid for masses $m_{\nu\,s}\,c^2 \lesssim 24$ keV. The most stringent constraints for masses $m_{\nu\,s}\,c^2 > 24$ keV come from the comparison between the unresolved X-ray background and the expected contribution from sterile neutrino decays (Mapelli & Ferrara 2005; Boyarsky et al. 2006a; see the Appendix C of this Thesis for details):

$$m_{\nu\,s}\,c^2 \lesssim 25 \text{ keV } \left(\frac{\Omega_{\rm DM}}{0.198}\right)^{-0.2} \left(\frac{\sin^2 2\theta}{1.55\times 10^{-11}}\right)^{-0.2}. \tag{5.46}$$

For masses lower than ~ 3.5 keV the main constraints arise from the positivity of the lepton number.

On the other hand, the study of matter power spectrum fluctuations provides a conservative lower limit of $m_{\nu\,s}\,c^2 \gtrsim 2$ keV (Viel et al. 2005), even if more recent estimates significantly increase this lower limit ($m_{\nu\,s}\,c^2 \gtrsim 14$ keV, Seljak et al. 2006; $m_{\nu\,s}\,c^2 \gtrsim 10$ keV, Viel et al. 2006). It is worth noting that these lower limits are independent of the mixing angle.

According to the X-ray observational constraints discussed above, the minimum possible lifetime for sterile neutrino radiative decays is (Mapelli & Ferrara 2005; MFP06):

$$\tau_{\rm DM} = 2.23\times 10^{27} \text{ s } \left(\frac{m_{\nu\,s}\,c^2}{10 \text{ keV}}\right)^{-5} \left(\frac{6.6\times 10^{-11}}{\sin^2 2\theta}\right), \tag{5.47}$$

if $3.5 \lesssim m_{\nu\,s}\,c^2/\text{keV} \lesssim 24$, and

$$\tau_{\rm DM} = 9.67\times 10^{25} \text{ s } \left(\frac{m_{\nu\,s}\,c^2}{25 \text{ keV}}\right)^{-5} \left(\frac{1.55\times 10^{-11}}{\sin^2 2\theta}\right), \tag{5.48}$$

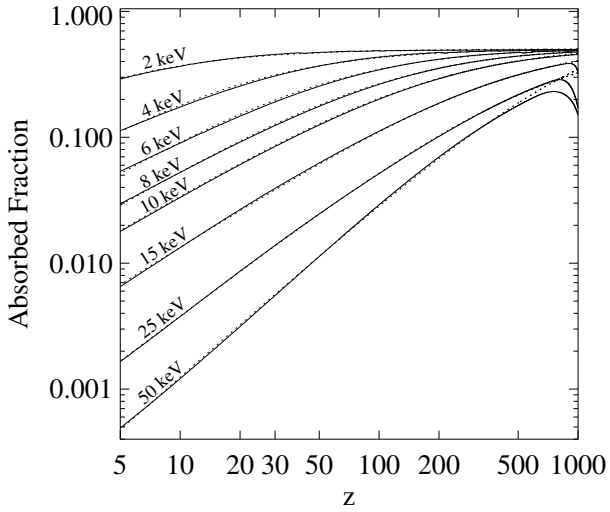

Figure 5.3: Absorbed fraction as a function of redshift for sterile neutrinos of masses between 2 and 50 keV (solid lines). The dotted lines, mostly superimposed to the solid ones, show the fitting functions listed in Appendix D. The decrease in f_{abs} which can be seen for $z \gtrsim 800$ for the 15, 25 and 50 keV curves might be an artifact caused by our choice of the redshift where the integration is started ($z_{max} = 1100$), as is discussed in Appendix D.

if $m_{\nu\,s}\,c^2/\mathrm{keV} \gtrsim 24$.

The current number density of sterile neutrinos $n_{s,0}$ is proportional to the current number density of active neutrinos [$n_a = 3\,n_b(0)/(11\,\eta)$, where η is the baryon-to-photon density]. If we assume also that sterile neutrinos account for all the DM, we can write the number of sterile neutrinos per baryon as (cfr. Mapelli & Ferrara 2005):

$$n_{s,0} = 5.88 \times 10^5 \left(\frac{\rho_{\mathrm{crit}}}{10^{-29}\,\mathrm{g\,cm^{-3}}}\right)\left(\frac{\Omega_{\mathrm{DM}}}{0.198}\right)\left(\frac{m_{\nu\,s}\,c^2}{8\ \mathrm{keV}}\right)^{-1}\left(\frac{\eta}{6.13\times10^{-10}}\right)^{-1}. \quad (5.49)$$

where $\rho_{\mathrm{crit}} \simeq 1.88 \times 10^{-29}\,h^2\ \mathrm{g\,cm^{-3}}$ is the critical density of the Universe.

Imposing $n_{\mathrm{DM},0} = n_{s,0}$ and $m_{\mathrm{DM}} = m_{\nu\,s}$ we have all the ingredients needed to calculate $\dot{n}_{\mathrm{DM}}(z)$ through equation (6.9), for each considered mass.

Each sterile neutrino decay produces one active neutrino and one photon, each of them with an energy $\simeq \frac{1}{2} m_{\mathrm{DM}} c^2$. Since the active neutrino does not interact with the IGM, we only need to consider the photon. Then, we use equations (5.19) and (5.20) with $\zeta_1 = 1$ and $\zeta_2 = 1/2$, in order to get the injection rate and average energy of photons, and proceed to the integration of equation (5.12).

The resulting absorbed fraction, $f_{abs}(z)$, is shown in Fig. 5.3. In the case of

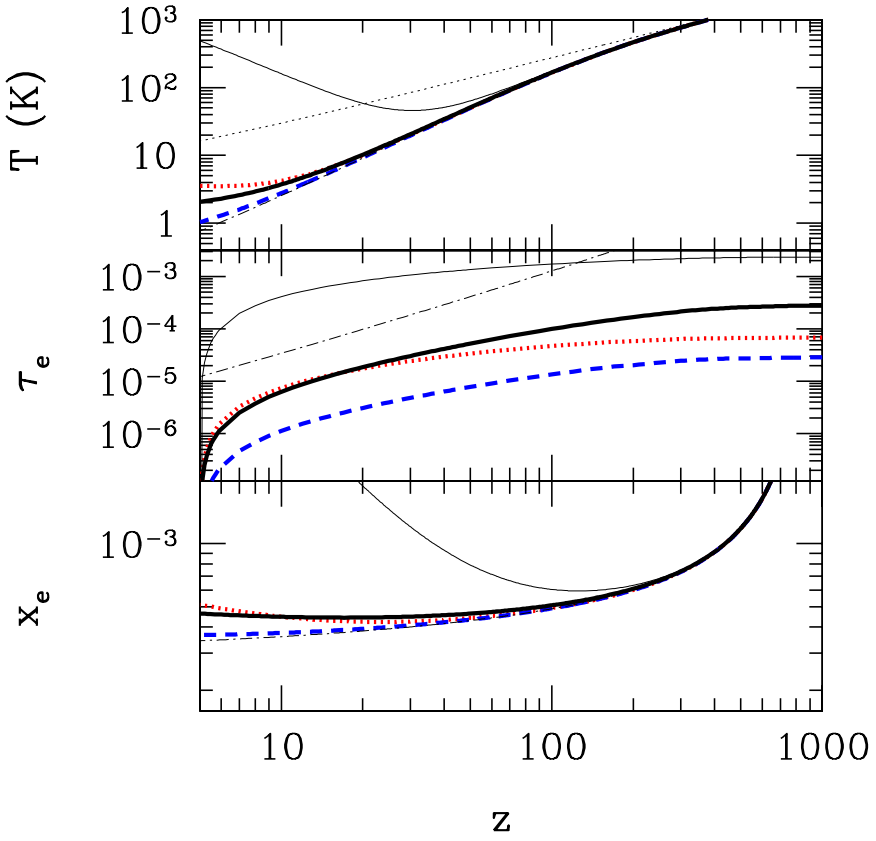

Figure 5.4: Ionized fraction (bottom panel), Thomson optical depth (central panel) and IGM temperature (top panel) as a function of redshift due to sterile neutrinos. The thick lines are obtained taking into account the effective absorbed fraction (Fig. 5.3) for sterile neutrinos of masses 4 (thick dotted line), 15 (dashed), and 25 keV (solid). The thin solid line shows the contribution of sterile neutrinos of mass 25 keV, if we assume an absorbed fraction $f_{\rm abs} = 0.5$. The thin dotted line in the top panel and the thin dot-dashed line in all the panels are the same as in Fig. 5.1.

complete and immediate absorption of the photon energy, $f_{abs}(z)$ would be 0.5 (i.e. the case studied by Mapelli, Ferrara & Pierpaoli 2006), because half of the sterile neutrino mass-energy is taken away by the active neutrino. It is clear that the complete absorption approximation is pretty good at high redshift, especially for low mass sterile neutrinos ($m_{\nu,\,s}\,c^2 \lesssim 4$ keV), whereas at low redshift it fails by a possibly large factor. In the Appendix D, we provide analytical fits to the $f_{\rm abs}(z)$ curves shown above, for $3 \leq z \leq 1000$.

Implementing $\epsilon(z)$ in RECFAST (equations 5.4-5.6), we derive the effective influence of sterile neutrinos on the ionization fraction and IGM temperature (Fig. 5.4). The Thomson optical depth, τ_e, shown in Fig. 5.4 and in the following figures has been calculated by integrating the well known formula:

$$\tau_e = \int_{z_1}^{z_2} dz \frac{dt}{dz}\, c\, \sigma_T\; x\, n_{\rm b}(z), \tag{5.50}$$

where we take z_2=1000, i.e. the low-redshift boundary of the last scattering surface, and $z_1 = 5$, that is approximately the lowest redshift where our fits of the absorbed fraction are valid (mostly because of our underlying assumption of a largely neutral IGM).

In Fig. 5.4, the solid thin line represents the effect of 25 keV neutrinos if we assume complete absorption by the IGM ($f_{\rm abs} = 0.5$ at every z), whereas the solid thick line was calculated using the derived absorbed fraction $f_{\rm abs}$. As could be expected from Fig. 5.3, the difference between the complete and the effective absorption cases (i.e. the thin and the thick line) increases as the redshift decreases. For instance, the ionization fraction in the total absorption case (thin line) is higher by a factor ~ 4 at $z = 20$, which becomes a factor ~ 24 at $z = 5$. The IGM temperature in the case of effective absorption $\epsilon(z)$ (thick line) is reduced by a significant factor (~ 235 at $z = 5$) with respect to the total absorption case. The Thomson optical depth is quite negligible, always remaining $< 10^{-3}$.

In conclusion, accounting for the effective energy absorption significantly reduces the effect of sterile neutrino decays on reionization and heating, when compared to the case of total absorption (see MFP06).

The other two thick lines reported in Fig. 5.4 represent the effects of sterile neutrinos of 4 (dotted line) and 15 keV (dashed), using the derived absorbed fraction $f_{\rm abs}$. One can be surprised by the fact that 4 keV sterile neutrinos have a higher impact on ionization

and heating than more massive neutrinos. This result comes from two different factors.

First of all, it depends on the fact that less massive sterile neutrinos have higher $f_{\rm abs}$, especially at low redshift. As one can see from the behaviour of x_e and τ_e, at high redshift 25 keV sterile neutrinos give a stronger contribution to ionization than 4 keV sterile neutrinos. It is only at $z \lesssim 20$ that this tendency is reversed.

The second reason is not 'physical', but it depends on the state of the art of observations. In fact, we adopted for each sterile neutrino mass the shortest lifetime consistent with observations. Present-day observational constraints happen to be much stronger for a 15 keV (Watson et al. 2006) than for a 25 keV sterile neutrino (Boyarsky et al. 2006a), independently of the intrinsic properties of the decay process.

5.6 Light dark matter

We define as light dark matter (LDM) particles all the DM candidates whose mass is between 1 and 100 MeV. Such particles have recently become of interest, because they provide a viable explanation for the detected 511-keV excess from the Galactic centre (Knödlseder et al. 2005). If they are source of the 511-keV excess, then their maximum allowed mass $m_{\rm LDM}$ should be 20 MeV, not to overproduce detectable gamma rays via internal Bremsstrahlung (Beacom, Bell & Bertone 2004). If we consider also the production of gamma rays for inflight annihilations of the positrons, this upper limit might become ~ 3 MeV (Beacom & Yüksel 2006).

In principle, LDM can both decay and annihilate, producing photons, neutrinos and pairs. We will treat both LDM decays and annihilations, making the assumption that the only decay/annihilation products are pairs. This represents quite an upper limit, because neutrinos do not interact with the IGM and MeV photons have a low probability to be significantly absorbed (see Fig. 5.5, and also the discussion in Chen & Kamionkowski 2004).

As we did for sterile neutrinos, we assume that LDM particles compose the entire

DM. So the current number of LDM particles per baryon is

$$n_{\rm LDM,0} = 4.46 \times 10^3 \left(\frac{\rho_{\rm crit}}{10^{-29}{\rm g\ cm^{-3}}}\right) \left(\frac{\Omega_{\rm DM}}{0.198}\right) \left(\frac{m_{\rm LDM}\, c^2}{1\,{\rm MeV}}\right)^{-1} \left(\frac{n_{\rm b}(0)}{2.5 \times 10^{-7}\ {\rm cm^{-3}}}\right)^{-1} \quad (5.51)$$

where $m_{\rm LDM}$ is the mass of a LDM particle.

5.6.1 Decays

The LDM lifetime can be derived by assuming that LDM decays produce the detected 511-keV emission from the Galactic centre (Hooper & Wang 2004):

$$\tau_{\rm DM} \sim 4 \times 10^{26}\ {\rm s} \left(\frac{m_{\rm LDM}\, c^2}{\rm MeV}\right)^{-1}. \quad (5.52)$$

From equations (5.51) and (5.52) we can derive $\dot{n}_{\rm DM}(z)$, defined in equation (6.9).

We assume that LDM decays produce pairs. So, the parameters needed in equations (5.30) and (5.31) are $\zeta_1 = 1$ (each decay produces a single electron and a single positron) and $\zeta_2 = 1/2$ (both the electron and the positron receive approximately half of the available energy).

Having defined these values, we then found the rate of energy absorption per baryon, $\epsilon(z)$, by integrating equation (5.12). The corresponding energy absorption fraction f_{abs} is shown in Fig. 5.5, where the cases of $m_{\rm LDM}\, c^2 = 3$ and 10 MeV are shown (dashed and solid line, respectively).

In the case of pair production, the assumption of immediate and complete energy absorption corresponds to $f_{abs} = 1$ at every redshift, because both the electron and the positron energy can be absorbed. The effective value f_{abs} is always significantly less than 1.

At high redshift ($z \gtrsim 100 - 200$), the absorbed fraction is relatively high (0.3-0.7, depending on the particle mass), and it is dominated by the inverse Compton scattering onto CMB photons and by the positron annihilation.

In fact, positron annihilations contribute to $f_{\rm abs}$ only at high redshift, because both the annihilation rate (see equation 5.32) and the probability of absorption of the photons they produce (equation 5.35) scale as positive powers of the baryon density.

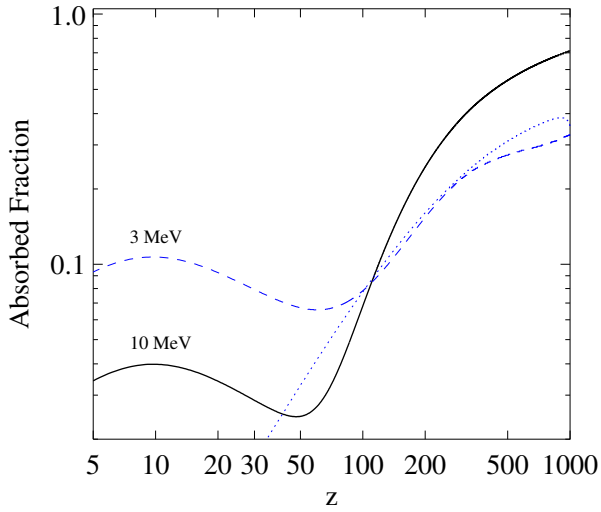

Figure 5.5: Absorbed fraction as a function of redshift for LDM particles of mass 3 (dashed line) and 10 MeV (solid line) decaying into pairs, and for LDM particles of mass 3 MeV (dotted line) decaying into photons.

Furthermore, CMB photons at high redshift are sufficiently energetic to be scattered up to the ionization threshold, because $\langle E_\gamma \rangle \sim 30\ \mathrm{eV}\,(E/5\ \mathrm{MeV})^2\,[(1+z)/1001]$ (where $\langle E_\gamma \rangle$ is the average energy of the photon after inverse Compton scattering and E is the energy of the electron/positron). At lower redshift, the starting energies of CMB photons is lower, and the energy boost due to the inverse Compton is not sufficient to turn them into ionizing photons, so the absorbed fraction drops significantly.

At low redshift ($z \lesssim 50$), the absorbed fraction f_{abs} stabilizes, because collisional ionizations become dominant. However, $f_{abs}(z < 50)$ is always ~ 0.1 for 3 MeV particles, or $\sim 0.03 - 0.04$ for 10-MeV particles. We derived a fit for the absorbed fraction, reported in the Appendix D.

For completeness, Fig. 5.5 also shows the case of LDM decays producing an active neutrino and a photon (dotted line) for 3 MeV LDM particles. In this case, at high redshift ($z \gtrsim 100$), the absorbed fraction for the LDM radiative decay is quite similar to that for the decay into a pair (especially if $m_{\rm LDM} \lesssim 3$ MeV). However, at redshifts $z \lesssim 100$ f_{abs} drops to much lower values for photons than for pairs, regardless of $m_{\rm LDM}$.

In Fig. 5.6 we show the effects of LDM decays on reionization and heating, both considering the energy absorption rate $\epsilon(z)$ (thick lines) and the upper limit of complete

absorption (thin lines, $f_{abs} = 1$). For LDM decays the difference between the two cases is even more important than for sterile neutrinos. For example, if $m_{\rm LDM}\,c^2$=10 MeV, the ionization fraction (the IGM temperature) at $z \sim 5$ is a factor ~ 25 (~ 65) higher in the case of total absorption than if we consider our estimate of f_{abs}. The Thomson optical depth is reduced by a factor ~ 7, and it is only $\tau_e \lesssim 1.8 \times 10^{-3}$ (instead of $\tau_e \lesssim 1.3 \times 10^{-2}$).

5.6.2 Annihilations

We now consider the case of LDM particles of mass $m_{\rm LDM}\,c^2$ =1, 3 and 10 MeV, assuming that they annihilate and produce electron-positron pairs. Recently Zhang et al. (2006) found that, in order to be consistent with the 1-yr WMAP results at the $1-\sigma$ level, the thermally averaged annihilation cross-section for LDM annihilations must be[4]

$$\langle \sigma v \rangle \leq 2.2 \times 10^{-29}\ {\rm cm}^3\ {\rm s}^{-1}\ f_{abs}^{-1} \left(\frac{m_{\rm LDM}\,c^2}{\rm MeV} \right), \tag{5.53}$$

The absorbed fraction f_{abs} depends on the redshift. However, as a conservative approximation, we take the value of f_{abs} in equation (5.53) to be the maximum value $f_{abs,max}$ that we derive with our method (see Fig. 5.7). In particular, $f_{abs,max} \simeq 0.5$ for 1 and 3 MeV LDM particles, and $f_{abs,max} \simeq 0.9$ for 10 MeV particles; these values (and the whole function f_{abs}) are actually almost independent from the value we adopt for $\langle \sigma v \rangle$.

We chose to use values of $\langle \sigma v \rangle$ which are close to the upper limit given by the above formula, *i.e.* 4, 12, and 24 $\times 10^{-29}$ cm^3 s^{-1} for $m_{\rm LDM}\,c^2$ = 1, 3, and 10 MeV, respectively. Such values of $\langle \sigma v \rangle$ are quite close to those ($\langle \sigma v \rangle$=0.3, 2.7 and 30 $\times 10^{-29}$ cm^3 s^{-1}, for the same masses) which have been inferred by Ascasibar et al. (2006) in order to reproduce the 511 keV excess from the Galactic centre.

From equations (5.53) and (5.51) we then derive the rate of change of the number of DM particles per baryon through equation (6.10). In this case, the parameters for the injection equations (5.30) and (5.31) are $\zeta_1 = 1/2$, $\zeta_2 = 1$, because an electron and a positron are produced for every annihilation (which obviously involves two annihilating particles).

The integration of equation (5.12) with these parameters provides us with the energy absorption rate per baryon, $\epsilon(z)$, and the corresponding absorbed fraction f_{abs}, which

[4] In eq. (5.53) the upper limit actually given by Zhang et al. 2006 was multiplied by a factor of 2 in order to account for differences between the two treatments.

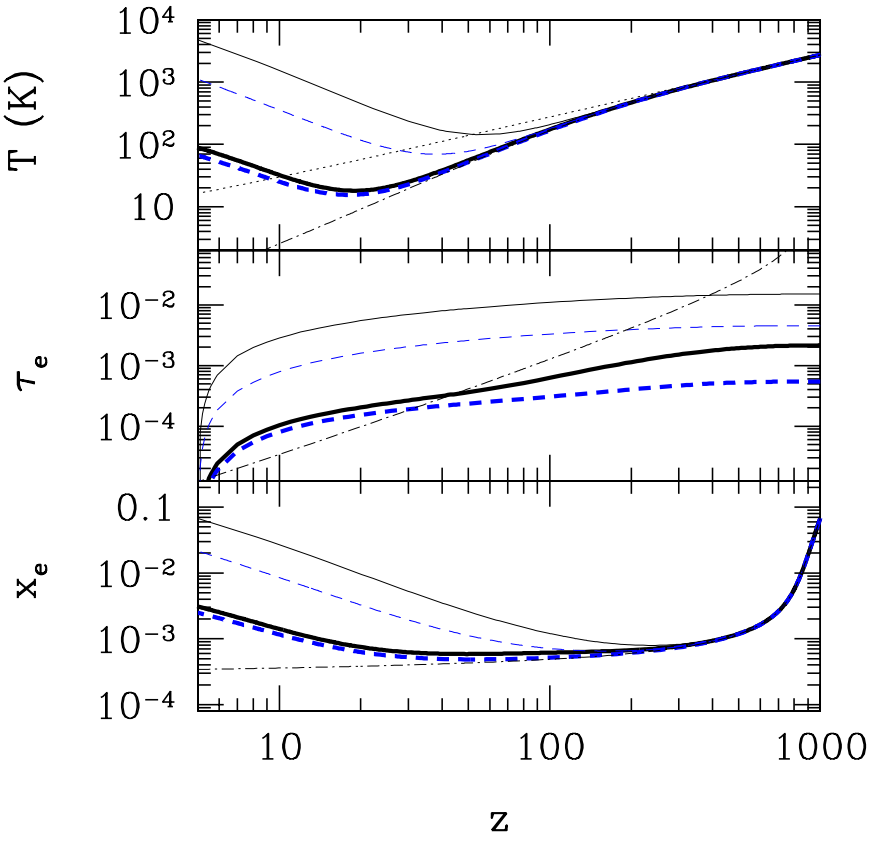

Figure 5.6: Ionized fraction (bottom panel), Thomson optical depth (central panel) and IGM temperature (upper panel) as a function of redshift due to LDM decays. The thick lines are obtained using the effective absorbed fraction (Fig. 5.5) for decaying LDM of masses 3 (thick dashed line) and 10 MeV (solid). The thin solid (dashed) line shows the contribution of decaying LDM of mass 10 (3) MeV, if we assume an absorbed fraction of 1. The thin dotted line in the top panel and the thin dot-dashed line in all the panels are the same as in Fig. 5.1.

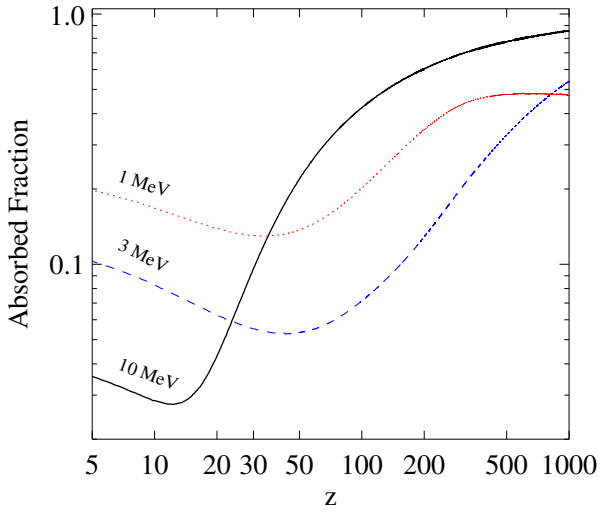

Figure 5.7: Absorbed fraction as a function of redshift for annihilating LDM of mass 1 (dotted line), 3 (dashed line) and 10 MeV (solid line).

is shown in Fig. 5.7. The behaviour of $f_{abs}(z)$ is quite similar to the case of LDM decays. At high redshift ($z \gtrsim 100$) $f_{abs}(z)$ is close to the complete and immediate absorption value ($f_{abs} = 1$) and it is dominated by inverse Compton scattering and positron annihilations. At low redshift collisional ionizations alone contribute to f_{abs}, which suffers a large drop between the two regimes.

We note that the contribution of positron annihilations to the absorbed fraction is particularly crucial for low mass LDM particles. In fact, for the case $m_{\rm LDM}\, c^2 = 1$ MeV, inverse Compton scattering is not able to produce ionizing photons, even at $z \sim 1000$. For this reason, in absence of positron annihilation, the absorbed fraction for 1 MeV LDM particles (dotted line in Fig. 5.7) would depend only on collisional ionization, and its plot would essentially be a straight line from $f_{abs}(5) \sim 0.2$ to $f_{abs}(1000) \sim 0.08$.

On the contrary, for the highest mass we consider, $m_{\rm LDM}\, c^2 = 10$ MeV, the high redshift bump is essentially due to inverse Compton energy loss.

The impact of LDM annihilations on reionization and heating (Fig. 5.8) is quite different from the case of LDM decays. In fact, LDM annihilations start to contribute both to reionization and heating already at very high redshift ($z \sim 800$); but their role remains negligible at low redshift. In particular, the ionization fraction becomes $\sim 10^{-3}$ and the

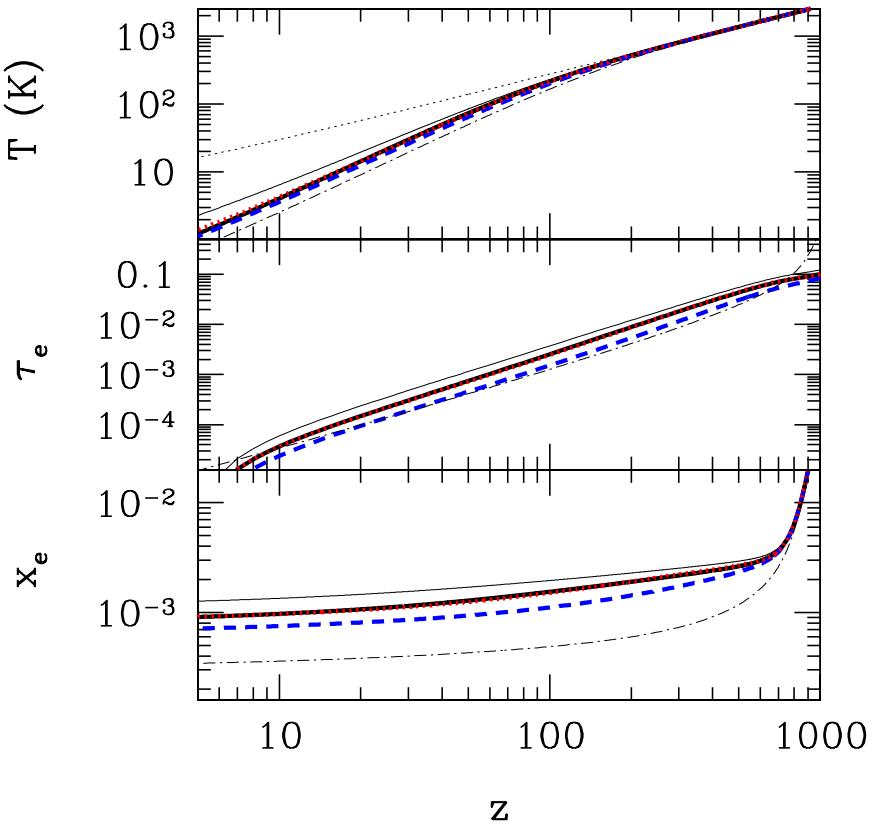

Figure 5.8: Ionized fraction (bottom panel), Thomson optical depth (central panel) and IGM temperature (upper panel) as a function of redshift due to LDM annihilations. The thick lines are obtained taking into account the effective absorbed fraction (Fig. 5.7) for annihilating LDM of masses 1 (thick dotted line), 3 (dashed) and 10 MeV (solid). The thin solid line shows the contribution of annihilating LDM of mass 10 MeV, if we assume an absorbed fraction=1. The thin dotted line in the top panel and the thin dot-dashed line in all the panels are the same as in Fig. 5.1.

IGM temperature at $z \sim 10$ is much lower than 10 K. This mainly is due to the fact that the annihilation rate depends on the square of the baryon density (see equation 6.10).

The Thomson optical depth reported in the central panel of Fig. 5.8 is quite high: $\tau_e = 0.12 - 0.15$ for all the considered LDM particles, *i.e.* close to the 1-σ upper limit ($\tau_e = 0.12$) of the 3-yr WMAP data. Nevertheless, the effects of LDM ionization can be very hardly detected by WMAP. The reason is that, differently from the relatively rapid and large variation of the electron fraction occurring in standard reionization scenarios, the x_e evolution produced by LDM annihilations tracks very closely, albeit at a slightly higher level, and for a long time the relic abundance one. This behavior dilutes the effects of these extra electrons, making their imprint on the CMB spectrum very tiny (see next Section).

5.7 Effects on the CMB spectrum

In the previous Sections we showed that decaying DM, and especially LDM and sterile neutrinos, can modify the ionization fraction, with respect to the value due to relic electrons, already at high redshift. This fact should leave some imprint on the CMB spectrum (Chen & Kamionkowski 2004; Pierpaoli 2004; Padmanabhan & Finkbeiner 2005). To check whether these effects are measurable, we simulated the expected CMB spectrum in the case we take into account DM decays. This has been done by implementing our modified version of RECFAST in the version 4.5.1 of the public code CMBFAST (U. Seljak & M. Zaldarriaga 1996; U. Seljak et al. 2003).

Fig. 5.9 (Fig. 5.10) shows the temperature - temperature (TT), polarization - polarization (EE) and temperature - polarization (TE) spectra, in the case of 10-MeV decaying (annihilating) LDM (i.e. the particle for which we achieved the maximum contribution to the reionization among the considered ones), compared with the recent WMAP 3-yr data (Spergel et al. 2006; Page et al. 2006).

The contribution due to DM decays alone is negligible. There is a sensible difference only in the lowest multipoles ($l < 10$) of the EE spectrum. This effect can be seen in the central panel of Fig. 5.9, where the thin lines show the expected EE spectra by considering (dashed line) and neglecting (solid line) DM decays, respectively. This effect,

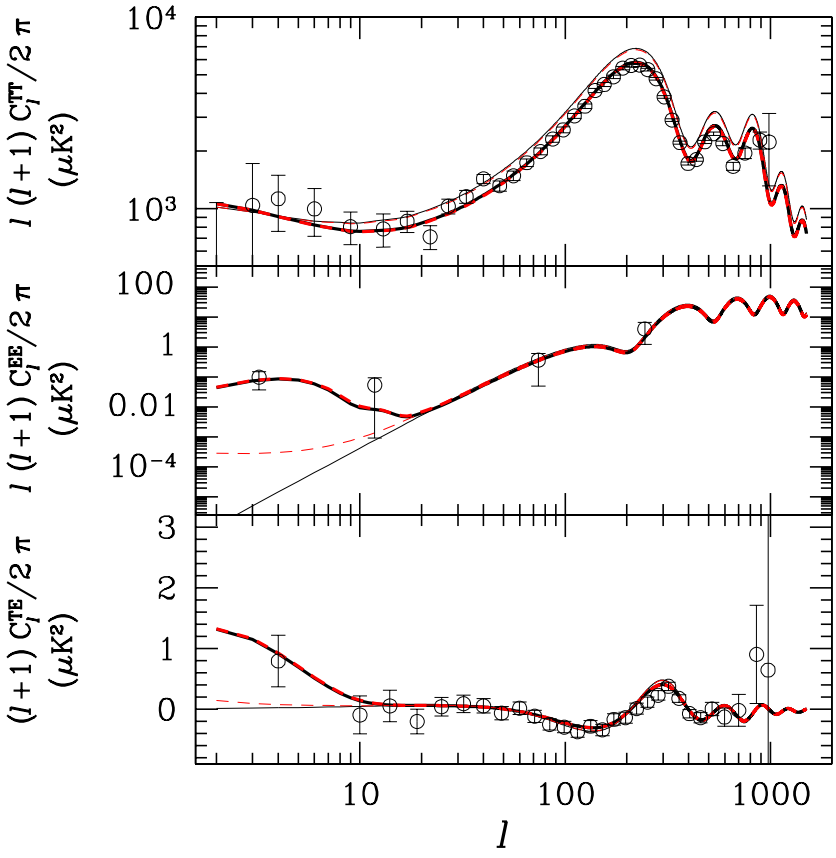

Figure 5.9: TT (top panel), EE (central panel) and TE (bottom panel) spectra. Thick lines indicate the CMB spectrum derived assuming Thomson optical depth $\tau_e = 0.09$ and a sudden reionization model (consistent with the 3-yr WMAP data); thin lines indicate the CMB spectrum derived assuming $\tau_e = 0$. Dashed (solid) lines indicate the CMB spectrum obtained (without) taking into account the decays of 10-MeV LDM particles. Open circles in all the panels indicate the 3-yr WMAP data (Hinshaw et al. 2006; Page et al. 2006; Spergel et al. 2006).

small and concentrated at low multipoles, is justified by the fact that DM decays produce a very small Thomson optical depth ($\tau_e \lesssim 0.01$) and that they are important especially at very low redshift, due to their long lifetime. Is such a modification of the EE spectrum measurable? If there are other sources of reionization besides DM decays (as it seems to be likely, considering the Thomson optical depth, $\tau_e = 0.09 \pm 0.03$, measured by WMAP; Spergel et al. 2006), the influence exerted on the EE spectrum by the decaying DM would be completely hidden by the stronger effects due to these other reionizing sources. This can be seen in Fig. 5.9, where the thick lines show the TT/EE and TE spectra assuming $\tau_e = 0.09$ in the case with (dashed line) and without (solid line) DM decays. We found that the effects of DM decays are washed out by those of other reionizing sources also for lower values of τ_e consistent with the 3-yr WMAP results (down to $\tau_e = 0.06$, corresponding to a sudden reionization at $z \sim 6$).

For the annihilations, the scenario is quite different. Even if the Thomson integrated optical depth is quite high, the effects of LDM annihilations can be very hardly detected by WMAP. The reason is that the x_e evolution produced by LDM annihilations tracks very closely, albeit at a slightly higher level, and for a long time the relic abundance one. This behavior dilutes the effects of these extra electrons, making their imprint on the CMB spectrum very tiny.

However, the Thomson optical depth produced by LDM annihilations should influence the CMB spectra at quite high multipoles, as implied by the results of Zhang et al. (2006). The main effects of LDM annihilations are a certain damping in the TT peaks, a sensible variation of the EE spectra for $l \lesssim 100$ and some negligible distortions in the TE spectra (Fig. 5.10). However, the simulated spectra agree within 1-σ with the 3-yr WMAP results. Our plot is obtained assuming that all the cosmological parameters have the best fit value indicated by the 3-yr WMAP data. Leaving the cosmological parameters free to change, it should be possible to get an even better agreement between the WMAP data and the simulated CMB spectra derived accounting for LDM annihilations (Zhang et al. 2006).

Beyond these differences, we can conclude that the influence of both decaying and annihilating LDM particles on the CMB spectra is quite negligible. Because LDM particles produce the highest ionization fraction among the considered models, the effects on the

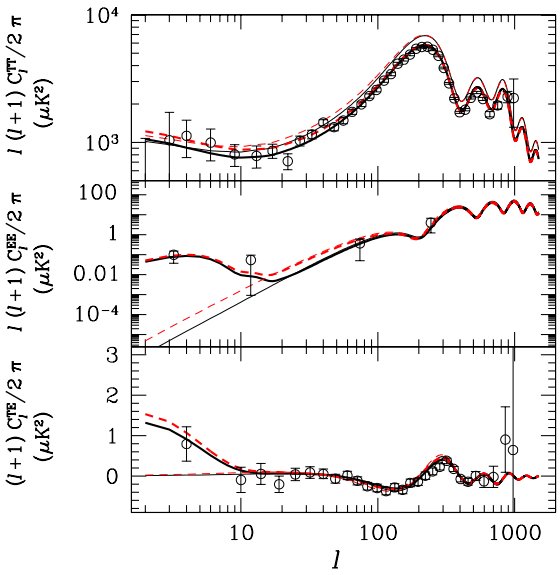

Figure 5.10: TT (top panel), EE (central panel) and TE (bottom panel) spectra. Thick and thin lines are the same as in Fig. 5.9. Dashed (solid) lines indicate the CMB spectrum obtained (without) taking into account the annihilations of 10-MeV LDM particles. Open circles are the same as in Fig. 5.9.

CMB spectra due to other species of DM particles will be far more negligible.

5.8 Conclusions

We examined the contribution to cosmic reionization and heating of different models of decaying/annihilating DM. The main result is that there is a substantial difference between heavy and light DM particles: the influence of the heaviest DM particles (> 100 MeV, i.e. gravitinos and neutralinos) on reionization and heating is completely negligible, whereas the light particles ($\lesssim 10$ MeV, i.e. sterile neutrinos and LDM) can be source of early partial reionization and can significantly increase the temperature of the IGM.

For the heaviest particles we assumed that all the energy released by decays/annihilations is absorbed by the IGM. Then, our results represent an upper limit.

Instead, for the light particles (sterile neutrinos and LDM), which decay/annihilate into photons, electron-positron pairs and neutrinos, we modelled in detail the absorption rate of the energy released in the IGM.

In the case of radiatively decaying sterile neutrinos (mass 2-50 keV), at $z > 200$ a fraction $f_{abs} \simeq 0.5$ of the particle energy is transferred to the IGM, predominantly via ionizations; at lower redshifts f_{abs} decreases rapidly to values of 0.0005-0.3 depending on the neutrino mass. LDM particles can decay or annihilate. In both cases $f_{abs} \approx 1$ at high (> 300) redshift, due to positron annihilation and inverse Compton scattering, and it drops to values around 0.1 below $z = 100$.

Our determination of f_{abs} has a dramatic impact on the results of previous studies (which adopted naive assumptions for this parameter) concerned with the IGM heating by DM.

To illustrate this point, we have re-calculated the IGM thermal and ionization history induced by either sterile neutrinos or LDM particles, using the previous findings. We find that sterile neutrino (LDM) decays are able to increase the IGM temperature by $z = 5$ at most up to 4 K (100 K). Both these values are 50-200 times lower than the estimates based on the assumption of complete energy transfer to the gas. In addition, significant departures from the adiabatic temperature evolution induced by the Hubble expansion occur only below $z \approx 30$, at an epoch at which heating and ionization by conventional sources (stars or accretion-powered objects) are likely to swamp the DM signal.

LDM annihilations instead produce a very extended ($5 < z < 800$) electron fraction plateau, at a level of 5-10 times the relic one. The main effect of these extra electrons is to extend the cosmic time interval during which the IGM kinetic temperature is coupled to the CMB one down to $z \approx 100$. Although the electron scattering optical depth in this case is large (0.08-0.10), its effects on the CMB temperature/polarization spectra are hardly appreciable.

The detailed computation of the f_{abs} presented in this Chapter and summarized by the fits given in the Appendix D, might be useful for a large number of future applications in which the cosmological role of the DM is investigated. Among these are the effects of DM decays/annihilations on the 21 cm emission (Shchekinov & Vasiliev 2006) and on the structure formation history (Shchekinov & Vasiliev 2004; Biermann & Kusenko 2006; Ripamonti, Mapelli & Ferrara 2006b).

Chapter 6

Impact of dark matter on structure formation

6.1 Introduction

One of the fundamental questions concerning the formation of first structures is the minimum halo mass (critical mass, m_{crit}) for collapse at a given redshift (Silk 1977; Rees & Ostriker 1977; White & Rees 1978; Couchman 1985; Couchman & Rees 1986; de Araujo & Opher 1988, 1991; Haiman, Thoul & Loeb 1996).

Tegmark et al. (1997; T97) thoroughly addressed such question, pointing out how m_{crit} crucially depends on the abundance of H_2, the main coolant present in the metal free Universe. Subsequent studies (Abel et al. 1998; Fuller & Couchman 2000; Galli & Palla 1998, 2002; Ripamonti 2006) refined the model of T97, accounting also for minor effects, such as the cooling induced by HD molecules.

The production of molecules and m_{crit} are sensitive to any physical process which can release energy in the intergalactic medium (IGM). In fact, the injection of energy in the IGM can either delay the collapse of first halos (because of the increased gas temperature, or of photodissociation of molecules) or favour structure formation (because of the enhancement in the abundance of free electrons, which act as catalysts for the formation of molecules).

For this reason, it is crucial to understand the influence of reionization sources on structure formation. Many studies have shown that massive metal free stars are efficient in dissociating H_2 molecules, quenching star formation in the first halos (Haiman, Rees & Loeb 1997; Ciardi, Ferrara & Abel 2000; Ciardi et al. 2000; Haiman, Abel & Rees 2000; Ricotti, Gnedin & Shull 2002; Yoshida et al. 2003). Intermediate mass black holes, produced by the collapse of first stars, are thought to efficiently re-heat the IGM, increasing m_{crit} and reducing star formation in the smaller mass halos (Ricotti & Ostriker 2004; Ricotti, Ostriker & Gnedin 2005; Zaroubi et al. 2006).

Also particle decays and annihilations can be sources of partial reionization and heating (see Mapelli, Ferrara & Pierpaoli 2006 and references therein), and could influence structure formation. For example, Shchekinov & Vasiliev (2004) investigated the possible effect on m_{crit} due to ultra-high energy cosmic rays (UHECRs) emitted by particles decaying in the early Universe. Biermann & Kusenko (2006) considered the impact on structure formation due to sterile neutrino decays. Both these studies found a substantial enhancement on the abundance of molecular coolants (H_2 and/or HD). However, they neglected the possible increase of gas temperature due to UHECRs or decays, respectively.

More recently, Stasielak, Biermann & Kusenko (2006) evaluated the effect of sterile neutrino decays accounting also for the heating of the gas. However, their single-zone model is likely to oversimplify the crucial behaviour of gas density during the halo collapse.

In this Chapter, we consider the influence of dark matter (DM) decays and annihilations on structure formation, taking into account variations induced both in the chemical and in the thermal evolution of the IGM and of the gas inside halos. Furthermore, we substitute the single-zone models, which are commonly adopted in previous papers (Haiman et al. 1996 is an important exception), with more sophisticated 1-D simulations. We focus on relatively low mass DM particles, such as sterile neutrinos and light DM (LDM), as their effect on the IGM is expected to be much more important than that of heavier ($\gtrsim 100$ MeV) DM particles (Mapelli et al. 2006).

Sterile neutrinos are expected to decay into active neutrinos and keV-photons (Dolgov 2002), while LDM can either decay or annihilate producing electron-positron pairs (Boehm et al. 2004; Hooper & Wang 2004; Picciotto & Pospelov 2005; Ascasibar et

al. 2006). keV-photons interact with the IGM both via Compton scattering and photo-ionization; instead, the electron-positron pairs undergo inverse Compton scattering, collisional ionizations, and positron annihilations (Zdziarski & Svensson 1989; Chen & Kamionkowski 2004; Ripamonti, Mapelli & Ferrara 2006, hereafter RMF06). RMF06 derived the fraction $f_{abs}(z)$ of energy emitted by sterile neutrino decays and LDM decays or annihilations which is effectively absorbed by the IGM through these processes. In this Chapter, we adopt the fits of $f_{abs}(z)$ given by RMF06.

In Section 6.2 we describe the hydro-dynamical code used to derive m_{crit} and the DM models which we adopt. In Section 6.3 we discuss the effect of DM decays and annihilations on the chemical and thermal evolution of the IGM, giving an estimate of the Jeans mass. In Section 6.4 we describe the chemical and thermal evolution of the gas inside the halos, deriving m_{crit}. In the discussion (Section 6.5) we address various points, such as the variations in the baryonic mass fraction inside the halos induced by DM decays/annihilations and the influence of the concentration of the DM profile.

We adopt the best-fit cosmological parameters after the 3-yr WMAP results (Spergel et al. 2006), i.e. $\Omega_{\rm b} = 0.042$, $\Omega_{\rm M} = 0.24$, $\Omega_{\rm DM} \equiv \Omega_{\rm M} - \Omega_{\rm b} = 0.198$, $\Omega_\Lambda = 0.76$, $h = 0.73$, $H_0 = 100\,h$ Mpc km^{-1} s^{-1}.

6.2 Method

6.2.1 The code

In order to estimate the effects of the energy injection from DM decays and annihilations, it is necessary to follow the chemical and thermal evolution of primordial gas. This can be done with single-zone models such as the one originally described in T97, or the adaptations by Shchekinov & Vasiliev (2004), and by Stasielak et al. (2006). However, this kind of models is bound to use some approximations which can be very crude. First of all, single-zone models cannot follow the density evolution of a virialized halo because of their lack of "resolution", so that it is usually assumed that after virialization the gas density in a halo is both *uniform* in space and *constant* in time. Even in the linear phase of the collapse, the top-hat model provides a reasonable description of the DM component, but

it becomes a rough approximation when the baryonic component is considered, as hydrodynamical effects are likely to become important at scales below the Jeans or the filtering length (Peebles 1993; Gnedin 2000).

An exact description would require a 3-D simulation (such as those of Abel, Bryan & Norman 2002, and of Bromm, Coppi & Larson 2002); but it is possible to capture the basic features of the collapse phenomenon by an intermediate, time-efficient approach, e.g. by means of 1-D simulation, as they are both more accurate than single-zone models, and much faster than 3-D simulations (Haiman et al. 1996).

In this Chapter, we use the 1-D Lagrangian, spherically symmetric code described by Ripamonti et al. (2002), as updated in Ripamonti (2006). Such a code includes the treatment of:

- the gravitational and hydro-dynamical evolution of the gas (by means of an artificial viscosity scheme);

- the chemical evolution of 12 species (H, H^+, H^-, H_2, H_2^+, D, D^+, HD, He, He^+, He^{++}, and e^-; see table 1 of Ripamonti 2006 for a list of the considered reactions and of the adopted reaction rates);

- the cooling (or heating) due to a number of components, such as the compressional (adiabatic) heating, the emission and absorption of line radiation from H, H_2 and HD (accounting for the effects of the cosmic microwave background, CMB), the heating (or cooling) from the Compton scattering of CMB photons off free electrons, and the heating (or cooling) due to chemical reactions (e.g. the formation or dissociation of H_2 molecules);

- the gravitational effects of DM, according to a simple model which is based on the top-hat formalism up to the turn-around redshift, smoothly evolving into a concentrated profile after virialization (see Section 6.2.2 for more details).

6.2.2 DM profiles

The code does not include a self-consistent treatment of DM. Instead, the function $\rho_{\rm DM}(r,z)$, describing the DM density profile and its redshift evolution, must be chosen *a priori*. Since our results might depend on this choice, we decided to study two quite different cases, which we call 'isothermal' and 'NFW' (from the profile described in Navarro, Frenk & White 1997) depending on the shape of the density profile after virialization.

In both cases the DM distribution was assumed to be spherically symmetric, and concentric with the simulated region, whose central part represents the halo which is being investigated. At any redshift a DM mass $M_{\rm DM} = M_{\rm halo}\Omega_{\rm DM}/\Omega_{\rm M}$ is assumed to be within the truncation radius

$$R_{\rm tr}(z) = \begin{cases} \left(\frac{3}{4\pi}\frac{M_{\rm DM}}{\rho_{\rm TH}(z)}\right)^{1/3} & \text{if } z \geq z_{\rm ta} \\ R_{\rm vir}\left[2 - \frac{t(z)}{t(z_{\rm vir})-t(z_{\rm ta})}\right] & \text{if } z_{\rm ta} > z \geq z_{\rm vir} \\ R_{\rm vir} & \text{if } z < z_{\rm vir} \end{cases} \tag{6.1}$$

where $t(z)$ is the time corresponding to redshift z, and $z_{\rm vir}$, $z_{\rm ta}$, $R_{\rm vir}$ and $\rho_{\rm TH}(z)$ are the halo virialization and turn-around redshifts, its virial radius, and the DM density inside the halo at $z > z_{\rm ta}$ (as derived from the evolution of a simple *top-hat* fluctuation; see e.g. Padmanabhan 1993, or T97), respectively. The exact definition of these quantities can be found in Ripamonti 2006.

The isothermal and NFW assumptions differ only after the halo virialization ($z < z_{\rm vir}$); both of them refer to a static DM profile. In the isothermal case

$$\rho_{\rm DM}(r,z) = \begin{cases} \rho_{\rm core} & \text{if } r \leq R_{\rm core}; \\ \rho_{\rm core}(r/R_{\rm core})^{-2} & \text{if } R_{\rm core} \leq r \leq R_{\rm tr}; \\ \rho_0\Omega_{\rm DM}(1+z)^3 & \text{if } r > R_{\rm tr}; \end{cases} \tag{6.2}$$

instead, in the NFW case the DM density profile is chosen to be

$$\rho_{\rm DM}(r,z) = \begin{cases} \frac{\rho_{\rm NFW}}{(r/R_{\rm core})(1+r/R_{\rm core})^2} & \text{if } r \leq R_{\rm tr}; \\ \rho_0\Omega_{\rm DM}(1+z)^3 & \text{if } r > R_{\rm tr}; \end{cases} \tag{6.3}$$

where $\rho_0 \simeq 1.88 \times 10^{-29}\, h^2$ g cm^{-3} is the critical density of the Universe at present. In both cases $R_{\rm core} = \xi R_{\rm vir}$, where $\xi = 0.1$ is a parameter (cfr. Hernquist 1993, and Burkert

1995 for the choice of its value; in the NFW case ξ the inverse of the more commonly uses concentration parameter), and the densities $\rho_{\rm core}$ and $\rho_{\rm NFW}$ can be found by requiring the DM mass within $R_{\rm tr}$ to be equal to $M_{\rm DM}$.

At $z > z_{\rm vir}$ both the isothermal and NFW case assume the DM density profile described by equation 6.2. However, at such redhift the profile is not static, because the core radius is evolved with redshift

$$R_{\rm core}(z) = \begin{cases} R_{\rm tr}(z) & \text{if } z \geq z_{\rm ta} \\ R_{\rm vir}\left[2 - \frac{(2-\xi)\,t(z)}{t(z_{\rm vir})-t(z_{\rm ta})}\right] & \text{if } z_{\rm ta} > z \geq z_{\rm vir} \end{cases} \tag{6.4}$$

Such a choice combines the behaviour of a *top-hat* fluctuation (the density inside R_{tr} is assumed to be uniform until the turn-around) with a transition to the final density profiles.

We only considered the case $\xi = 0.1$ (i.e. concentration 10 for the NFW profile), instead of varying ξ, because the differences between the isothermal and NFW cases are quite relevant even with the same value of ξ. In fact, the NFW case is representative of concentrated halos, whereas the isothermal case is representative of relatively shallow potentials.

However, it is important to note that the flat central profile of the isothermal case helps to ensure that the behaviour we observe near the centre is due to the self-gravity and hydrodynamics of the *simulated* gas, rather than to the *assumed* DM profile.

6.2.3 Treatment of the DM energy injection

The above code was modified in order to include the effects of the energy injection from DM decays/annihilations on both the chemical and thermal evolution of the gas.

The gas can be heated, excited and ionized by the energy input due to DM decays/annihilations. It is important to note that the fraction of the absorbed energy going into each one of these components is quite unrelated to how the energy was deposited in the IGM at the first step. For example, if a keV a photon ionizes an atom, the resulting electron will generate a cascade of collisions, and the energy of the photon will go not only into ionizations, but also into excitations and heating.

Thus, given the energy injection per baryon from DM decays and annihilations,

$\epsilon(z)$ (described in Section 6.2.4), we split it into an heating and ionization component[1]

$$\epsilon_{heat}(z) = \tilde{C}[1-(1-x(z))^{\tilde{a}}]^{\tilde{b}}\epsilon(z) \quad (6.5)$$

$$\epsilon_{ion}(z) = \frac{1-x(z)}{3}\epsilon(z), \quad (6.6)$$

where $x(z)$ is the ionization fraction. In the first equation we are using the fit to the results of Shull & Van Steenberg (1985) which is provided in their paper (with $\tilde{C} = 0.9971$, $\tilde{a} = 0.2663$, and $\tilde{b} = 1.3163$), while in the second equation we are using the fit to the same results given by Chen & Kamionkowski (2004).

The heating component is simply added to the equations describing the thermal state of the gas. Instead, the ionization component is further split between H, He, He^+, D, H_2, HD and H_2^+, according to their number abundance:

$$\epsilon_i(z) = \frac{\tilde{N}_i}{\sum_{j\in(H,He,He^+,D,H_2,HD,H_2^+)}\tilde{N}_j}\epsilon_{ion}(z) \quad (6.7)$$

where the indices i and j indicate chemical species, and $\tilde{N}_i \equiv N_i$ if the species i is atomic, or as $\tilde{N}_i \equiv 2N_i$ if the species i is molecular; N_i is the number density (per unit volume) of the chemical species i. In principle, the terms in the sum above should be weighted by the cross-section for each species. However both the cross-section and the energy spectrum are too complex to be implemented in our simple calculations. In particular, the energy spectrum is expected to be the result of a cascade (Shull & Van Steenberg 1985). The error in neglecting these factors is quite small, as m_{crit} is more sensitive to the temperature increase than to the chemistry (see Section 6.4).

The quantity ϵ_i approximates the energy which is absorbed by chemical reactions dissociating the species i, and is translated into a reaction rate (number of reactions per particle per unit time) through a division by the energy threshold $E_{th,i}$ of the considered reaction. The list of the reactions and of the energy thresholds is given in Table 1.

We neglect the absorption of ionization energy by H^+, He^{++}, D^+ and e^-, because these species cannot be ionized further. We also neglect the ionization energy absorption

[1]The sum of these two components is less than $\epsilon(z)$, as a significant fraction of the injected energy goes in atomic/molecular excitations and does not affect the chemical or thermal state of the gas.

Table 6.1: List of chemical reactions stimulated by the DM energy injection.

Species	Reaction	Threshold
H	$H \rightarrow H^+ + e^-$	13.6 eV
He	$He \rightarrow He^+ + e^-$	24.6 eV
He^+	$He^+ \rightarrow He^{++} + e^-$	54.4 eV
D	$D \rightarrow D^+ + e^-$	13.6 eV
H_2	$H_2 \rightarrow H + H$	4.48 eV
HD	$HD \rightarrow H + D$	4.51 eV
H_2^+	$H_2^+ \rightarrow H + H^+$	2.65 eV

by H^- because the energy threshold for the transformation of H^- into H is negative, and cannot be treated with our simple formalism. However the number abundance of H^- is always very small, and the number of dissociations induced by DM decays/annihilations is likely to be negligible.

6.2.4 DM models

We apply this formalism to two different DM candidates, i.e. sterile neutrinos and LDM. Sterile neutrinos are one of the most popular warm DM (WDM) candidates (Colombi, Dodelson & Widrow 1996; Sommer-Larsen & Dolgov 2001; Bode, Ostriker & Turok 2001). They can decay via different channels (Dolgov 2002; Hansen & Haiman 2004). In this Chapter we are interested in the radiative decay, i.e. the decay of a sterile neutrino into a photon and an active neutrino, because of its direct impact on the IGM (Mapelli & Ferrara 2005; Mapelli et al. 2006). The photon produced in the decay interacts with the IGM both via Compton scattering and photo-ionization (RMF06).

LDM particles have recently become of interest, because they provide a viable explanation for the detected 511-keV excess from the Galactic centre (Boehm et al. 2004; Knödlseder et al. 2005). If they are source of the 511-keV excess, then their maximum allowed mass $m_{\rm LDM}$ should be 20 MeV, not to overproduce detectable gamma rays via internal Bremsstrahlung (Beacom, Bell & Bertone 2004). If we consider also the production of gamma rays for inflight annihilation of the positrons, this upper limit might become ~ 3 MeV (Beacom & Yüksel 2006).

LDM can either decay or annihilate, producing photons, neutrinos and pairs. In

this Chapter we consider both LDM decays and annihilations, but we restrict their treatment to the case where the product particles are $e^+ - e^-$ pairs. In fact, in the case of pair production the impact of LDM on the IGM is maximum (RMF06). The $e^+ - e^-$ pairs are expected to interact with the IGM via inverse Compton scattering, collisional ionization and positron annihilation (RMF06).

Table 6.2: List of the main characteristics of the considered DM models. In particular, from the leftmost to the rightmost column: DM model, $n_{\rm DM,0}$, $\tau_{\rm DM}$ (if decaying particle), $\langle\sigma\, v\rangle$ (if annihilating), comoving free-streaming lengths ($\lambda_{\rm FS,n}$ and $\lambda_{\rm FS,i}$) and the associated mass scale. $\lambda_{\rm FS}$ is taken to be the maximum between $\lambda_{\rm FS,n}$ and $\lambda_{\rm FS,i}$.

DM model	$n_{\rm DM,0}/10^3$	$\tau_{\rm DM}/(10^{27}$ s)	$\langle\sigma\, v\rangle/(10^{-29}$ cm^3 s$^{-1})$	$\lambda_{\rm FS,n}$(pc)	$\lambda_{\rm FS,i}$(pc)	$M_{\rm FS}(M_\odot)$
ν 4 keV (decaying)	1176	2.96	–	3×10^5	<60	5×10^8
ν 15 keV (decaying)	314	1.98	–	8×10^4	<35	1×10^7
ν 25 keV (decaying)	188	0.097	–	4.8×10^4	<25	2×10^6
LDM 3 MeV (decaying)	1.49	1.2	–	2.2	<0.1	2×10^{-7}
LDM 10 MeV (decaying)	0.446	4.0	–	0.5	<0.1	3×10^{-8}
LDM 1 MeV (annihilating)	4.46	–	4	9.5	300	0.5
LDM 3 MeV (annihilating)	1.49	–	12	2.2	300	0.5
LDM 10 MeV (annihilating)	0.446	–	24	0.5	300	0.5

The energy input from the "background"

We first consider the energy injected in the general IGM after cosmic DM decays/annihilations.

Both in the case of sterile neutrinos and of LDM, the rate of energy transfer (per baryon) to the IGM because of this "background" contribution can be written as:

$$\epsilon_{bkg}(z) = f_{abs}(z)\,\dot{n}_{\rm DM}(z)\,m_{\rm DM}\,c^2, \tag{6.8}$$

where $m_{\rm DM}$ is the mass of a DM particle and c is the speed of light. The energy absorbed fraction, $f_{abs}(z)$, has been derived in RMF06; $\dot{n}_{\rm DM}(z)$ is the decrease rate of the number of DM particles per baryon.

In the case of DM decays, $\dot{n}_{\rm DM}(z)$ is given by

$$\dot{n}_{\rm DM}(z) \simeq \frac{n_{\rm DM,0}}{\tau_{\rm DM}}, \tag{6.9}$$

where $n_{\rm DM,0}$ and $\tau_{\rm DM}$ are the current number of DM particles per baryon and the lifetime of DM particles, respectively. $\tau_{\rm DM}$ is assumed to be much longer than the present value of the Hubble time, as is the case for all the models we are considering.

For the annihilations:

$$\dot{n}_{\rm DM}(z) \simeq \frac{1}{2}\,n^2_{\rm DM,0}\,N_{\rm b}(0)\,\langle\sigma\,v\rangle(1+z)^3, \tag{6.10}$$

where $N_b(0) = 2.5\times10^{-7}$ g cm^{-3} is the current baryon number density (Spergel et al. 2006), and $\langle\sigma v\rangle$ is the thermally averaged DM annihilation cross-section.

Both for sterile neutrinos and LDM, the values of $n_{\rm DM,0}$, $\tau_{\rm DM}$ and $\langle\sigma v\rangle$ adopted in this Chapter are the same reported in RMF06; for convenience, they are listed in Table 2.

The "local" energy input

In addition to the background energy injection discussed above, the baryons inside a halo absorb extra energy from the additional decays/annihilations of overdense halo DM. In the case of decays the total excess energy "produced" inside the halo is

$$\begin{aligned} E_{loc}(z) &= \frac{4\pi\,N_b(0)(1+z)^3\,m_{\rm DM}\,c^2}{\tau_{\rm DM}} \\ &\times \int_0^{R_{tr}(z)} dr\,r^2[n_{\rm DM}(r,z) - n_{\rm DM,0}], \end{aligned} \tag{6.11}$$

and in the case of annihilations

$$\begin{aligned} E_{loc}(z) &= 4\pi\,[N_b(0)(1+z)^3]^2\, m_{\rm DM}\, c^2\, \langle\sigma v\rangle \\ &\times \int_0^{R_{tr}(z)} dr\, \frac{1}{2}\, r^2\, [n^2_{\rm DM}(r,z) - n^2_{\rm DM,0}(z)], \end{aligned} \tag{6.12}$$

where $n_{\rm DM}(r,z) = \rho_{\rm DM}(r,z)/[m_{\rm DM} N_b(0)(1+z)^3]$ is the number of DM particles per baryon at redshift z and at a distance r from the centre of the halo.

Then, we compute the baryon column density Σ_b from the halo centre to the truncation radius, and find the fraction of the energy E_{loc} which is absorbed by such a column density, f_{loc}. If the DM produces photons of energy E_γ,

$$f_{loc} = \Sigma_b \left[\sigma_{He+H}(E_\gamma) + \sigma_T \frac{E_\gamma}{m_e c^2} g\left(\frac{E_\gamma}{m_e c^2}\right)\right] \tag{6.13}$$

where $\sigma_{He+H}(E)$ is the photo-ionization cross-section (see Zdziarski & Svensson 1989; RMF06), σ_T is the Thomson cross section, and the function g is defined in equation 4.9 of Zdziarski & Svensson (1989). Instead, if the DM produces electron-positron pairs with Lorentz factor γ (and energy E=$\gamma\, m_e\, c^2$),

$$f_{loc} = \frac{\Sigma_b}{c\, N_b(0)(1+z)^3}\, \phi_{e,ion}(z,E) + \frac{R_{tr}(z)}{c} \phi_{e,com}(z,E) \tag{6.14}$$

where $\phi_{e,ion}(z,E)$ and $\phi_{e,com}(z,E)$ give the fraction of the energy of an electron/positron which is absorbed per unit time by the IGM, because of collisional ionizations and of Compton scattering of CMB photons, respectively. Such functions are given by equations 14-15, and 16-18 of RMF06.

We then assume that all the baryons inside the halo absorb the same amount of energy from this local contribution. So, the "local" energy deposition in each baryon within the truncation radius $R_{tr}(z)$ is

$$\epsilon_{loc}(z,r) = E_{loc} f_{loc} \frac{M_{gas}[R_{\rm tr}(z)]}{m_H} \tag{6.15}$$

where $M_{gas}(R_{\rm tr})$ is the mass of the gas inside the truncation radius, and m_H is the mass of an H atom. Instead, for baryons at a distance larger than $R_{tr}(z)$ from the centre of the halo we assume $\epsilon_{loc}(z,r) = 0$.

The total energy input per baryon from DM decays/annihilations is then

$$\epsilon(r,z) = \epsilon_{bkg}(z) + \epsilon_{loc}(r,z). \tag{6.16}$$

6.2.5 The free-streaming/damping lengths

We need to take into account that small DM fluctuations might be washed out by damping mechanisms, and in particular by free-streaming (see *e.g.* Padmanabhan 1993; Sommer-Larsen & Dolgov 2001; Boehm et al. 2005).

The free-streaming scale depends on the considered particle, and on the strength of its interactions. If such interactions are negligible, the comoving free-streaming length is

$$\lambda_{\rm FS,n} \simeq \begin{cases} 0.3 \left(\frac{m_{\rm DM}c^2}{4\,{\rm keV}}\right)^{-1} \left(\frac{\langle p\,c/(k_B\,T)\rangle}{3.15}\right) {\rm Mpc} & \text{for neutrinos} \\ 0.20\,(\Omega_{\rm DM}h^2)^{1/3} \left(\frac{m_{\rm DM}c^2}{1\,{\rm keV}}\right)^{-4/3} {\rm Mpc} & \text{for LDM,} \end{cases} \tag{6.17}$$

where $m_{\rm DM}$ is the mass of the considered DM particle, p and T are the modulus of the proper momentum and the temperature of the particle, respectively. The above expressions are derived from Abazajian et al. (2001a), and from Boehm et al. (2005), respectively.

However, if the DM particle interacts at a non negligible rate, the comoving free-streaming length is (Boehm et al. 2005)

$$\lambda_{\rm FS,i} = 0.3 \left(\frac{m_{\rm DM}c^2}{1\,{\rm MeV}}\right)^{-1/2} \left(\frac{\tilde{\Gamma}_{\rm dec,DM}}{6\times10^{-24}\,{\rm s}^{-1}}\right)^{1/2} {\rm Mpc} \tag{6.18}$$

with

$$\tilde{\Gamma}_{\rm dec,DM} = \Gamma_{\rm DM}(z_{\rm dec})(1+z_{\rm dec})^{-3}, \tag{6.19}$$

where $\Gamma_{\rm DM}(z_{\rm dec})$ is the DM interaction rate at its decoupling redshift $z_{\rm dec}$.

In the case of decaying particles, we assume that this rate is simply the inverse of the present lifetimes of DM particles; so, $\Gamma_{\rm DM}(z_{\rm dec}) < 10^{-24}\,{\rm s}^{-1}$ in all the cases we are considering (cfr. Table 2). Since $z_{\rm dec} \gg 10^3$, equations (6.17) and (6.18) imply that $\lambda_{\rm FS,i} \ll \lambda_{\rm FS,n}$; so, for decaying particles we will use a free-streaming scale $\lambda_{\rm FS} = \lambda_{\rm FS,n}$.

Instead, when annihilating particles are considered, the interaction rate is $\Gamma_{\rm DM}(z_{\rm dec}) = \frac{1}{2} n_{\rm DM,0} N_{\rm b}(0) \langle\sigma v\rangle_{\rm dec} (1+z_{\rm dec})^3$, where $\langle\sigma v\rangle_{\rm dec} \sim 10^{-26} (m_{\rm DM}\,c^2/{\rm MeV})^{-1}\ {\rm cm}^3\,{\rm s}^{-1}$ (see, for example, Ascasibar et al. 2006) is the thermally averaged annihilation cross-section at the epoch of decoupling. Then, in the case of annihilating particles, $\lambda_{\rm FS,i} \gg \lambda_{\rm FS,n}$, and we must assume $\lambda_{\rm FS} = \lambda_{\rm FS,i}$. In Table 2 we give the detailed list of the free-streaming lengths for

each DM model. The same table also lists the free-streaming mass scale

$$M_{\rm FS} = \frac{4\pi}{3}\left(\frac{\lambda_{\rm FS}}{2}\right)^3 \rho_0 \Omega_{\rm M} h^2. \tag{6.20}$$

Damping erases fluctuations on scales smaller than $\lambda_{\rm FS}$. Thus, objects of mass $\lesssim M_{\rm FS}$ are unlikely to form, unless the small scale power spectrum is regenerated by non-linear effects at low redshift (see Boehm et al. 2005; however, this regeneration appears to take plate at $z \sim 2$, which is much later than the epoch we are considering). To introduce corrections for this effect in our models is beyond the purposes of this Chapter.

Damping might also affect the density profile of halos, erasing cusps on scales $\lesssim \lambda_{\rm FS}$. The values of $\lambda_{\rm FS}$ and $M_{\rm FS}$ listed in Table 2 show that this effect of damping can be important only for sterile neutrinos. In the case of isothermal density profiles, we account for it adopting the following correction. If the core radius $R_{\rm core}(z)$ (equation 6.4) is smaller than $\lambda_{\rm FS}/2$, we increase its value to $R_{\rm core,new}(z) = min(R_{\rm tr}(z), \lambda_{\rm FS}/2$. Instead, in the case of simulations with NFW density profile we do not introduce this correction, because these simulations are intended to explore the effects of high concentration (see Section 6.4.2).

6.2.6 The simulations

Our code was used to run a large number of simulations, in order to explore a wide range of the $z_{vir} - M_{halo}$ parameter space: we considered halo masses in the range $10^4 - 10^7\, M_\odot$, and virialization redshifts between 10 and 100.

We actually simulate a mass which is 1000 times higher than that of the collapsing halo, in order to include in the simulation a mass which is larger than the cosmological filtering mass (Gnedin 2000); otherwise, our treatment of hydrodynamics might be incorrect. The simulated object is divided in 150 shells, whose spacing was chosen so that (i) the mass of the shells smoothly increases when moving outwards, (ii) the central shell always encloses a gas mass of $\sim 0.3\, M_\odot$, and (iii) the central 100 shells initially enclose a mass $\sim M_{halo}$ (including the DM).

The simulations are started at $z = 1000$, when we assume that the gas density is uniformly equal to the cosmological value (whereas the DM density profile is not perfectly uniform; see Section 6.2.2), the gas temperature is equal to the CMB temperature ($\simeq$

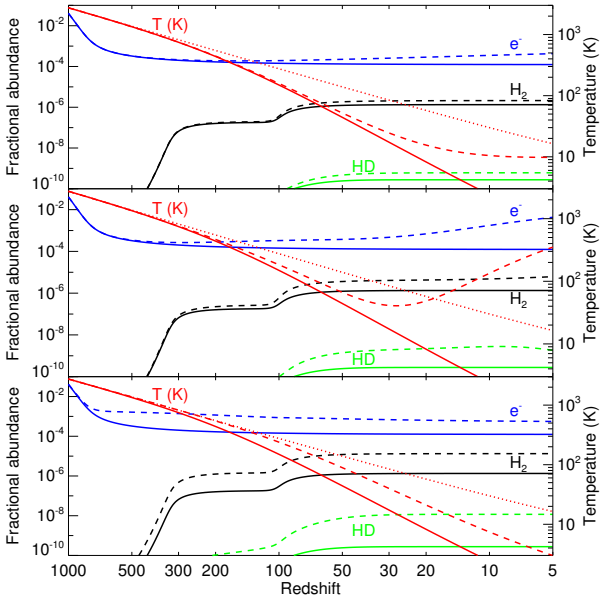

Figure 6.1: Effects of decaying/annihilating DM on the IGM evolution. Left axis: fractional abundances of free electrons (e^-), H_2 and HD as a function of the redshift. Right axis: matter temperature as a function of the redshift. Top panel: Effect of decaying sterile neutrinos of mass 25 keV (dashed line). Central panel: decaying LDM of mass 10 MeV (dashed line). Bottom panel: annihilating LDM of mass 1 MeV (dashed line). In all the panels the dotted line is the CMB temperature and the solid line represents the thermal and chemical evolution without DM decays/annihilations.

2.728 K), and adopt the chemical abundances listed in table 2 of Ripamonti 2006[2].

They are stopped either when the gas density reaches the threshold $\rho/m_H = 10^5\,\mathrm{cm}^{-3}$, or after a time $2t(z_{vir})$ has elapsed.

Each set of simulations was repeated for each different DM decay/annihilation model, and also for the "standard" case without any energy injection from DM, which is used as a reference against which we compare our results.

6.3 IGM evolution

In order to look at the influence of DM decays and annihilations upon the IGM, we have used a simplified version of our code (where the density was assumed to evolve as

[2]The most important abundances listed there are the H ionization fraction (at $z = 1000$) $N_{H^+}/N_H = 0.0672$, the helium abundance $N_{He}/N_H = 0.0833$, and the deuterium abundance $N_D/N_H = 2.5 \times 10^{-5}$.

the cosmological value).

6.3.1 Chemistry and temperature

Our code follows the chemical evolution of 12 chemical species (see previous Section). Two of them, molecular hydrogen (H_2) and HD are particularly important for our purposes, because they are the main coolant of the metal free gas. In Fig. 6.1 we show the fractional abundances of both H_2 and HD together with the ionized fraction and the matter temperature as a function of redshift for the considered DM models.

In all the DM models, both the matter temperature and the abundance of H_2, HD and free electrons are enhanced by DM decays/annihilations. This effect is smaller for sterile neutrinos than for LDM particles. The main difference between decays and annihilations is represented by the redshift range in which the influence of DM is important. For all the considered quantities (i.e. temperature and abundance of e^-, H_2 and HD) the energy injection from DM decays starts to be significant at redshift lower than ~ 100. Instead, the influence of annihilations is important already at redshift ~ 900. The annihilations represent also the case where the abundance of the two coolants is most enhanced (a factor ~ 17 for the H_2 and ~ 90 for the HD). Furthermore, the annihilations keep the matter temperature close to the CMB temperature everywhere, up to $z \sim 50 - 100$. This fact can have important consequences for experiments searching for high redshift HI 21-cm line signals (Shchekinov & Vasiliev 2006).

6.3.2 Jeans mass

In order to establish the influence of DM decays or annihilations on the structure formation, the key point is the following. DM decays and annihilations increase both the matter temperature and the abundance of coolants. The former effect tends to delay the formation of structures, while the latter favours an early collapse of the halos. Which of these two opposite effects is dominant? When looking at the average properties of the IGM, the most popular diagnostic is the cosmological Jeans mass, m_J (Peebles 1993):

$$m_J(T, \rho, \mu) = \frac{\pi}{6} \left(\frac{\pi k_B T}{G \mu m_H} \right)^{3/2} \rho^{-1/2}$$

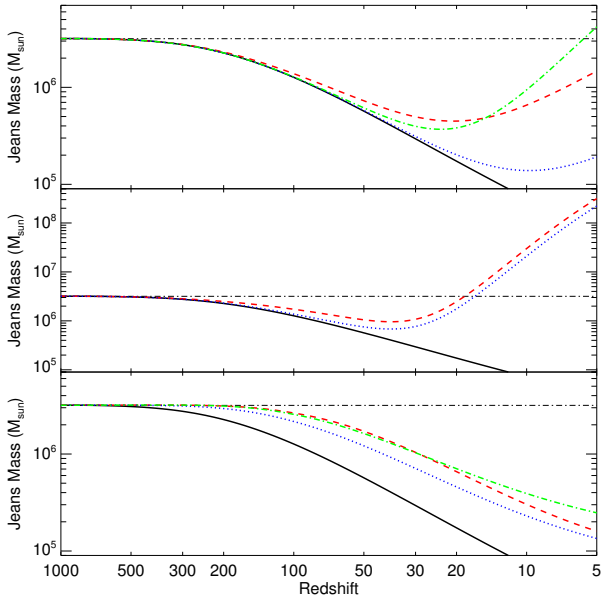

Figure 6.2: Jeans mass as a function of redshift. Top panel: Effect of decaying sterile neutrinos of mass 25 (dashed line), 15 (dotted) and 4 keV (dot-dashed). Central panel: Decaying LDM of mass 10 (dashed line) and 3 MeV (dotted). Bottom panel: Annihilating LDM of mass 10 (dashed line), 3 (dotted) and 1 MeV (dot-dashed). In all the panels the solid line represents the thermal and chemical evolution without DM decays/annihilations. The horizontal dot-dashed line shows the behaviour of the Jeans mass calculated by assuming that the gas temperature is always equal to the CMB temperature.

$$\simeq \quad 50\, M_{\odot} T^{3/2} \mu^{-3/2} \left(\frac{\rho}{m_H} \right)^{-1/2} , \tag{6.21}$$

where k_B is the Boltzmann constant, G the gravitational constant and μ the mean molecular weight.

In Fig. 6.2 we show the evolution of m_J. For all the considered DM models m_J is considerably increased by the effect of decays and annihilations. This means that, when the IGM is considered, the increase of the matter temperature dominates over the enhancement of the coolant abundance. For example, at $z = 10$ $m_J = 3.0 \times 10^7 M_{\odot}$ in the case of 10-MeV LDM decays, a factor ~ 420 higher than in the unperturbed case (for which $m_J = 7.2 \times 10^4\, M_{\odot}$). The increase of m_J is less pronounced, but nevertheless significant in the case of sterile neutrino decays ($m_J = 6.6 \times 10^5\, M_{\odot}$ for 25-keV sterile neutrinos) and LDM annihilations ($m_J = 3.9 \times 10^5\, M_{\odot}$ for 1-MeV LDM).

From this fact one could naively infer that DM decays and annihilations strongly

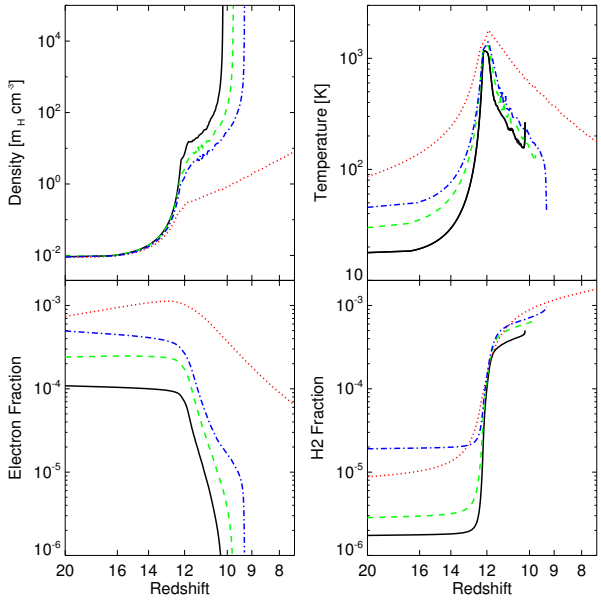

Figure 6.3: Evolution of the central region of a $6 \times 10^5\, M_\odot$ isothermal halo virializing at $z_{vir} = 12$. From left to right and from top to bottom: density, temperature, electron abundance and H_2 abundance as function of redshift. The solid line represents the unperturbed case (i.e. without DM decays and annihilations). The dashed, dot-dashed and dotted lines account for the contribution of 25-keV sterile neutrino decays, 1-MeV LDM annihilations and 10-MeV LDM decays, respectively.

delay the formation of the first structures. However, m_J refers only to the global properties of the IGM, and does not account for the non-linear evolution of collapsing halos.

6.4 Evolution inside halos

6.4.1 Chemistry and temperature

To assess the star forming ability of the first halos, it is necessary to follow their hydro-dynamical and chemical evolution. This has been done by using the code described in Section 6.2. Fig. 6.3 (Fig. 6.4) shows, as an example, the evolution of the most relevant properties of the gas at the centre of a $6 \times 10^5\, M_\odot$ ($2 \times 10^6\, M_\odot$) halo, virializing at $z_{vir} = 12$. In these figures the effects of different DM decay/annihilation scenarios are compared with the unperturbed case. For the smaller halo (Fig. 6.3) LDM annihilations and sterile neutrino decays delay the collapse by ~ 1 redshift units, and in the case of LDM decays this effect

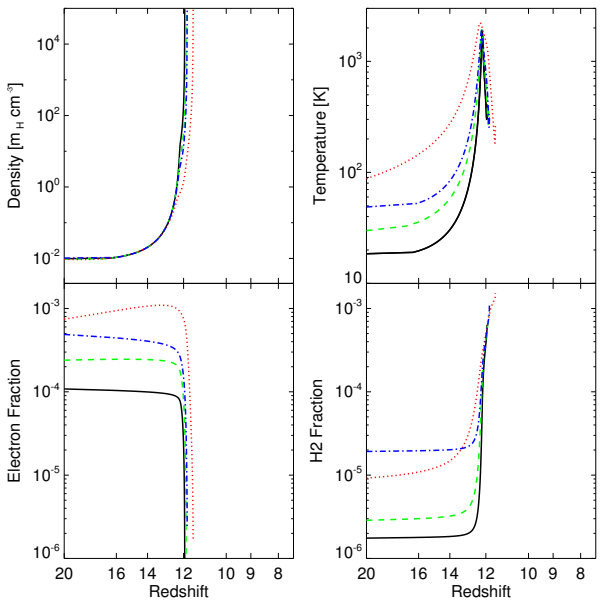

Figure 6.4: Evolution of the central region of a $2 \times 10^6\, M_\odot$ isothermal halo virializing at $z_{vir} = 12$. From left to right and from top to bottom: density, temperature, electron abundance and H_2 abundance as function of redshift. The dashed, dot-dashed and dotted lines are the same as in Fig. 6.3.

is even more significant: in presence of 10 MeV-LDM decays the halo has not collapsed yet after one Hubble time from virialization. Instead, for the larger halo (Fig. 6.4) the difference between the case with and without DM decays/annihilations is negligible.

It is worth to discuss in detail the gas temperature (T) and number density ($N = \rho/m_H$) evolution shown in Fig. 6.3. At the epoch of turn-around ($z \sim 19-20$) all the models have the same N; but in the unperturbed one T is 1.5-5 times lower than in the others. This is important, because the fast increase in T and N due to the virialization process is essentially adiabatic, as it happens on a time-scale much faster than that for cooling. In the adiabatic approximation, $\Gamma_{ad} = -P\, dV \propto P\, [N^{-1} - (N + \Delta N)^{-1}]$ (where P is the gas pressure), is proportional to the initial T for any given increase in N. T and P increase faster in models "pre-heated" by DM decays/annihilations, so that the pressure gradient slowing and halting the collapse develops earlier. In fact, the phase of unimpeded collapse stops at $N \sim 10$ cm^{-3} for the unperturbed case, but only at $N \sim 0.3-3$ cm^{-3} for the other models. At these densities the cooling per unit mass is proportional both to the H_2 fraction

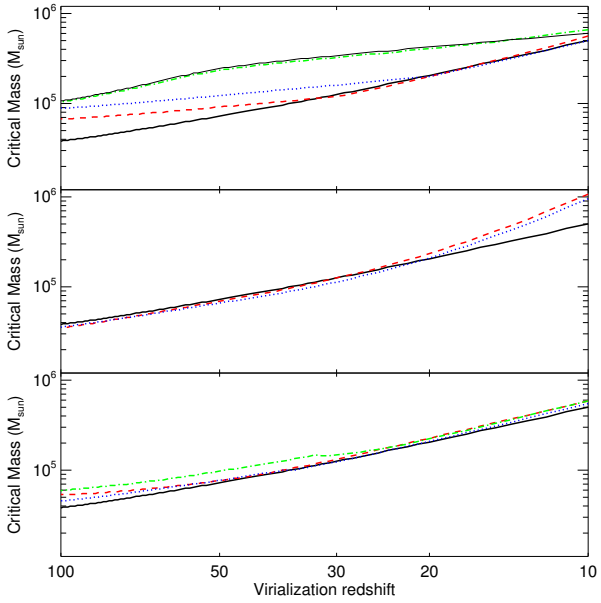

Figure 6.5: The critical mass as a function of the virialization redshift z_{vir} for isothermal halos. Top panel: Effect of decaying sterile neutrinos. Central: Decaying LDM. Bottom: Annihilating LDM. The lines used in the three panels are the same as in Fig. 6.2. The thin solid line used in the top panel represents the case of non-decaying WDM (with mass 4 keV).

and to N, so that the higher central density of the model without DM decays/annihilations largely compensates its lower H_2 abundance, i.e. the unperturbed case is the *fastest* cooling one. However, it is interesting to note that the final T is much lower for the cases where DM energy input is included, because of the enhancement of the HD fraction, which provides an efficient cooling mechanism also at $T \lesssim 200$ K (Ripamonti 2006).

6.4.2 Critical mass

Each of our simulated halos was classified as collapsing (or, equivalently, efficiently cooling) or non-collapsing (inefficiently cooling), depending on whether it reaches a maximum density larger than $10^5\, m_H$ cm^{-3} in less than a Hubble time. We define the critical mass, m_{crit}, as the minimum mass of a collapsing halo at a given virialization redshift z_{vir}.

The values of m_{crit} as a function of the virialization redshift are shown in Fig. 6.5 for isothermal halos, and in Fig. 6.6 for NFW halos. The main trend inferred from the

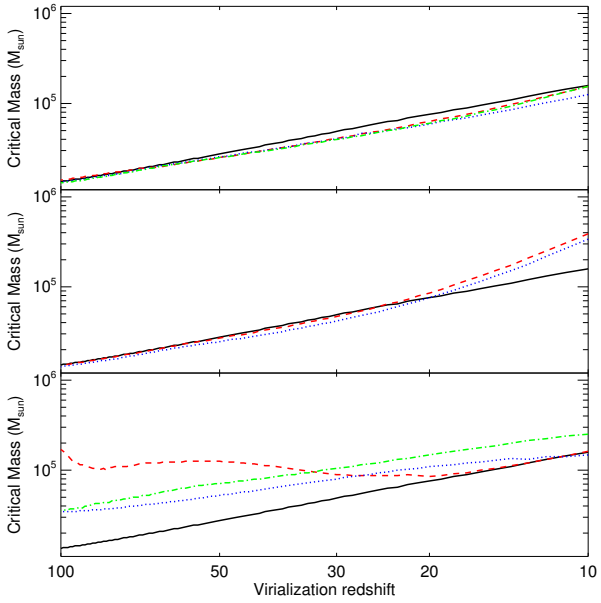

Figure 6.6: The critical mass as a function of the virialization redshift z_{vir} for NFW halos. The lines used in the three panels are the same as in Fig. 6.5.

behaviour of m_J (i.e. the delay of structure formation) is confirmed by m_{crit}. However, the influence of DM decays and annihilations on m_{crit} is much smaller than could be expected from m_J.

In the case of isothermal halos, the effects of the DM decays on m_{crit} (top and central panel) are completely negligible at high redshift and become significant only at redshift less than 20. Even for $z_{vir} = 10$ and 10-MeV decaying LDM (which has the strongest effect), m_{crit} increases only of by a factor 2.

Sterile neutrinos (especially with mass of 4 keV) seem to significantly increase m_{crit}. However, this is not connected with sterile neutrinos decays; but it is due to differences in the assumed DM density profile, as the free-streaming length for these WDM halos is larger than the "standard" value of the core radius ($0.1R_{\rm vir}$) and the "damping" correction described in Section 6.2.5 is important. In fact, if we assume the same WDM density profile, m_{crit} does not depend on whether we consider (thick dot-dashed line in Fig. 6.5) or neglect (thin solid line) sterile neutrino decays.

In the case of LDM annihilations in isothermal halos, m_{crit} is higher than in the unperturbed case for every considered virialization redshift ($z_{vir} = 10 - 100$), confirming

that the annihilations play a role even at very high z. However, the difference with respect to the unperturbed m_{crit} is always less than a factor ~ 2.

If we assume a NFW profile for DM halos (Fig. 6.6), the general effect is a substantial decrease of m_{crit} (independently of DM decays/annihilations), due to the higher central densities, and the consequent stronger gravitational pull. LDM decays tend to increase m_{crit} (at $z < 20$) with respect to the unperturbed case; the increase factor is only marginally larger than in the case of isothermal halos. Sterile neutrino decays appear to slightly reduce m_{crit} with respect to the unperturbed case; but this result is unphysical, as it does not account for damping. It is worth to note that, even if we ignore damping effects and adopt the models with the highest possible concentration, the influence of sterile neutrino decays on structure formation remains very small.

Instead, in the case of LDM annihilations, m_{crit} generally increases more in NFW halos than in isothermal halos. This is due to the importance of the local contribution for annihilations (see Section 6.5.2).

6.5 Discussion

6.5.1 Gas fraction

Why considering either m_J or m_{crit} leads to such widely different conclusions? As mentioned earlier, m_J is a rough tracer of the minimum halo mass for collapse; but it is not sensitive to the local properties of the halo. For example, to calculate m_J one has to assume that the density is uniform. On the contrary, m_{crit} depends on the evolution of the central region of the halo, where the density increases much more rapidly than in the outskirts, driving the collapse (Figs. 6.3 and 6.4). When the density becomes sufficiently high, the molecular cooling largely overcomes the heating due to DM decays/annihilations (Figs. 6.3 and 6.4). This is the reason why m_{crit} does not increase significantly in the presence of DM decays/annihilations. Instead, m_J, which does not account for the density increase and for the consequent cooling enhancement, dramatically grows. Then, we can conclude that m_J does not provide a realistic estimate of the effects of DM decays/annihilations.

Is there any physical implication of the growth of m_J? m_J is directly related to

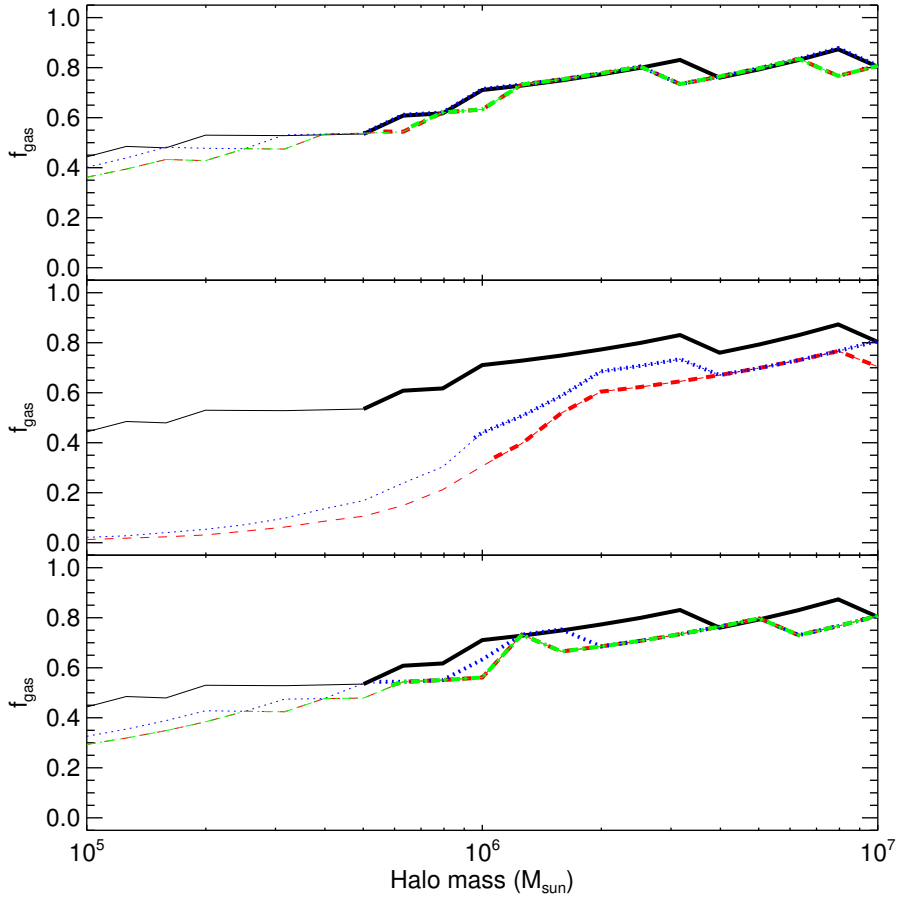

Figure 6.7: Halo baryonic mass fraction (see definition in equation 6.22) as a function of the halo mass for a fixed virialization redshift ($z_{vir} = 10$) and for an isothermal DM profile. Top panel: Effect of decaying sterile neutrinos. Central: Decaying LDM. Bottom: Annihilating LDM. The lines used in the three panels are the same as in Fig. 6.2. Thick (thin) lines indicate that the halo mass is larger (smaller) than m_{crit}.

the global hydro-dynamical behaviour of the gas inside a halo: in halos with mass below m_J the gas pressure prevents the development of a large gas overdensity, while in more massive halos the gas accumulation should proceed almost unimpeded. If so, the mass fraction in baryons within the virial radius of a halo should be of the order of the cosmological average Ω_b/Ω_M when $M_{halo} \gtrsim m_J$, but it should be lower when $M_{halo} \lesssim m_J$. To check this hypothesis, we derive the baryonic mass fraction (f_{gas}) normalized to Ω_b/Ω_M, i.e.

$$f_{gas} = \frac{M_{gas}(R_{vir})}{M_{\rm halo}} \frac{\Omega_M}{\Omega_b}, \tag{6.22}$$

where $M_{gas}(R_{vir})$ is the mass of gas within the virial radius at the final stage of each simulation; instead M_{halo} is the total mass of the halo at the beginning of the simulation.

In Fig. 6.7 we show f_{gas} as a function of mass inside halos virializing at redshift $z_{vir} = 10$. The comparison between the various scenarios clearly shows that the energy injection from DM decays/annihilations can substantially reduce the gas fraction inside all halos, especially the smallest ones. This is clearly related to the increase in m_J, as the largest variation in f_{gas} occurs in the LDM decay scenario, where the increase of m_J is maximum (Fig. 6.2).

6.5.2 Concentration and local contribution

In this Chapter we basically considered two different DM profiles: isothermal and NFW halos. These two models are comparable in terms of virial radius and main properties; but the NFW one is much more concentrated. From the comparison between Fig. 6.5 and Fig. 6.6 we have already seen that this difference has important effects on the critical mass: m_{crit} is generally much lower for a NFW than for an isothermal halo, independently of DM decays and annihilations. For decaying particles, higher concentrations lead to marginally stronger effects in delaying the formation of structures, but the effect is minimal. For annihilations this effect of high concentrations is much larger (see Figs. 6.5, 6.6 and 6.8).

Another significant characteristic of our model is the estimate of the local contribution due to DM decays/annihilations occurring inside the halo (see Section 6.2.4). Pointedly, the local contribution strongly depends on the DM profile. But what is the

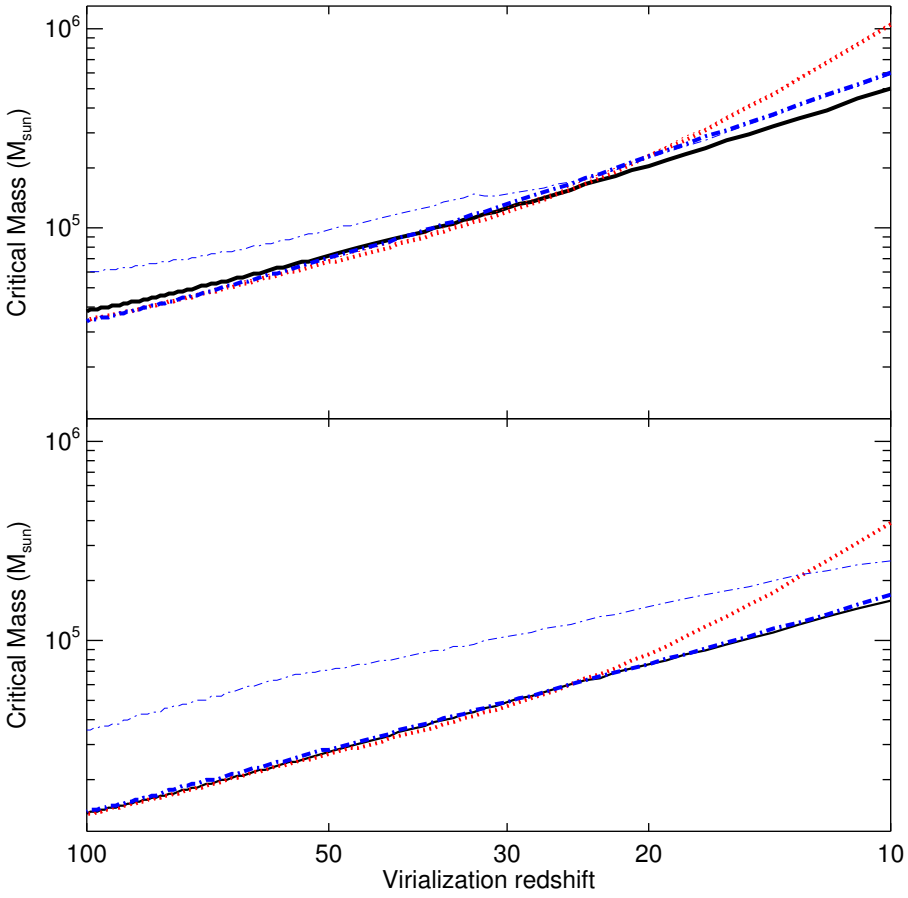

Figure 6.8: Evolution of m_{crit} as a function of the virialization redshift in the case without DM (solid lines), with 3-MeV LDM decays (dotted) and with 1-MeV LDM annihilations (dot-dashed). Thin (thick) lines are with (without) the local contribution of the DM inside the halo. Note that the thin dotted line is completely superimposed to the thick dotted line, because the local contribution of decaying DM is always negligible. Top panel: isothermal halos. Bottom panel: NFW halos.

importance of the local contribution? In Fig. 6.8 we indicate the effect on m_{crit} of LDM decays (dotted line) and annihilations (dot-dashed), by including (thin line) or not (thick) the local contribution. In the case of DM decays the thin and thick dotted lines appear superimposed, both in the isothermal (top panel) and NFW (bottom) profile, indicating that the local contribution is always negligible for decays.

Instead, if we consider the annihilations, the case with (thin line) and without (thick) the local contribution are very different, especially for the NFW profile. If we do not include the local contribution, m_{crit} is very close to the unperturbed value. If we switch on the local contribution in the isothermal profile, m_{crit} is substantially higher (a factor ~ 2) than in the unperturbed case, at least for high virialization redshifts ($z_{vir} > 30$). Finally, if we account for the local contribution in a NFW halo, m_{crit} is always higher (a factor $\sim 2 - 4$) than in the unperturbed case (even at low virialization redshifts). This is consistent with the fact that the annihilation rate strongly depends on the local DM density.

6.6 Conclusions

In this Chapter we derived the effects of DM decays and annihilations on structure formation. We considered only moderately massive DM particles (sterile neutrinos and LDM), as they are expected to give the maximum contribution to heating and reionization (Mapelli et al. 2006). To describe the interaction between the IGM and the decay/annihilation products we followed the recipes recently derived by RMF06.

We accounted not only for the diffuse cosmological contribution to heating and ionization, but also for the local contribution due to DM decays and annihilations occurring in the halo itself. The local contribution results to be dominant in the case of DM annihilations especially for cuspy DM profiles.

The energy injection from DM decays/annihilations produces both an enhancement in the abundance of coolants (H_2 and HD) and an increase of gas temperature. We found that for all the considered DM models (sterile neutrino decays, LDM decays and annihilations) the critical halo mass for collapse, m_{crit} is often higher than in the unperturbed case. This means that DM decays and annihilations tend to delay the formation of

structures. However, the variation of m_{crit} is minimal. In the most extreme cases, i.e. considering LDM annihilations (decays) and halos virializing at redshift $z_{vir} > 30$ ($z_{vir} \sim 10$), m_{crit} increases of a factor ~ 4 (~ 2). In the case of decays, the variations of m_{crit} are almost independent from the assumed concentration of the DM halo, although higher concentrations (corresponding to smaller values of m_{crit}) seem to be associated with slightly stronger effects of the DM energy injection. The dependence on concentration is more evident in the case of annihilating particles, where higher concentrations lead to substantially larger effects. This happens because the "local" contribution is important.

In summary, the effects of DM decays and/or annihilations on structure formation are quite small, except in some extreme cases (e.g. very high concentration for annihilations). However, the energy injection from DM decays/annihilations has important consequences on the fraction of gas which is retained inside the halo. This fraction can be substantially reduced, especially in the smallest halos ($\lesssim 10^6\, M_\odot$).

Finally, we point out that our results are quite different from the conclusions of Biermann & Kusenko (2006) and Stasielak et al. (2006)[3], who suggest that sterile neutrino decays can favour the formation of first objects. The discrepancy is likely due to our more complete treatment which includes the hydrodynamics of the collapsing structures. In fact, our hydro-dynamical treatment allows to describe the detailed gas density evolution during the collapse, resulting in markedly different temperature and chemical properties with respect to those found by a simple one-zone model.

[3]Biermann & Kusenko (2006) and Stasielak et al. (2006) do not calculate the critical mass m_{crit}. So, it is quite difficult to make a quantitative comparison between their results and ours.

Appendix A

Initial conditions for the N-body model of the Milky Way

A.1 Bulge

For the density profile of the bulge we adopted the Hernquist (1993) profile in the case of a spherically symmetric bulge.

$$\rho_b(r) = \frac{M_b\, a}{2\pi}\frac{1}{r\,(a+r)^3}, \tag{A.1}$$

where M_b is the bulge mass, a the bulge scale length and $r = \sqrt{R^2+z^2}$. We choose $a = 0.2\,R_d$, consistent with Kent, Dame & Fazio (1991; $a = 0.7 \pm 0.2$ kpc).

This profile can be analytically integrated over the spherical volume element to derive the mass $M_b(r)$ enclosed within a certain radius r:

$$M_b(x) = M_b\,\frac{x^2}{(1+x)^2}, \tag{A.2}$$

where $x \equiv r/a$. Then, the probability $\mathcal{P}(x)$ that a bulge star particle is at distance x from the center can be written as:

$$\mathcal{P}(x) = \frac{M_b(x)}{M_b(\infty)} = \frac{x^2}{(1+x)^2}. \tag{A.3}$$

Then, we can derive the distribution of r by assigning uniformly generated random numbers to $\mathcal{P}(x)$.

To determine the position of the bulge star particles we have also to randomly generate two position angles, ϕ and θ. The distribution of probability of the former is homogeneous between 0 and $2\,\pi$, that of the latter is homogeneous in $\cos(\theta)$ between -1 and 1.

Then, the Cartesian coordinates of the bulge particles can be written as:

$$\begin{aligned} x &= r\ \sin\theta\ \cos\phi \\ y &= r\ \sin\theta\ \sin\phi \\ z &= r\ \cos\theta \end{aligned} \tag{A.4}$$

For the distribution of velocities we followed an analogous procedure. In particular, for a spherical and isotropic bulge, the dispersion velocity σ_b can be derived as (Hernquist 1993):

$$\sigma_b^2(r) = \frac{1}{\rho_b(r)} \int_r^\infty \rho_b(\tilde{r})\ \frac{G\,M_b(\tilde{r})}{\tilde{r}^2}\,\mathrm{d}\tilde{r}. \tag{A.5}$$

The velocity distribution at each radius r can be approximated with a Maxwellian distribution, parametrized by $\sigma_b(r)$ (Hernquist 1993). Then, the probability $\mathcal{P}(v,\,r)$ that a bulge star particle at distance r from the center has a velocity v is:

$$\begin{aligned} \mathcal{P}(v,\,r) &= 4\,\pi \int_0^v \left(\tfrac{1}{2\,\pi\sigma_b^2}\right)\ \tilde{v}^2\ \exp\left[-\tfrac{\tilde{v}^2}{2\,\sigma_b^2}\right] \\ &= \tfrac{4}{\sqrt{\pi}}\ \left[-\tfrac{1}{2}\ \tfrac{\tilde{v}}{\sqrt{2}\,\sigma_b}\ \exp\left[-\tfrac{\tilde{v}^2}{2\,\sigma_b^2}\right]\ +\ \tfrac{\sqrt{\pi}}{4}\,\mathrm{erf}\left(\tfrac{\tilde{v}}{\sqrt{2}\,\sigma_b}\right)\right]\mathrm{d}\tilde{v}, \end{aligned} \tag{A.6}$$

where we wrote σ_b instead of $\sigma_b(r)$ in order to simplify the notation.

We need also two angles, ϕ and θ, generated as explained for the position distribution, and the velocity of a bulge star particle in Cartesian coordinates is:

$$\begin{aligned} v_x &= v\ \sin\theta\ \cos\phi \\ v_y &= v\ \sin\theta\ \sin\phi \\ v_z &= v\ \cos\theta. \end{aligned} \tag{A.7}$$

A.2 Disk

For the density profile of the disk we chose an exponential distribution convolved with a hyperbolic secant (Hernquist 1993):

$$\rho_d(R,z) = \frac{M_d}{4\pi R_d^2\,z_0}\ \exp\left(-R/R_d\right)\mathrm{sech}^2(z/z_0), \tag{A.8}$$

where M_d is the disk mass, R_d is the disk scale radius and z_0 is the disk scale height. The procedures adopted to generate the positions and velocities of disk particles are similar to those described for the bulge. The main difference is the kind of symmetry, the disk being axisymmetric instead of spherical.

In particular, the mass $M_d(R,\, z)$ enclosed within a certain radius R and a certain height z is:

$$M_d(R,\, z) = \frac{M_d}{2}\,\left[1 - \left(1 + \frac{R}{R_d}\right)\,\exp\,\left[-\frac{R}{R_d}\right]\right]\,\left[\tanh\,\left(\frac{z}{z_0}\right) + 1\right]. \tag{A.9}$$

Luckily, the dependence on R and the dependence on z are decoupled. So, the probability $\mathcal{P}(R)$ that a bulge star particle is at distance R from the center can be written as:

$$\mathcal{P}(R) = \left[1 - \left(1 + \frac{R}{R_d}\right)\,\exp\,\left[-\frac{R}{R_d}\right]\right], \tag{A.10}$$

and the probability $\mathcal{P}(z)$ that a bulge star particle is at a distance z from the center can be written as:

$$\mathcal{P}(z) = \frac{1}{2}\,\left[\tanh\,\left(\frac{z}{z_0}\right) + 1\right]. \tag{A.11}$$

Where $\mathcal{P}(R)$ and $\mathcal{P}(z)$ can be uniformly generated to get R and z. We need also an angle ϕ, uniform between 0 and $2\,\pi$, and we can write the Cartesian coordinates of a disk particle as:

$$\begin{aligned} x &= r\,\cos\phi \\ y &= r\,\sin\phi \\ z &= z. \end{aligned} \tag{A.12}$$

For the velocity distribution, we have to calculate three different components: the radial (σ_R), vertical (σ_z) and azimuthal (σ_ϕ) velocity dispersion.

The vertical velocity dispersion can be expressed as (Hernquist 1993):

$$\sigma_z^2(R) = \pi\,G\,\Sigma(R)\,z_0 = G\,z_0\,\tfrac{M_d}{2\,R_d^2}\,\exp\left[-\tfrac{R}{R_d}\right], \tag{A.13}$$

where $\Sigma(R)$ is the surface density and G the gravitational constant. The term $\exp\left[-\frac{R}{R_d}\right]$ can be changed to $\exp\left[-\frac{\sqrt{R^2+2\,a_{soft}^2}}{R_d}\right]$, where $a_{soft} = R_d/4$ is a correction accounting for softening effects (Quinn, Hernquist & Fullagar 1993).

Also the radial dispersion velocity is proportional to the surface density. Then we can write:

$$\sigma_R(R) = \sigma_R(R_{ref})\, \exp\left[-\frac{R}{2\,R_d}\right], \tag{A.14}$$

where $\sigma_R(R_{ref})$ is the radial dispersion velocity measured at a reference radius R_{ref} and can be expressed as:

$$\sigma_R(R_{ref}) = \mathcal{Q}\,\sigma_{crit}(R_{ref}) \sim \mathcal{Q}\,\frac{3.36\,G\,\Sigma(R_{ref})}{\kappa}, \tag{A.15}$$

where $\sigma_{crit}(R_{ref})$ is the critical velocity dispersion for stability (see Binney & Tremaine 1987), $\mathcal{Q}$ is the Toomre parameter[1] ($\mathcal{Q} > 1$ means that the disk is stable; see Toomre 1964), and κ is the epicyclic frequency ($\kappa^2 \equiv \frac{3}{R}\frac{\partial\Phi}{\partial R} + \frac{\partial^2\Phi}{\partial R^2}$, Φ being the potential). Evaluating $\sigma_R(R_{ref})$ at the characteristic radius and substituting in equation (A.14), we find:

$$\sigma_R(R) = \mathcal{Q}\,\frac{3.36\,G}{\kappa}\,\frac{M_d\,\exp(-2)}{2\,\pi\,R_d^2}\,\exp\left[\frac{\sqrt{4\,R_d^2 + 2\,a_{soft}^2}}{2\,R_d}\right]\,\exp\left[-\frac{\sqrt{R^2 + 2\,a_{soft}^2}}{2\,R_d}\right], \tag{A.16}$$

where the two exponential terms containing a_{soft} account for softening effects.

Finally, the azimuthal velocity dispersion is directly proportional to the radial velocity dispersion:

$$\sigma_\phi(R) = \sigma_R(R)\,\frac{\kappa}{4\,\Omega}, \tag{A.17}$$

where Ω is the angular frequency.

Also for the disk we adopt the Maxwellian approximation of the velocity distribution. Therefore, we generate random velocities v_R, v_z and v_ϕ (along R, z and ϕ, respectively) by using Maxwellian distributions parametrized by σ_R, σ_z and σ_ϕ respectively.

Since the disk is rotating, we need a further component along ϕ, the free streaming azimuthal velocity v_{fs}:

$$v_{fs}^2 = v_c^2 + \sigma_R^2(R)\,\left[1 - \frac{\kappa^2(R)}{4,\Omega^2(R)} - 2\frac{R}{R_d}\right], \tag{A.18}$$

where $v_c \equiv R\,\frac{\partial\Phi}{\partial R}$ is the circular velocity (Binney & Tremaine 1987). Then, the total velocity along ϕ is $v_{\phi,\,tot} = v_\phi + v_{fs}$. Finally, the velocity of a disk particle in Cartesian coordinates

[1] In our runs we used the standard conservative value $\mathcal{Q} = 1.5$.

is the following.

$$\begin{aligned} v_x &= v_R \cos\phi - v_{\phi,\,tot} \sin\phi \\ v_y &= v_R \sin\phi + v_{\phi,\,tot} \cos\phi \\ v_z &= v_z, \end{aligned} \tag{A.19}$$

where ϕ is the same angle generated for the positions.

A.3 Halo

In Chapter 3 I described simulations made adopting a rigid halo. However, for completeness, I also want to summarize how to generate the initial conditions for halo particles (which I used to make some test with a "living" halo). The procedure to generate the initial conditions for a spherically symmetric, isotropic halo is very similar to that described for bulge particles.

The density profile I chose is a Navarro, Frenk & White (NFW; 1996) profile[2], i.e.:

$$\rho_h(r) = \frac{\rho_s}{(r/r_s)^\gamma \left[1 + (r/r_s)^\alpha\right]^{(\beta-\gamma)/\alpha}}, \tag{A.20}$$

where we choose $(\alpha, \beta, \gamma) = (1, 3, 1)$, and $\rho_s = \rho_{crit}\, \delta_c$, ρ_{crit} being the critical density of the Universe and

$$\delta_c = \frac{200}{3} \frac{c^3}{\ln(1+c) - (c/(1+c))}, \tag{A.21}$$

where c is the concentration parameter and r_s is the halo scale radius, defined by $r_s = R_{200}/c$; R_{200} is the radius encompassing a mean overdensity of 200 with respect to the background density of the Universe, i.e. the radius containing the virial mass M_{200}.

The NFW profile can be analytically integrated over the spherical volume element in the case where $(\alpha, \beta, \gamma) = (1, 3, 1)$. Then, the halo mass $M_h(r)$ enclosed within a radius r is:

$$M_h(x) = 4\,\pi \rho_s\, r_s^3 \left[-\frac{x}{(1+x)} + \ln(1+x) \right], \tag{A.22}$$

where $x = r/r_s$. Then, the probability $\mathcal{P}(x)$ that a halo particle is at distance $x \leq R_{200}/r_s$ from the center can be written as:

$$\mathcal{P}(x) = \left[-\frac{x}{(1+x)} + \ln(1+x) \right] \left[-\frac{R_{200}/r_s}{(1+R_{200}/r_s)} + \ln(1+R_{200}/r_s) \right]^{-1}. \tag{A.23}$$

[2]I also made some check with an Hernquist halo density profile (1993)

From $\mathcal{P}(x)$ (uniformly generated between 0 and 1), we derive r. The two position angles (ϕ and θ) are generated exactly as for the bulge.

Also the velocities of halo particles are generated exactly as described for the bulge (equations A.5-A.7), by changing the density $\rho_b(r)$ to $\rho_h(r)$.

Appendix B

Initial conditions for three body encounters

The initial conditions for the three body encounters have been chosen as suggested by Hut & Bahcall (1983). They are valid for a system represented by a binary and a third object initially located 'at the infinity', i.e. at a distance much greater than the orbital separation of the binary. The reference frame is the center of mass of the binary.

The parameters of the system are indicated in Table B.1 and Fig. B.1.

Among these parameters, we fixed, for simplicity, the values of M_1, M_2, m, e, a and D (see Chapter 4 for details); whereas we generated b, v, ϕ, θ, ψ and f following suitable probability distributions. Let us discuss the chosen range (see Table B.2) and probability

M_1, M_2, m	mass of the two components of the binary and of the bullet star
e	orbital eccentricity of the binary
a	orbital separation of the binary
D	initial distance of the bullet
b	impact parameter
v	initial velocity (in modulus) of the bullet relative to the center of mass of the binary
ϕ, θ, ψ	impact orientations
f	initial phase of the binary

Table B.1: Definition of the initial parameters.

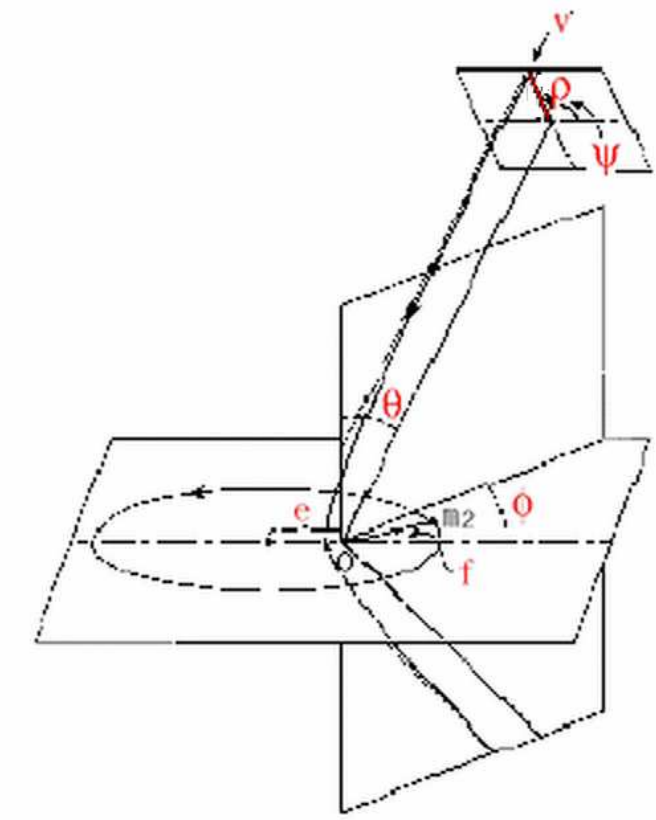

Figure B.1: Initial parameters of the three-body code (Hut & Bahcall 1983)

distribution for these 6 free parameters.

B.1 Range of the initial parameters

The range of allowed values for the orientation angles is simply due to the geometry of the system. The choice of the range for v and especially for b is more difficult.

For the initial velocity, we take the central three-dimensional dispersion velocity σ_{3D} of the globular cluster we are considering and we generate the initial velocities between $v_{min} = \sigma_{3D} - 1\,\sigma$ and $v_{max} = \sigma_{3D} + 1\,\sigma$, where σ is the standard deviation in the observations. In the case of M4, $v_{min} = 5.5$ km s^{-1} and $v_{max} = 6.6$km s^{-1}.

For the impact parameter, the choice of the maximum value b_{max} is critical. As I said in Chapter 4, Section 4.3.4, one has to derive the value of b_{max} for which all the

Parameter	Range
v	$[v_{min},\, v_{max}]$
b	$[0,\, b_{max}]$
ϕ	$[0,\, 2\pi)$
θ	$[0,\, \pi/2]$
ψ	$[0,\, 2\pi)$
f	$[0,\, 2\pi)$

Table B.2: Range of the initial parameters.

encounters with non-negligible energetic exchanges are taken into account. Otherwise, the statistics derived from the simulations is unreliable. The energetic exchange can be roughly estimated by the following expression (see Chapter 4):

$$\frac{\Delta E_{\rm BH}}{E^{in}_{\rm BH}} \sim 4.5\times10^{-3}\left(\frac{m}{0.5\,{\rm M}_\odot}\right)\left(\frac{100\,{\rm M}_\odot}{M_1}\right)\left(\frac{50\,{\rm M}_\odot}{M_2}\right)\left(\frac{a}{1\,{\rm au}}\right)\left(\frac{u^{fin}}{20\,{\rm km\ s^{-1}}}\right)^2, \quad \text{(B.1)}$$

where $E^{in}_{\rm BH}$ is the initial binding energy of the binary, $\Delta E_{\rm BH}$ the energetic exchange and u^{fin} the post-encounter asymptotic velocity of the bullet. This equation indicates that, if we want outcoming stars with velocity $u^{fin} \gtrsim 20$ km s^{-1}, we have to consider all the encounters which involve energetic exchanges $\frac{\Delta E_{\rm BH}}{E^{in}_{\rm BH}} \gtrsim 10^{-3}$.

Unfortunately, there are no general equations which directly relate $\frac{\Delta E_{\rm BH}}{E^{in}_{\rm BH}}$ and b_{max}. So one must do some test to determine the best value of b_{max}. A good *Ansatz* to start with is represented by the following expression:

$$b_{approx} \sim \left(\frac{2\,G\,(M_1+M_2+m)\,a}{v^2}\right)^{1/2}, \quad \text{(B.2)}$$

which comes from assuming a pericenter distance equal to the orbital separation. We expect (Sigurdsson & Phinney 1993) that b_{approx} is of the same order of magnitude of b_{max}.

After calculating b_{approx}, we run some test-simulations with $b_{max} = 10\,b_{approx}$. From these simulations we extract the cumulative cross-section $\sigma\left(\frac{\Delta E_{\rm BH}}{E^{in}_{\rm BH}} \gtrsim 10^{-3},\ \leq b\right)$ (see Fig. B.2), defined as:

$$\sigma\left(\frac{\Delta E_{\rm BH}}{E^{in}_{\rm BH}} \gtrsim 10^{-3},\ \leq b\right) = f\left(\frac{\Delta E_{\rm BH}}{E^{in}_{\rm BH}} \gtrsim 10^{-3},\ \leq b\right)\pi\,b^2, \quad \text{(B.3)}$$

where $f\left(\frac{\Delta E_{\rm BH}}{E^{in}_{\rm BH}} \gtrsim 10^{-3},\ \leq b\right)$ is the fraction of encounters with $\frac{\Delta E_{\rm BH}}{E^{in}_{\rm BH}} \gtrsim 10^{-3}$ and impact parameter $\leq b$, and $\pi\,b^2$ is the geometric cross-section.

Since $b_{max} = 10\, b_{approx}$ is always an overestimate of the true b_{max}, then the cumulative cross-section $\sigma\left(\frac{\Delta E_{\rm BH}}{E^{in}_{\rm BH}} \gtrsim 10^{-3},\ \leq b\right)$ becomes flat for $b \ll 10\, b_{approx}$. The value for which the cross-section becomes flat is chosen as b_{max} for the definitive simulations (see Fig. B.2).

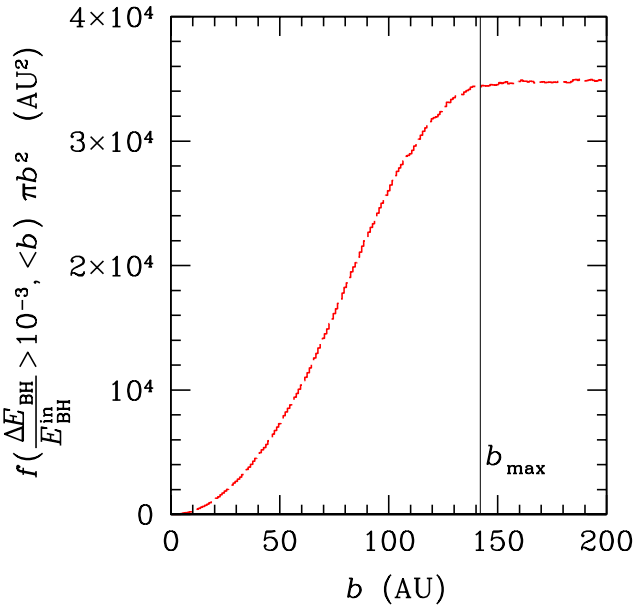

Figure B.2: The red dashed line represents the cumulative cross-section as a function of the impact parameter. The solid black line is the derived correct value of b_{max}.

B.2 Probability distribution of the initial parameters

The probability distributions of the 6 free parameters are reported in Table B.3.

The choice of these distributions is quite obvious. In the case of the orientation angles ϕ, θ and ψ, the probability distribution is dictated by the geometry. Also in the case of the impact parameter the probability distribution is chosen on the basis of the geometrical cross-section.

For the initial velocity we assume a uniform distribution. This is a quite rough approximation. However, we made some tests (with a truncated Gaussian velocity distri-

Parameter	Probability homogeneous in
v	v
b	b^2
ϕ	ϕ
θ	$\cos\theta$
ψ	ψ
f	$\mathcal{E} - e\sin\mathcal{E}$

Table B.3: Probability distribution for the free parameters.

bution) and found that the final velocity distribution does not depend on the initial one.

For the phase f of the binary we use the keplerian relation which links the eccentric anomaly $\mathcal{E}$ and the time elapsed from the pericenter passage t_p:

$$\frac{2\pi}{T}\, t_p = \mathcal{E} - e\sin\mathcal{E}, \tag{B.4}$$

where T is the orbital period. Once we have randomly generated the eccentric anomaly $\mathcal{E}$ by using this probability distribution, we can derive the phase f by using the relation between the two quantities:

$$\tan(f/2) = \left(\frac{1+e}{1-e}\right)^{1/2} \tan(\mathcal{E}/2). \tag{B.5}$$

B.3 The initial conditions

The initial conditions (in Cartesian coordinates) can be expressed in terms of the initial parameters (M_1, M_2, m, a, e, b, v, ϕ, θ, ψ and f) in the following way (for more details see Michela Mapelli's laurea Thesis, `http://www.sissa.it/ mapelli/images/tesi.ps.gz`).

$$\begin{aligned}
x_1 &= -\tfrac{M_2}{(M_1+M_2)}\,\tfrac{a\,(1-e^2)\cos f}{(1+e\cos f)}\\
y_1 &= -\tfrac{M_2}{(M_1+M_2)}\,\tfrac{a\,(1-e^2)\sin f}{(1+e\cos f)}\\
z_1 &= 0
\end{aligned}$$

$$\begin{aligned}
\dot{x}_1 &= -\tfrac{M_2}{(M_1+M_2)}\left(\tfrac{e\cos f}{(1+ecosf)} - 1\right)\sin f\sqrt{\tfrac{G(M_1+M_2)}{a\,(1-e^2)}}(1+e\cos f)\\
\dot{y}_1 &= -\tfrac{M_2}{(M_1+M_2)}\left(\tfrac{e\sin^2 f}{(1+e\cos f)} + \cos f\right)\sqrt{\tfrac{G(M_1+M_2)}{a\,(1-e^2)}}(1+e\cos f)\\
\dot{z}_1 &= 0
\end{aligned}$$

$$
\begin{aligned}
x_2 &= \tfrac{M_1}{(M_1+M_2)} \tfrac{a\,(1-e^2)\cos f}{(1+e\cos f)} \\
y_2 &= \tfrac{M_1}{(M_1+M_2)} \tfrac{a\,(1-e^2)\sin f}{(1+e\cos f)} \\
z_2 &= 0
\end{aligned}
$$

$$
\begin{aligned}
\dot{x}_2 &= \tfrac{M_1}{(M_1+M_2)} \left(\tfrac{e\cos f}{(1+ecosf)} - 1 \right) \sin f \sqrt{\tfrac{G(M_1+M_2)}{a\,(1-e^2)}} (1 + e\cos f) \\
\dot{y}_2 &= \tfrac{M_1}{(M_1+M_2)} \left(\tfrac{e\sin^2 f}{(1+e\cos f)} + \cos f \right) \sqrt{\tfrac{G(M_1+M_2)}{a\,(1-e^2)}} (1 + e\cos f) \\
\dot{z}_2 &= 0
\end{aligned}
$$

$$
\begin{aligned}
x_3 &= D \left(\sin\phi\cos\psi \left(\tfrac{b}{D}\right) - \cos\phi \left(\sqrt{1 - \left(\tfrac{b}{D}\right)^2} \sin\theta + \left(\tfrac{b}{D}\right) \cos\theta sin\psi \right) \right) \\
y_3 &= -D \left(\sin\phi \left(\sqrt{1 - \left(\tfrac{b}{D}\right)^2} \sin\theta + \left(\tfrac{b}{D}\right) \cos\theta sin\psi \right) + \left(\tfrac{b}{D}\right) \cos\phi\cos\psi \right) \\
z_3 &= D \left(-\cos\theta \sqrt{1 - \left(\tfrac{b}{D}\right)^2} + \left(\tfrac{b}{D}\right) \sin\theta\sin\psi \right)
\end{aligned}
\tag{B.6}
$$

$$
\begin{aligned}
\dot{x}_3 &= v\sin\theta\cos\phi \\
\dot{y}_3 &= v\sin\theta\sin\phi \\
\dot{z}_3 &= v\cos\theta
\end{aligned}
$$

Appendix C

Upper limits on sterile neutrino mass

C.0.1 Photon flux from neutrino decays

Radiative decay channel

Stecker (1980) calculated the flux emitted by sterile neutrinos radiatively decaying at different redshift. Correcting its calculations and updating them to present values of cosmological parameters[1], we find a photon flux (units of $\mathrm{cm}^{-2}\ \mathrm{s}^{-1}\ \mathrm{sr}^{-1}$):

$$I(E_{obs}) = \frac{n_s\, c}{4\pi\, H_0\, \tau} \int_0^z \frac{e^{-t(z)/\tau} E_{em}\, \delta((1+z)E_{obs} - E_{em})}{(1+z)\left[(1+z)^3\Omega_{0M} + \Omega_\Lambda\right]^{1/2}} \mathrm{d}z, \tag{C.1}$$

where n_s and τ are the present number density and the lifetime of sterile neutrinos respectively; E_{em} and E_{obs} are the emitted and the observed energy of the photon, and $t(z)$ is the time elapsed from the Big Bang to redshift z, which can be approximated at high redshift as

$$t(z) \simeq \frac{2}{3} H_0^{-1} \Omega_{0M}^{-1/2} (1+z)^{-3/2} \tag{C.2}$$

[1]We adopt the following cosmological parameters: Hubble constant H_0=72 km s^{-1} Mpc^{-1}, $\Omega_{0M} \equiv \Omega_{DM} + \Omega_b$=0.27, Ω_Λ=0.73, which are in agreement with the first year WMAP determination (Spergel et al. 2003).

Since $\delta((1+z)E_{obs} - E_{em}) \neq 0$ if and only if $(1+z) = E_{em}/E_{obs}$, the eq. (C.1) becomes (for comparison, see Massó & Toldrà 1999)

$$I(E_{obs}) = \frac{1}{4\pi}\frac{c}{H_0}\frac{n_s}{\tau}\frac{e^{-t(E_{em}/E_{obs})/\tau}}{[(E_{em}/E_{obs})^3\Omega_{0M} + \Omega_\Lambda]^{1/2}} \tag{C.3}$$

This equation depends on two fundamental, substantially unknown, parameters: the density n_s and the lifetime τ of sterile neutrinos. A reasonable upper limit of n_s can be obtained by imposing that all the dark matter is composed by sterile neutrinos (Dolgov & Hansen 2002):

$$\frac{n_s}{n_a} = 1.2 \times 10^{-2} \left(\frac{\mathrm{keV}}{m_{\nu s}}\right) \left(\frac{\Omega_{DM}}{0.23}\right) \left(\frac{h}{0.72}\right)^2, \tag{C.4}$$

where n_a is the present density of active neutrinos and $m_{\nu s}$ is the mass of sterile neutrinos.

The lifetime for sterile neutrino radiative decay is (Mapelli & Ferrara 2005; see Chapter 5):

$$\tau = \frac{512\,\pi^4}{9\,\alpha_{em}}\, G_F^{-2} m_{\nu\, s}^{-5} \sin^{-2}\theta, \tag{C.5}$$

where α_{em} is the fine structure constant, G_F the Fermi constant, $m_{\nu\, s}$ the sterile neutrino mass and $\sin\theta$ the mixing angle. To derive $\sin\theta$ we adopt the following relation (Abazajian 2006):

$$\sin^2\theta = 2.5{\times}10^{-9} \left[\left(\frac{3.4\,\mathrm{keV}}{m_{\nu\, s}}\right) \left(\frac{\Omega_{DM}}{0.26}\right)^{1/2}\right]^{1.626} \left\{0.527\,\mathrm{erfc}\left[-1.15\left(\frac{T_{QCD}}{170\ \mathrm{MeV}}\right)^{2.15}\right]\right\}^{1.626}, \tag{C.6}$$

where Ω_{DM} is the dark matter density and T_{QCD} the temperature of quark-hadron transition.

Pion decay channel

As an alternative to the radiative decaying sterile neutrinos, Hansen & Haiman (2004) have recently considered heavier sterile neutrino candidates. They noticed that very massive sterile neutrinos ($140 \leq m_{\nu s} \leq 500$ MeV) mainly decay into pions and leptons (electrons or positrons). These electrons are sufficiently energetic to Compton-scatter CMB photons, which can then ionize hydrogen atoms directly or through secondary electrons.

We can derive the same quantities calculated for radiative decays in the case of pion decay considered by Hansen & Haiman (2004). If the sterile neutrino has a mass in the range 140-500 MeV, the dominant decay channel is (Astier et al. 2001)

$$\nu_s \rightarrow l + \pi, \tag{C.7}$$

where π is a pion and l can be an electron, a positron or a neutrino. We will focus on the case in which l is an electron. It will have an energy $E_e = (m_{\nu s} - m_\pi)/2$, where m_π is the pion total mass. Then, because the rest mass of the pion is 139.7 MeV, $0 < E_e < 180$ MeV. As pointed out by Hansen & Haiman (2004), an electron in this range of energies has a mean free path to inverse Compton-scattering with CMB photons generally lower than the mean free path to collisionally ionizing hydrogen. Then the most important interaction these electrons will experience is the inverse Compton-scattering with CMB photons. Can these scattered CMB photons significantly contribute to the background radiation? To answer this question we made the following calculations. As a first approximation, we assume that the electrons produced by neutrino decay follow a power law energy distribution with spectral index p (this assumption takes into account the fact that each electron interacts more than once with CMB photons, gradually degrading its energy). The final spectrum of photons, initially a Planckian, due to inverse Compton-scattering by a power law distribution of electrons is given by (Abramowitz & Stegun 1965; Rybicki & Lightman 1979)

$$\frac{\mathrm{d}E}{\mathrm{d}V\,\mathrm{d}t\,\mathrm{d}E\,\mathrm{d}\Omega} = \frac{1}{4\pi}\frac{8\pi^2 r_0^2\,A}{h_{Pl}^3 c^2} F(p)\ (k_B T)^{(p+5)/2}\ E^{-(p-1)/2} \tag{C.8}$$

where r_0 is the classical radius of the electron, h_{Pl} the Planck constant, k_B the Boltzmann constant, T the initial black body temperature of photons, p the spectral index of the electron distribution and E the final photon energy. $F(p)$ is defined by:

$$F(p) = 2^{(p+3)}\frac{p^2 + 4\,p + 11}{(p+3)^2(p+5)(p+1)}\Gamma\left(\frac{p+5}{2}\right)\zeta\left(\frac{p+5}{2}\right),$$

where Γ is the Euler's Gamma function and ζ is the Riemann's Zeta function. A is a normalization factor defined by

$$n_e = \int_{\gamma_{min}}^{\gamma_{max}} A\,\gamma^{-p}\mathrm{d}\gamma \tag{C.9}$$

where n_e and γ are respectively the density and the Lorentz factor of the electrons ($0 < \gamma < 360$).

We included in eq. (C.8) the dependences on the redshift and we integrated it over the line-of-sight, obtaining the following equation.

$$\begin{aligned} I(E_{obs}) &= \int_0^z \frac{\mathrm{d}E}{\mathrm{d}V\,\mathrm{d}t\,\mathrm{d}E\,\mathrm{d}\Omega}\frac{\mathrm{d}l}{\mathrm{d}z}\mathrm{d}z \\ &= \frac{1}{4\pi}\frac{8\pi^2 r_0^2}{h_{Pl}^3 c^2}F(p)\ (k_B T_0)^{(p+5)/2}\ E_{obs}^{-(p-1)/2} \\ &\quad \times \frac{c}{H_0}\int_0^z \frac{A(z)\,(1+z)^{-1}}{[(1+z)^3\Omega_{0M}+\Omega_\Lambda]^{1/2}}\mathrm{d}z \end{aligned} \tag{C.10}$$

where T_0 is the present temperature of the CMB[2] and $E_{obs} \equiv E\,(1+z)$ is the final energy of the photon at redshift z=0. $A(z)$ can be derived from eq. (C.9). In particular we want to express the proper density of electrons $n_e(z)$ as a function of the initial density of sterile neutrinos $n_s(z)$ and of their lifetime τ. The production rate of electrons is approximately given by $\mathrm{d}n_e/\mathrm{d}t = n_s(z)\exp\left[-t(z)/\tau\right]/\tau$. Integrating, we obtain

$$n_e(t) = \int_0^t \frac{n_s(z)}{\tau} e^{-\tilde{t}(z)/\tau}\, f(\tilde{t})\,\mathrm{d}\tilde{t} \tag{C.11}$$

where $f(t)$ is a function which takes into account the fact that the electrons have a finite lifetime. In the simplest case, $f(t)$ is a step function

$$f(\tilde{t}) = \begin{cases} 1 \text{ if } (t(z) - t_C(z)) < \tilde{t} < t(z) \\ 0 \text{ otherwise} \end{cases}$$

where $t_C(z)$ is defined as the electron cooling time due to repeated Compton-scatterings with CMB photons, $t_C(z) \sim 6\times10^4 (E_e/100\text{ MeV})^{-1}[(1+z)/21]^{-4}$ yr (Hansen & Haiman 2004). Substituting $f(t)$ in eq. (C.11), we obtain:

$$\begin{aligned} n_e(t) &= \int_{(t(z)-t_C(z))}^{t(z)} \frac{n_s(z)}{\tau} e^{-\tilde{t}(z)/\tau}\mathrm{d}\tilde{t} \\ &= n_s(z)\, e^{-t(z)/\tau}\left(e^{t_C(z)/\tau} - 1\right) \end{aligned} \tag{C.12}$$

where $t(z)$ is computed according to eq. (C.2).

Finally $n_s(z) = n_s\,(1+z)^3$ (where n_s is the present sterile neutrino density) can be easily

[2]We adopted $T_0 = 2.275$ K (Spergel et al. 2003).

expressed as a function of the present density of active neutrinos n_a and of the lifetime τ and the mass $m_{\nu s}$ of sterile neutrinos (Hansen & Haiman 2004):

$$n_s \sim \frac{4.8}{(m_{\nu s}/m_\pi)^2 - 1} n_a \, \tau^{-1} \tag{C.13}$$

Taking into account that $n_a = \frac{3}{11} n_b/\eta$ (where n_b is the present baryon density and η is the present baryon-to-photon ratio[3]), we finally obtain:

$$A(z) = \frac{4.8\,(1+z)^3}{[(m_{\nu s}/m_\pi)^2 - 1]} \, \frac{3\,n_b}{11\,\eta} \, \frac{\tau^{-1}}{\int_{\gamma_{min}}^{\gamma_{max}} \gamma^{-p} \mathrm{d}\gamma} \, e^{-t(z)/\tau} \left(e^{t_C(z)/\tau} - 1 \right), \tag{C.14}$$

which can be substituted into eq. (C.10).

C.0.2 X-ray background radiation

Now we have all the equations we need to estimate the contribution of sterile neutrinos to the background radiation. Using eqs. (C.3) and (C.10) we can derive the observed flux respectively due to radiative and not-radiative neutrino decays. In our calculations, we assume that all the photons produced (or Compton-scattered) by neutrinos decaying at $z > 1000$ are thermalized by CMB photons, and then are not visible. We assume also, for simplification, that all the photons produced (or Compton-scattered) by neutrinos decaying at $z < 1000$ are not absorbed or scattered. For this reason, our calculation represents an upper limit for the optical and infrared background; however it should give a good estimate of the X-ray flux.

Soft X-ray background

A recent estimate of the soft X-ray background (SXRB), in the energy range 0.5-2.0 keV, is provided by Moretti et al. (2003; hereafter M03). Combining 10 different measurements reported in the literature, they found a flux of $2.47 \pm 0.11 \times 10^{-8}$ erg s^{-1} cm^{-2} sr^{-1}, which must be lowered to about 1.48×10^{-9} erg s^{-1} cm^{-2} sr^{-1}, if the mean contribution of both point and diffuse unresolved sources is subtracted at the level estimated by M03. Dijkstra, Haiman & Loeb (2004; hereafter D04) derive the slightly lower value $1.15 \pm 1.64 \times 10^{-9}$ erg s^{-1} cm^{-2} sr^{-1}, as they subtract a further 1.0-1.7% contribution by the diffuse component

[3]We used $n_b = 2.5 \times 10^{-7}$ cm^{-3} and $\eta = 6 \times 10^{-10}$, according to WMAP (Spergel et al. 2003).

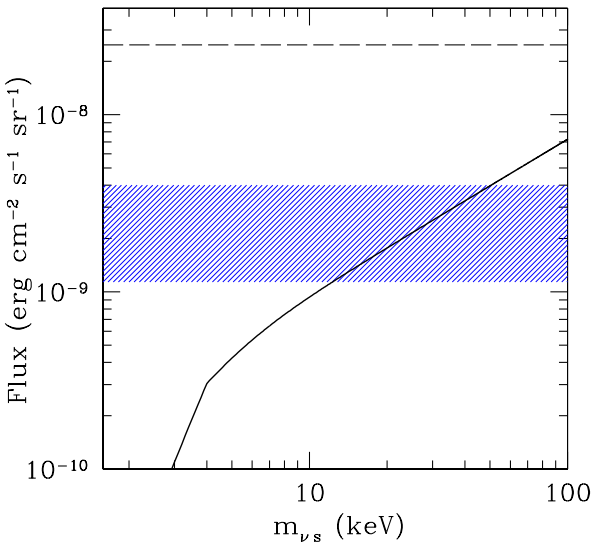

Figure C.1: Integrated flux between 0.5 and 2 keV due to radiatively decaying neutrinos as a function of the neutrino mass (*solid line*). The horizontal *dashed line* represents the total measured background (M03). The shaded area indicates the flux due to unresolved sources (B04).

due to Thomson-scattered point source radiation (Soltan 2003). D04 also suggest a maximum possible value $\sim 4.04 \times 10^{-9}$ erg s^{-1} cm^{-2} sr^{-1}, by subtracting the lower limit of unresolved sources and of Thomson scattered flux. D04 further notice that the theoretically expected amount of X-ray emission in the soft band from thermal emission by gas in clusters (Wu & Xue 2001) should represent $\sim 9\%$ of the total SXRB, considerably higher than the 6% estimated by M03. However, D04 do not include in their estimate of the background this probable additional contribution. Otherwise, the flux due to unaccounted sources should be lowered to $\sim 4.0 \times 10^{-10}$ erg s^{-1} cm^{-2} sr^{-1}.

More recently, Bauer et al. (2004; hereafter B04) investigated the X-ray number counts in the Chandra Deep Fields (CDFs). Adopting for the total SXRB from 0.5 to 2 keV the value suggested by M03 (i.e. $2.47 \pm 0.11 \times 10^{-8}$ erg s^{-1} cm^{-2} sr^{-1}), they found that its resolved fraction is $89.5^{+5.9}_{-5.7}\%$. The resolved sources are predominantly AGNs ($\sim 83\%$) and star forming galaxies ($\sim 3\%$). This means that unresolved sources produce a flux $2.59^{+1.41}_{-1.46} \times 10^{-9}$ erg s^{-1} cm^{-2} sr^{-1}.

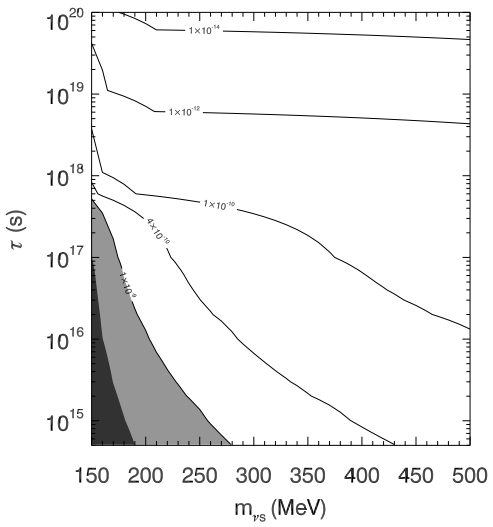

Figure C.2: Isocontours of integrated X-ray flux in the band 0.5-2 keV (units of erg cm^{-2} s^{-1} sr^{-1}) due to pion-decaying neutrinos as a function of the neutrino mass and lifetime. The light gray area indicates flux due to unresolved sources (B04). The dark gray area indicates the "forbidden" region in which the flux exceeds the maximum background flux due to unaccounted sources (B04; M03).

These limits on the SXRB are moderately important to constraint the mass of sterile neutrinos. We base our analysis on the paper by B04; in addition we have checked the values derived by M03 and by D04. The latter are consistent with those reported by B04 and give only slightly different constraints on the sterile neutrino mass. In Fig. C.1 we report the integrated flux between 0.5 and 2 keV due to radiative neutrino decays for different neutrino masses. To calculate this flux we derived the neutrino comoving density from eq. (C.4), i.e. assuming that all the dark matter is due to sterile neutrinos. Given the mass and the density, the lifetime is completely determined by eqs. (C.5) and (C.6). The flux due to sterile neutrinos is compared with the total flux predicted by M03 and with the flux due to unresolved sources (B04). As we can see from Fig. C.1, only neutrinos with masses $\lesssim 50$ keV do not exceed the maximum value of the flux due to unresolved sources (4.00×10^{-9} erg s^{-1} cm^{-2} sr^{-1}, B04); the same conclusion can be drawn by using D04 data.

We repeat the same calculation for heavy sterile neutrinos ($140 < m_{\nu s} < 500$ MeV) decaying into pions and electrons. In this case we consider the flux due to CMB

photons Compton-scattered by the electrons coming from the neutrino decay (eq. (C.10), assuming p=1). Fig. C.2 shows the isocontours of the integrated flux between 0.5 and 2 keV due to Compton-scattered CMB photons, as a function of the progenitor neutrino mass and lifetime. As we can see from the eq. (C.13), the density of neutrinos depends strongly on their mass and on the lifetime. In particular, less massive neutrinos have much higher comoving density. For this reason, and because of the largely different mass range, the observed flux has an opposite behavior with respect to radiatively decaying neutrinos. In this case the soft X-ray flux decreases increasing the neutrino mass. The flux produced by 150-500 MeV neutrinos does not violate the SXRB limit (B04), if the lifetime is $\geq 10^{17}$ s. For shorter lifetimes, neutrinos with mass lower than 190 MeV do violate the constraint imposed by unresolved sources, according to both M03/D04 and B04 estimates.

Hard X-ray background

M03 estimated the total background flux in the hard band (2-10 keV, HXRB) to be $6.63 \pm 0.36 \times 10^{-8}$ erg cm^{-2} s^{-1} sr^{-1}. They also show that the resolved fraction of this background is $88.8^{+7.8}_{-6.6}$%.Then, only the 11.2% of the hard X-ray background can be due to unaccounted sources (like sterile neutrinos).
B04 studied the HXRB flux from 2 to 8 keV, using the X-ray number counts in the CDFs. They adopted a total HXRB flux $5.88 \pm 0.36 \times 10^{-8}$ erg cm^{-2} s^{-1} sr^{-1} and found that the resolved fraction is $92.6^{+6.6}_{-6.3}$, dominated by AGNs ($\sim 95\%$). This means that the unresolved flux is only $4.35^{+3.70}_{-3.88} \times 10^{-9}$ erg cm^{-2} s^{-1} sr^{-1}.

We compared the hard X-ray flux due to sterile neutrinos with the background level estimated by B04, and we checked for consistency with M03. In particular, for radiatively decaying sterile neutrinos we found that the integrated flux in the range 2-8 keV is lower than the background flux due to unresolved sources, as estimated by B04, only if $m_{\nu s} \lesssim 11$ keV (Fig. C.3). This is a significant constraint, even if not so strong as it can be derived from clusters of galaxies (8 keV, Abazajian 2006). We must be aware of two uncertainties in our calculations. First, we made the assumption that all the dark matter is composed by sterile neutrinos. In addition, we have not taken into account the clustering of matter at low redshift, which can lead to an overestimate of the flux due to neutrinos (Abazajian et

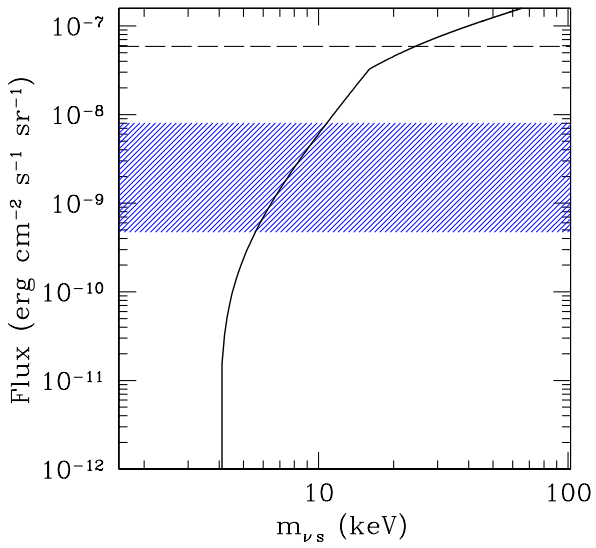

Figure C.3: Integrated X-ray flux in the range 2-8 keV due to radiatively decaying neutrinos as a function of the neutrino mass (*solid line*). The horizontal *dashed line* indicates the total background in the same band; the shaded area indicates the flux due to unresolved sources (B04).

al. 2001b).

On the other hand, the integrated flux (in the range 2-8 keV) of CMB photons scattered by heavy pion-decay neutrinos is lower than the upper limit of the background due to unresolved sources (B04) for all the neutrino masses from 150 to 500 MeV, if the lifetime is longer than $\sim 4 \times 10^{17}$ s (Fig. C.4). We obtain the same result by considering (in the range 2-10 keV) the flux due to unaccounted sources as estimated by M03. For shorter lifetimes, the minimum allowed mass increases. For example, if $\tau = 10^{15}$ s, neutrinos with masses lower than ~ 215 MeV exceed the upper limit of the background due to unresolved sources as derived by B04; whereas, using the estimate of M03, we find ~ 200 MeV.

In summary, using the HXRB we put much stronger constraints on the mass of radiatively decaying neutrinos ($m_{\nu s} \lesssim 11$ keV) than using the SXRB. This constraint is quite stronger than the value derived in Mapelli & Ferrara 2005 for the HXRB ($m_{\nu s} \lesssim 14$ keV). The difference is due to the assumption in this Thesis of a most recent expression for $\sin^2(\theta)$ (equation C.6, Abazajian 2006).

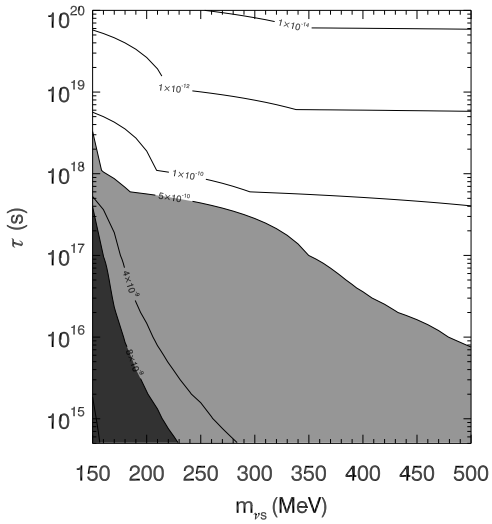

Figure C.4: Isocontours of the integrated X-ray flux in the band 2-8 keV (units of erg cm^{-2} s^{-1} sr^{-1}) due to pion-decaying neutrinos as a function of the neutrino mass and lifetime. The light gray area indicates the flux due to unresolved sources (B04). The dark gray area indicates the "forbidden" in which the flux exceeds the maximum background flux due to unresolved sources (B04).

Instead, in the case of heavy sterile neutrinos decaying into pions, all the masses from 150 to 500 MeV are allowed, provided a lifetime longer than 4×10^{17} s.

To compare our results with those obtained by Abazajian et al. (2001b), we have repeated this analysis using Gruber's model of HXRB (1992). We found that, assuming this model of HXRB, the mass of radiatively decaying neutrinos must be $m_{\nu s} \lesssim 3$ keV, in agreement with Abazajian et al. (2001b). However, in the following we will use the constraints derived using the estimates by B04 and M03, because they come from more recent data and do not require any assumption about the shape of the HXRB due to unresolved sources.

Appendix D

Absorbed energy fraction for LDM and sterile neutrinos

It can be useful to derive a fit of the energy absorbed fraction ($f_{\rm abs}$) for each considered DM particle. We calculated fits with errors smaller than 5% for $5 \lesssim z \lesssim 1000$. In the redshift range $3 \lesssim z \lesssim 5$ the errors are larger ($\lesssim 10 - 20\%$); however, at such low redshift our absorbed fractions are likely inaccurate by a larger factor, as our assumption of a mostly neutral IGM breaks down.

D.0.3 Sterile neutrinos

For the case of sterile neutrino with mass $2 \leq m_{\nu,s}\, c^2/\ {\rm keV} \leq 10$, a fit was found depending only on the redshift and the mass of the particle.

$$f_{\rm abs}(z, m_{\nu,s}) = \left[0.5 + 0.032 \left(\frac{m_{\nu,\,s}\, c^2}{8\ {\rm keV}}\right)^{1.5}\right] \left[\frac{z}{110 \left(\frac{m_{\nu,\,s}\, c^2}{8\ {\rm keV}}\right)^{2.4} + z}\right]^{0.93} . \qquad \text{(D.1)}$$

This general formula does not hold for higher masses, for which we have found

$$f_{\rm abs}(z, 15{\rm keV}) \;=\; 0.99 \left[0.5 + 0.032 \left(\frac{15\ {\rm keV}}{8\ {\rm keV}}\right)^{1.5}\right] \left[\frac{z}{110 \left(\frac{14\ {\rm keV}}{8\ {\rm keV}}\right)^{2.4} + z}\right]^{1.0}$$

$$
\begin{aligned}
f_{\rm abs}(z, 25{\rm keV}) &= 0.89 \left[0.5 + 0.032 \left(\frac{25\ {\rm keV}}{8\ {\rm keV}}\right)^{1.5}\right] \left[\frac{z}{110 \left(\frac{17\ {\rm keV}}{8\ {\rm keV}}\right)^{2.4} + z}\right]^{1.2} \\
f_{\rm abs}(z, 50{\rm keV}) &= 1.08 \left[0.5 + 0.032 \left(\frac{50\ {\rm keV}}{8\ {\rm keV}}\right)^{1.5}\right] \left[\frac{z}{110 \left(\frac{22\ {\rm keV}}{8\ {\rm keV}}\right)^{2.4} + z}\right]^{1.4} \qquad \text{(D.2)}
\end{aligned}
$$

As can be seen in fig. (5.3), these last fits do not take into account the decrease of $f_{\rm abs}$ at very high redshift, which is caused by the fact that we start integrating eq. (5.12) at redshift 1100. In fact, if we start the integration at $z = 1500$, the high redshift discrepancies between the fitting formulae above and the actual $f_{\rm abs}$ disappear; however, such a procedure is uncertain because the equations we use for describing the energy absorption might not be applicable at an epoch before recombination.

Luckily, the energy injection from sterile neutrino decays is completely negligible at such high redshift, and this uncertainty by a factor $\lesssim 2$ can be safely ignored.

D.0.4 Light Dark Matter

For LDM particles decaying into pairs, we derived two different fits, for 3 and 10-MeV particles, respectively.

$$
\begin{aligned}
f_{\rm abs}(z,\ 3\ {\rm MeV}) &= 0.49\,(1+z)^{-0.5} \exp\left[-\left(\frac{5}{1+z}\right)^{1.4}\right] + \\
&\quad + 0.058\,(1+z)^{0.28} \exp\left[-\left(\frac{164}{1+z}\right)^{1.4}\right] - 0.265 \exp\left[-\left(\frac{1220}{1+z}\right)^{1.4}\right] \\
f_{\rm abs}(z,\ 10\ {\rm MeV}) &= 0.21\,(1+z)^{-0.55} \exp\left[-\left(\frac{5.1}{1+z}\right)^{1.4}\right] + 0.222\,(1+z)^{0.18} \exp\left[-\left(\frac{185}{1+z}\right)^{1.36}\right] \qquad \text{(D.3)}
\end{aligned}
$$

Finally, for annihilating LDM particles, we derived the following fits.

$$
\begin{aligned}
f_{\rm abs}(z,\ 1\ {\rm MeV}) &= 0.32\,(1+z)^{-0.27} + 0.55\,(1+z)^{0.06} \exp\left[-\left(\frac{195}{1+z}\right)^{0.9}\right] \times \exp\left[-\left(\frac{1+z}{1900}\right)^{1.2}\right] \\
f_{\rm abs}(z,\ 3\ {\rm MeV}) &= 0.21\,(1+z)^{-0.39} + + 0.155\,(1+z)^{0.20} \exp\left[-\left(\frac{350}{1+z}\right)^{0.7}\right] + \\
&\quad + 2.9 \times 10^{-4}\,(1+z) \exp\left(-\frac{550}{1+z}\right)
\end{aligned}
$$

$$f_{\rm abs}(z,\ 10\ {\rm MeV}) \quad = \quad 0.064\,(1+z)^{-0.34} \ + \ 0.335\,(1+z)^{0.14}\,\exp\left[-\left(\frac{52}{1+z}\right)^{1.3}\right] \tag{D.4}$$

Appendix E

Blue stragglers: radial distribution and progenitors

E.1 Introduction

In this Appendix I describe a study of blue straggler stars (BSS) which I presented in Mapelli et al. 2004 and Mapelli et al. 2006. This study is not related to reionization sources; but it represents a significant part of my work during my PhD.

Blue straggler stars (BSS) are stars lying above and blue-ward of the turn-off in the color-magnitude diagram (CMD) of a star cluster. At least two different processes have been proposed to explain their formation (Fusi Pecci et al. 1992; Bailyn 1995; Bailyn and Pinsonneault 1995; Procter Sills, Bailyn & Demarque 1995; Sills & Bailyn 1999; Sills et al. 2000; Hurley et al. 2001). The first, dubbed the *mass-transfer scenario*, suggests that BSS are generated by primordial binaries (hereafter PBs) that evolve mainly in isolation until they start mass-transfer and possibly coalesce (McCrea 1964; Carney et al. 2001). The second, known as the *collisional scenario*, states that BSS are the product of a merger between two main sequence stars (MSs) in a dynamical interaction that involves a MS-MS collision, most likely in a binary-MS encounter (Davies, Benz & Hills 1994; Lombardi et al. 2002). The collisional BSS (COL-BSS) differ kinematically from the mass-transfer BSS (MT-BSS), since they are believed to acquire kicks due to dynamical recoil. In both these

hypotheses, the resulting BSS have mass exceeding the turn-off mass of the cluster and are fueled by hydrogen thanks to the mixing of the hydrogen-rich surface layers of the two progenitor stars.

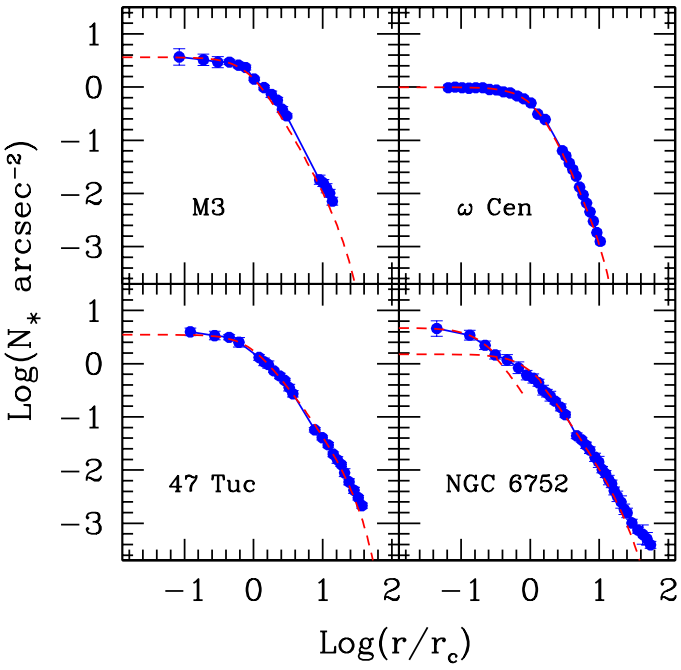

Figure E.1: Comparison between the observed surface star density profile of the considered GCs (solid line and full circles) and the adopted multi-mass King model (dashed line). The units on the y-axis are number of stars per arcsec^2. The observed profiles are taken from Ferraro et al. (1997a) for M3, Ferraro et al. (2006a) for ω Cen, Mapelli et al. (2004) for 47 Tuc, Ferraro et al. (2003b) for NGC 6752.

The two aforementioned scenarios do not necessarily exclude each other and might coexist within the same star cluster (Ferraro et al. 1993; Davies, Piotto & De Angeli 2004; Mapelli et al. 2004). However, until recently, it has been difficult to estimate the relative importance of the two formation channels in a given globular cluster (GC). A new approach to solve this problem has been presented by Mapelli et al. (2004; hereafter paper I), who revised and upgraded an original attempt by Sigurdsson, Davies & Bolte (1994). The basic input for the new method is the observation of the shape of the BSS radial distribution in a star cluster. After the pioneering works on M3 (Ferraro et al. 1993; Ferraro et al. 1997a)

and M55 (Zaggia et al. 1997), accurate determinations of the spatial distribution of BSS are now being obtained for an increasing sample of GCs (Ferraro et al. 2004 for 47 Tuc; Sabbi et al. 2004 for NGC 6752; Ferraro et al. 2006a for ω Cen; Warren, Sandquist & Bolte 2006 for M5). A very interesting result is emerging from these observations: BSS display a clear tendency to follow a bimodal spatial distribution, with a peak in the core, decreasing at intermediate radii and rising again at larger radii.

In paper I, Mapelli et al. focused on 47 Tuc and showed that the bimodal distribution can be reproduced assuming a suitable combination of the two proposed mechanisms for forming BSS. In particular, it was suggested (paper I) that the BSS in the core of 47 Tuc are mainly COL-BSS, while the external BSS are MT-BSS. This result agrees with studies of the BSS luminosity function in 47 Tuc (Bailyn & Pinsonneault 1995; Sills & Bailyn 1999; Sills et al. 2000; Ferraro et al. 2003b; Monkman et al. 2006).

In this Appendix, we explore two other GCs, whose BSS have a bimodal radial distribution. The aim is to test whether the conclusions drawn for 47 Tuc can be extended to GCs having different mass, concentration, central density, and velocity dispersion with respect to 47 Tuc. In particular, we study whether the position of a BSS in a GC can reliably be regarded as a signature for its origin. We also consider the case of ω Cen, whose radial distribution of BSS is flat. We follow the same procedure of paper I, carrying out dynamical simulations of BSS evolved in the gravitational potential well of their associated cluster. Details about the simulations are illustrated in Section E.2; the sample of the investigated clusters is presented in Section E.3. The results for M3, NGC 6752 and 47 Tuc are discussed in Section E.4, whilst Section E.5 is devoted to the outlier, ω Cen. In Section E.6 we discuss our findings in comparison with the findings of Davies et al. (2004). Finally in Section E.7 we present our conclusions.

E.2 The simulations

The simulations have been performed with an upgraded version (fully described in paper I) of the code originally developed by Sigurdsson & Phinney (1995). This code follows the dynamical evolution of a BSS in a static cluster background, which is modeled using a

Table E.1: Globular cluster parameters

	r_c (pc)	σ (km s^{-1})	n_c (stars pc^{-3})	W_0	c	references[a]
47 Tuc	0.47	10	2.5×10^5	12	1.95	1, 2
M3	1.5	4.8	6×10^3	10	1.77	1, 3
NGC 6752	0.1, 0.58[b]	4.9, 12.4[c]	2×10^5	13, 12[b]	2.03, 1.95[b]	1, 4
ω Cen	4.1	17	5.6×10^3	6.5	1.40	5

[a]References: 1 Dubath et al. 1997; 2 Mapelli et al. 2004; 3 Sigurdsson et al. 1994; 4 Drukier et al. 2003; 5 Merritt, Meylan & Mayor 1997.

[b] The double value of W_0 and c for NGC 6752 is due to the fact that the profile of this cluster is fit with a double King model. $W_0 = 13$ and $c = 2.03$ refer to the inner King (with core radius 5.7"= 0.1 pc for a distance of 4.3 kpc from the Sun; Ferraro et al. 2003); while $W_0 = 12$ and $c = 1.95$ refer to the outer King (with core radius 28"= 0.58 pc; Ferraro et al. 2003).

[c] The double value of σ for NGC 6752 refers to the two measurements σ=$4.9^{+2.4}_{-1.4}$ km s^{-1} (Dubath et al. 1997) and σ=12.4±0.5 km s^{-1} (Drukier et al. 2003).

multi-mass King density profile. In this case, once the classes of mass have been selected, the cluster background is uniquely determined by imposing a central velocity dispersion σ, a core stellar density n_c and a dimensionless central potential W_0 ($W_0 \equiv \Psi(0)/\langle\sigma\rangle^2$, where $\langle\sigma\rangle$ is the mean core velocity dispersion and $\Psi(0) \equiv \Phi(r_t) - \Phi(0)$, with $\Phi(r)$ the gravitational potential at the radius r and r_t the tidal radius). In practice, we have chosen 10 classes of mass (the same classes reported in Table 1 of paper I) and have adopted the best available estimates of σ and n_c for each of the considered clusters. The values of W_0 for each GC have been derived by fitting the simulated star density profile to the observed one (see Section E.3 and Table E.1 for details).

Once the background has been determined, the dynamical evolution of the current population of BSS is simulated assuming a value for the ratio between the number of MT-BSS and that of COL-BSS. As far as the birth places are concerned, we assume that COL-BSS are generated exclusively in the innermost region, within the core radius (r_c), where the star density highest, leading to a high collision rate (Leonard 1989; Pooley et al. 2003). MT-BSS can be generated everywhere in the cluster, but are expected to be more frequent in the peripheral regions, where PBs can evolve in isolation, without suffering exchange or ionization by gravitational encounters (Sigurdsson & Phinney 1993; Ivanova et

al. 2004). For this reason, in our simulations the MT-BSS, formed in PBs, are generated outside the cluster core with initial locations distributed in several radial intervals, between 1 and 80 r_c. Within this region, all initial positions are randomly chosen following a flat probability distribution, according to the fact that the number of stars N in a King model scales as $dN = n(r)\, dV \propto r^{-2}\, \pi r^2 dr \propto dr$.

BSS velocities are randomly generated following the distribution illustrated in Section 3 of Sigurdsson & Phinney 1995 (eq. 3.3). In addition, we assign a natal kick velocity $v_{\rm kick}$ equal to $1 \times \sigma$ to those BSS formed collisionally in the core. We tried also different values of $v_{\rm kick}$. In agreement with paper I, we find that $v_{\rm kick}$ higher than $2 - 3 \times \sigma$ causes the ejection of most of the BSS from the cluster, while there are no significant differences in the results for kick velocities ranging between 0 and $2 \times \sigma$. The masses of the BSS range between 1.2 and 1.5 $M_\odot$. In paper I, we extended our analysis up to a mass of 2 $M_\odot$ (Ferraro et al. 1997a; Gilliland et al. 1998); but now more stringent constraints are coming from observations (*e.g.* the upper limit for the mass of BSS in ω Cen is 1.4 $M_\odot$; Ferraro et al. 2006a). On the other hand, in paper I we found that there is not significant difference between the behaviour of a 1.2 and a 2 $M_\odot$ BSS. Each single BSS is evolved for a time $t_i = f_i\, t_{\rm last}$, where f_i is a random number uniformly generated in [0, 1] and $t_{\rm last}$ is the maximum lifetime attributed to a BSS. Given the uncertainty on the value of $t_{\rm last}$, we have performed various sets of runs with $t_{\rm last}$ spanning the range between 1 and 5 Gyr. Consistent with the results of paper I, the best fits are all obtained for $t_{\rm last}$= 1.5 Gyr. For 1 Gyr $\lesssim t_{\rm last} \lesssim$ 2 Gyr the distribution does not change dramatically. If we choose a longer lifetime (3 Gyr or more), the dynamical friction washes out any peak of peripheral BSS; whereas for shorter lifetimes (less than 1 Gyr) any BSS could be hardly observable today.

Our code follows the dynamical evolution of the BSS in the cluster potential, subject to the action of dynamical friction and to the effects of distant encounters (eq. [3.4] of Sigurdsson and Phinney 1995).

The final positions of the BSS in each run determine the simulated radial distribution, to be compared with the observed one. We ran 10000 experiments for each of the considered cases. Since we studied $\sim$ 10 different cases for each cluster, we made about $\sim$ 400000 runs in total.

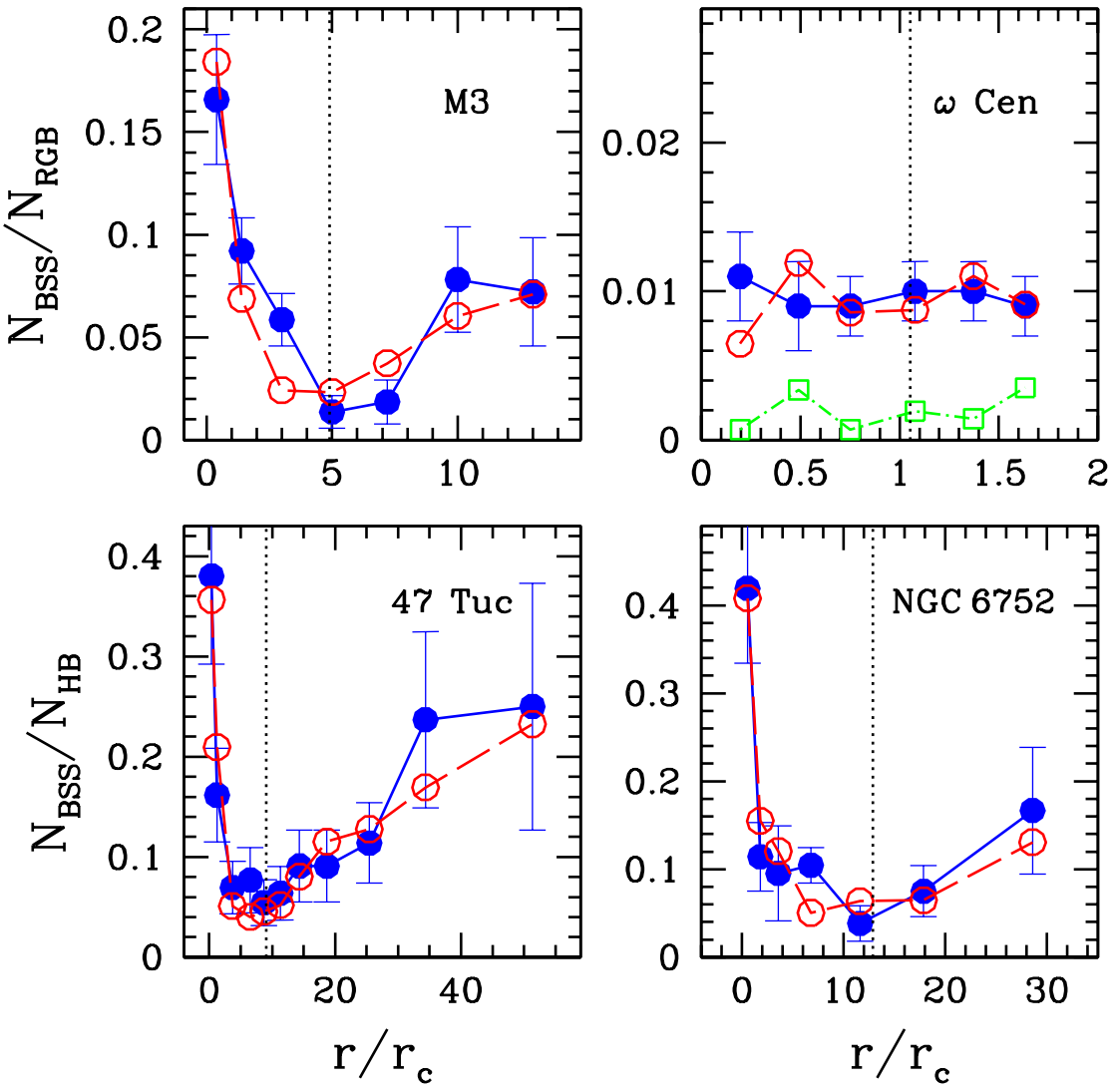

Figure E.2: Radial distribution of BSS normalized to the distribution of horizontal branch (HB) stars (47 Tuc, NGC 6752) or red giant branch (RGB) stars (M3, ω Cen). Filled circles and solid lines indicate the data taken from Ferraro et al. 1997a (M3), Ferraro et al. 2006a (ω Cen), Ferraro et al. 2004 (47 Tuc), Sabbi et al. 2004 (NGC 6752). Open circles and dashed lines indicate the best fits obtained from our simulations. For NGC 6752 we adopted $r_c = 28''$ (see caption of Table E.1). The dotted vertical line in all the panels shows the characteristic radius of the zone of avoidance r_{av} (see text and Table E.2). In the panel of ω Cen, the open squares and the dot-dashed line connecting them report the ratio N_{XMM}/N_{RGB}, that is the number of X-ray sources detected in ω Cen by XMM (Gendre et al. 2003) normalized to the number of RGB stars.

E.3 The sample of globular clusters

We have studied the distribution of BSS in four different GCs: M3, 47 Tuc, NGC 6752 and ω Cen. They represent a very inhomogeneous sample of GCs. M3 is an intermediate density (6×10^3 stars pc^{-3}; Sigurdsson, Davies & Bolte 1994), low velocity dispersion (4.8 km s^{-1}; Dubath, Meylan & Mayor 1997) cluster. 47 Tuc and NGC 6752 are two very concentrated, maybe core collapsed clusters. ω Cen is the most massive among the Galactic GCs ($5 \times 10^6\,M_\odot$; Pryor & Meylan 1993; Meylan et al. 1995) and it is still a matter of debate whether it is a GC or the remnant of a dwarf galaxy (Zinnecker et al. 1988; Freeman 1993; Ideta & Makino 2004): it is a very loose cluster, with a wide metallicity spread and a clear evidence for rotation (van Leeuwen et al. 2000; Reijns et al. 2006; van de Ven et al. 2006).

The first step of our work consisted in finding the best match between the simulated star density profile of each cluster and the observed one. The results are shown in Fig. E.1. The data of the star density profile of M3, NGC 6752 and ω Cen are from Ferraro et al. (1997a), Ferraro et al. (2003) and Ferraro et al. (2006a), respectively. The star density profile of 47 Tuc is the same published in paper I. Note that we fit the profile of NGC 6752 with a double King model, as in Ferraro et al. (2003). The adopted values of σ and n_c, and the fit values of W_0 are given in Table E.1, as well as the concentration parameter c (where $c = \log(r_t/r_c)$) and the fiducial values of r_c in parsec. The latter quantities are derived by assuming a distance from the Sun of 4.6 kpc (47 Tuc, Ferraro et al. 1999, see also Table 3 by Beccari et al. 2006), 10.1 kpc (M3, Ferraro et al. 1999), 4.3 kpc (NGC 6752, Ferraro et al. 1999) and 5.5 kpc (ω Cen, Bellazzini et al. 2004).

The data for the radial distribution of BSS are taken from Ferraro et al. (1997a) for M3, Ferraro et al. (2004) for 47 Tuc, Sabbi et al. (2004) for NGC 6752 and Ferraro et al. (2006a) for ω Cen. As usual, the number of BSS is normalized to the number of red giant branch (RGB) stars or to the number of horizontal branch (HB) stars. Even if the considered GCs are very different from each other, the observed radial distributions of BSS are similar (see Fig. E.2), with the exception of ω Cen. In fact, the radial distribution of BSS displays a maximum in the central region of the GC, decreases down to a minimum at

intermediate radii (of order $5\,r_{\rm c} - 10\,r_{\rm c}$) and increases again at outer radii. ω Cen differs as it shows an almost flat distribution.

E.4 Results and Discussion for M3, 47 Tuc and NGC 6752

We have explored whether the radial distribution of BSS observed in our sample of GCs can be reproduced with a model which predicts two different classes of progenitors for the BSS: *(i)* PBs evolved in isolation and *(ii)* binary (or single) stars which underwent collisions in the high density environment of the GC core. Fig. E.2 shows the results obtained for M3, 47 Tuc, NGC 6752 and ω Cen. In all cases, our adopted model provides a statistically acceptable fit to the observations. The best fit value of the fraction $\eta_{\rm MT}$ of MT-BSS with respect to the total number of BSS [*i.e.* $\eta_{\rm MT} \equiv N_{\rm MT-BSS}/(N_{\rm MT-BSS} + N_{\rm COL-BSS})$, where $N_{\rm MT-BSS}$ and $N_{\rm COL-BSS}$ are the number of mass-transfer and collisional BSS, respectively] is reported in Table E.2, as well as the reduced χ^2 of the best fit solution.

In order to determine the best fit solution, we have created a one-dimensional grid of simulations for each cluster, allowing the only free parameter in our model[1], $\eta_{\rm MT}$, to vary between 0 and 1 with an initial step of 0.2. Then, the grid was iteratively refined down to a step of 0.01 for the values surrounding the best fit.

The values $\tilde{\chi}^2$ of the reduced χ^2 were derived by comparing each simulation with the observed data and their uncertainties. The range of values for $\eta_{\rm MT}$ in the second column of Table E.2 is calculated at $2-\sigma$ level, *i.e.* by selecting all the simulations for which $\chi^2 \leq \chi^2_{\rm best} + 4$, where $\chi^2_{\rm best}$ is the value for the best fit solution.

Inspection of Table E.2 reveals a clear dichotomy between the cases of 47 Tuc, M3 and NGC 6752 and that of ω Cen. The $2-\sigma$ intervals of confidence for $\eta_{\rm MT}$ for the first three GCs are in agreement with an almost even distribution of MT-BSS and COL-BSS (a slight predominance of COL-BSS being indicated by the best fit models). Instead, in the best fit model of ω Cen only 14% of BSS are COL-BSS and the $2-\sigma$ interval of confidence

[1]Other possible parameters (such as the initial velocity of BSS) were found to have only minor impact on the results (see Section E.2) and have been set to a fixed value in all the considered runs. Also, the cluster properties are not free parameters in the fitting procedure, because they have been chosen *a priori* (see Section E.3) and kept fixed in all simulations of a given cluster. An exception was made only for the peculiar case of the velocity dispersion in NGC 6752 (see Section E.4.3).

is compatible with $\eta_{\rm MT} = 1$.

In the following, we will discuss the case of these three clusters separately, whereas ω Cen will be examined in Section E.5.

E.4.1 M3

In the case of M3, our findings contrast earlier suggestions by Sigurdsson et al. (1994). They hypothesized that the BSS observed in the peripheral regions of M3 could be COL-BSS born initially in the core and then ejected in the periphery because of their natal kick. Indeed, our dynamical simulations show that COL-BSS are ejected from the entire cluster (if the kick is too high), or sink back to the core in $\lesssim 1$ Gyr, if the kick is low enough to retain them in the cluster potential well. Hence, they cannot account for the peripheral BSS. Instead, MT-BSS have in general much more circular orbits than the COL-BSS and can remain in the peripheral regions of the GC for a time comparable to the typical lifetime of a BSS.

E.4.2 47 Tuc

As for 47 Tuc, we confirm the main outcome from paper I: *i.e.* most of the central BSS of 47 Tuc are born from collisions and all the peripheral BSS originate from mass-transfer in binaries. However, in paper I it was suggested that only $\sim 25\%$ of the total BSS are MT-BSS. The upward correction of this estimate is due to the fact that we have refined our parameter grid with respect to paper I. In paper I we considered only cases with a relatively low fraction of MT-BSS ($\lesssim 30\%$) and one single case with $\eta_{\rm MT} = 1$. For this Appendix we explored a more complete parameter space (see Mapelli et al. 2006), the percentage of MT-BSS (with respect to the total number of BSS) going from 0 to 100%. Our present best fit (46% MT-BSS and 54% COL-BSS) is still consistent (at $2-\sigma$) with the result of paper I (25% MT-BSS and 75% COL-BSS), given the observational uncertainties, especially in the central bins (see Fig. E.2).

E.4.3 NGC 6752

The parameters of the best fit model for NGC 6752 are similar to those inferred for M3 and 47 Tuc. However, for this cluster there may be a caveat about the central velocity dispersion, whose value is still very uncertain. From the integrated-light spectra of the core, Dubath et al. (1997) derived $\sigma = 4.9^{+2.4}_{-1.4}$ km s^{-1}. More recently, from proper motion measurements of a sample of $\sim$ 1000 stars with the WFPC2/HST, Drukier et al. (2003) obtained $\sigma = 12.4 \pm 0.5$ km s^{-1}. Thus, we ran simulations for each of these two possibilities.

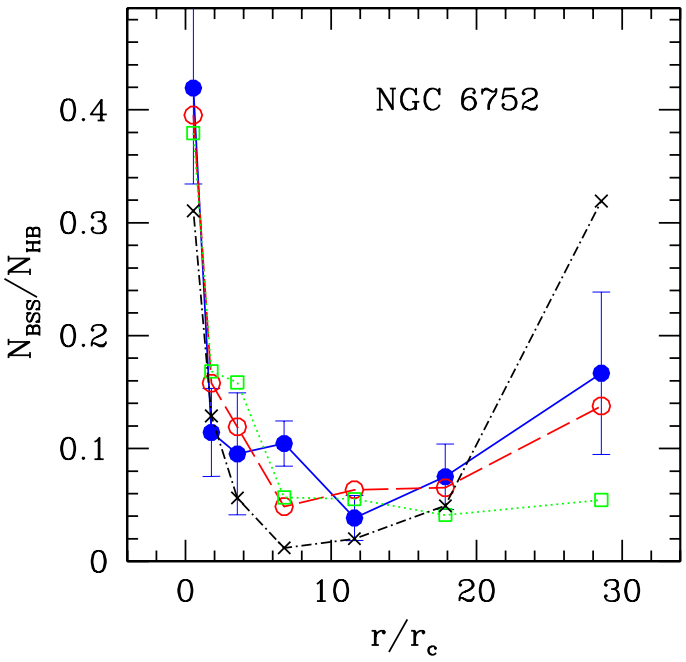

Figure E.3: Distribution of BSS normalized to the distribution of HB stars in NGC 6752. The solid line indicates the observations (filled circles; Sabbi et al. 2004). The dotted line (connecting open squares) reports the best fit numerical simulation for $\sigma = 4.9$ km s^{-1}; the long-dashed line (connecting open circles) is for $\sigma = 7$ km s^{-1} (reported also in Fig. E.2); the dot-dashed line (connecting crosses) is for the case $\sigma = 12.4$ km s^{-1}. In all these cases $t_{\rm last} = 1.5$ Gyr. The short-dashed line connecting open triangles is obtained for $\sigma = 12.4$ km s^{-1} and $t_{\rm last} = 4$ Gyr.

If we assume $t_{\rm last} = 1.5$ Gyr, the best fit model obtained for $\sigma = 4.9$ km s^{-1}

(Fig. E.4.3) is not satisfactory, since we cannot reproduce the increasing number of BSS located in the cluster outskirts. In fact, a low velocity dispersion implies that the dynamical friction time-scale is too short ($\ll 1$ Gyr) and PBs rapidly shrink towards the core. If we adopt $\sigma = 12.4$ km s^{-1}, the rising trend of the BSS radial distribution in the cluster periphery can be reproduced; but the $\tilde{\chi}^2$ (~ 5) is still unacceptable, because of the disagreement with the data points in the inner regions. Since none of the two options were satisfying, we ran new simulations for other values of σ (ranging between 4.9 and 12.4 km s^{-1}), until we found an acceptable fit to the observed BSS distribution. That occurs for $\sigma = 7^{+3}_{-1}$ km s^{-1} ($\tilde{\chi}^2 = 1.7$, reported in Table E.2), marginally consistent with the measurement of Dubath et al. (1997).

However, for this cluster other marginally acceptable solutions for the BSS radial profile exist: *e.g.* assuming $t_{\rm last} = 4$ Gyr, a fit ($\tilde{\chi}^2 \lesssim 3$) can be obtained also for $\sigma = 12.4$ km s^{-1} (open triangles and short-dashed line in Fig. E.4.3). Considering this uncertainty and the peculiarities of NGC 6752 (*e.g.* the unusual density profile), the aforementioned best fit value $\sigma = 7^{+3}_{-1}$ km s^{-1} cannot be taken as an indirect measurement of the central velocity dispersion in the cluster. A new measurement of σ is strongly needed to understand the dynamics and evolution of NGC 6752.

E.4.4 The location of the minimum in the BSS radial distributions

The radial distribution of BSS (normalized to the number of RGB or HB stars) in M3, 47 Tuc, and NGC 6752 clearly displays a minimum at a distance from the cluster center in the range $5 - 10\, r_{\rm c}$. The area surrounding this minimum was dubbed "zone of avoidance" (paper I). We expect that its location roughly corresponds to the radius $r_{\rm av}$ below which all the PBs of mass $\gtrsim m_{\rm BSS}$ (where $m_{\rm BSS}$ is the minimum mass for generating BSS via mass-transfer) have already sunk towards the cluster center because of dynamical friction. In other words, there is a small probability of observing a MT-BSS located at a distance from the cluster center of the order of $r_{\rm av}$. Most likely, the MT-BSS which were originally located at $r \lesssim r_{\rm av}$ can now be detected at $r \lesssim r_{\rm c}$.

The time of dynamical friction $t_{\rm df}$ for a mass $m_{\rm BSS}$ located at a radius r from the

center of a GC is given by (Binney & Tremaine 1987)

$$t_{\rm df} = \frac{3}{4\,\ln\Lambda\,G^2(2\,\pi)^{1/2}}\,\frac{\sigma(r)^3}{m_{\rm BSS}\,\rho(r)}, \tag{E.1}$$

where $\ln\Lambda \sim 10$ is the Coulomb logarithm and G the gravitational constant. $\rho(r)$ and $\sigma(r)$ are the cluster density and the velocity dispersion at the radius r. We note the dependence of $t_{\rm df}$ on the density $\rho(r)$ and especially on the cube of the velocity dispersion. Given the definition of this time-scale, $r_{\rm av}$ can be calculated setting $t_{\rm df} = t_{\rm gc}$, where $t_{\rm gc}$ is the lifetime of the cluster ($\sim$ 12 Gyr), and using the simulated stellar density profile and the velocity dispersion distribution of the cluster for inferring $r_{\rm av}$ from $\rho(r_{\rm av})$ and $\sigma(r_{\rm av})$. In doing the calculation, we choose $m_{\rm BSS} = 1.2\,{\rm M}_\odot$.

The results (for $r_{\rm av}$ normalized to $r_{\rm c}$) are shown in the last column of Table E.2 and in Fig. E.2 (vertical dotted line). The values of $r_{\rm av}$ are always consistent with the zone of avoidance observed in the data. This confirms for M3 and NGC 6752 what had been found for 47 Tuc (paper I).

Third and fourth columns of Table E.2 report the values of the fraction $\eta_{\rm MT}$ *(i)* for the MT-BSS located within the GC core $r_{\rm c}$ ($\eta_{\rm MT}(< r_{\rm c})$), and *(ii)* for the MT-BSS found at a distance from the cluster center larger than $r_{\rm av}$ ($\eta_{\rm MT}(> r_{\rm av})$). These findings indicate that the position of a BSS in a GC (at least in those showing a bimodal distribution of the BSS) can be used as a strong indication of the nature of the progenitor. In particular, a BSS which is located outside the zone of avoidance almost certainly is a MT-MSS; on the contrary, a BSS found close to the cluster core is a COL-BSS.

Among the considered clusters, only ω Cen does not show any zone of avoidance. If we calculate the expected radius of avoidance also for this cluster, we find $r_{\rm av} \sim r_{\rm c}$. This indicates that in ω Cen the dynamical friction is far less efficient than in the other clusters. In ω Cen the value of $\eta_{\rm MT}(> r_{\rm av})$ is similar to the other clusters, whereas $\eta_{\rm MT}(< r_{\rm c})$ is much higher (see Section E.5).

We note that very similar values of both $\eta_{\rm MT}$ and $r_{\rm av}/r_{\rm c}$ have been obtained for an intermediate density GC (M3) and for two much denser clusters (47 Tuc and NGC 6752). The analogy between these three clusters is even more evident in Fig. E.4.4, where radial distances are normalized to the avoidance radius, $r_{\rm av}$. The radial distributions of BSS in

M3, 47 Tuc and NGC 6752 nearly superimpose. This also indicates that $r_{\rm av}$ is a crucial parameter in describing the bimodal distribution of BSS.

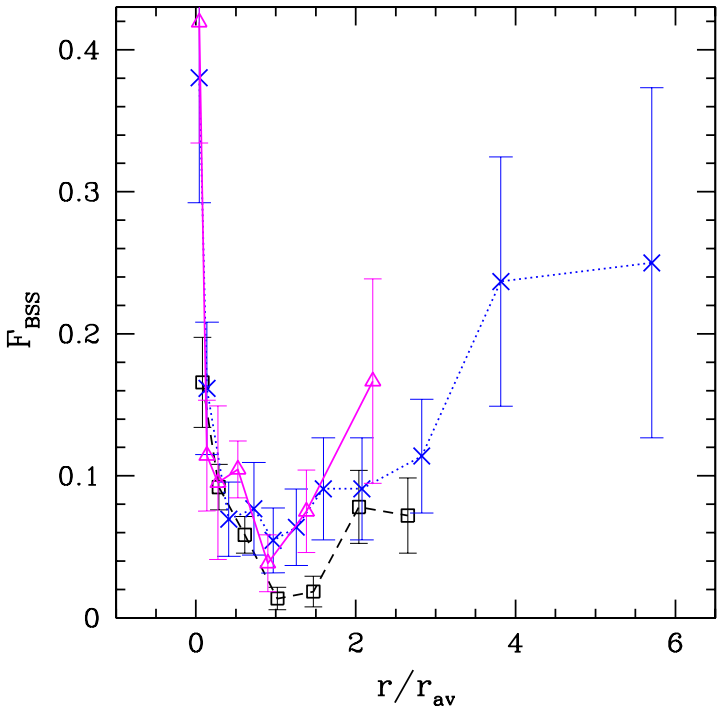

Figure E.4: Observed distribution of BSS normalized to the distribution of HB (47 Tuc, NGC 6752) or RGB stars (M3). On the x-axis we plot the distance from the center normalized to $r_{\rm av}$. Crosses indicate the observational data for 47 Tuc, open squares for M3 and open triangles for NGC 6752. The observational points are connected by a dashed line for M3, a dotted line for 47 Tuc and a solid line for NGC 6752.

E.5 The case of ω Centauri

The main characteristic of the BSS radial distribution of ω Cen, with respect to the other clusters discussed here, is the absence of any central peak. In Fig. E.2 we show the high-resolution portion of the data-set presented by Ferraro et al. (2006a): the distribution appears to be flat. This is quite unusual, since in all the other GC surveyed up to now the BSS distribution is peaked at the cluster center. Fig. 6 by Ferraro et al. (2006a) suggests that this behaviour extends up to at least $\sim 7\,r_{\rm c}$ ($\sim 20'$ from the cluster center).

Table E.2: Mass Transfer vs Collisional Scenario

	$\eta_{\rm MT}$	$\eta_{\rm MT}(< r_{\rm c})$	$\eta_{\rm MT}(> r_{\rm av})$	$\tilde{\chi}^2$	$r_{\rm av}/r_{\rm c}$
47 Tuc	$0.46^{+0.06}_{-0.22}$	$0^{+0.002}_{-0}$	$0.95^{+0.02}_{-0.10}$	0.5	9.0
M3	$0.41^{+0.16}_{-0.20}$	$0^{+0.002}_{-0}$	$0.91^{+0.02}_{-0.01}$	2.2	4.9
NGC 6752	$0.41^{+0.12}_{-0.04}$	$0.02^{+0.03}_{-0.02}$	$0.97^{+0.01}_{-0.05}$	1.7	12.9
ω Cen	$0.86^{+0.14}_{-0.08}$	$0.64^{+0.36}_{-0.04}$	$0.90^{+0.10}_{-0.002}$	0.8	1.05

The second column reports the fraction $\eta_{\rm MT}$ of MT-BSS with respect to the total number of BSS (the errors are at $2-\sigma$, *i.e.* referred to $\chi^2 = \chi^2_{\rm best} + 4$). The third (fourth) column reports the fraction of MT-BSS inside $r_{\rm c}$ (outside $r_{\rm av}$) with respect to the total number of BSS inside $r_{\rm c}$ (outside $r_{\rm av}$). The fifth column lists the reduced χ^2 obtained for the best fit models. The rightmost column reports $r_{\rm av}$ normalized to $r_{\rm c}$.

This peculiarity adds to the many other unique features displayed by ω Cen (see Section E.3); but our simple model provides a satisfactory fit to the data (see Fig. E.2 and Table E.2) also in this case. However, at variance with the results for the three clusters examined in Section E.4, the best fit model requires that a large majority of the BSS are born from PBs (see Table E.2). In other words, only a mere $\sim 14\%$ of the BSS detected in ω Cen may have a collisional origin, *i.e.* we expect that only ~ 44 of the 313 BSS reported by Ferraro et al. (2006a) are COL-BSS.

The alternative hypothesis that all the others BSS formed via collisions have been ejected from ω Cen sounds unrealistic, since the central escape velocity of ω Cen (~ 40 km s^{-1}) is comparable with that of other clusters in our sample and there is no motivation for assuming that collisions in ω Cen should generate larger recoil velocities with respect to other clusters. As a consequence, the dynamical modeling of the BSS presented in this work predicts that COL-BSS are now produced with a low rate in ω Cen.

Are there viable explanations for this underproduction of COL-BSS in ω Cen? We can just note that the characteristic radius $r_{\rm av}$ for ω Cen is much smaller (both in terms of $r_{\rm c}$ and of physical units) than in the other clusters of our sample ($r_{\rm av} \sim r_{\rm c}$ instead of the typical value ranging between 5 $r_{\rm c}$ and 15 $r_{\rm c}$). This means that only a small number of PBs had enough time to sink into the core due to mass segregation.

PBs that sink within the core are thought to be the progenitors (as far as modified

by three body interactions) of most of the binaries hosted in the core of current GCs, since the formation of binaries from two-body interactions is a quite unlikely process. Because of their large cross-section, core binaries suffer repeated three- and four-body interactions, eventually exchanging companions, being ionized or hardened. Thus, core binaries are required to form COL-BSS, via three- or four-body encounters. Then, the relative lack of binaries in the core of ω Cen, due to the inefficiency of dynamical friction, could have quenched the formation of COL-BSS.

This view could be strongly supported by the observation of a low ($\ll$ 10 %) fraction of binaries in the core of ω Cen. Unfortunately, this fraction cannot be derived with classical methods (Rubenstein & Bailyn 1997; Bellazzini et al. 2002), because of the wide spread in metallicity of the stars in this GC (Norris et al. 1996; Suntzeff & Kraft 1996). An indirect indication of the occurrence of a low fraction of binaries in the core of ω Cen comes from inspection of Fig. E.2, which shows the radial distribution of the X-ray sources observed in ω Cen by XMM (Gendre et al. 2003), normalized to the number of RGB stars. Most of the X-ray sources are believed to be cataclysmic variables or low mass X-ray binaries (Gendre et al. 2003). So they should be among the most massive objects in the GC. Their flat radial distribution further supports the hypothesis that mass segregation in ω Cen has not driven yet a sizeable number of massive binaries in the central region.

E.6 Number of BSS versus M_V

Until now, we only considered the relative frequency of BSS, *i.e.* the number of BSS normalized to that of HB and/or RGB stars. But what happens if we consider just the number of BSS hosted in each cluster, without any normalization?

First of all, it is worth noting that NGC 6752 (ω Cen) hosts about three times fewer (more) BSS than either 47 Tuc or M3 (Fig. E.6). We can ask whether this is at all correlated to the mass of the host cluster, or, equivalently, to its absolute magnitude M_V? Plotting in Fig. E.6 the total number of observed BSS per cluster against M_V for our four clusters, we do not see any straight correlation. This result agrees with the fact that Piotto et al. (2004) found evidence, in a large sample of GCs, of a lack of correlation of the

number of observed BSS with either stellar collision rate (as would be expected if all BSS were collisional in origin) or mass (which is proportional to the collision rate).

This fact led Davies et al. (2004) to propose that BSS are made through both channels, suggesting that the number of COL-BSS tends to increase with cluster mass, while MT-BSS tend to decrease with total mass, as PBs drifting by dynamical friction in the core had already time to burn as BSS in the past. The combination of these two competing behaviours was found to produce a population of BSS weakly dependent on the total mass and core collision rate of their host GC.

Fig. E.6 sketches the predictions by Davies et al. (2004). In particular, the dashed (dotted) line indicates the contribution expected from the MT- (COL-)BSS; the solid line is the total.

47 Tuc and M3 lie close to the solid line and, according to the Davies et al.'s model, their current BSS population is obtained by a blending of COL-BSS and MT-BSS contributing in roughly equal number. This fully agrees with what we found from the comparison between our simulations and the radial distribution of BSS.

In contrast, our model and Davies et al.'s scenario disagree in the case of both NGC 6752 and ω Cen. NGC 6752 lies well below the solid curve. According to Davies et al. (2004), its BSS should predominantly be MT-BSS; whereas in our model NGC 6752 should host MT-BSS and COL-BSS nearly in equal number. In the Davies et al.'s model ω Cen is expected to have only COL-BSS, while we have shown that MT-BSS should dominate[2].

Moreover, though the picture proposed by Davies et al. (2004) is interesting, detailed cluster-to-cluster comparisons suggest a much more complex scenario, where the dynamical history, the original PB content and the current dynamical state of each cluster seem to play a major role (Ferraro et al. 2003b). Indeed, clusters with the same integrated magnitude harbor quite different BSS populations. In particular, two GC pairs offer the possibility of demonstrating the complexity of the emerging scenario: *(i)* M3 and M13 are almost twins GCs (Ferraro et al. 1997b). They have the same integrated magnitude ($M_V \sim -8.6$), same metallicity ($[Fe/H] = -1.6$), same mass, but display a quite different BSS content (Ferraro et al. 2003b). In particular, M13 harbors a factor 5 fewer BSS than

[2]Davies et al. (2004) admit that their model is not adaptable to slow evolving GCs like ω Cen.

M3. *(ii)* NGC 6752 has an integrated magnitude ($M_V \sim -7.7$) which is quite similar to M80 ($M_V \sim -7.9$); but again the BSS content in the two clusters turns out to be quite different: NGC 6752 harbors a BSS population which is a factor 10 lower than that found in M80 (note that the BSS population of M80 is comparable in size to that found in ω Cen). Ferraro et al. (1999) suggested that the anomalously large population of BSS in M80 could have originated in the core-collapsing phase of this cluster.

The model discussed in this Appendix is based on a different approach from that of Davies et al. (2004). Neither this work nor Davies et al.'s accounts for the dynamical evolution of the cluster; but we consider additional information in comparison with Davies et al. (2004), *i.e.* the observed BSS radial distribution.

Davies et al. (2004) try to predict the properties of the BSS from the present properties of the host cluster, and these properties might not reflect all the stages in the cluster evolution. In particular, they risk overlooking the importance of the earlier evolutionary phases which can have a strong impact on the characteristics of BSS population.

In our approach the cluster evolution is frozen for the last 2 Gyr only, when the cluster properties are not expected to have changed significantly. All the effects of the previous evolution of the cluster onto BSS are intrinsically stored in the initial parameters which we impose on the BSS population: masses, lifetimes, velocities, locations and the amount of injected MT-BSS and COL-BSS. Hence, we can use the observed BSS radial profile for inferring the ratio between the injected MT-BSS and COL-BSS (which is related to their location), and for investigating the effects of the cluster (present) properties on that (*e.g.* what is the importance of collisions in the recent life of the cluster; and, what is the residual fraction of PBs needed to remain in periphery up to now).

Both these methods need refinements; however, the approach presented in this Appendix has the advantage that it is able to fit the BSS population also in clusters where Davies et al.'s method appears inaccurate. A complete understanding of the relation between a cluster and its BSS population will likely be possible only by running N-body simulations of the cluster from its formation, accounting also for three-body encounters, PB evolution, stellar evolution, etc.

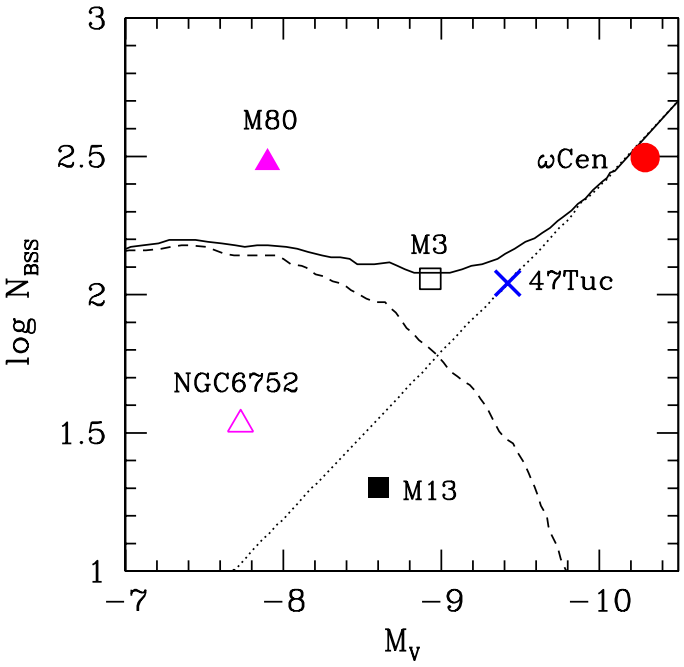

Figure E.5: Number of BSS as a function of the cluster absolute magnitude M_V. Open triangle refers to NGC 6752, filled triangle to M80, open square to M3, filled square to M13, cross to 47 Tuc, filled circle to ω Cen. The values of M_V come from the Harris catalogue (Harris 1996; `http://physwww.mcmaster.ca/%7Eharris/mwgc.dat`). The solid line shows the model by Davies et al. (2004), while the dashed (dotted) line refers to the MT-BSS (COL-BSS) according to the same model.

E.7 Summary

We have exploited the recent determination of the radial distribution of BSS in four GCs, in order to investigate which mechanism of BSS formation prevails in these stellar systems. Our conclusion is that the two main formation paths proposed so far, *i.e.* mass-transfer in PBs and merging of MS stars due to collisions in the cluster core, must *coexist and have similar efficiency both in a low density cluster (M3) and in much denser clusters, like 47 Tuc and NGC 6752.*

In particular, in M3, 47 Tuc, and NGC 6752 the COL-BSS sum to $\sim 50-60\%$ of the total and mostly reside in the central region of the cluster. The MT-BSS are slightly less abundant than the COL-BSS, but populate all the GC. The density of BSS reaches a

minimum in a so-called zone of avoidance, which separates the portion of the GC mostly occupied by COL-BSS from the cluster outskirts, where the MT-BSS dominate. The location of the zone of avoidance is explained by accounting for the effects of the dynamical friction on the PBs which were massive enough for generating the observed BSS.

The picture described above can also be applied to ω Cen; but in this case the lack of a central peak in the BSS radial distribution requires that the large majority of the BSS derive from PBs. The very low rate of production of COL-BSS could be in turn attributed to the fact that mass segregation has not yet driven a sizeable number of PBs to the central region of the cluster to produce BSS.

A very interesting further development of this research will be to perform a comparison between the location of a significant sample of BSS in a GC and their spectroscopic properties. According to the findings of this work, the position in the GC might represent a strong dynamical clue for the formation mechanism of a given BSS. If it is located outside the zone of avoidance, the BSS almost certainly results from evolution of a PB; if it is harbored in the cluster core, the BSS has most likely a collisional origin. On the other hand, indication about the origin of the same BSS can be independently obtained from high resolution spectroscopy. Indeed the chemical signature of the MT-BSS formation process has been recently discovered in 47 Tuc (Ferraro et al. 2006b). The acquisition of similar sets of data in clusters with different structural parameters and/or in different regions of the same cluster will provide an unprecedented tool for confirming the scenario presented here and to finally address the BSS formation processes and their complex interplay with the dynamical evolution of the cluster.

Bibliography

[1] Abazajian K., 2006, PhRvD, 73f, 3506

[2] Abazajian K., Fuller G. M., Patel M., 2001a, PhRvD, 64b, 3501

[3] Abazajian K., Fuller G. M., Tucker W. H., 2001b, ApJ, 562, 593

[4] Abazajian K., Koushiappas S. M., 2006, PhRvD, 74b, 3527

[5] Abel T., Anninos P., Norman M. L., Zhang Y., 1998, ApJ, 508, 518

[6] Abel T., Bryan G. L., Norman M. L., 2000, ApJ, 540, 39

[7] Abel T., Bryan G. L., Norman M. L., 2002, Sci, 295, 93

[8] Abel T., Wise J. H., Bryan G. L., 2006, ApJL, submitted, astro-ph/0606019

[9] Abramovitz M., Stegun I. A., 1965, *Handbook of Mathematical Functions*, Dover Publications. Inc, New York

[10] Agol E., Kamionkowski M., 2002, MNRAS, 334, 553

[11] Aharonian F. et al., 1997, A&A, 327, 5

[12] Aharonian F. et al., 1999a, A&A, 349, 29

[13] Aharonian F. et al., 1999b, A&A, 350, 757

[14] Aharonian F. et al., 2001a, ApJ, 546, 898

[15] Aharonian F., 2001b, proceedings of the 27th ICRC, Hamburg, August 2001, ed. Schlickeiser R., p.250, astro-ph/0112314

[16] Aharonian F. et al., 2002a, A&A, 384, 23

[17] Aharonian F. et al., 2002b, A&A, 393, 89

[18] Aharonian F. et al., 2003, A&A, 403, 523

[19] Aharonian F. et al., 2005a, A&A, 430, 865

[20] Aharonian F. et al., 2005b, accepted for publication in Nature, astro-ph/0508073

[21] Aoki W. et al., 2006, ApJ, 639, 897

[22] Arras P., Wasserman I., 1999, MNRAS, 306, 257

[23] Ascasibar Y., Jean P., Boehm C., Knödlseder J., 2006, MNRAS, 368, 1695

[24] Astier P. et al. [NOMAD Collaboration], 2001, Phys. Lett. B, 506, 27

[25] Baade W., 1944,Contributions from the Mount Wilson Observatory / Carnegie Institution of Washington, 696, 1

[26] Bailyn C. D., 1995, ARA&A, 33, 133

[27] Bailyn C. D., & Pinsonneault M. H., 1995, ApJ, 439, 705

[28] Baker P. L., Burton W. B., 1975, ApJ, 198, 281

[29] Barkana R., Loeb A., 2001, PhR, 349, 125

[30] Bauer F. E., Alexander D. M., Brandt W. N., Schneider D. P., Treister E., Hornschemeier A. E., Garmire G. P., 2004, AJ, 128, 2048 [B04]

[31] Baumgardt H., Hopman C., Portegies Zwart S., Makino J., 2005, MNRAS, in press, astro-ph/0511752

[32] Baumgardt H., Hut P., Makino J., McMillan S., Portegies Zwart S., 2003a, ApJL, 582, 21

[33] Baumgardt H., Makino J., Hut P., McMillan S., Portegies Zwart S., 2003b, ApJL, 589, 25

[34] Baumgardt H., Portegies Zwart S. F., McMillan S. L. W., Makino J., Ebisuzaki T., 2004, ASP Conf. Ser. 322: The Formation and Evolution of Massive Young Star Clusters, 322, 459

[35] Beacom J. F., Bell N. F., Bertone G., 2005, PhRvL, 94q, 1301

[36] Beacom J. F., Yüksel H., 2006, PhRvL, 97g, 1102

[37] Beccari, G., Ferraro, F.R., Possenti, A., Valenti, E., Origlia, L., Rood, R.T., 2006, AJ, 131, 2551

[38] Becker R. H. et al., 2001, AJ, 122, 2850

[39] Begelman M. C., Volonteri M., Rees M. J., 2006, MNRAS, 370, 289

[40] Bellazzini M., Ferraro F. R., Sollima A., Pancino E., Origlia L., 2004, A&A, 424, 199

[41] Bellazzini M., Fusi Pecci F., Messineo M., Monaco L., Rood R. T.,2002, AJ, 123, 1509

[42] Bernstein R. A., Freedman W. L., Madore B. F., 2002, ApJ, 571, 56

[43] Bertone G., Hooper D., Silk J., 2005, Phys.Rept., 405, 279

[44] Beskin G. M., Karpov S. V., 2005, A&A, 440, 223

[45] Biermann P. L., Kusenko A., 2006, PhRvL, 96L, 1301

[46] Binney J., Merrifield M., 1998, *Galactic astronomy*, Princeton University Press

[47] Binney J., Tremaine S., 1987, "Galactic dynamics", Princeton University Press, 747

[48] Bird A. J. et al. 2004, ApJL, 607, 33

[49] Bird A. J. et al. 2006, ApJ, 636, 765

[50] Blecha L., Ivanova N., Kalogera V., Belczynski K., Fregeau J., Rasio F., 2006, ApJ, 642, 427

[51] Bode P., Ostriker J. P., Turok, N., 2001, ApJ, 556, 93

[52] Boehm C., Hooper D., Silk J., Casse M., Paul J., 2004, PhRvL, 92j, 1301

[53] Bond J. R., Arnett W. D., Carr B. J., 1984, ApJ, 280, 825

[54] Bond J. R., Carr B. J., Hogan C. J., 1986, ApJ, 306, 428

[55] Boyarsky A., Neronov A., Ruchayskiy O., Shaposhnikov M., 2006a, MNRAS, 370, 213, astro-ph/0512509

[56] Boyarsky A., Neronov A., Ruchayskiy O., Shaposhnikov M., 2006b, astro-ph/0603368

[57] Bregman J. N., Kelson D. D., Ashe G. A., 1993, ApJ, 409, 682

[58] Bromm V., Coppi P. S., Larson R. B., 1999, ApJ, 527L, 5

[59] Bromm V., Coppi P. S., Larson R. B., 2002, ApJ, 564, 23

[60] Bromm V., Kudritzki R. P., Loeb A., 2001, ApJ, 552, 464

[61] Bromm V., Loeb A., 2003, ApJ, 596, 34

[62] Bullock J. S., Kravtsov A. V., Weinberg D. H., 2000, ApJ, 539, 517

[63] Burkert A., 1995, ApJ, 447L, 25

[64] Carney B. W., Latham D. W., Laird J. B., Grant C. E., Morse J. A., 2001, AJ, 122, 3419

[65] Carr B. J., Sakellariadou M., 1999, ApJ, 516, 195

[66] Cassé M., Fayet P., 2005, to appear in Proc. 21st IAP Colloquium "Mass Profiles and Shapes of Cosmological Structures", Paris 4-9 July 2005 (EAS Publications Series, G. Mamon, F. Combes, C. Deffayet, B. Fort eds.), astro-ph/0510490

[67] Chen X., Kamionkowski M., 2004, PhRvD, 70d, 3502

[68] Chiappetti L. et al., 1999, ApJ, 521, 552

[69] Choudhury T. R. & Ferrara A., 2006a, invited review (to be published by RSP), edited by R. Fabbri, astro-ph/0603149

[70] Choudhury T. R., Ferrara A., 2006b, astro-ph/0603617

[71] Christlieb N., Bessell M. S., Beers T. C., Gustafsson B., Korn A., Barklem P. S., Karlsson T., Mizuno-Wiedner M., Rossi S., 2002, Nature, 419, 904

[72] Christlieb N., Gustafsson B., Korn A. J., Barklem P. S., Beers T. C., Bessell M. S., Karlsson T., Mizuno-Wiedner M., 2004, ApJ, 603, 708

[73] Ciardi B., Ferrara A., Abel T., 2000, ApJ, 533, 594

[74] Ciardi B., Ferrara A., Governato F., Jenkins A., 2000, MNRAS, 314, 611

[75] Ciardi B., Ferrara A., White S. D. M., 2003, MNRAS, 344L, 7

[76] Ciardi B., Madau P., 2003, ApJ, 596, 1

[77] Colafrancesco S., Profumo S., Ullio P., 2006, A&A, 455, 21

[78] Colbert E. J. M., Miller M. C., 2005, Invited review talk at the Tenth Marcel Grossmann Meeting on General Relativity, Rio de Janeiro, July 20-26, 2003. Proceedings edited by M. Novello, S. Perez-Bergliaffa and R. Ruffini, World Scientific, Singapore, 2005

[79] Colombi S., Dodelson S., Widrow L. M., 1996, ApJ, 458, 1

[80] Colpi M., Mapelli M., Possenti A., 2003, ApJ, 599, 1260

[81] Colpi M., Possenti A., Gualandris A., 2002, ApJ, 570L, 85

[82] Cordes J. M., Lazio T. J. W., 2001, ApJ, 549, 997

[83] Costamante L., Aharonian F., Horns D., Ghisellini G., 2004, NewAR, 48, 469

[84] Couchman H.M.P., 1985, MNRAS, 214, 137

[85] Couchman H.M.P., Rees M.J., 1986, MNRAS, 221, 53

[86] D'Amico N., Possenti A., Fici L., Manchester R. N., Lyne A. G., Camilo F., Sarkissian J., 2002, ApJ, 570L, 89

[87] Davies M. B., Benz W., Hills J. G., 1994, ApJ, 424, 870

[88] Davies M. B., Piotto G., De Angeli F., 2004, MNRAS, 349, 129

[89] Davies R. E., Pringle J. E., 1980, MNRAS, 191, 599

[90] de Araujo J.C.N., Opher R., 1988, MNRAS, 231, 923

[91] de Araujo J.C.N., Opher R., 1991, ApJ, 379, 461

[92] De Rjula A., Glashow S. L., 1980, Phys. Rev. Lett., 45, 942

[93] Dickey J. M., Lockman F. J., 1990, ARA&A, 28, 215

[94] Diemand J., Madau P., Moore B., 2005, MNRAS, 364, 367 (DMM)

[95] Dijkstra M., Haiman Z., Loeb A., 2004, ApJ, 613, 646 [D04]

[96] Djannati-Ataï A. et al., 2002, A&A, 391, 25

[97] Djorgovski S. G., Castro S., Stern D., Mahabal A. A., 2001, ApJ, 560L, 5

[98] Dolgov A. D., 2002, Physics Reports, Volume 370, Issue 4-5, p. 333-535 (hep-ph/0202122)

[99] Dolgov A. D., Hansen S. H., 2002, APh, 16, 339

[100] Dove J. B., Shull J. M., 1994, ApJ, 430, 222

[101] Dove J. B., Shull J. M., Ferrara A., 2000, ApJ, 531, 846

[102] Drees M., Wright D., 2000, hep-ph/0006274

[103] Drukier G. A., Bailyn C. D., Van Altena W. F., Girard T. M., 2003, AJ, 125, 2559

[104] Dubath P., Meylan G., Mayor M., 1997, A&A, 324, 505

[105] Dube R. R., Wickes W. C. & Wilkinson D. T., 1977, ApJL, 215, 51

[106] Dube R. R., Wickes W. C. & Wilkinson D. T., 1979, ApJ, 232, 333

[107] Dwek E., Arendt R. G., Hauser M. G., Kelsall T., Lisse C. M., Moseley, S. H., Silverberg R. F., Sodroski T. J., Weiland J. L., 1995, ApJ, 445, 716

[108] Dwek E., Krennrich F., 2005, ApJ, 618, 657

[109] Dwek E., Krennrich F., Arendt R. G., 2005, ApJ, 634, 155

[110] Edgar R., 2004, NewAR, 48, 843

[111] Eisenstein D. J., Loeb A., 1995, ApJ, 443, 11

[112] Elbaz D., Cesarsky C. J., Chanial P., Aussel H., Franceschini A., Fadda D., Chary R. R., 2002, A&A , 384, 848

[113] Fan X. et al. 2001, AJ, 122, 2833

[114] Fan X. et al. 2002, AJ, 123, 1247

[115] Fan X. et al. 2003, AJ, 125, 1649

[116] Fazio et al., 2004, ApJS, 154, 39

[117] Ferrara A., Perna R., 2001, MNRAS, 325, 1643

[118] Ferraro F. R. et al., 2006b, ApJ, 647, L53

[119] Ferraro F. R., Beccari G., Rood R. T., Bellazzini M., Sills A., Sabbi E., 2004, ApJ, 603, 127

[120] Ferraro F. R., Carretta E., Corsi C. E., Fusi Pecci F., Cacciari C., Buonanno R., Paltrinieri B., Hamilton D., 1997a, A&A, 320, 757

[121] Ferraro F. R., Fusi Pecci F., Cacciari C., Corsi C., Buonanno R., Fahlman G. G., Richer H. B., 1993, AJ, 106, 2324

[122] Ferraro F. R., Messineo, M., Fusi Pecci F., De Palo, M.A., Straniero, O., Chieffi, A., Limongi, M., 1999, AJ, 118, 1738

[123] Ferraro F. R., Paltrinieri, B., Fusi Pecci, F.,Cacciari, C., Dorman, B., rood, R.T., 1997b, ApJ, 484, L145

[124] Ferraro F. R., Possenti A., Sabbi E., Lagani P., Rood R. T., D'Amico N., Origlia L., 2003, ApJ, 595, 179

[125] Ferraro F. R., Sills A., Rood R. T., Paltrinieri B., Buonanno R., 2003b, ApJ, 588, 464

[126] Ferraro F. R., Sollima A., Rood R. T., Origlia L., Pancino E., Bellazzini M., 2006a, ApJ, 638, 433

[127] Fossati G., Celotti A., Chiaberge M., Zhang Y. H., Chiappetti L., Ghisellini G., Maraschi L., Tavecchio F., Pian E. & Treves A., 2000, ApJ, 541, 16

[128] Frebel A. et al., 2005, Nature, 434, 871

[129] Freeman K. C., 1993, The globular clusters-galaxy connection. Astronomical Society of the Pacific Conference Series, Volume 48, Proceedings of the 11th Santa Cruz Summer Workshop in Astronomy and Astrophysics, held July 19-29, 1992, at the University of California, Santa Cruz, San Francisco: Astronomical Society of the Pacific (ASP), edited by Graeme H. Smith, and Jean P. Brodie, 608

[130] Freudenreich H. T., 1998, ApJ, 492, 495

[131] Fryer C. L., Woosley S. E., 2001, ApJ, 550, 372

[132] Fujita Y., Inoue S., Nakamura T., Manmoto T., Nakamura K. E., 1998, ApJL, 495, 85

[133] Fukugita M., Hogan C. J., Peebles P. J. E. Peebles, 1998, ApJ, 503, 518

[134] Fuller T. M., Couchman H. M. P., 2000, ApJ, 544, 6

[135] Furlanetto S. R., Hernquist L., Zaldarriaga M., 2004, MNRAS, 354, 695

[136] Furlanetto S. R., Oh S. P., 2005, MNRAS, 363, 1031

[137] Furlanetto S., Pritchard J. R., 2006, MNRAS, submitted (astro-ph/0605680)

[138] Fusi Pecci F., Ferraro F. R., Corsi C. E., Cacciari C., Buonanno R., 1992, AJ, 104, 1831

[139] Galli D., Palla F., 1998, A&A, 335, 403

[140] Galli D., Palla F., 2002, P&SS, 50, 1197

[141] Gardner J. P. et al. 2006, Space Science Reviews, in press

[142] Gebhardt K., Fisher P., 1995, AJ, 109, 209

[143] Gebhardt K. et al., 2000, ApJ, 543L, 5

[144] Gebhardt K. et al., 2003, ApJ, 583, 92

[145] Gebhardt K., Rich R. M., Ho L. C., 2002, ApJL, 578, 41

[146] Gebhardt K., Rich R. M., Ho L. C., 2005, ApJ, 634, 1093

[147] Gendre B., Barret D., Webb N. A., 2003, A&A, 400, 521

[148] Gerssen J., van der Marel R. P., Gebhardt K., Guhathakurta P., Peterson R. C., Pryor C., 2002, AJ, 124, 3270

[149] Gerssen J., van der Marel R. P., Gebhardt K., Guhathakurta P., Peterson R. C., Pryor C., 2003, AJ, 125, 376

[150] Ghez A. M. et al., 2003, ApJL, 586, 127

[151] Gilliland R. L., Bono G., Edmonds P. D., Caputo F., Cassisi S., Petro L. D., Saha A., Shara M. M., 1998, ApJ, 507, 818

[152] Gnedin N. Y., 2000, ApJ, 542, 535

[153] Gorjian V., Wright E. L., Chary R. R., 2000, ApJ, 536, 550

[154] Gould R. J. & Schréder G. P. 1967, Phys. ReV., 155, 1404

[155] Governato F., Mayer L., Wadsley J., Gardner J. P., Willman B., Hayashi E., Quinn T., Stadel J., Lake G., 2004, ApJ, 607, 688

[156] Granato G. L., Silva L., Bressan A., Lacey C. G., Baugh C. M., Cole S., Frenk C. S., 2001, ApSSS, 277, 79

[157] Grimm H., Gilfanov M., Sunyaev R., 2003, MNRAS, 339, 793

[158] Gruber D. E., 1992, in *The X-Ray Background*, ed. X. Barcons & A. C. Fabian (Cambridge: Cambridge Univ. Press), 44

[159] Gunn J. E., Peterson B. A., 1965, ApJ, 142, 1633

[160] Haehnelt M. G., Rees M. J., 1993, MNRAS, 263, 168

[161] Haiman Z., Abel T., Rees M. J., 2000, ApJ, 534, 11

[162] Haiman Z., Cen R., 2005, ApJ, 623, 627

[163] Haiman Z., Rees M. J., Loeb A., 1997, ApJ, 476, 458

[164] Haiman Z., Thoul A.A., Loeb A., 1996, ApJ 464, 523

[165] Hansen S. H., Haiman Z., 2004, ApJ, 600, 26

[166] Harris W.E., 1996, AJ, 112, 1487

[167] Hauser M. G., Arendt R. G., Kelsall T., Dwek E., Odegard N. et al., 1998, ApJ, 508, 25

[168] Hauser M. G., Dwek E., 2001, ARA&A, 39, 249

[169] Heger A., Fryer C. L., Woosley S. E., Langer N., Hartmann D. H., 2003, ApJ, 591, 288

[170] Heger A., Woosley S. E., 2002, ApJ, 567, 532

[171] Heger A., Woosley S. E., 2003, From Twilight to Highlight: The Physics of Supernovae. Proceedings of the ESO/MPA/MPE Workshop held in Garching, Germany, 29-31 July 2002, 3

[172] Heggie D. C., 1975, MNRAS, 173, 729

[173] Heitler W., 1960, The Quantum Theory of Radiation (London: Oxford Univ. Press)

[174] Hernquist L., 1993, ApJS, 86, 389

[175] Hills J. G., 1975, AJ, 80, 809

[176] Hills J. G., 1990, AJ, 99, 979

[177] Hinshaw G. et al., 2006, submitted to ApJ, astro-ph/0603451

[178] Hooper D., Wang L.-T., 2004, PhRvD, 70f, 3506

[179] Hopman C., Portegies Zwart S. F., 2005, MNRAS, 363L, 56

[180] Hopman C., Portegies Zwart S. F., Alexander T. 2004, ApJL, 604, 101

[181] Horan D. et al., 2002, ApJ, 571, 753

[182] Hurley J. R., Tout C. A., Aarseth S. J., Pols O. R., 2001, MNRAS, 323, 630

[183] Hut P., 1993, ApJ, 403, 256

[184] Hut P., Bahcall J. N., 1983, ApJ, 268, 319

[185] Ideta M., Makino J.,2004, ApJ, 616L, 107

[186] Inoue S. & Takahara F., 1996, ApJ, 463, 555

[187] Kelsall T., Weiland J. L., Franz B. A., Reach W. T., Arendt R. G., et al., 1998, ApJ, 508, 44

[188] Islam R. R., Taylor J. E., Silk J., 2003, MNRAS, 340, 647

[189] Islam R. R., Taylor J. E., Silk J., 2004a, MNRAS, 354, 427

[190] Islam R. R., Taylor J. E., Silk J., 2004b, MNRAS, 354, 443

[191] Islam R. R., Taylor J. E., Silk J., 2004c, MNRAS, 354, 629

[192] Ivanova N., Belczynski K., Fregeau J. M., Rasio F. A., 2005, MNRAS, 358, 572

[193] Iwamoto N., Umeda H., Tominaga N., Nomoto K., Maeda K., 2005, Science, 309, 451

[194] Kalogera V., Henninger M., Ivanova N., King A. R. 2004, ApJL, 603, 41

[195] Kaaret P., Prestwich A. H., Zezas A., Murray S. S., Kim D.-W., Kilgard R. E., Schlegel E. M., Ward M. J., 2001, MNRAS, 321L, 29

[196] Kaaret P., Ward M. J., Zezas A., 2004, MNRAS, 351L, 83

[197] Kasuya S., Kawasaki M., 2004, PhRvD, 70j, 3519

[198] Kasuya S., Kawasaki M., 2006, PhRvD, 73f, 3007, astro-ph/0602296

[199] Kasuya S., Kawasaki M., Sugiyama N., 2004, PhRvD, 69b, 3512

[200] Kasuya S., Takahashi F., 2005, PhRvD, 72h, 5015

[201] Kawasaki M., Yanagida T., 2005, Physics Letters B, Volume 624, Issue 3-4, p. 162, hep-ph/0505167

[202] Kazantzidis S., Magorrian J., Moore B., 2004, ApJ, 601, 37

[203] Kent S. M., Dame T. M., Fazio G., 1991, ApJ, 378, 131

[204] King A. R., 2003, to appear in 'Compact Stellar X-Ray Sources', eds. W.H.G. Lewin and M. van der Klis, Cambridge University Press, astro-ph/0301118

[205] King A. R., Davies M. B., Ward M. J., Fabbiano G., Elvis M., 2001, ApJL, 552, 109

[206] King A. R., Dehnen W., 2005, MNRAS, 357, 275

[207] Klessen R., Burkert A., 1996, MNRAS, 280, 735

[208] Klypin A., Zhao Hs., Somerville R. S., 2002, ApJ, 573, 597

[209] Knödlseder J. et al., 2005, A&A, 441, 513

[210] Kogut A. et al., 2003, ApJS, 148, 161

[211] Konopelko A., Mastichiadis A., Kirk J., de Jager O. C., Stecker F. W., 2003, ApJ, 597, 851

[212] Koushiappas S. M., Bullock J. S., Dekel A., 2004, MNRAS, 354, 292

[213] Krennrich F. et al., 1999, ApJ, 511, 149

[214] Krennrich F. et al., 2002, ApJ, 575, 9

[215] Krolik J. H., 2004, ApJ, 615, 383

[216] Krumholz M. R., McKee C. F., Klein R. I., 2006, ApJ, 638, 369

[217] Kudritzki R. P., 2002, ApJ, 577, 389

[218] Kuijken K., Dubinski J., 1995, MNRAS, 277, 1341

[219] Lacey C. G., Ostriker J. P., 1985, ApJ, 299, 633

[220] Lambert H. C., Rickett B. J., 2000, ApJ, 531, 883

[221] Lang K. R., *Astrophysical Formulae*, 3rd edition, 1999, Springer, Berlin

[222] Larsen J. A., Humphreys R. M., 2003, AJ, 125, 1958

[223] Larson R. B., 1981, MNRAS, 194, 809

[224] Leonard P. J. T., 1989, AJ, 98, 217

[225] Liu J.-F., Bregman J. N., 2005, ApJS, 157, 59

[226] Liu J.-F., Bregman J. N., Seitzer P., Irwin J., 2005, astro-ph/0501310

[227] Lockman F. J., Gehman C. S., 1991, ApJ, 382, 182

[228] Lockman F. J., 2002, Seeing Through the Dust: The Detection of HI and the Exploration of the ISM in Galaxies, ASP Conference Proceedings, 276, 107. Edited by A. R. Taylor, T. L. Landecker, and A. G. Willis

[229] G. Lodato, P. Natarajan, 2006, MNRAS, 371, 1813

[230] Loeb A., Rasio F. A., 1994, ApJ, 432, 52

[231] Lombardi J. C. Jr., Warren J. S., Rasio F. A., Sills A., Warren A. R., 2002, ApJ, 568, 939

[232] Machida M. N., Matsumoto T., Hanawa T., Tomisaka K., 2006, ApJ, 645, 1227

[233] MacTavish C. J. et al., 2006, ApJ, 647, 799

[234] Madau P., Phinney S. E., 1996, ApJ, 456, 124

[235] Madau P., Pozzetti L., 2000, MNRAS, 312, L9

[236] Madau P., Rees M. J., Volonteri M., Haardt F., Oh S. P., 2004, ApJ, 604, 484

[237] Madau P., Silk J., 2005, MNRAS, 359, 37

[238] Madhusudhan N., Justham S., Nelson L., Paxton B., Pfahl E., Podsiadlowski Ph., Rappaport S., 2006, ApJ, 640, 918

[239] Magliocchetti M., Salvaterra R., Ferrara A., 2003, MNRAS, 342, 25

[240] Malhotra S., Rhoads J. E., 2004, ApJ, 617L, 5

[241] Malhotra S., Rhoads J. E., 2006, ApJ, 647L, 95

[242] Malkan M. A. & Stecker F. W., 2001, ApJ, 555, 641

[243] Mapelli M., Colpi M., Possenti A., Sigurdsson S., 2005, MNRAS, 364, 1315

[244] Mapelli M., Ferrara A., 2005, MNRAS, 364, 2

[245] Mapelli M., Ferrara A., Pierpaoli E., 2006, MNRAS, 369, 1719

[246] Mapelli M., Ferrara A., Rea N., 2006, MNRAS, 368, 1340

[247] Mapelli M., Salvaterra R., Ferrara A., 2006, NewA, 11, 420

[248] Mapelli M., Sigurdsson S., Colpi M., Ferraro F. R., Possenti A., Rood R. T., Sills A., Beccari G.,2004, ApJ, 605L, 29

[249] Mapelli M., Sigurdsson S., Ferraro F. R., Colpi M., Possenti A., Lanzoni B., 2006, MNRAS, accepted

[250] Massó E., Toldrà R., 1999, Phys. Rev. D, 60, 083503

[251] Mattila K., 1976, A&A, 47, 77

[252] Mattila K., 2003, ApJ, 591, 119

[253] Matsumoto H., Tsuru T. G., Koyama K., Awaki H., Canizares C. R., Kawai N., Matsushita S., Kawabe R., 2001, ApJL, 547, 25

[254] Matsumoto T., Cohen M., Freund M. M., Kawaka M., Lim M., et al., 2000, in *ISO Surveys of a Dusty Universe*. Lecture Notes in Physics vol. 548, ed. Lemke D., Stickel M., Wilke K., pp.96-105, Berlin Heidelberg: Spinger Verlag

[255] Matsumoto T., Matsuura S., Murakami H., Tanaka M., Freund M., Lim M., Cohen M., Kawada M., Noda M., 2005, ApJ, 626, 31

[256] McCrea W. H., 1964, MNRAS, 128, 147

[257] McKee C. F., Ostriker J. P., 1977, ApJ, 218, 148

[258] Merritt D., Meylan G., Mayor M., 1997, AJ, 114, 1074

[259] Metcalfe L. et al., 2003, A&A, 407,791

[260] Meylan G., Mayor M., Duquennoy A., Dubath P., 1995, A&A, 303, 761

[261] Mii H., Totani T., 2005, ApJ, 628, 873

[262] Miller J. M., Fabian A. C., Miller M. C., 2004, ApJL, 614, 117

[263] Miller M. C., Hamilton D. P., 2002, MNRAS, 330, 232

[264] Miyaji T., Lehmann I., Hasinger G., 2001, AJ, 121, 3041

[265] Mo H. J., Mao S., White S. D. M., 1998, MNRAS, 295, 319

[266] Monkman E., Sills A., Howell J., Guhathakurta P., de Angeli F., Beccari G., ApJ, accepted

[267] Moore B., 1993, ApJL, 413, 93

[268] Moore B., Diemand J., Madau P., Zemp M., Stadel J., 2006, MNRAS.tmp, 346

[269] Moore B., Quinn T., Governato F., Stadel J., Lake G., 1999, MNRAS, 310, 1147

[270] Moretti A., Campana S., Lazzati D., Tagliaferri G., 2003, ApJ, 588, 696 [M03]

[271] Murali C., Arras P., Wasserman I., 2000, MNRAS, 313, 87

[272] Mushotzky R., 2004, Progress of Theoretical Physics Supplement, 155, 27

[273] Narayan R., Mahadevan R., Quataert E., 1998, Theory of Black Hole Accretion Disks, edited by Abramowicz M. A., Bjornsson G., and Pringle J. E.. Cambridge University Press, 148

[274] Narayanan V. K., Spergel D. N., Dav R., Ma C. P., 2000, ApJL, 543, 103

[275] Navarro J. F., Frenk C. S., White S. D. M., 1996, ApJ, 462, 563 (NFW)

[276] Nikishov A. I., 1962, Soviet Phys. JETP, 14, 393

[277] Norris J. E., Freeman K. C., Mighell K. J, 1996, ApJ, 462, 241

[278] Nowakowski M., Rindani S. D., 1995, Phys.Lett., B348, 115

[279] Omukai K., Palla F., 2001, ApJ, 561L, 55

[280] Omukai K., Palla F., 2002, Ap&SS, 281, 71

[281] Orosz J. A., 2003, A Massive Star Odyssey: From Main Sequence to Supernova, Proceedings of IAU Symposium 212, held 24-28 June 2001 in Lanzarote, Canary island, Spain. Edited by van der Hucht K. A., Herrero A., and Esteban C.. San Francisco: Astronomical Society of the Pacific, 365

[282] O'Shea B. W., Abel T., Whalen D., Norman M. L., 2005, ApJ, 628L, 5

[283] Ostriker J. P., Binney J., Saha P., 1989, MNRAS, 241, 849

[284] Ostriker J. P., Steinhardt, P., 2003, Sci, 300, 1909

[285] Padmanabhan N., Finkbeiner D. P.,2005, PhRvD, 72b, 3508

[286] Padmanabhan T., *Structure Formation in the Universe*, Cambridge University Press, 1995

[287] Page L. et al., 2006, submitted to ApJ, astro-ph/0603450

[288] Pakull M. W., Mirioni L., 2003, Winds, Bubbles, and Explosions: a conference to honor John Dyson, Pátzcuaro, Michoacán, México, September 9-13 (Eds. S. J. Arthur & W. J. Henney), Revista Mexicana de Astronomía y Astrofísica (Serie de Conferencias), 15, 197

[289] Palla F., Salpeter E.E., Stahler S.W., 1983, ApJ 271, 632

[290] Patruno A., Colpi M., Faulkner A., Possenti A., 2005, MNRAS, 364, 344

[291] Papovich C. et al., 2004, ApJS, 154, 70

[292] Peebles P. J. E.,*Principles of physical cosmology*, Princeton University Press, 1993

[293] Persic M., Salucci P., 1992, MNRAS, 258P, 14

[294] Peters P. C., 1964, Phys. Rev. B136, 1224

[295] Peterson R. C., Rees R. F., Cudworth K. M., 1995, ApJ, 443, 124

[296] Picciotto C., Pospelov M., 2005, PhLB, 605, 15

[297] Pierpaoli E., 2004, Phys. Rev. Lett., 92, 031301

[298] Piotto G. et al., 2004, ApJ, 604L, 109

[299] Pooley D., et al., 2003, ApJ, 591, L131

[300] Portegies Zwart S. F., Dewi J., Maccarone T., 2004, MNRAS, 355, 413

[301] Portegies Zwart S. F., Makino J., McMillan S. L. W., Hut P., 1999, A&A, 348, 117

[302] Portegies Zwart S. F., McMillan S. L. W., 2002, ApJ, 576, 899

[303] Press W. H., Schechter P., 1974, ApJ, 187, 425

[304] Press W. H., Teukolsky S. A., Vetterling W. T., Flannery B. P., 1992, "Numerical Recipes in C", Second Edition, Cambridge University Press

[305] Primack J. R., Bullock J. S., Somerville R. S., MacMinn D., 1999, APh, 11, 93

[306] Procter Sills A., Bailyn C. D., Demarque P., 1995, ApJ, 455, L163

[307] Protheroe R. J., Biermann P. L., 1997, APh, 6, 293

[308] Pryor C., Meylan G., 1993, Structure and Dynamics of Globular Clusters. Proceedings of a Workshop held in Berkeley, California, July 15-17, 1992, to Honor the 65th Birthday of Ivan King. Editors, S.G. Djorgovski and G. Meylan; Publisher, Astronomical Society of the Pacific, Vol. 50, 357

[309] Psaltis, D., 2006, To appear in "Compact Stellar X-ray Sources", eds. W.H.G. Lewin and M. van der Klis, astro-ph/0410536

[310] Quataert E., Narayan R., 1999, ApJ, 520, 298

[311] Quinlan G. D., 1996, NewA, 1, 35

[312] Quinn P. J., Hernquist L., Fullagar D. P., 1993, ApJ, 403, 74

[313] Rees M.J., Ostriker J.P., 1977, MNRAS, 179, 541

[314] Reijns R. A., Seitzer P., Arnold R., Freeman K. C., Ingerson T., van den Bosch R. C. E., van de Ven G., de Zeeuw P. T., 2006, A&A, 445, 503

[315] Richer H. B. et al., 2004, AJ, 127, 2771

[316] Rickett B. J., 1990, ARA&A, 28, 561

[317] Ricotti M., 2002, MNRAS, 336L, 33

[318] Ricotti M., 2004, The Formation and Evolution of Massive Young Star Clusters, ASP Conference Series, 322, 509

[319] Ricotti M., Gnedin N.Y., Shull J.M., 2002, ApJ, 575, 49

[320] Ricotti M., Ostriker J. P., 2004, MNRAS, 352, 547

[321] Ricotti M., Ostriker J. P., Gnedin N. Y., 2005, MNRAS, 357, 207

[322] Ricotti M., Shull J. M., 2000, ApJ, 542, 548

[323] Rieke G. H., the MIPS Team, 2004, American Astronomical Society Meeting 204, 3305

[324] Ripamonti E., 2006, MNRAS, submitted

[325] Ripamonti E., Abel T., 2004, MNRAS, 348, 1019

[326] Ripamonti E., Haardt F., Ferrara A., Colpi M., 2002, MNRAS, 334, 401

[327] Ripamonti E., Mapelli M., Ferrara A., 2006a, submitted to MNRAS

[328] Ripamonti E., Mapelli M., Ferrara A., 2006b, submitted to MNRAS

[329] Rosen A., Bregman J. N., 1995, ApJ, 440, 634

[330] Rubenstein E. P., Bailyn C. D., 1997, ApJ, 474, 701

[331] Rybicki G. B., Lightman A. P., *Radiative Processes in Astrophysics*, San Francisco, 1979

[332] Sabbi E., Ferraro F. R., Sills A., Rood R. T., 2004, ApJ, 617, 1296

[333] Salpeter E. E., 1955, ApJ, 121, 161 1955

[334] Salvaterra R., Ferrara A., 2003, MNRAS, 339, 973

[335] Samuelson F. W. et al., 1998, ApJ, 501, 17

[336] Sanders D. B., Solomon P. M., Scoville N. Z., 1984, ApJ, 276, 182

[337] Santos M. R., Bromm V., Kamionkowski M., 2002, MNRAS, 336, 1082

[338] Schaerer D., 2002, A&A, 382, 28

[339] Seager S., Sasselov D. D., Scott D., 1999, ApJ, 523L, 1

[340] Seager S., Sasselov D. D., Scott D., 2000, ApJS, 128, 407

[341] Seljak U., Makarov A., McDonald P., Trac H., 2006, submitted to PRL, astro-ph/0602430

[342] Seljak U., Sugiyama N., White M., Zaldarriaga M., 2003, PhRvD, 68h, 3507

[343] Seljak U., Zaldarriaga M., 1996, ApJ, 469, 437

[344] Shakura N. I., Sunyaev, 1973, A&A, 24, 337

[345] Shapiro S. L., 2005, ApJ, 620, 59

[346] Shaposhnikov M., 2006, CERN-PH-TH/2006-079

[347] Shchekinov Y.A., Vasiliev E.O., 2004, A&A 419, 19

[348] Shchekinov Y.A., Vasiliev E.O., 2006, MNRAS, submitted, astro-ph/0604231

[349] Shödel R., Ott T., Genzel R., Eckart A., Mouawad N., Alexander T., 2003, ApJ, 596, 1015

[350] Shlosman I., Frank J., Begelman M. C., 1989, proceedings of the 134th Symposium of the International Astronomical Union, held in Santa Cruz, California, August 15-19, 1988. Edited by Donald E. Osterbrock and Joseph S. Miller. International Astronomical Union. Symposium no. 134, Kluwer Academic Publishers, Dordrecht, 462

[351] Shlosman I., Begelman M. C., Frank J., 1990, Nature, 345, 679

[352] Shull J. M., van Steenberg M. E., 1985, ApJ, 298, 268

[353] Sigurdsson S., Davies M. B., Bolte M., 1994, ApJ, 431, L115

[354] Sigurdsson S., Hernquist L., 1993, Nature, 364, 423

[355] Sigurdsson S., Phinney E. S., 1993, ApJ, 415, 631

[356] Sigurdsson S., Phinney E. S., 1995, ApJS, 99, 609

[357] Silk J., 1977, ApJ, 211, 638

[358] Silk J., Langer M., 2006, MNRAS, 371, 444

[359] Sills A., Bailyn C. D., 1999, ApJ, 513, 428

[360] Sills A., Bailyn C. D., Edmonds P. D., Gilliland R. L., 2000, ApJ, 535, 298

[361] Silva L., De Zotti G., Granato G. L., Maiolino R., Danese L., 2004, astro-ph/0403166

[362] Smoot G. F. et al., 1992, ApJ, 396L, 1

[363] Solomon P. M., Rivolo A. R., Barrett J., Yahil A., 1987, ApJ, 319, 730

[364] Soltan, A. M. 2003, A&A, 408, 39

[365] Sommer-Larsen J., Dolgov A., 2001, ApJ, 551, 608

[366] Spergel D. N. et al., 2003, ApJS, 148, 175

[367] Spergel D. N. et al., 2006, submitted to ApJ, astro-ph/0603449

[368] Spinrad H. & Stone R. P. S., 1978, ApJ, 226, 609

[369] Springel V., 2005, MNRAS, 364, 1105

[370] Stanev T., Franceschini A., 1998, ApJ, 494, L159

[371] Stasielak J., Biermann P. L., Kusenko A., 2006, ApJ, accepted, astro-ph/0606435

[372] Stecker F. W., 1980, Phys. Rev. Lett., 45, 1460

[373] Stecker F. W., de Jager O. C., Salamon M. H., 1992, ApJ, 390L, 49

[374] Stecker F. W., de Jager O. C., Salamon M. H., 1993, American Astronomical Society, 183rd AAS Meeting, Bulletin of the American Astronomical Society, Vol. 25, p.1336

[375] Stecker F. W., de Jager O. C., 1997, ApJ, 476, 712

[376] Stecker F. W., 2003, J.Phys., G29, R47-R88

[377] Steidel C. C., Hunt M. P., Shapley A. E., Adelberger K. L., Pettini M., Dickinson M., Giavalisco M., 2002, ApJ, 576, 653

[378] Strohmayer T. E., Mushotzky R. F., 2003, ApJL, 586, 61

[379] Suntzeff N. B., Kraft R. P., 1996, AJ, 111, 1913

[380] Swartz D. A., Ghosh K. K., Tennant A. F., Wu K., 2004, ApJS, 154, 519

[381] Tan J. C., Blackman E. G., 2004, ApJ, 603, 401

[382] Tavecchio F., Maraschi L., Ghisellini G. 1998, ApJ, 509, 608

[383] Tegmark M., Silk J., Rees M. J., Blanchard A., Abel T., Palla F., 1997, ApJ, 474, 1

[384] Toomre A., 1964, ApJ, 139, 1217

[385] Totani T., Kawai N., Kosugi G., Aoki K., Yamada T., Iye M., Ohta K., Hattori T., 2006, PASJ, 58, 485

[386] Totani T., Takeuchi T. T., 2002, ApJ, 570, 470

[387] Totani T., Yoshii Y., Maihara T., Iwamuro F., Motohara K., 2001, ApJ, 559, 592

[388] Umeda H., Nomoto K., 2005, ApJ, 619, 427

[389] Umemura M., Loeb A., Turner E. L., 1993, ApJ, 419, 459

[390] van den Bosch R., de Zeeuw T., Gebhardt K., Noyola E., van de Ven G., 2006, ApJ, 641, 852

[391] van der Marel R. P., 2004, Coevolution of Black Holes and Galaxies, from the Carnegie Observatories Centennial Symposia. Published by Cambridge University Press, as part of the Carnegie Observatories Astrophysics Series. Edited by L. C. Ho, 37

[392] van de Ven G., van den Bosch R. C. E., Verolme E. K., de Zeeuw P. T., 2006, A&A, 445, 513

[393] van Leeuwen F., Le Poole R. S., Reijns R. A., Freeman K. C., de Zeeuw P. T., 2000, A&A, 360, 472

[394] Vestrand W. T., Stacy J. G., Sreekumar P., 1995, ApJ, 454, 93

[395] Viel M., Lesgourgues J., Haehnelt M. G., Matarrese S., Riotto A., 2005, PhRvD, 71f, 3534

[396] Viel M., Lesgourgues J., Haehnelt M. G., Matarrese S., Riotto A., 2006, PhRvL, 97g, 1301

[397] Vink, J., 2006, to be published in the proceedings of the Symposium 'The X-ray Universe' 2005, astro-ph/0601131

[398] Vishniac E. T., 1978, ApJ, 223, 986

[399] Volonteri M., Haardt F., Madau P., 2003, ApJ, 582, 559

[400] Volonteri M., Perna R., 2005, MNRAS, 358, 913

[401] Volonteri M., Rees M. J., 2005, ApJ, 633, 624

[402] Warren S. R., Sandquist E. L., Bolte M., 2006, ApJ, 648, 1026

[403] Wasserman I., Salpeter E. E., 1994, ApJ, 433, 670

[404] Watson C. R., Beacom J. F., Yüksel H., Walker T. P., 2006, PhRvD, 74c, 3009

[405] Weinmann S. M., Lilly S. J., 2005, ApJ, 624, 526

[406] White R. L., Becker R. H., Fan X., Strauss M. A., 2003, AJ, 126, 1

[407] White S.D.M., Rees M.J., 1978, MNRAS, 183, 341

[408] White S. D. M., Springel V., 2000, Proceedings of the MPA/ESO Workshop held at Garching, Germany, 4-6 August 1999, 327,astro-ph/9911378

[409] Widrow L. M., Dubinski J., 2005, ApJ, 631, 838

[410] Wise & Abel, 2005, ApJ, 629, 615

[411] Woosley, 1986,Saas-Fee Advanced Course 16, Nucleosynthesis and Chemical Evolution, given at the Swiss Society for Astronomy and Astrophysics (SSAA). Edited by B. Hauck, A. Maeder and G. Meynet. Publisher: Geneva Observatory, CH-1290 Sauverny, Switzerland, 1

[412] Wright E. L., 1997, American Astronomical Society, 191st AAS Meeting, Bulletin of the American Astronomical Society, Vol. 29, p.1354

[413] Wright E. L., 1998, ApJ, 496, 1

[414] Wright E. L., Reese E. D., 2000, ApJ, 545, 43

[415] Wright E. L., 2001, ApJ, 553, 538

[416] Wright E. L., Johnson B. D., 2001, submitted to ApJ (astro-ph/0107205)

[417] Wu X., Xue Y., 2001, ApJ, 560, 544

[418] Yoachim P., Dalcanton J. J., 2005, ApJ, 624, 701

[419] Yoshida N., Abel T., Hernquist L., Sugiyama N., 2003, ApJ, 592, 645

[420] Zaggia S. R., Piotto G., Capaccioli M., 1997, A&A, 327, 1004

[421] Zaroubi S., Thomas R. M., Sugiyama N., Silk J., MNRAS, submitted, astro-ph/0609151

[422] Zdziarski A. A., Svensson R., 1989, ApJ, 344, 551 [ZS89]

[423] Zhang L., Chen X., Lei Y.-A., Si Z., 2006, submitted to PRD, astro-ph/0603425

[424] Zinnecker H., Keable C. J., Dunlop J. S., Cannon R. D., Griffiths W. K., 1988, The Harlow Shapley Symposium on Globular Cluster Systems in Galaxies. Proceedings of the 126th Symposium of the International Astronomical Union, held in Cambridge, Massachusetts, U.S.A. August 25-29, 1986. Edited by Jonathan E. Grindlay and A. G. Davis Philip. Kluwer Academic Publishers, Dordrecht, 603

Acknowledgements

I thank all who read my thesis from the first to the last page and survived..